POLITECNICO DI TORINO

Master of Science in Aerospace Engineering

Department of Mechanical and Aerospace Engineering

Master Thesis

Analysis of the energy storage and thermal control subsystems of the Mars Science Laboratory rover

Supervisors:

Maggiore Paolo

Dalla Vedova Matteo Davide Lorenzo

Candidate:

Pittari Andrea

March 2021

Abstract

Interplanetary travel has always fascinated the human mind, especially the exploration of new environments to understand their habitability and whether they have hosted life in the past or present. The primary purpose of this thesis is to provide an overview of a mission to the planet Mars. Initially, an introduction of the possible forms of energy is shown, thanks to which a spacecraft can be powered. Subsequently, the focus is on energy production using Radioisotope Thermoelectric Generators (RTGs). For interplanetary and deep-space missions far from the Sun, it is inefficient to design a power system based on solar energy due to the solar radiation's weakness. Several missions have been implemented using a radionuclide power system such as: Cassini, New Horizons, Galileo, Ulysses, Pioneer 10&11, Voyager 1&2, MSL/Curiosity, Perseverance, etc. The use of MMRTGs has several advantages such as: 1) their power production does not depend on the spacecraft orientation and shadowing; 2) they guarantee the independence of distance from the Sun; 3) they provide low power levels, but for an extended period, and are not susceptible to radiation damage. The two most used radionuclides, Plutonium-238 and Americium-24, are discussed in more detail below, with their respective half-life and specific powers. Chapter 3 presents the MSL-rover's ten scientific instruments that work in synergy to acquire information about the geology, atmosphere, environmental conditions, and potential biosignatures on Mars. Each instrument's power consumption and the range of operating temperatures are described in detail to size the batteries and the thermal control system. Chapter 4 explains the reason for choosing a particular electrochemical cell, rather than others, in a specific configuration to enable the rover to supply payloads even in the highest power-demanding situation. The analysis leads to the solution proposed by NASA JPL, with all the parameters within the mission requirements, but with a slight variation in the number of strings in parallel, due to the conservative choice to consider higher power consumption. In the last chapter of the thesis, the thermal control system is sized (knowing the operating temperature ranges of each scientific instrument onboard the rover), trying to determine the volumetric flow rate required to keep the rover's avionics within the allowed temperature limits.

Acknowledgment

Contents

List of Figures

List of Tables

Acronyms and Abbreviations

$\mathcal{M}$	Molar mass
A	Mass number
N	Neutron number
Z	Atomic number
Ah	Ampere-hour
g	Gram(s)
h	Hour(s)
kg	Kilogram(s)
V	Volt
W	Watt
AFC	Alkaline Fuel Cell
AFTL	Allowable Flight Temperature Limit
Am	Americium
AMPPEX	Americium and Plutonium Purification by Extraction
AOCS	Attitude and Orbit Control System
APXS	Alpha Particle X-ray Spectrometer
ASIC	Application-Specific Integrated Circuit
ATR	Advanced Test Reactor
ATS	Air Temperature Sensor
AVL	Allowable Voltage Limits
AWG	American Wire Gauge
BL	Boundary Layer
BOL	Beginning Of Life
C&DH	Command and Data Handling
CCD	Charge-Coupled Device
CDSCC	Canberra Deep Space Communications Complex
ChemCam	Chemistry and Camera
CheMin	Chemistry and Mineralogy

CHIMRA	Collection and Handling for In-Situ Martian Rock Analysis
CHRS	Cruise Heat Rejection System
DAN	Dynamic Albedo of Neutrons
DE	Detectors and Electronics
DEA	Digital Electronics Assembly
DFE	Direct From Earth
DNS	Direct Numerical Simulation
DoD	Depth of Discharge
DOE	U.S. Department of Energy
DOF	Degree Of Freedom
DRT	Dust Removal Tool
DTE	Direct To Earth
EDL	Entry, Descent and Landing
EMW	Electromagnetic waves
EOL	End Of Life
EPS	Electrical Power System
FDLF	Fully Developed Laminar Flow
FDTF	Fully Developed Turbulent Flow
FOV	Field Of View
FPA	Focal Plane Assembly
FPGA	Field-Programmable Gate Array
GC	Gas Chromatograph
GCRs	Galactic Cosmic Rays
GDSCC	Goldstone Deep Space Communications Complex
GMM	Generalised Method of Moments
GPS	Gas Processing System
GTS	Ground Temperature Sensor
H	Hydrogen
Hazcams	Hazard avoidance cameras
HFIR	High Flux Isotope Reactor
HGA	High-Gain Antenna
HS	Humidity Sensor
HX	Heat exchanger
IC	Interband-Cascade
ICU	Instrument Control Unit
IFOV	Instantaneous Field Of View
INL	Idaho National Laboratory
JPL	Jet Propulsion Laboratory

LES	Large Eddy Simulation
LMST	Local Mean Sidereal Time
lpmm	Line per millimeter
LVDS	Low-Voltage Differential Signaling
LWR	Light-water reactor
MAC	Maximum Allowable Current
MAHLI	Mars Hand Lens Imager
MARDI	Mars Descent Imager
Mastcams	Mast Cameras
MCFC	Molten Carbonate Fuel Cell
MDSCC	Madrid Deep Space Communications Complex
MEX	Mars Express
MMRTG	Multi-Mission Radioisotope Thermoelectric Generator
MPFL	Mechanically Pumped Fluid Loop
MRO	Mars Reconnaissance Orbiter
MSL	Mars Science Laboratory
Navcams	Navigation cameras
NIR	Near-Infrared
Np	Neptunium
NVRAM	Non-Volatile Random-Access Memory
ORNL	Oak Ridge National Laboratory
PAFC	Phosphoric Acid Fuel Cell
PbSnTe	Lead Tin Telluride
PCB	Printed Circuit Board
PEMFC	Proton Exchange Membrane Fuel Cell
PID	Proportional-Integral-Derivative
PNG	Pulsing Neutron Generator
PS	Pressure Sensor
PS	Propulsion System
Pu	Plutonium
$Pu(C_2O_4)_2 6H_2O$	Plutonium (IV) oxalate
PuO_2	Plutonium dioxide
QE	Quantum Efficiency
QMS	Quadrupole Mass Spectrometer
RAD	Radiation Assessment Detector
RAE	RAD Analog Electronics
RAMP	Rover Avionics Mounting Platform
RCE	Rover Compute Element

RDE	RAD Digital Electronics
REB	RAD Electronics Box
REMS	Rover Environmental Monitoring Station
RH	Relative Humidity
RHRS	Rover Heat Rejection System
RMI	Remote Micro-Imager
RMS	Root Mean Square
RSE	RAD Sleep Electronics
RSH	RAD Sensor Head
RTP	Rubidium Titanyl Phosphate
RWEB	Rover Warm Electronics Box
S&M	Structure and Mechanism
SAM	Sample Analysis at Mars
SD	Solar Dynamic
SDD	Silicon Drift Detector
SDRAM	Synchronous Dynamic Random-Access Memory
SFE	Sensor Front-End
SKD	Skutterudite
SMS	Sample Manipulation System
SNAP	Systems for Nuclear Auxiliary Power
SNR	Signal to Noise Ratio
SOFC	Solid Oxide Fuel Cell
SSD	Solid-state Silicon Detector
SSIT	Solid Sample Inlet Tubes
TCS	Thermal Control System
TLM	Telemetry
TLS	Tunable Laser Spectrometer
TMM	Thermal Mathematical Model
TT&C	Tracking, Telemetry and Command
U	Uranium
UV	Ultraviolet
UVS	Ultraviolet Sensor
VIRENA	Voltage-Input Readout Electronics for Nuclear Applications
WS	Wind Sensor
XRD	X-ray Diffraction
XRF	X-ray Fluorescence

Introduction

The generation, management, and distribution of electricity on board a spacecraft are among the most critical prerogatives take into account during the design phase. All essential subsystems absorb a certain amount of energy to function correctly, and an anomaly in the energy distribution system can compromise the entire mission.

Since the launch of the first satellite (*Sputnik 1 - 1957*), the power required on board has increased dramatically, from about $1\,\mathrm{W}$ to thousands of watts, depending on the field of application, due to an increase in the operations to be carried out and the complexity of the devices on board. The most suitable energy source for a spacecraft depends on the mission's duration and the power required.

Purposes definition

This thesis aims to analyse the Mars Science Laboratory rover's storage system, comparing different space batteries to choose, through a series of requirements, the most suitable one to perform the required tasks during the entire duration of its mission to Mars. The battery has a narrow survival temperature range, and to ensure its survival in the severe Martian environment, it is essential to study a heating and cooling system in the event of strong solar activity associated with strong internal dissipation of the on-board avionics during a task requiring high power consumption or to survive all night at temperatures well below $0\,^{\circ}\mathrm{C}$. Therefore, the balance temperature without active control of the internal temperature in the worst cold and hot conditions is analysed, demonstrating the necessity of a Mechanically Pumped Single-phase Fluid Loop (MPFL) to monitor the internal temperature of the rover. The work has divided into 6 chapters analysing the different steps followed to study the subsystems mentioned above:

Chapter 1: Structure of an energy system This chapter introduces the state of the art of the spacecraft energy system, defining each component's function. Besides, the most important energy conversion mechanisms adopted in the design phase are described. The last section shows that it is unthinkable to use systems that depend on the Sun for interplanetary missions,

so it is necessary to find a solution to the problem, developing techniques that exploit nuclear energy to produce energy. This last section is important because it allows the introduction of the second chapter.

Chapter 2: Radioisotope Power Systems   This chapter introduces methods that exploit radioisotope decay to produce enough energy to power the spacecraft. After an overview of the systems used in the past for interplanetary missions, attention is focused on the electrical production system (i.e., *Multi-Mission Radioisotope Thermoelectric Generator*), adopted for the 2011 (*Mars Science Laboratory*) and 2020 (*Perseverance*) missions, explaining its components and operating principle, also describing the advantages and disadvantages of using this technology.

Chapter 3: Mars Science Laboratory rover   After introducing the structure of a spacecraft's energy subsystem and analysing how the MMRTG works, the focus is on NASA's Mars Science Laboratory mission, describing in detail each of the payloads that make up the rover, which investigates the Martian climate and geology and whether it has ever offered favourable environmental conditions for microbial life. For each component, the focus is on energy consumption and operating and survival temperature, so that the energy storage (batteries) and thermal control subsystems can be sized.

Chapter 4: Electrical energy storage subsystem   The information derived from the analysis of the power requirements of each payload of the MSL rover allows the dimensioning of the batteries, thus allowing the calculation of the number of cells for the series circuit and the number of cells for the parallel circuit to guarantee the correct nominal voltage and the proper operating current. This chapter compares different space batteries with the same input data to select the most suitable one to support mission's entire duration and understand what motivated NASA JPL to choose a specific battery rather than another.

Chapter 5: Heat transfer   This chapter describes the heat transfer laws between two thermodynamic systems at different temperatures. Heat transmission can occur in three ways: thermal conduction, convection, and thermal radiation (in the form of electromagnetic radiation). On Mars, all three modes occur because its atmosphere, although rarefied, consists mainly of carbon dioxide. The section on heat transfer by conduction focuses on wheels and suspension's thermal conduction, an essential study for defining the balance temperature.

Chapter 6: Thermal Control System   All the previous chapters are preparatory to the drafting of this chapter, which concerns the preliminary study of the thermal control of the rover,

so knowing all the thermal input and output powers, it is evaluated whether there is a need for active temperature control through the use of an MPFL or whether there is a need to use simple thermal control methods based on a passive connection between the inside and the outside. The analysis is carried out under worst-case hot and cold conditions, referring to the MSL rover landing point's latitude and longitude.

Conclusions The final part of the paper presents more efficient methods for managing the rover's internal temperature, which consists of creating a rover model so that it can be mathematically approximated. An alternative to the analytical approach is advanced software that allows the creation of models and combinations (in any configuration) of built-in objects of finite difference, finite element and lumped capacity.

1. Structure of an energy system

A satellite consists of several systems designed to meet specific requirements defined by the type of mission. All satellites require a standard set of subsystems classified into two groups: the *Payload*, which is the most important subsystem, and its requirements broadly define and size the spacecraft, so precisely, it consists of communication equipment in commercial satellites or scientific instruments in research ones; and the *Bus*, which represents all the remaining equipment grouped in different functional systems that support the payload. Of all the subsystems on board a spacecraft, the one that needs the most attention is the energy system that generates, stores, regulates, transforms, and distributes electrical energy to each spacecraft subsystem. Therefore, it is fundamental for the mission's success, and its functions represent the heart of the entire spacecraft. It allows to supply and distribute electrical energy to the single equipment in the various phases that characterise the whole mission (launch, transfer into orbit, or to planets, and duration in orbit or on the surface of planets).

1.1 State of art of an energy system

Technological growth has allowed the rapid development of energy systems, the backbone of each of which is shown in Figure 1.1. The basic components of the spacecraft energy system are:

1. Primary energy source: solar radiation, chemical fuel, radioisotopes, and nuclear reactors;

2. Energy conversion: may be photovoltaic, fuel cell, thermoelectric, all those appropriate mechanisms necessary to convert energy, to be used appropriately it on board;

3. Energy management: to work around the point of maximum power, it is essential to use appropriate devices, which manage the charge and discharge of batteries (if a secondary energy source is available) and which control the bus voltage to keep it as close as possible to the reference value;

4. Rechargeable secondary electric energy source: the use of rechargeable batteries, which differ from each other by the respective elements present in the battery cathode and anode, makes it possible to achieve medium-long term missions. A different result is observed in terms of energy density (Wh/l) and life cycle[1];

---

[1]It is the maximum number of charge and discharge cycles that a battery can perform up to the minimum voltage (cut-off voltage).

5. Payload: the set of hardware and software that allow interacting with the subject of the mission, which is the primary focus of interest for the mission;

6. Subsystems: single, predefined operating environment through which the system coordinates the workflow and resource use. They support the payload, allowing it to work in the on-design parameters, and ensure the mission's correct execution.
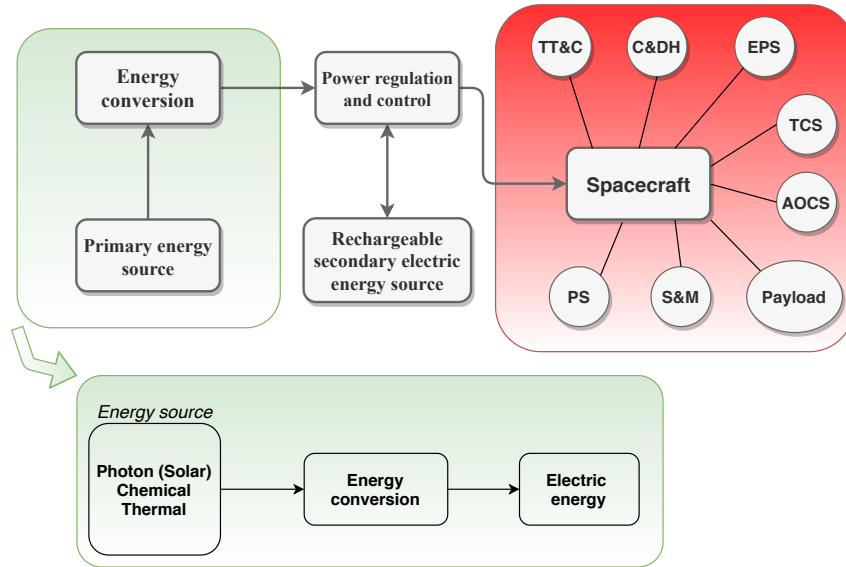
Figure 1.1: Structure of the energy system of a spacecraft.

1.2 Energy conversion mechanisms

As mentioned in Section 1.1, several energy sources can be used to provide power to a spacecraft. The technologies used to convert the source's energy form into usable onboard power depend on its energy source. For a given mission, the spacecraft level optimization study is ruled by choosing the best combination of essential components. Figure 1.2 shows that the use of batteries and *Fuel Cells* is limited to short-term missions. Simultaneously, Radioisotope Thermoelectric Generators (RTGs) or Photovoltaic Thermoelectric Generators (PTGs) are preferred as the primary energy source for medium to long-term missions. The latter are entirely inefficient as sun's distance increases since solar radiation's intensity decreases with the square of the distance.

1.2.1 Solar energy

Solar energy is the cleanest and most abundant renewable energy source available. Photovoltaic and solar dynamic generators can harness it.
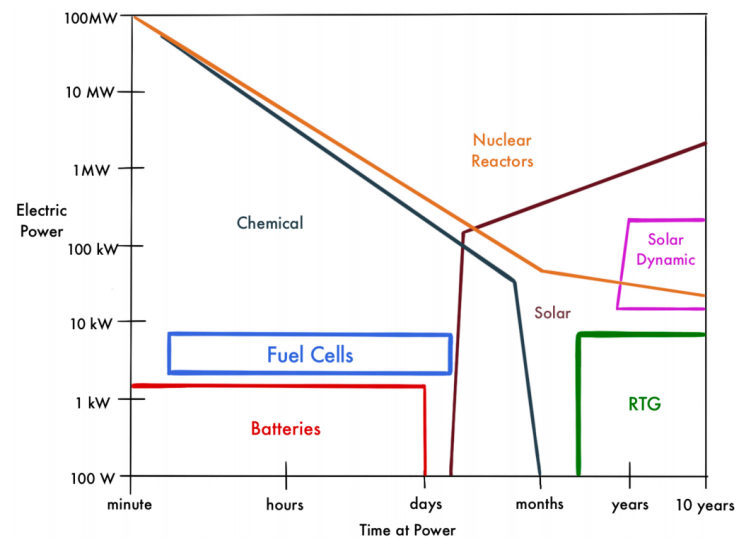
Figure 1.2: Common power generation technologies with associated mission duration.
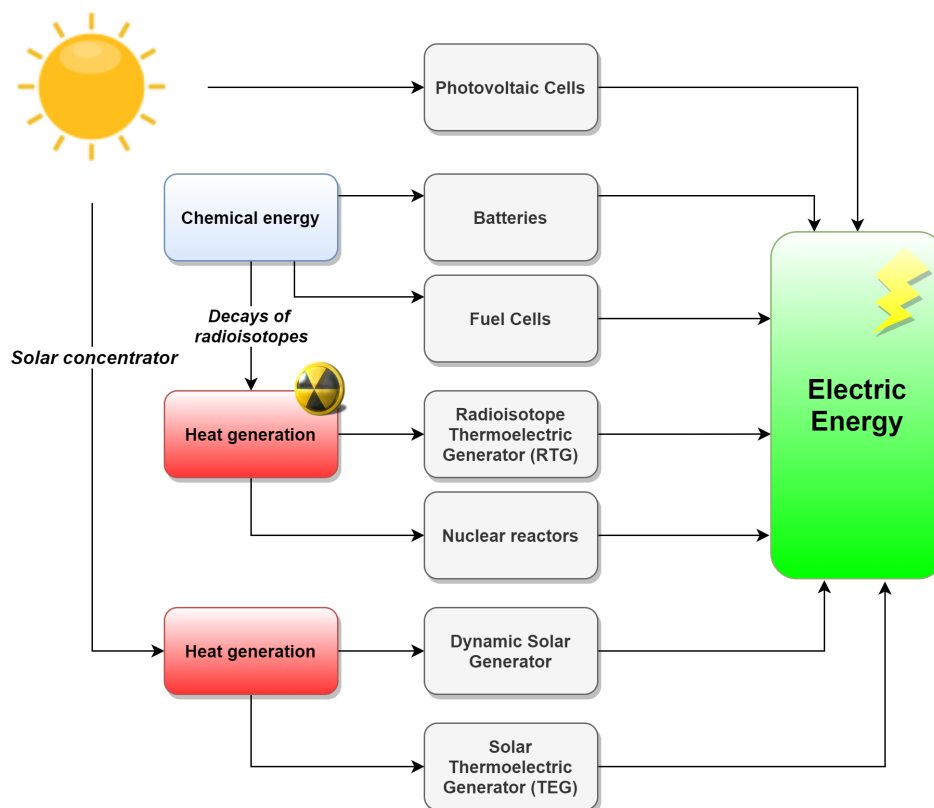
Figure 1.3: Different forms of energy and conversion mechanisms.

Photovoltaic generation   A photovoltaic cell is an energy harvesting technology that converts sunlight into usable current electricity through the *photovoltaic effect*.

This effect was discovered by the French physicist Antoine Henri Becquerel in 1839. Later in 1905, the German physicist Albert Einstein elaborated the physical-mathematical formulation of photoelectric conversion based on Max Plank's *quantum theory*. Einstein proposed that light is not a wave propagating through space. Still, it consists of discrete packets of energy (known as *photons*). When they strike a metal surface, they transfer their energy to the inner electrons ejected from atom with a kinetic energy proportional to the difference between the incident photon frequency and the metal threshold frequency. However, if the incident photons had a frequency less than the threshold no electrons are ejected.

Bell Laboratories produced the first silicon (Si) solar cell in 1954, and it was mounted in the Russian satellite, *Sputnik 1*, launched in 1957.

A photovoltaic cell consists of a *P-N junction* of two semiconductor materials suitably doped[2] to increase electrical conductivity and exploit the entire spectrum of incident solar radiation (Figure 1.4).
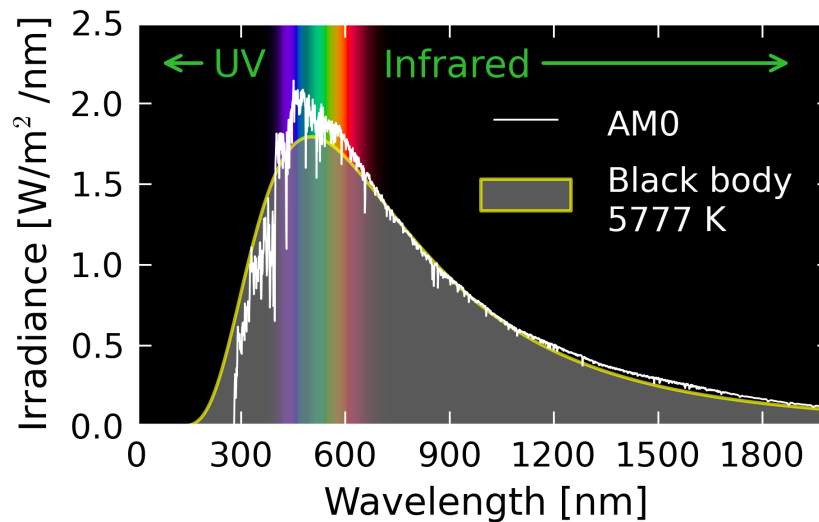
Figure 1.4: Spectrum of incident solar radiation.

Figure 1.5 shows the schematization of a solar cell: the photosensitive *N-region*, doped with excess electrons, generates a force, as a result of the electric field created, which produces a flow of electrons that moves from the N-region to the P-region through the union.

Dynamic Power System   Solar energy can be used in systems other than photovoltaic panels. An example is the use of a *Solar Dynamic Power System* to collect solar radiation (in the form

---

[2]P-type semiconductor is formed adding trivalent impurity to an intrinsic semiconductor, to create a large number of holes which can accept one electron, are known as *acceptor impurities*; N-type semiconductor is formed adding pentavalent impurity to an intrinsic semiconductor, to provides a large number of free electrons, are known as *donor impurities*
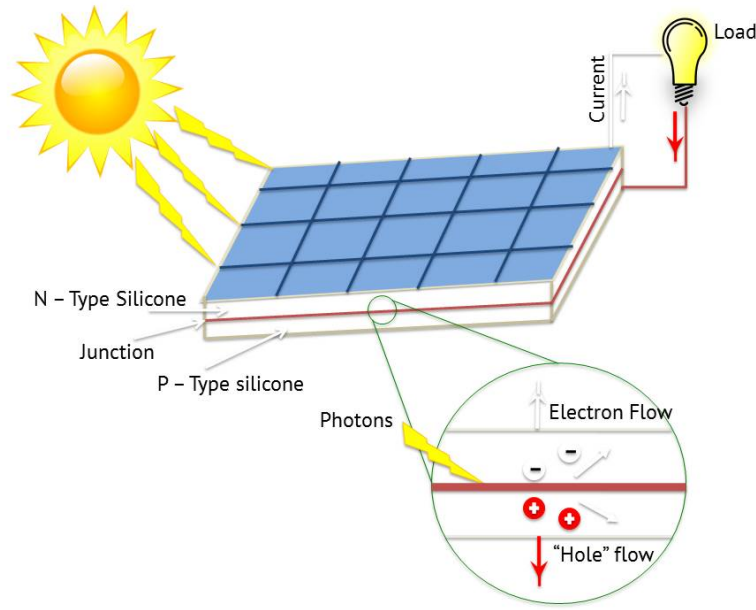
Figure 1.5: The schematized structure of a photovoltaic solar cell [1].

of heat) using a concentrator to generate steam from a working fluid, which drives a turbine, which in turn moves a rotary alternator to produce electrical power. According to the implemented thermodynamic cycle, the working fluid can be a liquid or an inert gas[3], such as a mixture of He and Xe (*PM = 40*).

Therefore, the dynamic energy production follows one of these thermodynamic cycles: Rankine (if the working fluid is a liquid), Stirling, or Brayton. The *State-of-the-art* SD system implements a **Brayton cycle engine** (Figure 1.6): from the receiver, the gas expands through a turbine, cools through a heat exchanger, and is pressurized in a compressor before being reheated. Furthermore, the waste heat is partly dissipated in deep space through a radiator panel and partially transferred to a liquid coolant. SD technology offers potential advantages in weight and efficiency, but is not yet proven in space flights. The system is adequately developed for use soon. They are expected to have lower specific mass, lower cost for reasonably high powers in the range of 10-100kW and long missions application, especially high-power LEO missions. Moreover, this system, compared with the Solar PV-Battery system, offer several benefits:

- High efficiency of the engine, about 20-40%, as compared to silicon solar cells, approximately 15-20%;

- Longer life cycle and less reduced end-of-life performance degradation;

- Reduced costs thanks to the elimination of costly semiconductor PV cells and batteries;

---

[3]Inert gas minimizes corrosion and sloshing problem due to the transport
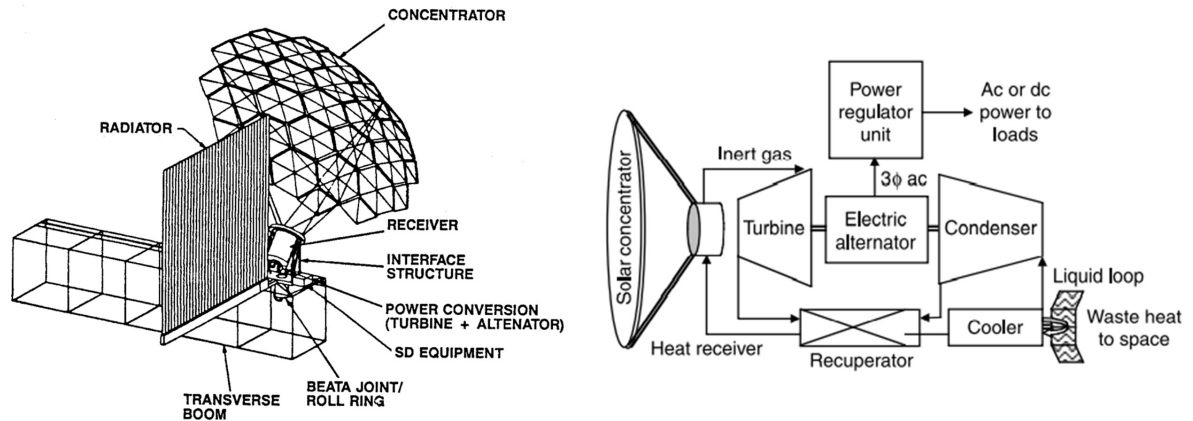
Figure 1.6: Schematization of a Solar Dynamic power system (on the left) and the Brayton cycle (on the right) [2].

- The receiver's high energy storage efficiency is about 85-90%, compared to 70-75% of the battery.

Reliability and long life are limited by mechanical parts fatigue and thermal degradation, due to high operating temperatures.

1.2.2 Chemical energy

Chemical energy is the energy stored in the bonds of molecules and atoms. Thus, it is the substance's capacity to undergo a change of composition, releasing energy (exothermic reaction) or requiring energy (endothermic reaction).

Batteries A device that stores energy in an electrochemical form is generally called an *accumulator* or *battery*, and it is the most widely used energy storage technology.

The batteries can be used as a primary power source, where the electrochemical reaction is irreversible (they must be replaced when the energy supplied is exhausted), for short-term missions or as a secondary power system with an efficiency greater than 70% for long-term missions. In the second case, the electrochemical reaction is reversible. After a discharge, it can be recharged and used simultaneously with a power generation system that uses an external source, such as solar energy.

The battery's operating principle is based on the *Nernst's Law*, that is the capacity of some metallic materials to gain or lose electrons when put in contact through an insulating separator, known as *electrolyte*, which allows the mass transfer (cations and anions) between the electrodes. The internal schematization of a typical electrochemical cell is shown in Figure 1.7. The battery consists of one or more electrochemical cells connected in a series–parallel circuit

9
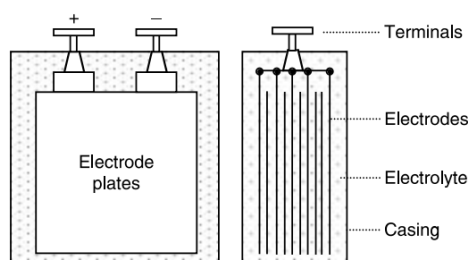
Figure 1.7: Structure of an electrochemical cell [2].

pattern to obtain the required current and voltage.

During the discharge phase, the more electronegative electrode (anode) loses electrons under-going oxidation[4], which means the *oxidation state*[5] of atoms increases. In contrast, the more electropositive electrode (cathode) gains electrons undergoing reduction, that is, oxidation state of atoms decreases, consequently between chemical species of the anode and cathode, *redox reactions* occur.

During the charging phase, the electrodes regenerate, which means that opposite reactions oc-cur: the previously anode oxidized, undergoes a reduction and, in turn, the cathode is oxidized. The theoretical cell capacity, denoted by *C*, is the cell's ability to transform a certain amount of matter into electrical energy, respecting *Faraday's first law*[6]. It is defined as the ampere-hours (Ah) charge transferred by a steady current of one ampere flowing for one hour at room tem-perature.

Furthermore, the theoretical voltage depends solely on the electrochemical reduction potential at 25 °C of the elements or molecules at the anode and cathode obtained by developing *Nernst's equation*. Different technologies of rechargeable batteries are shown in Table 1.1.

Fuel Cell   Figure 1.2 shows that it is impossible to supply energy to the loads for a few days or weeks through primary batteries; for this reason, fuel cells are used. The operating scheme is shown in Figure 1.8. Fuel cells consist of an anode, a cathode, and a solid or liquid electrolyte, allowing ions to move between the fuel cell's two sides. They generate electricity from the reaction of hydrogen (H_2) with oxygen (O_2) to form water[7], through a *static process* that is the reverse of the water electrolysis. However, this process is free of combustion because the hydrogen does not burn as in the internal combustion engine. Still, they cannot store electrical energy, so they must continuously supply fuel during the entire mission.

The *hydrogen–oxygen* fuel cells use hydrogen as fuel, oxygen as oxidant, and an aqueous acid

---

[4]An oxidized element loses mass. Consequently if it is reduced, it becomes more massive.

[5]The charge that the atom would take if the binding electrons were assigned to the more electronegative atom.

[6]One gram of equivalent mass, known as *equivalent weight* (atomic weight divided by the number of valence electrons), can develop an amount of charge equal to 96 487 C or 26.8 A.

[7]The water can be used to regenerate fuel cell through an electrolyzer or to support the crew on any manned missions.

Table 1.1: Different technologies of rechargeable batteries [2].

| **Technology** | **Energy** | | **Power** | | *Cycle life* | *Operating range* (°C) |
	Specific energy (Wh/kg)	*Energy density* (Wh/l)	*Specific power* (W/kg)	*Power density* (W/l)		
NiCd	$40-50$	$50-100$	$150-200$	$300-500$	$1000-2000$	-20 to 50
NiH$_2$	$45-65$	$35-50$	$150-200$	$200-300$	$2000-4000$	-10 to 50
NiMH	$50-70$	$140-180$	$150-200$	$300-500$	$1000-2000$	-10 to 50
Li-ion	$90-150$	$150-250$	$200-220$	$400-500$	$30000_{(50\% \text{ DOD})}$ $40000_{(40\% \text{ DOD})}$	-40 to 80
Li-polymer	$100-200$	$150-300$	> 200	> 400	$35000_{(25\% \text{ DOD})}$ $2000_{(100\% \text{ DOD})}$	-40 to 80
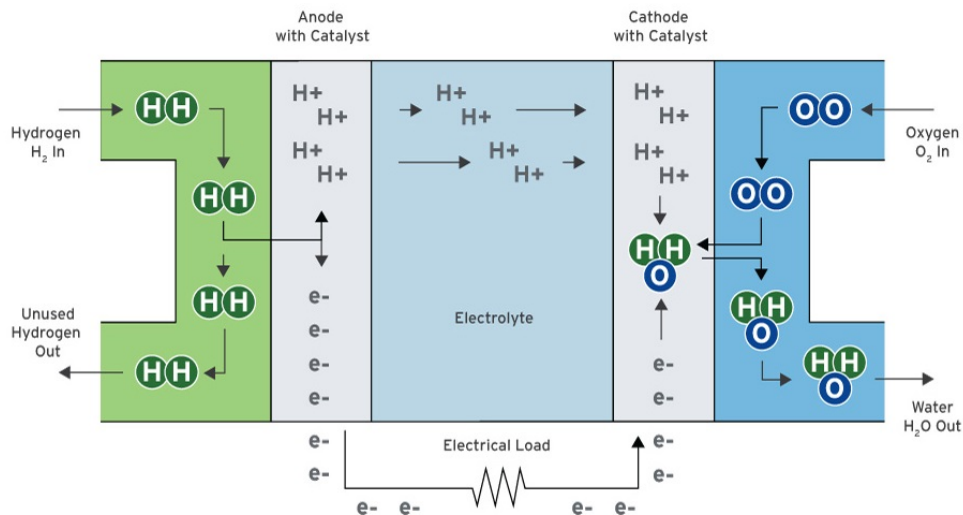
Figure 1.8: Proton Exchange Membrane Fuel Cell (PEMFC) schematization [3].

solution as electrolyte.

Anodic oxidation reaction: $2\,H_2 \longrightarrow 4\,H^+ + 4\,e^-$
Cathodic reduction reaction: $O_2 + 4\,H^+ + 4\,e^- \longrightarrow 2\,H_2O$
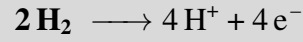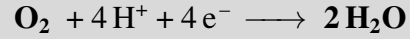
Their net reaction is $2\,H_2 + O_2 \longrightarrow 2\,H_2O$ with *energy release* in the process. The cell voltage of $1.23\,V$ is constant, and it depends solely on the oxygen electrochemical reduction potential at $25\,°C$, because that of hydrogen is, by convention, zero. However, even if the *Carnot cycle*[8] does not limit the conversion efficiency, the space-qualified fuel cell efficiency is around 10%. Table 1.2 shows different technologies of fuel cells.

Table 1.2: Various fuel cell performance compared [4].

Fuel Cell type	Typical Unit Sizes (kW)	Electric Efficiency
AFC	$\ll 100$	$\sim 70\%$
PEMFC	$0.1-500$	$\sim 50\%$
PAFC	$5-200$	$40-45\%$
MCFC	$800-2000$	$50-57\%$
SOFC	$2.5-100000$	$45-50\%$

1.2.3   Nuclear energy

For interplanetary and deep space missions, far from the Sun, it is inefficient to design a power system based on solar energy due to solar radiation's weakness. In Figure 1.9, is shown that for missions to the inner planets, characterized by higher solar flux, solar power generation is suitable. The main concern is to protect the spacecraft from high temperatures. For missions to the outer planets and deep space, it is essential to adopt different and reliable technologies, but at the same time efficient, mainly because in this case, it is necessary to protect the spacecraft from shallow temperatures. For long-term and deep space missions, Radioisotope Thermoelectric Generators (RTGs) or Nuclear Reactors must be used as power generation systems. For missions either too far or too close to the sun, RTGs becomes a strong candidate: the radioisotope decay of the fuel produces heat, which flows through devices made of two dissimilar materials[9], which in turn, when held at a different temperature, generate an electric potential difference linearly proportional[10] to the temperature difference (Figure 1.10). These devices, called *Thermocouples*, are connected in a series–parallel combination to obtain the desired voltage and

---

[8]This static process is isothermal, and the thermal-to-mechanical conversion is avoided.
[9]In space power application are semiconductor materials, one P-type and the other N-type (par. 1.2.1).
[10]A proportionality constant, which depends on the material properties, known as the *Seebeck coefficient.*, and the higher it is, the higher the voltage.
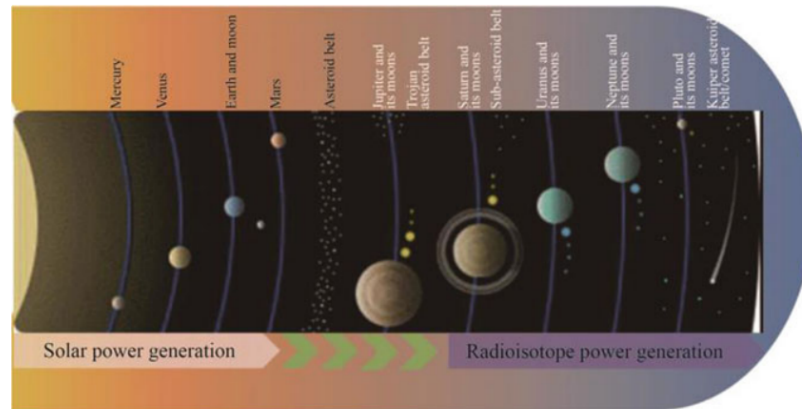
Figure 1.9: The more suitable power generation system based on the mission objectives [5].

current (Section 2.2) and are used to generate usable electric power due to the thermoelectric effect, known as *Seebeck effect*. The thermal power radiation decreases proportionally with the
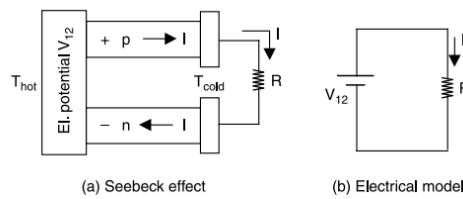
Figure 1.10: Thermoelectric converter [2].

residual mass, which decays following an exponential trendline and at a rate characterized by the half-life[11] ($\tau_{1/2}$) of the sample used.

The advantages of an RTG are the high reliability because there are no moving parts and the use over a long period. However, the power density of the radioisotope used inside is reasonably low; for this reason, the RTG is not feasible to build high power radioisotope generators. Therefore, it is regularly used for interplanetary missions requiring power levels of several hundred watts. Suppose the power demand increases in the 30 to 300 kW range. In that case, it is considered the use of a nuclear reactor with the disadvantage of installing a heavy radiation shielding to protect electronic components because the safe nuclear fuels affect the mission's budget.

---

[11]The time interval required for the initial substance quantity (such as a radioactive material) to be reduced by half; it is, essentially, an indication of how fast that process proceeds.

2. Radioisotope Power Systems

As already mentioned in Chapter 1 (Section 1.2.1), solar power is an excellent source to generate electricity onboard the spacecraft for most of the Earth or lunar orbits and places that offer adequate sunlight and natural heat. However, for interplanetary missions far from the Sun, a photovoltaic generator is not very efficient. For this reason, visiting the coldest and darkest places in the solar system could be impossible or extremely limited without the use of nuclear power. For those missions, an on-board nuclear energy source, known as *Radioisotope Thermoelectric Generator* (RTG), is used to generate usable electricity from the heat produced by the natural radioactive decay of some nuclei.

Besides, the RTG can be used to charge a set of lithium-ion batteries used to power a load (e.g., *Quadcopter*), as they have a high power density (Table 1.1). The first launch of an RTG-equipped spacecraft into Earth orbit was the *Transit 4A* with SNAP 3B (powered by $96\,\mathrm{g}$ of plutonium-238) and occurred in 1961, which provided the opportunity to explore the solar system for more than 50 years.

2.1   RPS missions

So far, over 45 RTGs have powered more than 25 US spacecraft, including the Apollo, Pioneer, Viking, Voyager, Galileo, Ulysses, Cassini, and New Horizons space missions, as well as many civil and military satellites:

- In 1969, *Nimbus III* was launched equipped with the **SNAP-19B RTG**, which provided an electrical power output of $28.2\,\mathrm{W}$ at the start of the mission;

- In 1972-1973, the *Pioneer 10* (1972-2003) and *Pioneer 11* (1973-1995) space probes were launched carrying a **SNAP-19 RTG**, which provided an electrical output of $40.3\,\mathrm{W}$;

- In December 1972, the *Apollo Lunar Surface Experiment Package* (ALSEP) was launched and installed on the lunar surface for all Apollo missions from Apollo 12 to Apollo 17 (in Apollo 11 the instrumentation consisted of a prototype of the ALSEP, called the *Early Apollo Scientific Experiments Package*), intending to study the lunar surface even after the astronauts returned to Earth. It was equipped with a SNAP-27 RTG, which was able to provide about $70\,\mathrm{W}$ of electrical power at the start of the mission;

- Later in 1975, the *Viking 1&2* landers and rovers were launched depending on RTG power sources (**SNAP-19 RTG**), which provided an electrical power output of $42.6\,\mathrm{W}$;

- In 1977, the *Voyager 1&2* space probes were launched, which sent images of distant planets (Jupiter, Saturn, Uranus, Neptune). They have operated for more than 43 years since launch and are expected to send signals powered by their RTGs until 2025. They are powered by a **Multi-Hundred Watt (MHW) RTG** that provides $158\,\text{W}$ of electrical power;

- *Galileo*, launched in 1989, carried two **General Purpose Heat Source (GPHS) RTGs** of $292\,\text{W}$ each and operated for nearly 14 years;

- *Ulysses* was launched in 1990 to study the heliosphere[1] and was equipped with a $292\,\text{W}$ **GPHS-RTG**;

- In 1996, three **RTGs** (each with 2.7 grams of plutonium dioxide-238) were deployed on the Mars Pathfinder lander, producing about $35\,\text{W}$ of electrical power and $1\,\text{W}$ of thermal power;

- The *Cassini* spacecraft, launched in 1997, was equipped with three **GPHS RTGs**, and each provided, also, $292\,\text{W}$ of power, carrying 18 *GPHS modules* totaling $33\,\text{kg}$ of plutonium-238 oxide onboard while exploring Saturn (1997-2017).

- *New Horizons*, launched in 2006 to study Pluto and its moons, was equipped with a single $292\,\text{W}$ **GPHS-RTG**;

- In November 2011, the *Mars Science Laboratory* rover (explained in detail in the next chapter), named Curiosity, was launched on Mars. It was equipped with a **Multi-Mission RTG (MMRTG)** and uses eight GPHS units with a total of $4.8\,\text{kg}$ of plutonium-238 dioxide as the source of the constant supply of heat, producing about $110\,\text{W}$ of electrical power at the beginning of its life to control the various subsystems, and its total weight is about 5 times that of its predecessors (*Spirit* and *Opportunity*[2]);

- In July 2020, the *Perseverance* rover was launched on Mars to follow the work of its "twin", Curiosity, which arrived on Mars eight years earlier and is still active. Its main task is to find traces of ancient microbial life forms and gather information on Mars' climate and geology by studying rock samples and regolith. Like Curiosity, Perseverance uses $4.8\,\text{kg}$ of plutonium-238 dioxide to produce about $110\,\text{W}$ of electrical power at launch, which are essential for powering the batteries, and which in turn allow the rover to carry out all the required activities.

---

[1]The heliosphere is the region of space influenced by the Sun and its magnetic field.

[2]The rovers previously sent to Mars, which are Sojourner (Mars Pathfinder, 1997), Spirit and Opportunity (Mars Exploration Rover A, 2004-2011; Mars Exploration Rover B, 2004-2019) did not use MMRTGs, but solar panels and batteries, with limited power and lifetime.

2.2   State of the art of an MMRTG

The *Multi-Mission Radioisotope Thermoelectric Generator* (MMRTG) (Figure 2.1) is a type of Radioisotope Thermoelectric Generator (RTG) developed and provided to NASA for civil space applications by the U.S. Department of Energy (DOE). The first MMRTG was mounted on the Curiosity Mars rover, which was launched in the *Mars Science Laboratory* (MSL) mission on 26 November, 2011, and landed on the surface of Mars on August 6, 2012 [6]. An MMRTG produces almost 2000 W of power at the beginning of life. Still it is not very
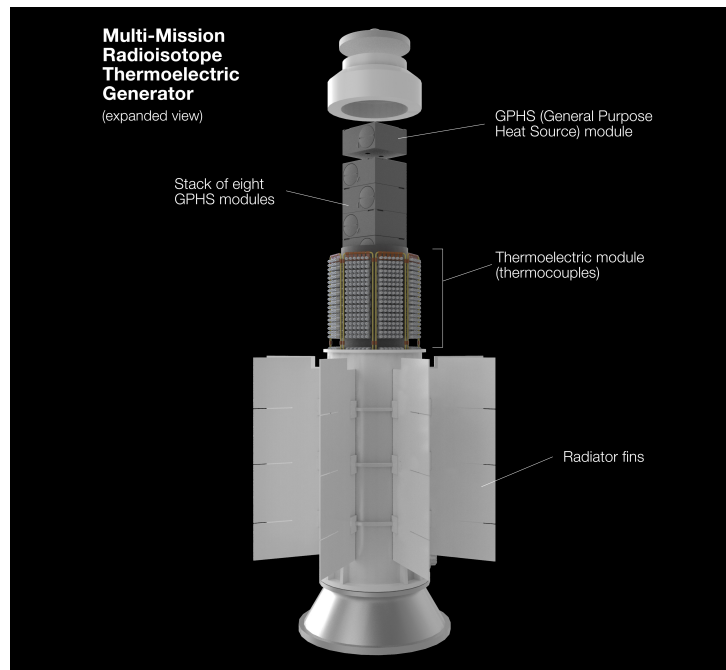
Figure 2.1: Multi-Mission Radioisotope Thermoelectric Generator [7].

efficient in converting heat into electricity: the most used combination of materials, such as plutonium-238 with Si–Ge TE cells, give about 7% conversion efficiency of the total generated power, about 110 W. The Heat Rejection System (*HRS*) uses some of the remainders to keep electronics warm to maintain temperatures in the operating range. Some of the waste heat is dissipated back to space or planet's surface via a radiator. An MMRTG is made up of different parts, each of which performs several functions:

- **GPHS modules**;

- **Cooling tube**;

- Heat Source liner;

- Heat distribution block;

- Loading cover;

- Mounting end cover;

- **Insulation**;

- **Fins**;

- **Thermoelectric modules**.

GPHS module   The General Purpose Heat Source (GPHS) module is the fundamental building block for the MMRTG, and it is designed to survive launch accidents because these modules contain and keep safe fuel, such as Plutonium-238. In Figure 2.2 are shown all constituent parts of a *GPHS module*:
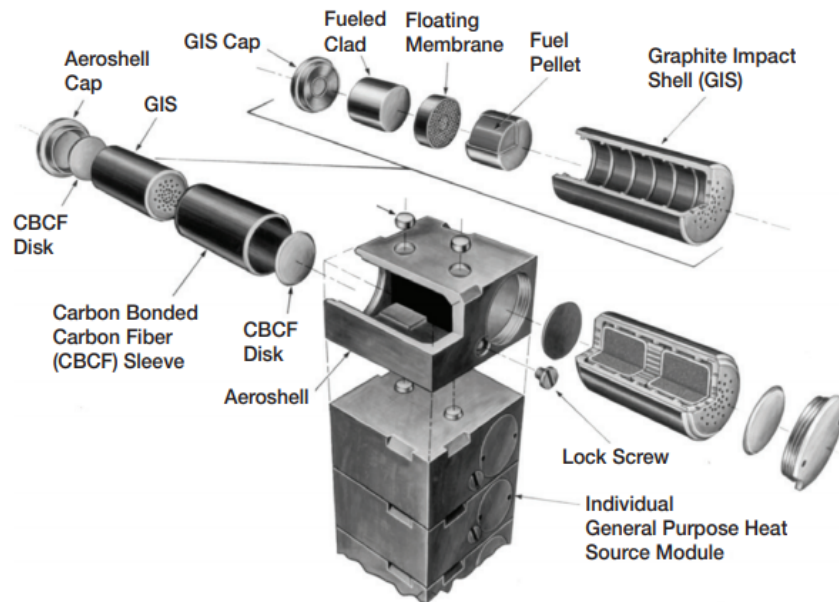
Figure 2.2: Illustration of a GPHS module [7].

◇ <u>Fuel Pellet</u>: the fuel is produced into ceramic pellets[3] of Plutonium-238 dioxide, $^{238}PuO_2$, encapsulated in a protective casing of a ductile, high-temperature iridium-based alloy, which blocks the alpha particles emitted in the decay, known as *Fueled Clad*. Besides, thanks to the ceramic compound, even if the pellets undergo high forces to break them, it will break into large blocks rather than dust that could be inhaled;

◇ <u>Graphite Impact Shell</u>: fuel clads, in turn, are encased and protected by graphite sleeves;

---

[3]Increase the melting point (Section 2.3.1) in case the cooling system fails.

◇ <u>Aeroshell</u>: the mentioned above elements are, in turn, enclosed and protected within nested layers of high stiffness and high chemical resistance carbon-fiber material, known as *Aeroshell*, which forms one of the eight GPHS modules that power an MMRTG.

Thermoelectric Modules   These solid-state devices convert heat flux into usable electricity, when any two dissimilar materials are maintained at different temperatures, through the Seebeck effect (Section 1.2.3). A pair of conductive materials joined in this way is called *Thermocouple*. A typical MMRTG has 16 *thermoelectric modules* connected in electrical series, and each module contains 48 thermocouples in an electrical series-parallel configuration for fault tolerance, increasing reliability. A thermocouple has a "hot shoe" and a "cold shoe", which is, in turn, separated into two parts: *N-Leg* and *P-Leg* (Figure 2.3a). The thermocouple's hot shoes is pressed by a spring loading system, mechanically integrated with the cold shoes (Figure 2.3b), to the heat distribution block typically made of AXF-5Q Graphite, while cold shoes touching the outer shell of the MMRTG and its convecting-radiating fins. The N-Leg Cold Shoe consists of PbTe (Lead Telluride) alloy named TE1010, while the P-Leg Cold Shoe is made up of PbSnTe[4]/TAGS[5]. Moreover, the P and N-Leg elements are suitably doped in order to increase and optimize the electrical conductivity. Besides, P-Leg is divided into two parts optimized to stay in contact with the hot and cold parts respectively, which typically operate at the temperature of $520\,°C$, for hot shoes, and $75\,°C$ for the cold shoes [8].
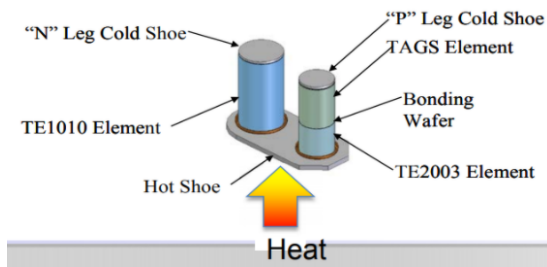
(a) Illustrative diagram of a thermocouple, with details on the different materials that make up the "hot shoe" and a "cold shoe".
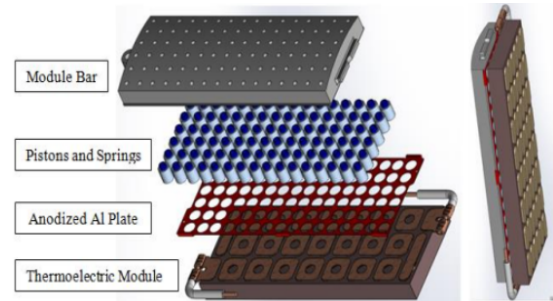
(b) Illustration of the assembly of thermoelectric modules.

Figure 2.3: Thermoelectric modules of an MMRTG [9].

Cooling tube   A fluid heat exchanger is used to dissipate the waste heat. Aluminium tubes (Al 6063) are used in MMRTGs that are designed to work in both vacuum and atmospheric conditions. The temperature can not fall below $-269\,°C$ $(4\,K)$ to not create strong temperature gradients in the materials.

---

[4]TE2003 element.

[5]The alloys $(GeTe)_x(AgSbTe_2)_{1-x}$, typically known as TAGS-x, are among the best performing p-type thermoelectric materials; the optimal composition value commonly used in MMRTG thermocouples is $x = 85$ (TAGS-85).

Insulation The thermocouples are surrounded and protected by insulating materials that minimize waste heat to the outside and reduce the sublimation rate of the thermoelectric materials. Different solutions have been proposed, such as using a *Sol-Gel coating*[6] of aluminium oxide (Al_2O_3), titanium oxide (TiO_2), or silicon (SiO_2): these materials strongly reduce the sublimation rate, but the coating is non-uniform and does not reach the required density to stem sublimation of the thermocouples material and to ensure good insulation. An *Auger Electron Spectroscopy*[7] (AES) indicates that Al_2O_3 provides the most favourable results of all the coatings and that Ge thermocouple component is the migrating species.

The problems of Sol-Gel process can be solved using the *Atomic Layer Deposition* (ALD) technique, based on a gas phase coating process which allows angstrom level precision, ensures very thin films and uniform coating; this process must be repeated for either 200 or 400 ALD cycle, to produce a thickness of $30/40\,\text{nm}$ of Al_2O_3. Therefore, the ALD-Al_2O_3 coating is typically used, because it leads to a significant reduction of the diffusion of Germanium (Ge), Tellurium (Te), and Silver (Ag) from the TAGS surface [10].

Fins As mentioned above, the MMRTG produces $110\,\text{W}$ to power the electronic systems, the remaining part is used to create the correct thermal operating environment, and some of the waste heat is dissipated to the outside. The only way to increase the heat flow is to increase the exchange surface area and to do so it is essential to install finned walls on the surface to be cooled, or if necessary to be heated. In Figure 2.1 are shown the technical specifications of an MMRTG.

2.2.1 Advantages and disadvantages of MMRTGs

As mentioned in the Table 2.1, over a period of time the available power supplied by the MMRTG decreases exponentially according to the law:

$$P_t = P_0 \exp\left(\frac{-0.693}{\tau_{1/2}}\,t\right) \tag{2.1}$$

where P_t is the power at time t after the initial time t_0 [11].

For a deep-space mission, two fundamental requirements: half-life of the isotope and its power density; for these reasons, often, depending on the duration of the mission, one isotope is chosen

---

[6]The Sol-Gel process involves the transition of the system from a liquid phase (Sol) to a solid phase (Gel) employing chemical reactions of hydrolysis and condensation of the metal precursors. Thanks to this technology, ceramic materials based on inorganic oxides are obtained, such as Al_2O_3, TiO_2, SiO_2, ZrO_2.

[7]It is a surface-sensitive analytical technique that utilizes a high-energy electron beam as an excitation source and when the previously excited atoms can relax, they release quantum energy, leading to the emission of *Auger electrons* (Appendix A), so with the kinetic energies of the ejected Auger electrons, it can be identified surface elements within the top $10\,\text{nm}$ of the piece.

Table 2.1: Technical specifications of an MMRTG.

Number of GPHS modules	8
Thermoelectric materials ($TAGS$)	
N-Leg	Lead telluride (PbTe, TE1010)
P-Leg	TAGS PbSnTe (TE20003)
Number of thermocouples	768
Beginning of life (BOL) power [W]	110
Estimate EOL power at 14 years [W]	98.48
BOL system efficiency	6%
Load voltage [V]	30
Fin-root temperature [°C]	157

rather than another (Table 2.2). Thus, for many missions Plutonium is used exclusively.

Table 2.2: Radioisotopes that can be used in an MMRTG. Polonium-210 provides a high power density (due to its high decay rate), emits almost only alpha α-particles (gamma emissions are insignificant), but is not widely used due to its very short half-life. Strontium-90 has a lower power density than plutonium, which translates into a lower temperature and, in turn, lower RTG efficiency, and also decays by β-emission (with low gamma emission), but the advantage is that it is highly available and cheap, being a high-yield waste product of nuclear fission. Plutonium-238 and Americium-241 are explained in detail in the next section.

Material	Shielding	Power density (W/g)	Half-life (years)
^{238}Pu	*Low*	0.57	87.7
^{90}Sr	*High*	0.46	28.8
^{210}Po	*Low*	140	0.378 (138 days)
^{241}Am	*Medium*	0.104	432.7

Advantages   The advantages of MMRTGs compared to other systems concern:

- Power production does not depend on the spacecraft orientation and shadowing: for this reason, they are suitable for missions with long eclipse periods;

- They guarantee the independence of distance from the Sun;

- They provide low power levels, but are not susceptible to radiation damage for an extended period.

Disadvantages   In addition to the advantages, disadvantages must also be considered:

- They affect the radiation environment of the spacecraft;

- The installation of the radioactive source requires careful handling procedures due to the risk of radiation;

- The high thermal gradient is essential for better energy conversion, however, this affects the thermal environment and vehicle configuration;

- They are an interference source for plasma diagnostic equipment.

2.3 Radioactive decay

The atomic nuclei can be divided into two groups:

- <u>Stable nuclei</u>: nuclei that remain the same for a very long period;

- <u>Unstable nuclei</u>: nuclei that are susceptible to decay or change by emitting particles generically known as *radiation*.

Among the periodic table elements: some are natural, and others are built in the laboratory. The element to which an atom belongs defines the number of protons in the nucleus, which, in turn, determines the number of electrons orbiting around the nucleus, and finally the atom chemical reactivity, which means how the atoms react with each other. Two nuclei belonging to the same element (i.e., the same proton number), may have a different number of neutrons, so they are *isotopes* (Appendix A) of a given element, which is commonly distinguished by the atomic species, and by the number of *nucleons* (i.e., neutron and proton present in the nucleus).

> *For example*:
> ⋄ H with 1 proton $\longrightarrow$ ^{1}H (Protium, hydrogen *stable* isotope);
> ⋄ H with 1 proton and 1 neutron $\longrightarrow$ ^{2}H (Deuterium, hydrogen *stable* isotope);
> ⋄ H with 1 proton and 2 neutrons $\longrightarrow$ ^{3}H (Tritium, hydrogen *unstable* isotope).

As mentioned above, there are stable and unstable isotopes of an element and up to Pb (Lead, $Z = 82$), each element has at least one stable isotope, with the two exceptions, Technetium ($Z = 43$) and Promethium ($Z = 61$), that do not have any stable nuclide. Besides, from the 83rd element of the periodic table all isotopes of all elements are unstable[8], and consequently,

---

[8]The instability of a nucleus depends essentially on the number of neutrons, because the protons present in the nucleus are subject to a significant electrostatic force, which means that particles with the same charge at a distance of 10^{-10} m (1 Å) should violently repel each other. This practically never happens because the protons are nucleus components and between them acts a very intense attractive force, known as *Strong Nuclear Interaction*, which balance the electrostatic repulsion. Actually, the nuclear interaction is not able to balance the electrostatic repulsion without the presence of neutrons, which stabilize the nucleus and do not have electric charge, in fact they contribute to increase nuclear interaction and minimize instability.

they decay by emitting ionizing radiation. The distinction between stable and unstable nuclei is not so marked; in fact, some stable nuclei have a high half-life and can be considered practically stable. In Figure 2.4 the graph shows the relationship between protons and neutrons in order to
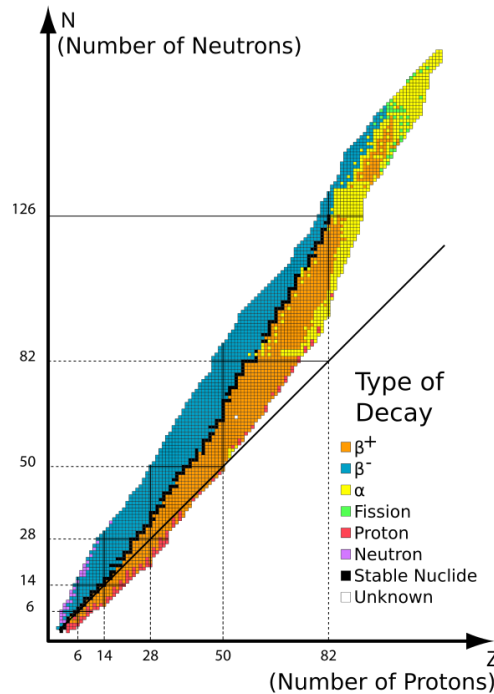
Figure 2.4: Isotope graph by type of nuclear decay.

have a stable nucleus. The distribution of stable nuclide coincides with the straight line $Z = M$ up to the atomic number $Z = 20$ and then deviates from linearity as Z increases; in fact, if the atomic number increases, the number of neutrons that allow stabilizing the nuclide also increases. The area around the nuclide stability line consists of unstable isotopes that spontaneously decay to corresponding more stable nuclides. Each radioactive isotope has preferential decay methods[9]:

- Decadimento α;

- Decadimento β^+;

- Decadimento β^-;

- Decadimento γ.

---
[9]For more details read the appendix A.

2.3.1 Plutonium properties

Plutonium is a radioactive chemical element with the highest atomic number present in nature, even if in small quantities. It was produced and isolated on December 14, 1940, bombarding with *deuteron* (nucleus of a deuterium atom, ^{2}H) Uranium-238 atoms. Initially, Neptunium-238 was synthesized, and, consequently, a beta decay forms *Plutonium-238* (94 protons + 144 neutrons). It produces mainly α-particle radiation[10] (helium atoms), which is relatively easy to shield against (can be blocked by simple barriers, such as a thin paper sheet) and few γ-radiation, making it not dangerous for humans and easy to handle. Like many radioactive isotopes of heavy metals, it is highly reactive and toxic, which means that it can cause cancer if inhaled or ingested due to contaminated substances. In Table 2.3 is shown that plutonium-

Table 2.3: Properties of pure plutonium-238.

^{238}Pu properties		
Molar mass	238	g/mol^{-1}
Density	1980	kg/m^3
Melting point	912.55	K
Half-life	87.7	years
Specific power	570	W/kg
Mode of decay	α-particle	-
α-energy decay	5.45	MeV
β-energy decay	0.011	MeV
γ-energy decay	0.0018	MeV
Specific activity	630	GBq/g

Table 2.4: Plutonium dioxide fuel form properties.

^{238}PuO$_2$ fuel form properties		
Molar mass	276.06	g/mol^{-1}
Density	960	kg/m^3
Melting point	2933.15	K
Half-life	87.7	years
Specific power	400	W/kg

238 has a relatively low melting point, and to solve this, it is used in a ceramic form (Table 2.4), also to reduce the possibility of dispersing the fuel in a launch or re-entry accident and to avoid inhaling microscopic particles. However, pure ^{238}Pu spontaneously oxidizes to ^{238}PuO$_2$ in an atmosphere of oxygen, takes on a yellow cast, but plutonium dioxide is mainly produced through the *calcination*[11] of plutonium oxalate, obtained during the reprocessing of nuclear fuel.

---

[10]Two methods can measure the energy of the α-particles: the first concerns absorption in thin mica of known thickness; the second concerns differential analysis, by electronic means, of the pulses produced by the α-particles in an ionisation chamber. The values from the two methods check closely at $5.45\,\text{MeV} \pm 0.05\,\text{MeV}$, obtained from direct comparison with standard samples of other alpha activities of known energies.

[11]Calcination refers to heating a solid to high temperatures in air or oxygen; in fact, when the plutonium (IV) oxalate, $Pu(C_2O_4)_2 \cdot 6\,H_2O$, is ignited or calcined in air up to $300\,^\circ\text{C}$, it decomposes, producing oxides of carbon, and leaving plutonium dioxide, PuO_2, as a residue [12].

Plutonium production   As mentioned above, ^{238}Pu can be produced from ^{235}U (Figure 2.5) or directly from ^{237}Np (Neptunium-237, half-life $2.144 \cdot 10^6$ years), which is a by-product of nuclear reactors. Production of ^{238}Pu is a complex process, but it is possible to summarize this process in some essential steps:

1. Processing of materials before irradiation: in this phase, the ^{237}Np residues are purified and modeled to optimize the geometry to improve the production process, which means to create suitable ^{237}Np targets;

2. Irradiate the targets: in this phase, the targets are irradiate with a neutron beam in a nuclear reactor to transform ^{237}Np into ^{238}Pu;

3. Processing of materials: which means extracting, separating and purifying ^{238}Pu, and the remaining ^{237}Np, which in turn, can be recycled and used to make more targets. Besides, the ^{238}Pu is processed to make fuel pellets for *GPHS modules*.
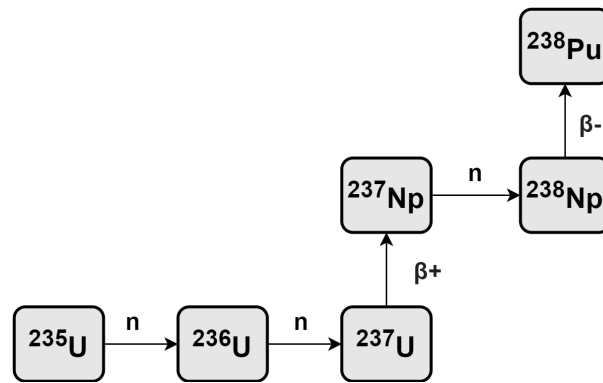
Figure 2.5: ^{238}Pu production.

NASA relies on *DOE's Idaho National Laboratory* (INL) and *Oak Ridge National Laboratory* (ORNL) to produce ^{238}Pu, specifically in two LWR reactors: the Advanced Test Reactor (ATR) at INL and the High Flux Isotope Reactor (HFIR) at ORNL, which give the United States the possibility of having access to the production of ^{238}Pu up to one kilo per year. Otherwise, if the targets are positioned correctly, annual production could increase considerably, for this reason, around the reactor cores, there are numerous empty cylindrical inlets placed in suitable positions, where targets can be inserted and irradiated. Moreover, in the ATR there are nine flux traps[12], six of these are dedicated full-time to the DOE's Office of Naval Reactors, so the target must be placed in other available positions, but if all the core positions were occupied by the target, the ATR could produce about $5 \, \text{kg}$ per year [13]. While HFIR can perform about $2 \, \text{kg}$ per

---

[12]Flux-trap type reactor consists of an annular fuel region surrounding a fuel-free moderating region; this configuration allows for moderating the fast neutrons leaking from the fuel to produce an area with high levels of thermal neutron radiation at the centre of the moderation region, ideal for isotope production with minimal impurities.

year of ^{238}Pu using standard target designs and reactor operating conditions. The plutonium-238 productions is limited by the lack of neptunium in nature. It is found in trace amounts in uranium ores. However, the United States can produce almost $5\,\mathrm{kg}$ per year for more than 50 years, reprocessing the cold war nuclear weapons by-products.

2.3.2 Americium properties

Americium ($_{95}$Am) is a radioactive chemical element of the actinide series and can be produced in large quantities in the form of the isotope ^{241}Am (95 protons and 146 neutrons). It is a synthetic white-silvery metal element more highly electropositive than uranium, neptunium, or plutonium. It can be prepared only by the action of powerful reductants on anhydrous americium salt at high temperatures. Moreover, the ^{241}Am is another energy source (Table 2.5), favoured by the European Space Agency, though it has high levels of relatively low-energy γ-radiation.

Americium-241 production   The target materials which have been successfully used in the production of these isotopes are ^{238}U, ^{237}Np and ^{239}Pu. The energetic helium bombardment of ^{238}U leads to the formation of plutonium isotopes of mass numbers between 236 and 241, of which ^{236}Pu, ^{238}Pu, ^{239}Pu are known to be beta-stable. ^{241}Pu is shown to be unstable and decays with the emission of β-particles, leading to the production of ^{241}Am. Moreover, the helium and deuteron bombardment (Figure 2.6) of ^{237}Np and ^{239}Pu are capable of forming americium isotopes directly. Still, the use limits of these mainly concern the emission of electromagnetic radiation, such as X-ray or γ-radiation [14]. Americium fuel in ceramic form or oxide can

Table 2.5: Physical property of americium ^{241}AmO$_2$ [15].

^{241}AmO$_2$ properties		
Molar mass	241.06	g/mol^{-1}
Density	1200	kg/m^3
Melting point	2373.15	K
Half-life	432.7	years
Specific power	104	W/kg
Mode of decay	α-particle + *EMW*	-
α-energy decay	5.4857	MeV
γ-energy decay	0.0596	MeV
Specific activity	128	GBq/g

be produced economically at high isotopic purity by the *AMPPEX process* (Figure 2.7) developed by the UK's National Nuclear Laboratory, using stored plutonium (produced during the reprocessing of civil fuel). In fact, spent civil reactor fuel can be reprocessed to extract the
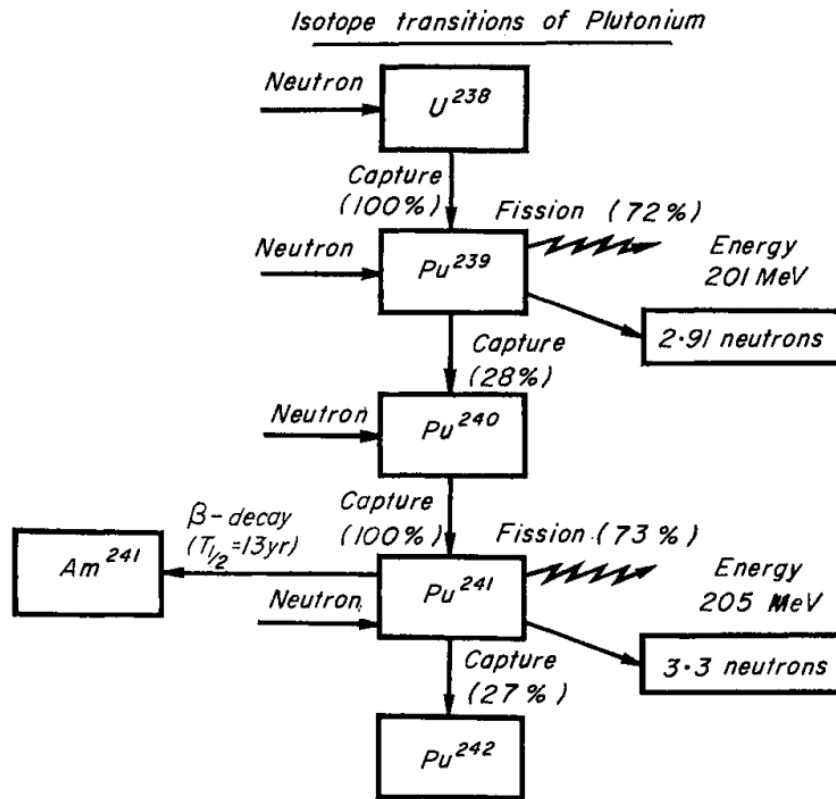
Figure 2.6: Synthesis and production of ^{241}AmO$_2$ [16].

plutonium isotopes by separating other fission products, such as uranium, and to store them for future utilisation in mixed oxide fuel to power either MMRTGs or nuclear reactors. The fuel extracting method is based on the dissolution of both plutonium and americium isotopes in nitric acid, enhanced by utilising a *silver II based solvent extraction method*. The process allows the separation of ^{241}Am from the plutonium and the introduction of oxalic acid leads to americium oxalate precipitation with, subsequent, calcination into an oxide ceramic powder of AmO$_2$ and other oxides, including Am$_2$O$_3$ [17]. Space agencies want to replace Plutonium-238 with Americium-241 for several reasons:

1. It has a reasonably high half-life, that is 432.2 years;

2. Although the power density is one quarter that of plutonium-238, despite this, however, small amounts of the isotope are required; for example, generation of $5\,\mathrm{W}$ of power requires either $62.5\,\mathrm{g}$ of ^{238}Pu or $250\,\mathrm{g}$ of ^{241}Am;

3. ^{241}Am is available at around $1\,\mathrm{kg}$ per year;

4. The fuel form of ^{241}Am, in ceramic form, can be produced economically and at high isotopic purity by separation from stored separated plutonium produced during the reprocessing of civil fuel [18].

The low power density, about one-quarter of ^{238}Pu, and the emission of γ-radiation limit its wide use. However, a protective tungsten shield is used to minimize any γ-photon emissions, but the advantages listed above guarantee a manageable impact on system mass and reasonably suitable production route.
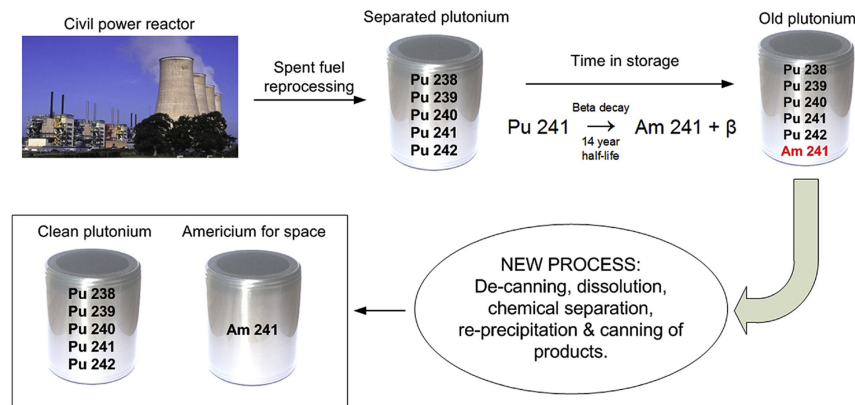
Figure 2.7: AMPPEX process [17].

3. Mars Science Laboratory rover

The objective of this chapter is to describe all the instruments installed on board the *Mars Science Laboratory* rover[1] to focus attention on energy consumption, that data will be taken up in the next chapter to make a *power budget* in order to calculate the flow rates needed to dispose of excess heat (keep the electronics warm or reject it outside).

The instruments of the Curiosity rover are state-of-the-art tools for acquiring information on the geology, atmosphere, environmental conditions and potential biosignatures on Mars; for mobility, sampling and photography; for sharing and communicating these information with the NASA Deep Space Network.

3.1 Instrument investigation

The MSL rover's scientific instruments are ten in number, and weigh around $75 \, \text{kg}$ (10 times more massive than those of previous Mars rovers) and working in synergy to achieve the same goal, which as mentioned above is to assess whether the Martian environment was ever habitable to life. Each performs specific functions in order to assess three conditions necessary for life: liquid water, specific chemicals and a source of energy. The body of the rover (*Warm Electronic Box*) is made of aluminium, measures about 163 by 117 by 46 centimetres and is painted white to keep the internal temperature under control and to reduce disturbance caused by reflected sunlight in the cameras (Figure 3.1).
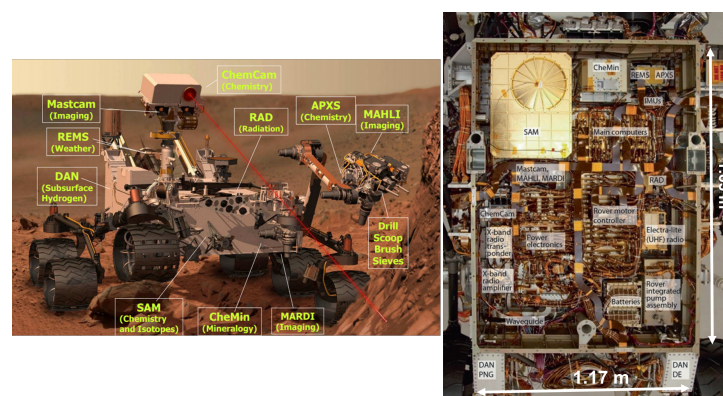
Figure 3.1: Location of the ten scientific instruments on the MSL rover and the respective electronics inside the rover that enable them to function. The other instruments that are not among the scientific payloads are also indispensable for the success of the mission [8] [19].

---

[1]The winning name "*Curiosity*" was submitted by 12-years-old Clara Ma of Lenexa, Kansas [8].

3.1.1   SAM: Sample Analysis at Mars

The Sample Analysis at Mars (SAM) consist of three different instruments whose main goal is to find various compounds of the element carbon (including methane) and the abundances of other lighter elements (like hydrogen, oxygen and nitrogen) potentially associated with life, in order to explore ways in which they are generated and destroyed in the Martian ecosphere and to evaluate whether Mars could have supported life in the past or present.

SAM tools

SAM is a suite of three instruments (Figure 3.2): a *Quadrupole Mass Spectrometer* (QMS), which separates elements and compounds by mass for identification and measurement; a *Gas Chromatograph* (GC), which heats rocks and soils until they turn into vapor, then separates escaped gasses into various components for analysis; a *Tunable Laser Spectrometer* (TLS), which can measure the abundance of isotopes of carbon, hydrogen, and oxygen in atmospheric gases. Usually, QMS and GC operate together for separation (GC) and identification (QMS) of organic compounds [20].
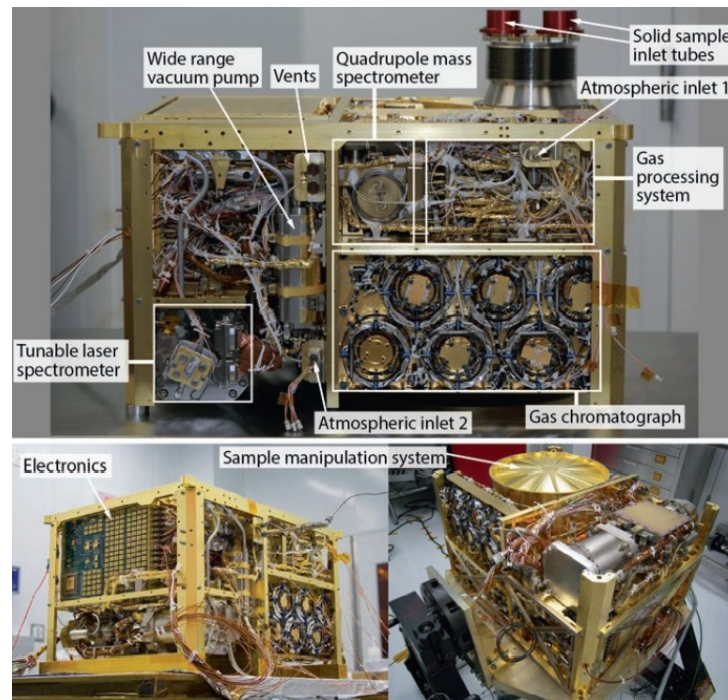
Figure 3.2: Component locations and sample inlets of the SAM instruments [8].

Gas Processing System   The Gas Processing System (Figure 3.3) manipulates the gases sampled from the atmosphere or extracted from solid samples. In addition, before their analysis by one

of the other SAM instruments, they are separated or enriched in trace species to improve sensitivity and accuracy in composition measurements. Additionally, it includes:

- 2 non-renewable helium reservoirs: Helium is used as a carrier gas to move sample gases through the GC system and to transfers evolved gases to both the QMS and TLS;

- 1 Low-Pressure Oxygen Gas Reservoir for combustion experiments;

- 1 Calibration Gas Cell, which contains a mix of four primary gases and traces of four higher-molecular-weight compounds (CO_2, N_2, Ar, XE_T, ^{129}Xe, PFTBA, IFN, DFBP and PFBP);

- 2 Turbomolecular Pumps (wide-range pumps) to move gases through the system: in the nominal mode of operation WRP1 is dedicated to pumping the QMS and WRP2 serves to evacuate the manifolds and the TLS, but they are also used for redundancy;

- 14 Manifolds, many Transfer Tubes wrapped with heaters, 2 High-Conductance Valves (HC1 and HC2) and 52 Micro-Valves (are shown in Figure 3.3 as numbered grey squares) welded directly to the manifolds to save mass;

- A Hydrocarbon Trap used to trap and transfer organic compounds to the GC system and, in addition, it can be cooled below room temperature to more efficiently trap species of interest and it can separate heavier from lighter noble gases;

- 2 Getters used to remove all active gases from the manifold, except CH_4 and the noble gases, and to pump them from the QMS at those times when the WRPs are not used;

- A Scrubber System that can remove CO_2 from the gas phase (the most abundant gas in Mars' atmosphere) and enrich other gases which are absorbed much more weakly. Additionally, this system is used to trap trace atmospheric water for subsequent thermal release and TLS analysis of its D/H ratio [21].

Quadrupole Mass Spectrometer   The Quadrupole Mass Spectrometer (QMS) uses electric and magnetic fields to separate charged particles according to their *mass-to-charge ratio* (m/z), specially it is sensitive to molecular masses over the range 1.5–$535.5\,\mathrm{Da}$, with a resolution of $0.1\,\mathrm{Da}$[2].

QMS scan begin after gas is introduced from the manifold to the ion source of the mass spectrometer through the valve V11 and, additionally, it can operate continuously, detecting the

---

[2]The *dalton* (Da) or unified atomic mass unit (u) is a unit of mass defined as the twelfth part of the mass of an unbound neutral atom of ^{12}C in its nuclear and electronic ground state.
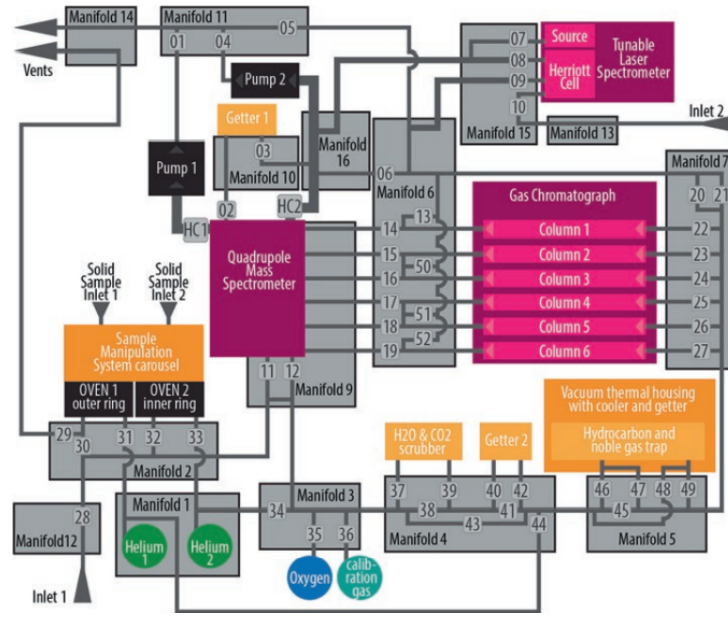
Figure 3.3: Schematic diagram of the SAM Gas Processing System [8].

number of ions every 0.02 seconds. It measures a single mass-to-charge ratio at a time: a specific mass range is chosen by changing the voltage of the power supplied to the spectrometer and if the mass range is very small, so small voltage steps are taken each time to reach maximum resolution, taking much longer. Alternatively, it can sweep an entire mass range using larger voltage steps. More specifically, a quadrupole consists of four parallel metal rods. Each opposing rod pair is connected together electrically, and a radio frequency (RF) voltage with a DC offset voltage is applied between one pair of rods and the other in order to achieve mass separation (Figure 3.4). The voltages $+(V_{dc} + V_{ac} \cdot \cos(\omega t))$ and $-(V_{dc} + V_{ac} \cdot \cos(\omega t))$, where
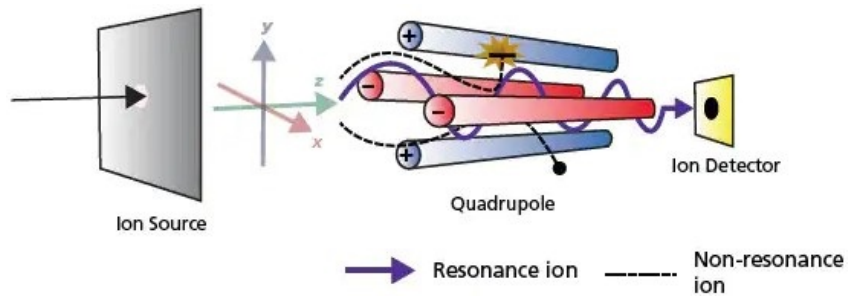
Figure 3.4: QMS operating model.

$\frac{\omega}{2\pi}$ is the frequency of V_{ac}, result in a two-dimensional quadrupole field of the form:

$$\varphi(x, y) = (V_{dc} + V_{ac} \cos(\omega t)) \left(x^2 - y^2\right) / R_0^2$$

where R_0 is the distance from the z-axis to the nearest rod surface, while x and y are the axes crossing both the z axis and nearest point of the adjacent rods [21]. The resulting electric field

forces the ions to follow a different oscillating trajectory for each m/z value. Only ions of a certain m/z ratio will reach the detector for a given ratio of voltages, other ions have unstable trajectories and will collide with the rods. This permits selection a particular ion with a specific m/z ratio by continuously varying the applied voltages. The instrument operating temperature range of -40–$50\,°C$.

Tunable Laser Spectrometer   The Tunable Laser Spectrometer allows to measure only three specific gases (CH_4, H_{20} and CO_2) and high-precision ratios of their isotopic species in C, H, and O. The method is a direct and non-invasive simple technique that can measure a precision of 2 parts per billion by volume the $^{13}C/^{12}C$ and D/H isotope ratios in CH_4; the $^{13}C/^{12}C$ and $^{16}O/^{17}O/^{18}O$ isotope ratios in CO_2; the D/H and $^{16}O/^{17}O/^{18}O$ in H_2O.

TLS consist of three chambers separated by windows: a *fore-optics* chamber containing lasers and mirrors, a *sample cell* and a *detector* chamber (Figure 3.5). It works by filling a cylindrical sample cell with gas, and then shooting into the sample cell two *semiconductor continuous-wave laser*, which can scan over specific wavelength regions, depending on gas abundances and isotope ratios:

- A *Near-Infrared* (NIR) tunable diode laser at $2.78\,\mu m$ for CO_2 and H_2O, which operates at room temperature with a single stage TEC;

- An *Interband-Cascade* (IC) laser at $3.27\,\mu m$ for CH_4, which operates at $-28\,°C$ with a two-stage TEC.

Mirrors at both ends of the cylinder allow IR light to bounce back and forth so many times giving the trace gases more opportunities to absorb IR light at wavelengths specific before it reaches the detector. By measuring the laser light intensity after it exits the cell, TLS can measure the abundance of gases. Therefore, the TEC temperature settings of the 2.78-micron laser (NIR) can be tuned to sequentially access two regions: one for carbon dioxide at $2.785\,\mu m$ and the other for water at $2.783\,\mu m$.

Gas Chromatograph   The Gas Chromatography distinguishes among different compounds by separating a gas mixture into its individual constituents, which are sent over time to the QMS. GC assembly consist of six complementary chromatographic columns, each tube (wound into coils) is $30\,m$ long, but only $0.25\,mm$ in internal diameter and provides a wide range of detection capability for both *hydrocarbons* and *atmospheric gases*. The inside surface of each column is coated with a different substance, which can grab hold of different gas molecules, depending on the greater or lesser affinity, and release them (Figure 3.2). In theory, each of the columns is designed to work on different ranges of molecular weights, even if there is significant overlapping of roles in many of the columns (such as GC1, GC2 and GC4). Nevertheless, each
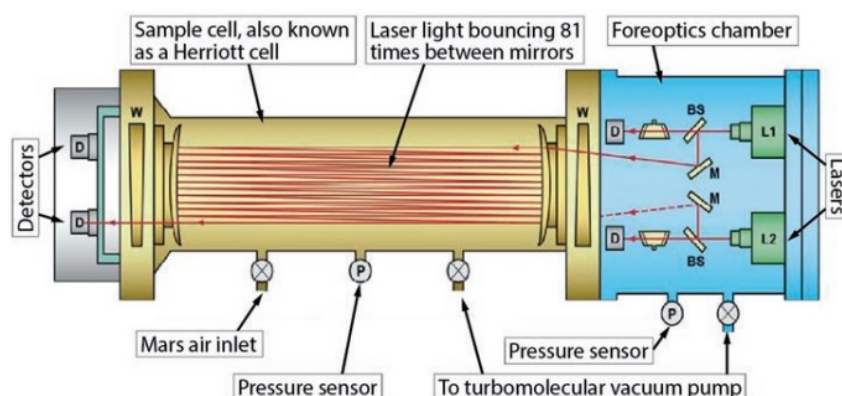
Figure 3.5: Diagram of the Tunable Laser Spectrometer. The TLS *Herriott Cell* is designed to provide 81 passes ($16.8\,\text{m}$) for CH_4 measurements and 43 passes ($8.93\,\text{m}$) for CO_2 and H_2O measurements. TLS can also avoid the mass interferences of QMS (e.g. CO, CO_2, N_2, N_2O, CH_3D, $^{13}CH_4$, HDO, $H_2^{17}O$, $^{13}CO_2$ and ^{17}OCO) or the need to convert CH_4 to CO_2 for isotopic analysis. Unluckily, the TLS has no capability for noble gas measurements, because IR spectroscopy relies on changes in *molecular dipole moments* with vibration [8].

column is independently heated by the PID heater circuit provided by the SAM electronics and only one column can operate at a time. Three of the six columns (GC4, GC5 and GC6) have injection traps to pre-concentrate the analytes and to release them after being flash-heated (at $350\,°\text{C}$) as quickly as possible in the GC columns to increase the separation power of the chromatograph [21].

Solid Sample Inlet Tubes   The Solid Sample Inlet Tubes consists of dual inlet funnels and tubes that direct the sample into the SAM Sample Manipulation System carousel. When SAM is ready to accept a solid sample, it positions a sample cup under an inlet tube, then the rover opens an inlet cover[3] and vibrates the SSIT using piezoelectric actuators (Figure 3.6) to prevent the incoming sample from sticking to the tubes.
 The system is designed to ensure that at least 98% of the sample passes through the tubes and enters the waiting sample cup.

Sample Manipulation System   The Sample Manipulation System is an electromechanical system with robotic features. It is an under-actuated (2 actuators, 3 degrees-of-freedom) system, which consists of a double-ringed carousel with 74 sample cups and is responsible for the sample handling. Thus, a solid material from SAM's sample inlet device is delivered through one of the two SSIT into any of 74 sample cups, this last sample cup selected is transported to a pyrolysis oven, which is designed to bring the sample to a maximum temperature of 900–$1100\,°\text{C}$ to release gasses for QMS, TLS, and GCMS analysis.

---

[3]A part of the Sample Acquisition, Processing, and Handling (SA/SPaH) system.

33
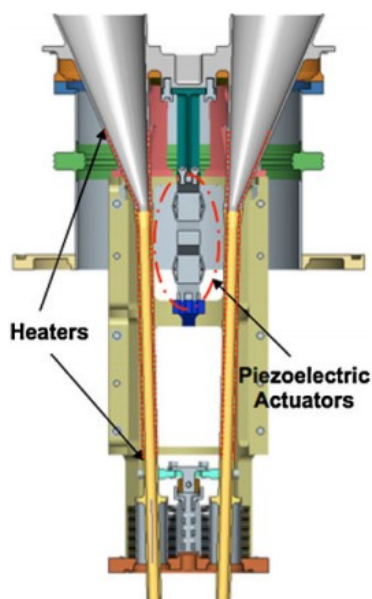
Figure 3.6: Model of the two SAM inlet funnels and tubes that transport the sample to the SMS cups. The tubes are $4.1\,\mathrm{mm}$ in diameter and are large enough to house any particles that have passed through the 1-millimetre sieve in CHIMRA. The heaters warm tubes to up to $120\,^{\circ}\mathrm{C}$ [21].
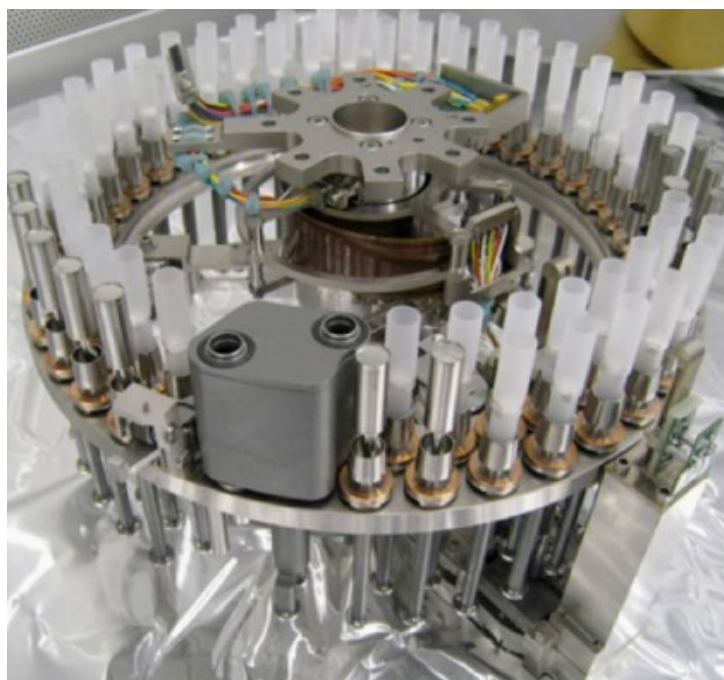
Figure 3.7: Double-ringed carousel with 74 sample cups [21].

Electronics and usage time   Many of SAM's components require heating to relatively high temperatures for operation, not only the ovens, but also tubes and manifolds operate at a temperature of $135\,°C$ in order to prevent sample from sticking to them; trap has to be flash-heated to $350\,°C$. These temperatures are all quite high, but other components (electronics, pumps) need to operate at lower temperatures. Thanks to the help of heaters, heat pipes and the Heat Rejection System (HRS), SAM, with more than 60 temperature sensors, is able to manage all these temperatures for cooling and heating equipment.

During SAM thermal vacuum qualification, the results measured after a full EGA/GCMS/TLS sequence of operations (lasting almost 6 hours) in a cold RAMP ($-30\,°C$) interface environment are shown in Figure 3.8. The complexity and high energy consumption of SAM experiments require prior planning, because a typical evolved gas analysis can take three sessions (preconditioning, sample preparation and delivery, and heating and evolved gas analysis) from 4 to 6 hours and can leave the rover with a relatively low battery state of charge. Therefore, SAM experiments are carried out over weekends, so that a weekend sol is used to recharge batteries. SAM has 8 electronics modules and can operate autonomously, turning itself off after finishing
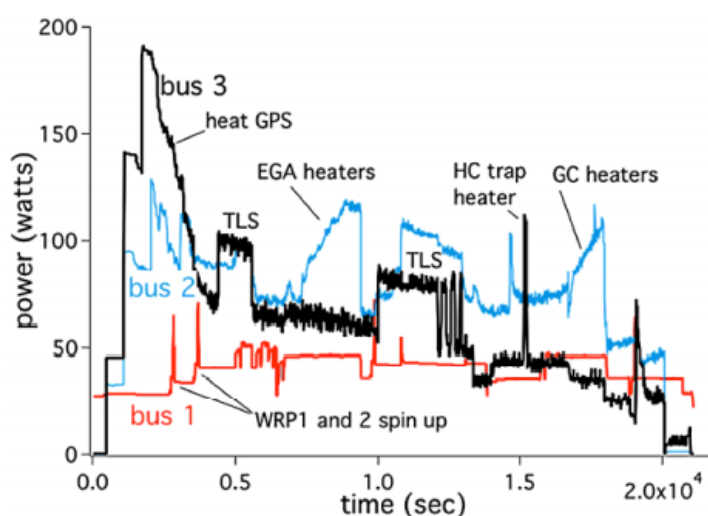
Figure 3.8: Energy consumption for each of the three MSL power buses during SAM thermal vacuum qualification [21].

an experiment, even while the rover is asleep. Total data volume for a single experiment is expected to be as much as $30\,\text{MB}$, which are stored in a $64\,\text{MB}$ flash memory array.

> **SAM - Power consumption**
> The interface with the rover takes place via 5 independent power feeds with 28 V as nominal voltage. The first Bus provides power to the instrument control functions, QMS and WRP system; the second one to TLS, GC, pyrolysis subsystem and regulated heater system. The remaining Busses (3, 4, and 5) provide power to switched resistive heater loads. The maximum possible power from all busses is approximately 990 W.
> *Idling operating mode:* 25 W (all on Bus 1);
> *Worst case power consumption:* 1050 Wh.

3.1.2 CheMin: Chemistry and Mineralogy

The Chemistry and Mineralogy instrument, located inside the main body of the MSL rover, identifies and characterizes past or present habitable environments by directly measuring the chemical and mineralogical composition of sediments and rocks on Mars, responding to the main objectives of the Mars exploration (Figure 3.9). The CheMin consist of two powerful analytical laboratory techniques: the X-ray Diffraction (XRD) and the X-ray Fluorescence (XRF). However, ChemCam and APXS identify the elements present in a target sample, while CheMin identifies how these elements are bonded together into minerals[4], depending on the physical and chemical conditions they have experienced and, in addition, integrating the analyses of these scientific instruments of the same samples maximizes the obtainable information by combining specific mineralogy with results from EGA/GCMS/QMS/TLS. There are differences between the various instruments in the size of the analysable samples [22]:

- CheMin analyse only drilled or scooped samples smaller than $< 150\,\mu m$;

- SAM can analyse the same sample size as CheMin, but it can also accommodate sizes smaller than $1\,mm$;

- APXS can analyse $1.7\,cm$ diameter areas on unmodified or brushed rock or soil;

- ChemCam can provide elemental compositional data on spots up to $7\,m$ distant and from 200 to $400\,\mu m$ in diameter and excavate several hundred micrometers into a sample.

As mentioned before, CheMin has 27 sample cells and can analyse as many as 74 samples of less than $150\,\mu m$[5] in diameter delivered by the SA/SPaH system during the nominal prime

---

[4]Minerals are natural crystalline materials of uniform inter-atomic structure with a well-defined chemical composition, which can provide important information to the environment in which a rock formed. CheMin has found in Mars rocks: Olivine, Pyroxene, Feldspar, Quartz, Magnetite, Hematite, Iron sulfides, Jarosite and Calcium sulfates [22].

[5]The requirement of less than $150\,\mu m$ powder is defined as the maximum crystal size that provides good diffraction.
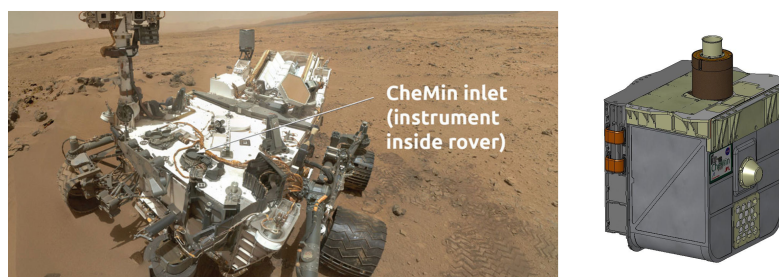
Figure 3.9: Chemin's position inside the main body of the MSL rover and its three-dimensional model [23].

mission (sample cells can be reused for additional analyses). The X-rays, through the lattice structures of minute crystals, generate a concentric ring diffraction pattern (this patten identifies the minerals present), which is recorded by a CCD detector. The impinging X-rays enables measurement of the elemental composition of the sample, producing X-ray fluorescence in the sample.

The CheMin X-Ray Source   CheMin has a micro-focus X-ray tube that produces a collimated X-ray beam using a cobalt anode. The beam-defining aperture on the Co anode is $50\,\mu m$ in diameter and produces an X-ray cone with an energy of $6.925\,keV$. A pinhole plate intersects the beam creating a $70\,\mu m$ wide collimated beam of X-radiation directed at the centre of the sample cell, illuminating only 2% of the entire material volume. After passing through the sample cell, the direct beam falls onto a beam trap mounted on the edge of the CCD detector. Additionally, the X-ray power supply is enclosed in a housing pressurized with a mixture of sulfur hexafluoride and nitrogen gas[6] [22].

The CheMin Sample Handling System   The CheMin sample handling system consists of: a funnel[7]; a sample wheel, which holds 27[8] reusable sample cells, mounted in pairs, and 5 reference standards, which are covered with high-efficiency filters to prevent their powder content from falling during wheel rotation; a sample sump, into which material is discarded after analysis (Figure 3.11). CheMin receives the sieved and portioned perforation powders from the SA/SPaH system (through the CHIMRA assembly) and vibrates three piezoelectric actuators

---

[6]This mixture must have a lower condensation temperature than the minimum expected in the rover body, to ensure that the gas never liquefies.

[7]The funnel contains a $1\,mm$ mesh screen to prevent larger grains from entering the CheMin sample processing system. Grains that do not pass through, remain there for the entire duration of the mission, although, in theory, no material is expected because the sample is pre-sieved to be less than $150\,\mu m$ in the CHIMRA sorting chamber to prevent clogging of the funnel screen [22].

[8]*Fourteen* have Kapton windows, which last longer but produce a peak in the diffraction patterns that could interfere with the detection of some clay minerals, and *thirteen* have Mylar windows, which exhibit a very flat diffraction background across, providing cleaner results, but are easily scratched and can be damaged by acidic samples [22].
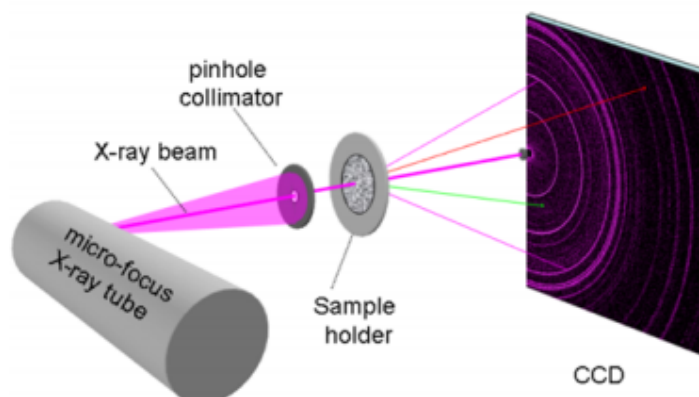
Figure 3.10: Geometry of the CheMin instrument [22].

around the funnel at a frequency range close to the resonance frequency of the sample cell to prevent sample sticking. CHIMRA provides a maximum of $76\,\mathrm{mm}^3$ of sample material entering through the rover deck (the CheMin inlet is protected by a cover to avoid contamination and clogging) and funnel into a sample cell with an active cell volume of $10\,\mathrm{mm}^3$ and a $400\,\mathrm{mm}^3$ miniature funnel-shaped reservoir above the cell, which holds excess material not used during analysis. Vibration dynamics are extremely important: the vibrations of the two sample cells in each pair balance each other, which means that little vibrational energy is transmitted to the rest of the instrument, but if the vibration happen at too low an intensity, phase separation may occur as a result of differences in size, density or shape between the individual mineral grains. To prevent this problem, CheMin periodically shakes the cells at increasing amplitudes to break up agglomerations and re-homogenise the material in the sample chamber. CheMin accepts from SA/SPaH and analyses samples with no more than 5% internal contamination between samples, mainly due to previous samples stuck in the funnel or left in previously used analysis cells (CheMin is capable of reusing each cell two to three times and performing 74 or more analyses during an extended mission). The cells are emptied after each analysis by turning the sample wheel 180° and vibrating the cell, so sample material is poured into a sump at the bottom of the instrument. Additionally, aliquots of a sample material may be poured directly to the sump through a *shunt* in the wheel or enter a previously used and appropriately cleaned sample cell, to reduce contamination, before receiving a second sample portion for analysis.

The CheMin Detector, XRD and XRF   CheMin uses a 600×1182 pixel E2V CCD-224 frame transfer imager, of which 600×582 pixels is the active area for data collection, which is typically exposed to X-ray photons for 5 to 30 seconds and can be quickly transferred to a 600×600 pixel
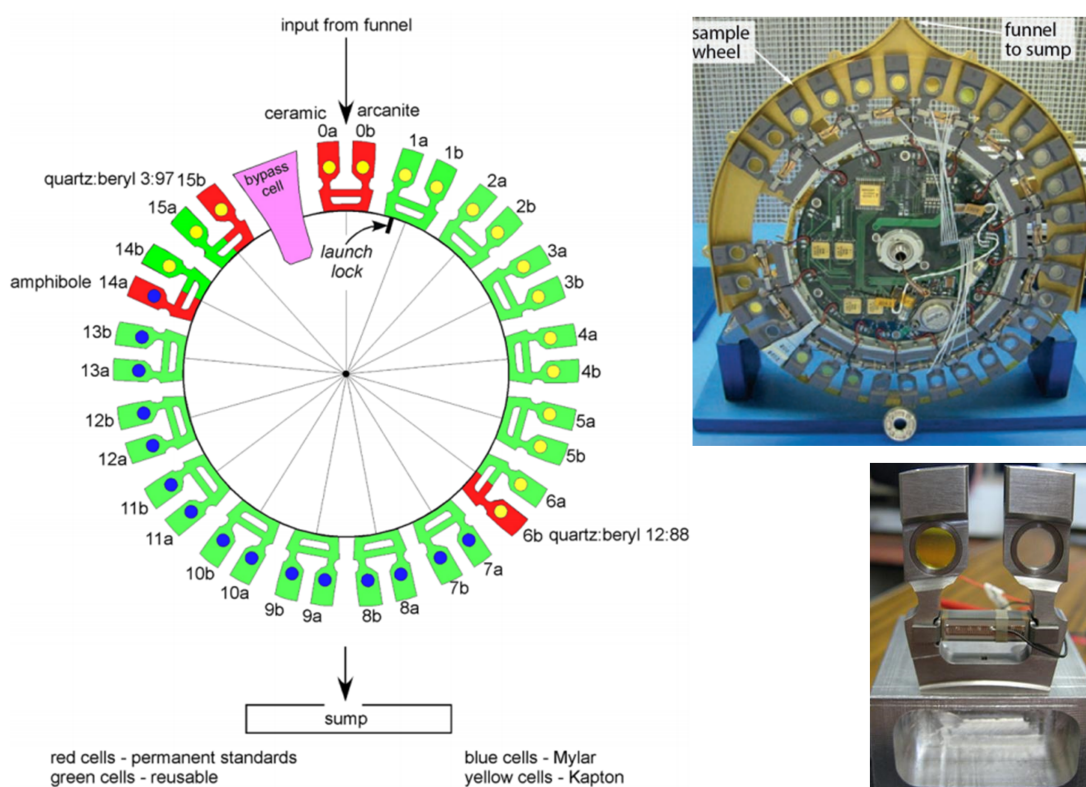
Figure 3.11: On the left: schematic diagram of the CheMin sample wheel. In green are shown the twenty-seven cells that can be reused for analysis and in red those that contain standard materials useful for calibration. The sample cells are filled at the top and dumped at the bottom. Middle: The CheMin sample wheel. The wheel is shown inverted in this image. On the right: assembled cell, ready for testing (yellow Kapton window on left and clear Mylar window on right) [22].

shielded area, the so-called *transfer frame*[9], to allow continuous data collection without the use of an X-ray shutter or electronically beam-suppressing device. The $40\,\mu m$ square pixels of the active area are unusually large for a CCD, compared to the $14\,\mu m$ of ChemCam's RMI, because when an X-ray photon impinges on the sensor it deposits thousands of electrons in an area tens of microns in diameter, so the large pixel size allows almost all of this charge to be captured in one pixel, rather than being spread over several pixels, so each time an X-ray photon hits the detector, not only the position but also the energy of the photon is recorded. In addition, a filter is placed in front of the CCD sensor to prevent it from being exposed to visible-wavelength photons (possible in the case of X-ray-induced optical fluorescence of the sample) during analysis, so a $150\,nm$ aluminium film supported by a $200\,nm$ polyimide film is suspended on a frame placed in front of the detector. When the X-rays reflected by the crystal lattice of the atoms in the sample constructively interfere (1st necessary condition) and the incidence (θ_i) and reflection (θ_r) angles are equal (2nd necessary condition), diffraction peaks are produced at different angles to the beam direction (*Bragg diffraction*). The diffraction angle 2θ ($\theta_i + \theta_r$) depends on the wavelength of the X-rays and the spacing between the atoms in the crystal lattice according to *Bragg's law*: $2\mathrm{d}\sin\theta = \mathrm{n}\lambda$. Thus, according to this expression, the CheMin detector can record X-rays diffracted at 2θ angles over the range $5°-50°$, with an angular resolution of $0.30°-0.35°$.

CheMin can store about 22 hours of data, up to 2730 images, which, since they cannot be transmitted to Earth, are processed by the rover's main computer, which composes 10 to 200 individual exposures into a single image, to form a smaller frame (*minor frame*) consisting only of pixels whose values correspond to the energy of the X-ray source ($6.925\,keV$). Thus, the CCD sensor is used to measure the charge generated by each photon (and hence its energy) and the diffracted X-rays hitting the detector produce a two-dimensional image (2-D diffractogram) that forms the diffraction pattern. Adding up the pixel values around the concentric circles of the 2-D image produces a 1-D model (1-D diffractogram), which is used by the CheMin team for mineral composition analysis. The individual peaks in the 1-D pattern can be diagnostic of specific minerals, because each mineral has a set of peak positions and intensities that determine its crystal structure, so all peaks are used to determine mineral abundances.

CheMin's X-ray fluorescence (XRF) detector is descoped from the instrument for economic reasons and perceived risks. The energy of the fluorescent X-rays depends on the elements present, in fact many X-rays are diffracted with the same energy as the cobalt source, while others of lower energy come from the X-ray fluorescence. The instrument is not sensitive to elements of mass less than potassium ($Z_K = 19$) as a result of the sample self-absorption, the aluminized light shield and the Mars atmosphere absorption [22]. Limited XRF data from the

---

[9]The CCD's frame-transfer region, protected by a metal bar, has pixels that are much smaller than those in the active region because they are designed only to hold the charge associated with an X-ray photon and not to absorb it.

CCD detector are provided when available and are useful in discriminating mineral phases, although data on the chemical composition of minerals are, purely, qualitative. A cryocooler, attached to the back of the CCD by a heat belt, brings the temperature of the detector to almost $48\,°C$ below the temperature of the Rover Avionics Mounting Platform (RAMP), between $0\,°C$ and $26\,°C$ during the mission, which is used as a heat sink by the cryocooler. Thus, the CCD detector operates between $-48\,°C$ and $-22\,°C$; in addition, dark currents[10] on the CCD are minimised by cooling.
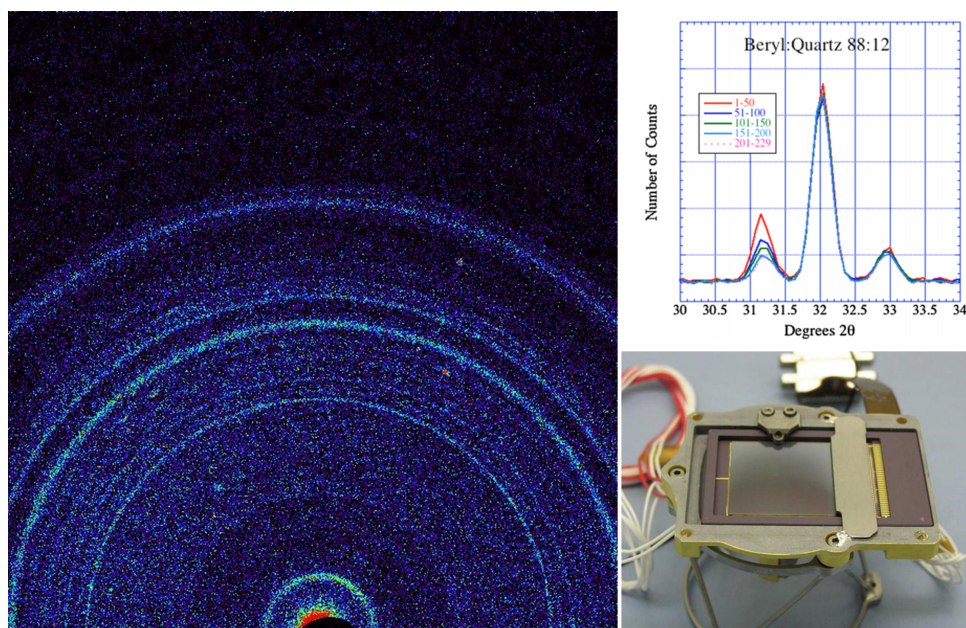
Figure 3.12: On the left: 2-D image of the diffraction pattern showing the results of the first analysis of Martian soil. The image reveals the presence of crystalline feldspar, pyroxenes and olivine mixed with some amorphous (non-crystalline) materials. The soil sample was taken from inside the Gale crater, where the rover landed [24]. Top right: Quantitative analysis of minor frames in the standard 88:12 Beryl:Quartz mixture (by weight) [25]. Minor frames were quantified using Rietveld refinement, which uses a non-linear least-squares algorithm to refine a theoretical line profile until it matches the measured profile; it becomes important when reflections are strongly overlapping. XRD highlights the maxima of Quartz 101 ($2\theta = 31.17°$) and Beryl 112 ($2\theta = 32.04°$) showing the analyses of 50 minor frames summed individually. However, the reduction in intensity of the Quartz 101 peak during the analysis clearly shows a phase segregation problem. Bottom left: the CheMin CCD, in which the active region (the exposed part in the centre) can be seen, while the frame transfer region of the CCD is the shielded part to the right of the active region [22].

Usage time   Each CheMin analysis can take up to 10 hours (typical overnight analysis) and repeated over two or more Martian nights to improve counting statics, (most sample are analysed

---

[10]Electric currents flowing through photosensitive devices.

for a total of $20-40$ hours) although useful data can be obtained in about $2-3$ hours. Actually, CheMin can continue to analyse a sample until a new sample is delivered for analysis, at which point the instrument usually dumps the old sample to receive the new one [8].

> **CheMin - Power consumption** [26]
> The MSL rover power system provides CheMin with $2\,A$ and $4\,A$ switches to supply the instrument with suitable current.
>
> *Normal operating mode:* $719\,Wh$.

3.1.3 ChemCam: Chemistry and Camera

The Chemistry and Camera (ChemCam) instrument mast package consists of two remote sensing instruments: the *Laser-Induced Breakdown Spectrometer* (LIBS), which measures elemental composition and a *Remote Micro-Imager* (RMI), which places the LIBS analyses in their geomorphological context. In addition, the mast package can be tilted or rotated for an optimum view of the targets. Both instruments, working together, can analyse a large number of samples and identify the chemical and mineral composition of rocks and soils, also help determine which targets are of sufficient interest to use the analytical laboratory tools for further testing. From a distance of up to 7 meters by firing a target, ChemCam is able to:

- Use multiple laser pulses to clean dust off of rock samples;

- Rapidly identify the kind of rock being studied and provide detail on its minerals and microstructure by measuring the elemental composition of the resulting plasma[11]; nonetheless, it is not able to analyse how the elements are arranged into minerals;

- Provide visual assistance during drilling of rocks and measure the abundance of all chemical elements in order to recognize ice and minerals with water molecules in their crystal structures.

Remote Warm Electronics Box - RWEB

The Mast Unit (MU) is located inside the RWEB (Figure 3.13). The maximum tolerable thermal excursion for the instrument health is between -40–$35\,°C$. Thermostats inside the EBOX activate survival heaters every night in order to maintain a minimum temperature of $-40\,°C$. The

---

[11]Extremely hot gas made of free-floating ions and electrons
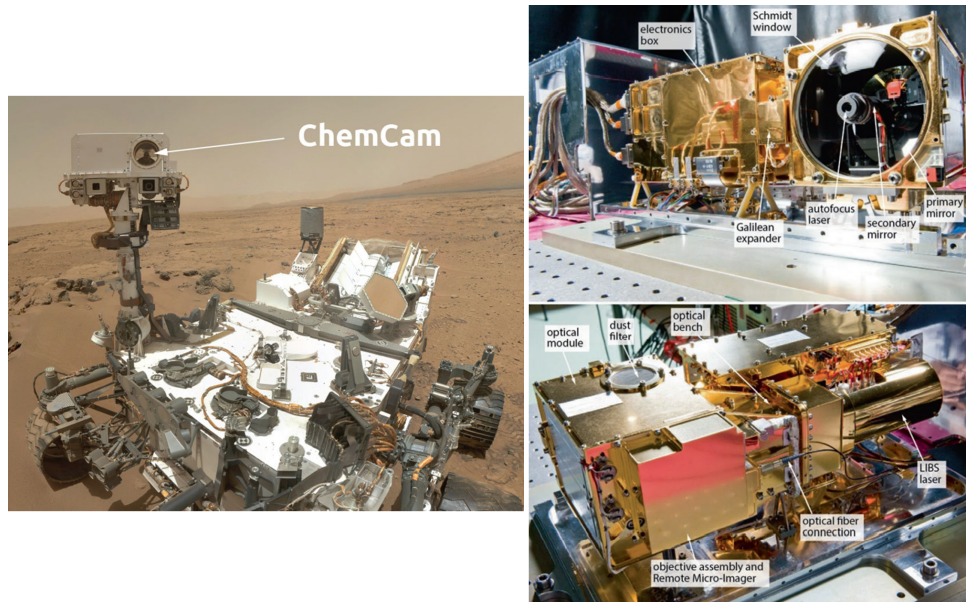
Figure 3.13: On the left the ChemCam on the Curiosity's Remote Sensing Mast and on the right the ChemCam Mast Unit [8] [27].

instrument is designed to be used over the range -20–$20\,°C$, so it often needs to be warmed-up to reach the lower operating temperature ($-30\,°C$) or the optimal one at $-15\,°C$.

LIBS The ChemCam laser is a Q-switched[12] compact laser developed for planetary applications. The LIBS laser is designed, starting from the commercial ones, respecting two requirements: smaller mass (by a factor of 10) and volume, in order to allow it to operate without active cooling and to improve its stability and reliability. The architecture of the laser is based on: a Diode Pumped (DP) oscillator, based on a Nd:KGW[13] rod longitudinally pumped by a diode stack, manufactured to optimize the emitted power around -5 $°C$; two slab DP amplifiers, which improve the output energy of the oscillator while maintaining good beam propagation characteristics. The RTP Pockels cell receives a $950\,V$ pulse with a rise time of less than $20\,ns$ and energies greater than $30\,mJ$ are obtained at the laser output. The components are protected and sealed by hermetic titanium covers, filled with dry air to mitigate the risks of contamination on the stacks and on the optics.

The laser operates in a *burst mode*, so the repetition rate (f_{laser} between 1–10 Hz) and the number of shots (N_{shots}) per burst need to be adjusted respecting precise constraints: if f_{laser} is equal to $10\,Hz$ (high repetition rate), a cooling time of $5\,min$, between two bursts sets of 100 shots, is essential to limit internal self-heating; while if f_{laser} is equal to $3\,Hz$ (medium rate), it has been

---

[12]Giant pulse formation or Q-switched: is a technique by which a laser can be made to produce a pulsed output beam, this allows to generate light pulses with a much higher peak power than that produced by the same laser in continuous wave mode.

[13]Neodymium doped Potassium-Gadolium Tungstate (Nd:KWG): the efficiency of such laser is 3–5 times better than that of the Yttrium-Aluminium Garnet (YAG) lasers.

demonstrated that 3000 shots are possible around -15 °C without stopping. When the temperature is too low, the laser diodes must be warmed-up with a ramp rate less than 5° per minute. In addition, the laser can modulate its output energy to a lower value (up to 50% of its nominal value) in order to avoid saturating the LIBS signal.

Table 3.1: Laser performances and mechanical specifications. The M^2 factor, known as Beam Quality Factor (BQF), is a common measure of the laser beam quality: it is defined as the Beam Parameter Product (BPP) divided by λ/π, which is the BPP for a diffraction-limited Gaussian beam ($M^2 = 1$) with the same wavelength. However, the far-field half-angle beam divergence is $\theta = M^2 \cdot \frac{\lambda}{\pi w_0}$, where w_0 is the beam radius at the beam waist [27].

Parameter	Value
Wavelength	1067 nm (NIR)
Energy	> 24 mJ $[-20\,°C, +20\,°C]$, > 30 mJ for one T
Stability	Shot to shot $\leq 2\%$ rms
Pulse duration	≤ 8 ns
Beam quality	$M^2 < 3$
Repetition rate	1–10 Hz
Functional T range	$[-30\,°C, +30\,°C]$
Beam diameter	$2.5 \leq \phi \leq 3.5$ mm
Overall mass	≤ 600 g
Volume	$\phi < 60$ mm, $L < 220$ mm
Pointing stability	Static ≤ 0.3 mrad, Dynamic ≤ 0.3 mrad
Pointing direction	Static ≤ 50 μrad, Dynamic ≤ 50 μrad
Maximum sustainable shots	20 million over lifetime

RMI   The Remote Micro-Imager is a heritage unit from the Comet Infrared and Visible Analyser (CIVA) camera system onboard the Philae lander on ESA's Rosetta mission, which consists of 9 identical imagers: seven panoramic cameras, one in a microscope and one for an ion-mass spectrograph. The RMI design is based on the TH7888A CCD image sensor (technical specifications in Table 3.2). RMI is able to capture black-and-white and has an auto-exposure feature. The RMI allows to provide context imaging for LIBS shot points at a better resolution than that achievable with the Mastcam-100. Nevertheless, the RMI camera head has the following additional characteristics:

- Fast acquisition of two images using internal DRAM to store the first one before transfer;

- Readout register and memory zone cleaning before imaging performed by taking two or more images with minimum integration time.

Table 3.2: CCD technical characteristics: the frame transfer time from imaging to memory zone is equal to $2.1\,\mathrm{ms}$ and the adjustable CCD integration time (i.e. successive frames may need to be integrated in the CCD camera to improve the SNR in the image) is over the range $1\,\mathrm{ms}$ to $65\,\mathrm{s}$ [27].

Parameter	Value
Type	Frame transfer with memory zone
Size	1024×1024 useful pixels
Pixel	$14 \times 14\,\mu\mathrm{m}$
Image zone	$14.34 \times 14.34\,\mathrm{mm}$
Sensitivity range (QE > 5%)	450–950 nm
Pixel saturation charge	$220\,000$ electrons
Maximum continuous frame rate	1 image per second

Autofocus laser   For autofocus operations, ChemCam uses a second laser with a wavelength of $785\,\mathrm{nm}$, mounted to the back of the secondary mirror. The focus mechanism translates the secondary mirror over $15\,\mathrm{mm}$ and consist of a moving microstage and a 2-phase stepper motor (Table 3.3), which moves the moving part thanks to a screw-nut coupling. The distance to the target is estimated using Navcam stereo ranging and this value is passed to ChemCam unit as part of the instrument's commands. Then, the autofocus laser illuminates the target, at that distance, at 638 different test focus steps and a photodiode records how the reflected light intensity varies with focus. Generally, the intensity followed a bell-shaped curve (graph depicting the normal distribution), but this data is sometimes affected by noise and the top of the curve is sometimes flat, so the electronics determine the best-focus position, for LIBS and imaging, by finding the axis of symmetry of that intensity curve [8]. If the autofocus laser fails,

Table 3.3: Autofocus laser technical characteristics: the switch from one operating mode to the other takes place automatically onboard and in case of a fault, a boost mode is also defined ($0.8\,\mathrm{A}$ and $50\,\mathrm{Hz}$ for a maximum torque) [27].

Parameter	Value
Step per round	200
Operating current	$600\,\mathrm{mA}$
Holding torque	$13\,\mathrm{mN/m}$
Detent torque	$2\,\mathrm{mN/m}$
Stepper motor operating range	$100\,\mathrm{Hz}$ at $T < \text{-}20\,\mathrm{°C}$ $150\,\mathrm{Hz}$ at $T > \text{-}20\,\mathrm{°C}$

it can be used a new autofocus capability using the RMI, which takes nine to eleven images to perform a simple algorithm in order to measure image contrast, selecting the highest-contrast one, and to determine the in-focus distance. RMI takes about two minutes to autofocus.

The ChemCam Body Unit

The analytical part, Body Unit (BU), is located in the rover body and consist of an optical demultiplexer (DEMUX), three spectrometers (SPECTRO), a digital processing unit (DPU) and a communication interface with the rover (COM). The MU is electrically connected to the BU by a fiber optic (FIBER) cable $5.743\,\mathrm{m}$ long and electrical harness (HARNESS). A set of calibration targets (CCCT) is also included on board. The block diagram is shown in Figure 3.14.
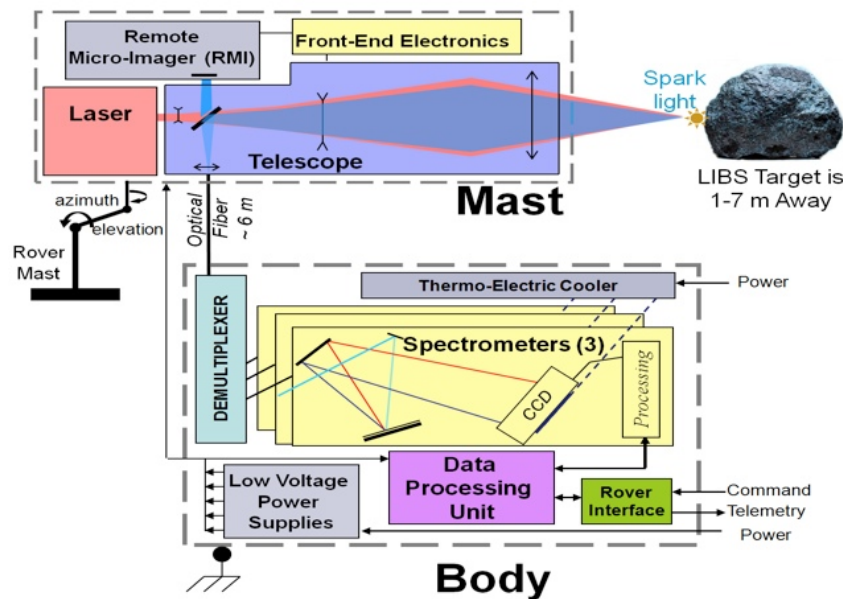
Figure 3.14: Block diagram of ChemCam Mast and Body. Mast Unit: *LASER + TELESCOPE + RMI + FOCUS + FPGA + POWER-1*; Body Unit: *DEMUX + SPECTROS + DPU + POWER-2 + COM + TEC*; MU − BU: *FIBER + HARNESS* [27].

ChemCam spectroscopy   Light is transmitted into the rover along the fiber optic cable and enters an optical demultiplexer (Figure 3.14), which allocate the plasma light to several spectrometers depending on their wavelength, so the demultiplexer splits off the incoming light into three bands first the UV and then the VIO ranges with dichroic mirrors and finally an aluminized mirror (at the left side in the Figure 3.15) to reflect the remaining light to the longest-wavelength spectrometer.

The three spectrometers are called:

- Ultraviolet (UV), 240.1–342.2 nm;

- Violet (VIO), 382.1–469.3 nm;

- Visible and near infrared (VNIR), 470.0–906.5 nm.

The light passes through a $1\,\text{mm}$ tall slit attached to the end of the fiber bundles to enter a spectrometer and then bounces off a $25\,\text{mm}$ diameter collimating mirror and a holographic grating (2400 lpmm for UV and VIO, 600 lpmm for VNIR) that spreads the light out by wavelength. Then another collimating mirror delivers the split light to a CCD, which has 2048 pixels across the active area. Because the UV and VIO spectrometers cover narrow wavelength ranges: 20 pixels per nm in the UV range and 23 pixels per nm in the VIO range, there is higher spectral resolution at shorter wavelengths. The wider wavelength range of the VNIR spectrometer covers only 4 pixels per nm producing a lower spectral resolution.

ChemCam also has the capability (but is not required) to provide passive spectroscopy data of Martian rock target simply by observing the radiation emitted by the plasma.

Usage time   Potentially the greatest energy consumption is required to preheat the shaft motors, if the analyses are carried out before the mast is naturally heated by sunlight: this can consume up to $100\,\text{Wh}$, depending on the duration of the heating. The duration and energy required to perform various ChemCam tasks are as follows [29]:

1. RMI pre-image + LIBS + Post-image (warm/coldest) with TEC: $11.6\,\text{Wh}$ (warm) and $21.2\,\text{Wh}$ (coldest);

2. RMI pre-image + LIBS + Post-image (nominal) with TEC: $13.8\,\text{Wh}$;

3. RMI pre-image + Depth Profile (900 laser pulses) + Post-image: $24\,\text{Wh}$;

4. 7 targets (RMI + LIBS as in 2) with TEC: $40.3\,\text{Wh}$, duration $1.0136\,\text{h}$;

5. 20 targets (RMI + LIBS as in 2) with TEC: $96.2\,\text{Wh}$, duration $2.86\,\text{h}$.

Each additional ChemCam target requires an incremental duration of approximately 7.5 minutes and $4.4\,\text{Wh}$.

> **ChemCam - Power consumption**
> The instrument power is measured under various conditions to analyse its operation at extreme voltages and temperatures.
> *Idling operating mode:* $11.8\,\text{W}$ (BU: $7.2\,\text{W}$, MU: $4.6\,\text{W}$);
> *Maximum power operating mode:* $64.7\,\text{W}$ (BU: $20.8\,\text{W}$, MU: $43.9\,\text{W}$), firing the laser at $10\,\text{Hz}$ (this state lasts few seconds). If the instrument fires the laser at a lower rate ($1\,\text{Hz}$) it uses only half of this power.
> The *TEC* works independently by drawing a constant $13.5\,\text{W}$.
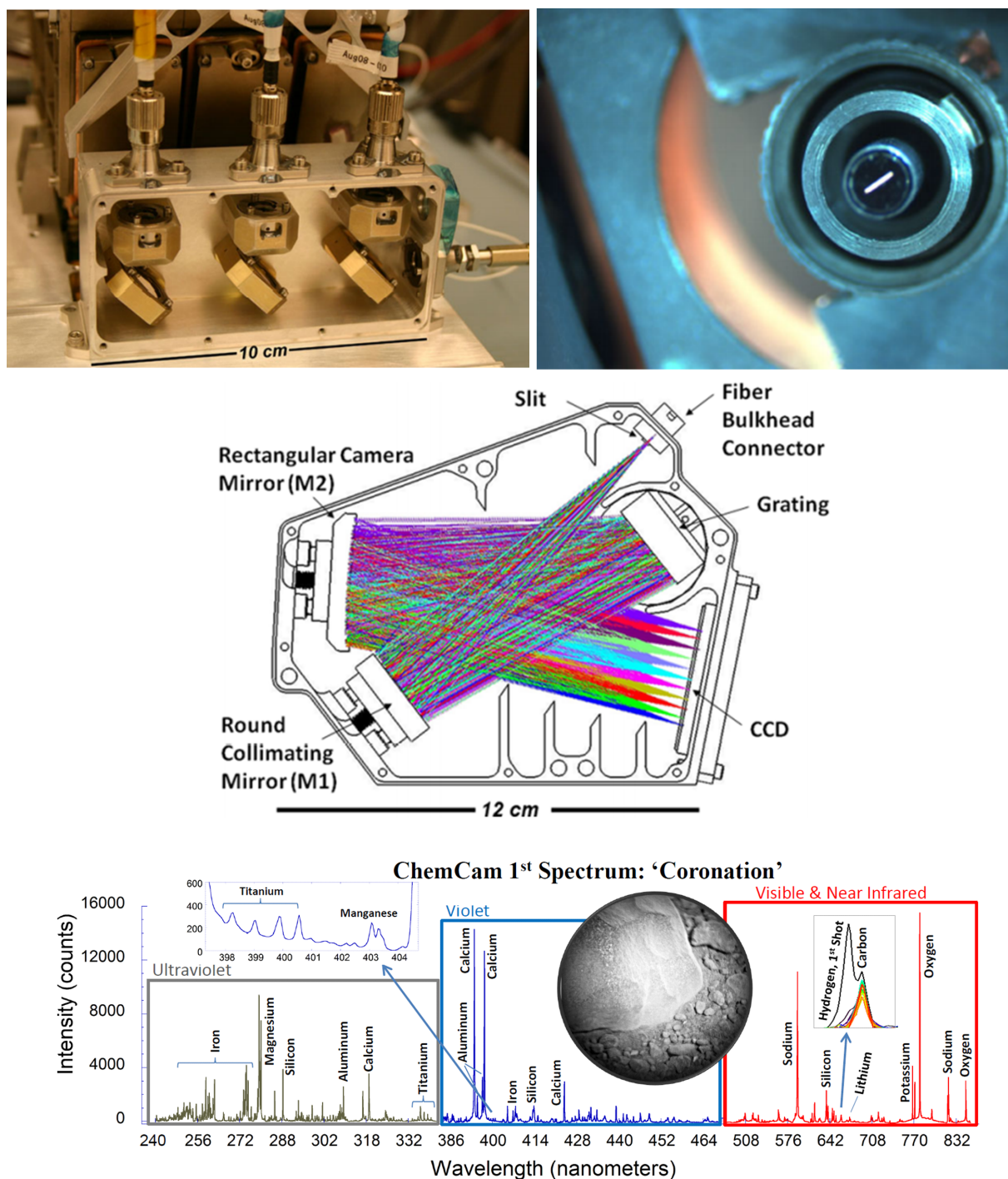
Figure 3.15: Top left to right: interior of the optical demultiplexer, where light enters through the fiber bulkhead on the right and exits via the three fiber bundles at the top; spectrometer aperture slit. In the middle, a spectrometric optical bench with ray-trace diagram. Below, the ChemCam spectrum: the instrument measures intensity of UV, VIO and VNIR light emitted when it fired its laser at Martian rock target [27] [28].

3.1.4   APXS: Alpha Particle X-ray Spectrometer

The Alpha Particle X-ray Spectrometer determines the relative abundances of different elemental composition of rocks and soils, in order to characterize the geological context of the rover surroundings, by emitting α-particles (*see* Appendix A) and X-rays, which interacting with atoms in the surface material knock electrons out of their orbits, producing an energy release, due to the emission of X-rays, that can be measured with detectors.

APXS instrument   APXS consist of three important part: a sensor head mounted on the robotic arm and separated from the turret by three springy wire rope assemblies to prevent vibrations caused by drilling and CHIMRA sample processing; an electronics unit in the rover's body; and a calibration target (Figure 3.16).

 The MSL APXS takes advantage of a combination of the terrestrial standard methods Particle-Induced X-ray Emission (PIXE) and X-ray Fluorescence (XRF) to determine elemental chemistry. It uses curium-244 sources for X-ray spectroscopy to determine the abundance of major elements down to trace elements from sodium to bromine and beyond. The sensor head contains six ^{244}Cm[14] sources: three of them are covered in a titanium foil and emit α-particles, which eject inner-shell electrons of the target atoms, resulting in characteristic X-ray photon emission when they fall back to their ground state, this process is called *Particle-Induced X-ray Emission* (PIXE). While, the other three are more thoroughly sealed and emit only X-rays over the range 14–18 keV, which achieve the same effect as before, in this case the process is called *X-ray Induced Fluorescence* (XRF).

PIXE process is a more efficient for low-Z elements (from sodium to titanium), while XRF process is more effective for high-Z elements (from chromium to strontium). The sensitivity of PIXE and XRF processes is shown in Figure 3.17. In addition, APXS uses a *Silicon Drift Detector* (SDD) to detect X-rays induces by radioactive source (Figure 3.17). With a half-life of 18.1 years, the degradation of ^{244}Cm should not have a significant impact on APXS use over the course of the mission. The atoms of each element emit X-rays with a specific frequency after being excited. Knowing that, the energy emitted by each atom can be determined by the frequency or wavelength of the radiation, so with this process the APXS can detect the elements present (Figure 3.18). Thanks to the analysis derived from observations of samples of known composition on Earth, it is possible to convert the X-ray spectra into elemental abundances. Before making an APXS measurement the rock surfaces are brushed off using the *Dust Removal Tool* (DRT[15]) in order to study the outermost composition of rocks. This approach improves APXS's ability to sense the abundances of lighter elements in the rock rather than the dust.

---

[14]Curium-244.

[15]A wire brush designed to clear dust and regolith fines from rock surfaces and to clean the rover's sample observation tray.
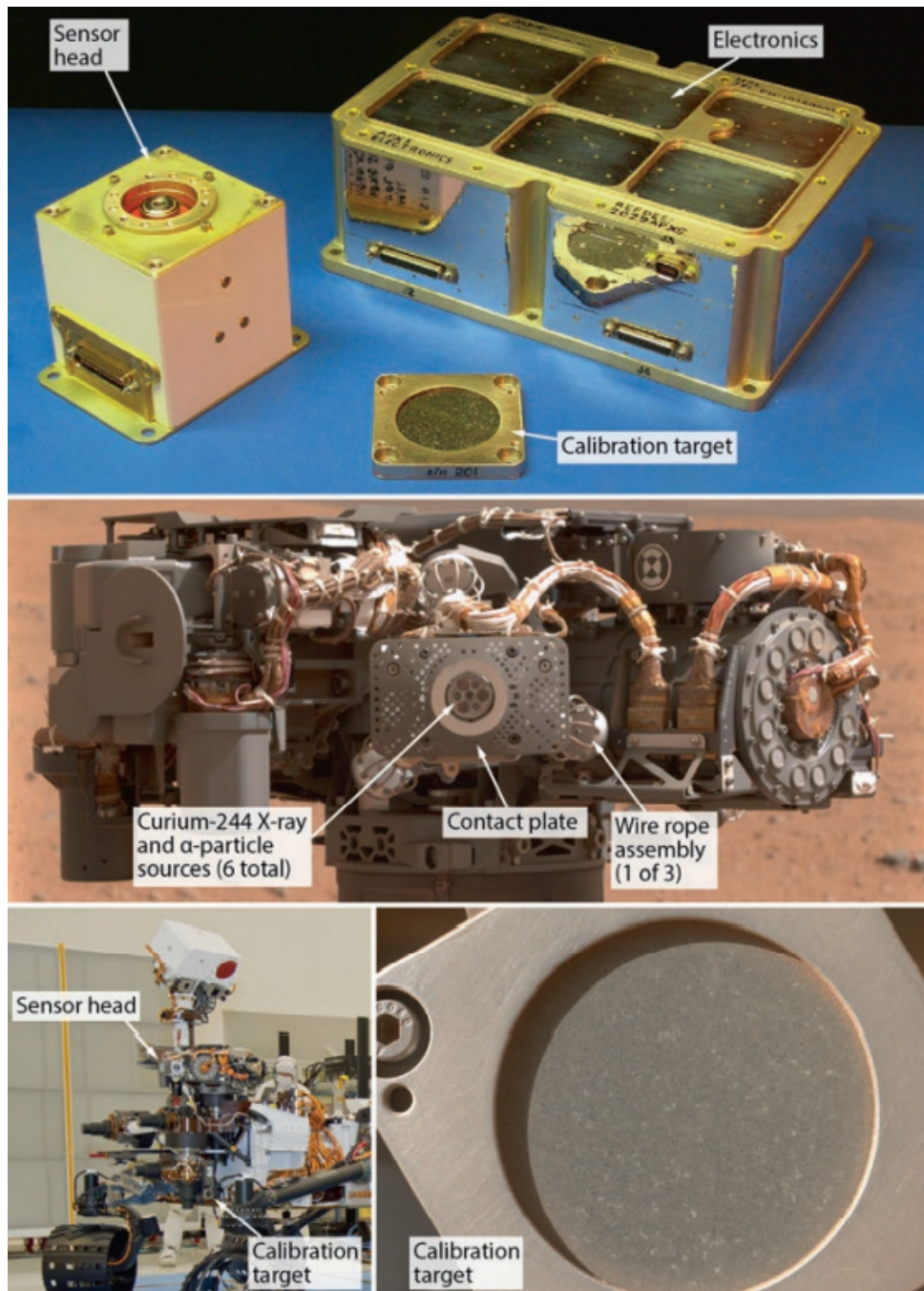
Figure 3.16: Parts of APXS and their location in the rover [8] [30].
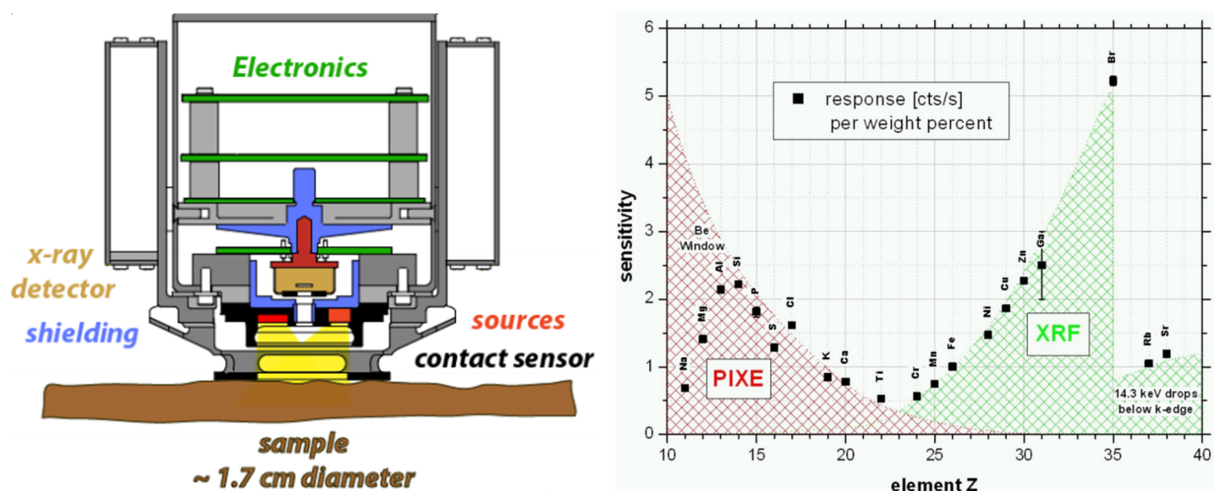
Figure 3.17: On the left: the cross-section of the APXS sensor head. On the right: the sensitivity of PIXE and XRF mode [30].
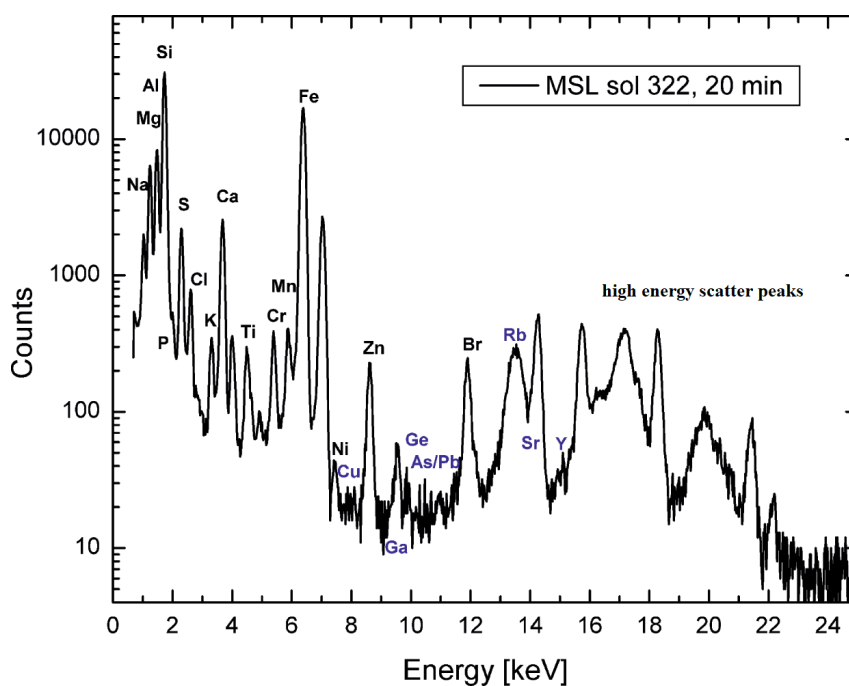
Figure 3.18: APXS spectrum measured on MSL on sol 322 of the rock sample Aillik: analyzing the height of peaks in the spectrum allows the APXS team to measure the composition of the rock. Curiosity's APXS can get a quick-look measurement of the major elements in only 20 minutes, and high-quality analysis in about 2 hours [31].

Changes and improvements   Curiosity's APXS has fundamental improvements over the ones of Spirit and Opportunity:

- The activated Peltier cooler for SSD allows APXS: to operate at ambient temperatures up to -5 °C, whereas before the limit was -40 °C; to significantly expand the operating window for APXS analyses during the daytime as well (before only at night-time), even if operating at night improves data quality; to improve the resolution (FWHM[16].) of less than $150\,\text{eV}$ during night.

- Having discarded the alpha channel (Curiosity does not detect backscattered alpha particles) allows the X-ray detector to be much closer to the surface ($19\,\text{mm}$ compared to $30\,\text{mm}$ for the others) and this, in turn, allows to: increase the sensitivity of the instrument by a factor of 3; reduce the spot size of an APXS measurement; decrease data acquisition by a factor of 5.

- The addition of standard XRF ^{244}Cm sources increases the sensitivity for high-Z elements by a factor of 2.

- The energy range is extended up to $25\,\text{keV}$, while before it was $17\,\text{keV}$.

Electronics and usage time   The APXS will take measurements both day and night by deploying and placing the sensor head towards a desired sample, in contact (when the targets are not irregular surfaces), with the sources typically less than $20\,\text{mm}$ from the surface. The operating temperature is over the range -130 °C to -5 °C (actually up to 10 °C but with degraded resolution). The emitted X-ray spectrum of the major elements is evaluated in only 10 minutes (quick-look), while for high-quality results it takes from 2 to 3 hours, without the need of further interaction by the rover. The longer the instrument is held in place on the surface of a rock or soil sample, the more clearly its signal can be determined. At the end of the measurement, the APXS uses only 32 kilobytes of memory to store up to 13 consecutively taken spectra and engineering data.

APXS - Power consumption
It is also cheap in terms of power, especially if used overnight, when its detector doesn't need to be cooled.
Normal operating mode: 8 W, including 3 W of the activated Peltier cooler.

---

[16]Full Width at Half Maximum: a quantity frequently used to characterize the resolution and corresponds to the percentage ratio between the width at half maximum and the value of the centroid of the peak. For example, in a Gaussian distribution the FWHM is related to the standard deviation according to the relation, FWHM = $2.355\,\sigma$.

3.1.5 MAHLI: Mars Hand Lens Imager

The Mars Hand Lens Imager (MAHLI) uses a 2-megapixel color camera with a focusable macro lens to observe textural, structural, and morphological details in geologic materials, so to acquire images in order to examine the grain size, the structure and mineralogy of rocks. Additionally, images from MAHLI is used to help select materials to be sampled or analyzed by the other instruments (particularly APXS, CheMin, and SAM). At the minimum working distance, MAHLI can take images with a pixel scale/spatial resolution of $13.9\,\mu m$ per pixel, so a $1600{\times}1200$ pixels image covers an area of about $2.22{\times}1.66\,cm$. Some MAHLI characteristics are shown in the Table 3.4.

Instrument Description

MAHLI has three hardware elements: a *Camera Head*, mounted on the turret at the end of the robotic arm; a *Digital Electronics Assembly* (DEA), located inside the rover's environment controlled body; a *Calibration Target*, mounted on the robotic arm shoulder azimuth actuator.
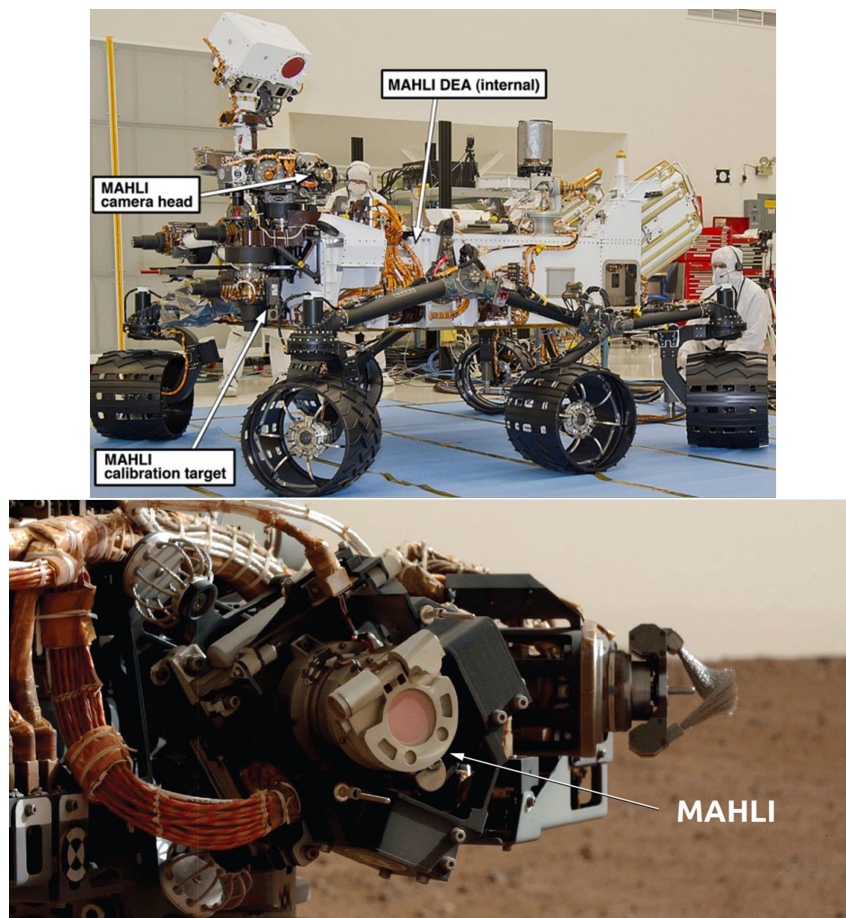
Figure 3.19: Location of MAHLI hardware aboard the MSL rover [32] [33].

Camera head   The Focal Plane Assembly (FPA) is designed around a Kodak KAI-2020CM CCD without a cover glass. The sensor has $1640{\times}1214$ pixels[17] and the photoactive area is $1600{\times}1200$ pixels. The sensor has red, green, blue (RGB) filtered micro-lenses arranged in a *Bayer pattern*[18]. The optics are an all-refractive design consisting of a group of stationary elements, a group of focus elements and a stationary sapphire window (Figure 3.20). The lens
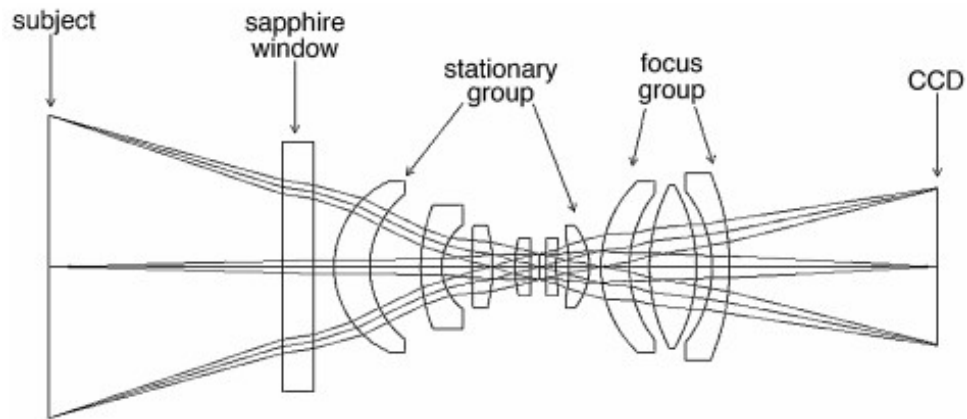
Figure 3.20: MAHLI optics with focus group shown in minimum working distance focus position [33].

is designed to focus on subjects and acquire images at working distances between $\sim20.5\,\mathrm{mm}$ and infinity (specs in Table 3.4). The opto-mechanical assembly includes the dust cover, which

Table 3.4: MAHLI instrument characteristics [33].

Parameter	Subject at working distances	Subject at infinity
Depth of field	1 mm	–
FOV diagonal	34.0°	38.5°
FOV horizontal	26.8°	31.1°
FOV vertical	20.1°	23.3°
IFOV	402 µrad	346 µrad
Focal ratio	f/9.8	f/8.5
Effective Focal Length	18.4 mm	21.4 mm

when the instrument is not in use, protects the front optical element (the sapphire window) and the LEDs from dust contamination. The same motor that used to focus, opens and closes the dust cover. Additionally, it is a stepper motor with up to 16100 step positions:

---

[17]Pixel size: $7.4{\times}7.4\,\mu\mathrm{m}$.

[18]A Bayer pattern is a chequerboard of colored pixels: in every 2-by-2 array of pixels, two corner pixels are covered by green filters, one is covered by a red filter, and one by a blue filter. The CCD sensor that detects each pixel in the image is covered by this grid of filters, so that the three colour components of the entire scene are obtained in a single exposure, then the electronics merge the separate sets of colour pixels into a single colour image.

- From 0 to 1460: the lens is at its minimum working distance and the cover remains closed;

- Between 1460 and 4490: the lens moves focus over the entire range, from $\sim 20.5\,\mathrm{mm}$ working distance to infinity;

- ~ 5100: at this point, the cover begin to open;

- Between 12570 and 15600: the cover is fully open, the lens moves focus respectively from infinity to the minimum working distances.

The empirical relationship between focus group stepper motor count and working distance is as follows:

$$d = (af^{-1} + b + cf + df^2 + ef^3)^{-1}$$

in which d is the working distance, f are the focus motor counts and from a to e are empirical number, specifically:

$a = 0.576786$;

$b = -11.8479$;

$c = 2.80153 \cdot 10^{-3}$;

$d = -2.266488 \cdot 10^{-7}$;

$e = 6.26666 \cdot 10^{-12}$.

In addition, MAHLI has the ability to make videos thanks to the fact that its electronic design is shared with Mastcam and MARDI, but it rarely uses this ability. Moreover, the Camera Head is connected to the electronics through $12.7\,\mathrm{m}$ of cable harness and operates, between -40–40 °C, using regulated $5\,\mathrm{V}$ and $\pm 15\,\mathrm{V}$ power provided by the DEA. In addition, the output signal from the CCD is AC-coupled and amplified, then it is digitized to 12 bits at a maximum rate of 10 megapixels per second. Camera head functions are supervised by a *Field-Programmable Gate Array* (FPGA), which generates the CCD clocks, according to commands from the DEA, reads samples from the ADC (Analog-to-Digital Converter) and performs digital CDS[19]; finally transmits the pixels to the DEA.

Digital Electronics Assembly (DEA)   The MAHLI DEA is packaged with the MARDI and Mastcam DEAs to save mass (Figure 3.21). The electronics are laid out on a single rectangular PCB. The DEA is the interface between the Camera Head and the rover avionics. All data interfaces use LVDS (Low-Voltage Differential Signaling) and each rover interface includes two flow-controlled serial links (Figure 3.22):

- $2\,\mathrm{Mbit/s}$: from the rover to the DEA;

---

[19]Correlated Double Sampling

Figure 3.21: DEA package for MAHLI, Mastcams and MARDI: each instrument is a separated unit [33].

- 8 Mbit/s: from the DEA to the rover.

MAHLI interfaces includes two serial link as well:

- 2 Mbit/s: to transmits a command from the DEA to the MAHLI;

- 8/60/120 Mbit/s: to send an image data from the Camera Head to DEA on a selectable rate 6-bit parallel link.

The DEA provides an image-processing pipeline (a chain of data-processing processes) that includes 11-to-8-bit companding[20] of input pixels, horizontal sub-framing, and optionally lossy or lossless predictive compression. The DEA memory subsystem consist of 128 MB of SDRAM and 8 GB of non-volatile NAND flash memory. The SDRAM is typically used to store file system information, but can also be used as a small image buffer too.

Calibration Target MAHLI's calibration target is attached to the robotic arm shoulder azimuth actuator (Figure 3.19) and is mounted vertically on the rover, theoretically to prevent dust accumulation and keep it relatively clean. The target consist of machined titanium to which are affixed eight elements: three color sample (red, green, blue), two gray swatches and one fluorescent swatch that glows red (at a wavelength of 626 nm) when struck by the MAHLI ultraviolet LEDs (at a wavelength of 365 nm). Machined elements include a stair-stepped target designed to monitor camera focus and resolution performance over time.

---

[20]The dynamic range of a signal is compressed before transmission and is expanded to the original value on reception.
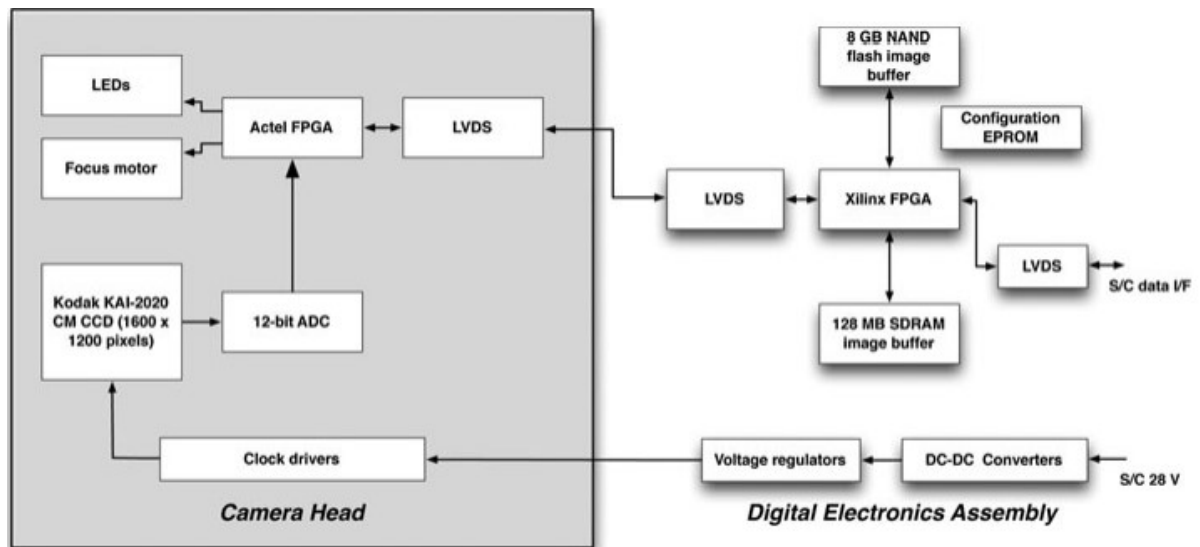
Figure 3.22: Schematic operation diagram of MAHLI electronics [33].

Figure 3.23: Flight MAHLI calibration target [33].

Using time   MAHLI is regularly used to inspect the rover hardware: mainly the rover wheels, because the mastcam can only partially see the right side wheels and the left side ones not at all. In addition, it monitors dust accumulation on the REMS UV sensor, on the ChemCam windows and has been used as a diagnostic tool for the condition of the REMS wind booms.

> **MAHLI - Power consumption**
> MAHLI
> ***Idling operating mode:*** 1.8 W;
> ***Imaging power operating mode:*** 3.5 W.
> DEA (including Mastcams, MAHLI, and MARDI)
> ***Idling operating mode:*** 6.4 W;
> ***Imaging power operating mode:*** 9.0 W.

3.1.6   Mastcams: Mast Cameras

The primary objective of the Mastcam investigation is to acquire and use images of the environment in which the MSL rover operates in order to characterize and determine details of the history and processes recorded in geologic material at the MSL landing site. The science objectives of Mastcam investigation are:

- Observe landscape physiography and processes in order to provide a data of the topography, geomorphology, and geologic environment of the landing site;

- Examine the properties of rocks and fines in order to determine texture, structure, morphology, stratigraphy, mineralogy, the processes that acted on these materials and individual grains within them (including mechanical and physical properties) and finally, the results of the interaction between the rover and Martian surface;

- Document atmospheric and meteorological events and processes in order to provide information on dust particle (size and composition), clouds, dust-raising events and deposition of fines by observing parts of the sky using color filters;

- Support and facilitate rover operations, sample extraction and documentation in order to ensure the overall scientific success of the mission, acquire images that help determine the position of the Sun and the characteristics of the horizon;

- View frost, ice and related landforms in order to characterize them, (if present) and determine its morphology, texture and thickness and observe changes over time.
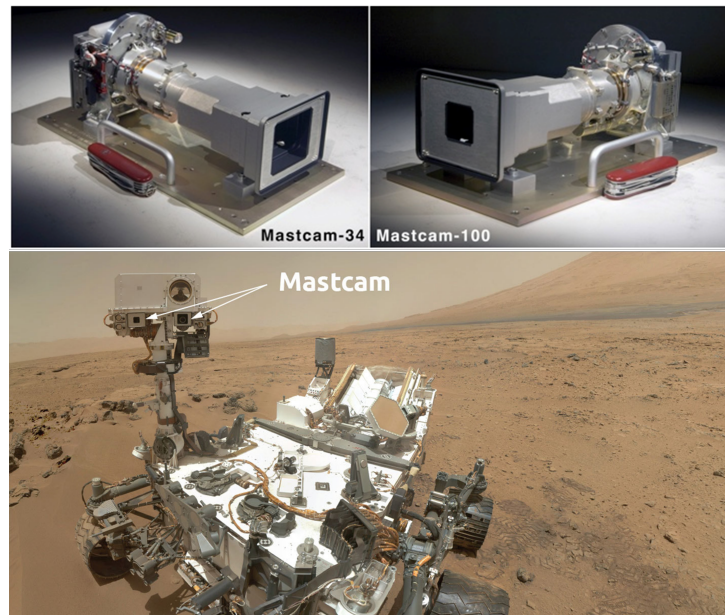
Figure 3.24: Mastcam on the MSL rover's Remote Sensing Mast [34] [35].

Mastcam components

The Mastcam instrument consists of: two Camera Heads located on the mast, which have different focal lengths and different science color filters (Figure 3.24); an electronic assembly (Figure 3.21) located inside the rover; a calibration target on the rover deck. Both Mastcams can acquire panoramic, color and multispectral images, mainly they are able to acquire stereoscopic observations to create and enhance the illusion of depth. The Mastcam-34 has shorter focal length, lower angular resolution, and wider FOV than the Mastcam-100, which has longer focal length, higher angular resolution, and narrower FOV; more information on the two Mastcam are shown in Table 3.5.

Table 3.5: Mastcam instrument characteristics [36].

Parameter	**Mastcam-34 mm**	**Mastcam-100 mm**
Stereo separation	24.64 cm	
FOV diagonal	20.6°	7.0°
FOV horizontal	15.0°	5.1°
FOV vertical	15.0°	5.1°
IFOV	218 µrad	74 µrad
Focal ratio	f/8	f/10
Effective Focal Length	34.0 mm	99.9 mm
Focus range	0.5 m to infinity	1.6 m to infinity
Exposure range	0–838.8 s in 0.1 ms increments	
Video frame rate	5.9–7.7 fps (1280×720)	
	3.9–4.7 fps for full frame	

Camera Head   The 2-megapixel Mastcams head contain electronics, a detector, a filter wheel assembly, a focus mechanism, and an aluminium sunshade that comprises nearly two thirds of the length of the cameras; each head contains two stepper motors, one to drive the filter wheel and one to drive the focus mechanism. The two Mastcams are angled inward by 2.5° (1.25° each) in order to ensure that the small FOV of the Mastcam-100 is entirely contained within the wider FOV of the Mastcam-34 for any subject located farther than $1.4\,\mathrm{m}$ away from the rover. The optical axes cross at a distance $2.8\,\mathrm{m}$ from the cameras, at a point on the ground $2\,\mathrm{m}$ away from the rover.

The optics for each Mastcam is an all-refractive focusable design:

- Mastcam-34 has six fixed elements and three in a single movable group. In addition, the front has a protective sapphire window (Figure 3.25 above);

- Mastcam-100 has five fixed and three in a single movable group, also in this camera the front has a protective sapphire window (Figure 3.25 below).
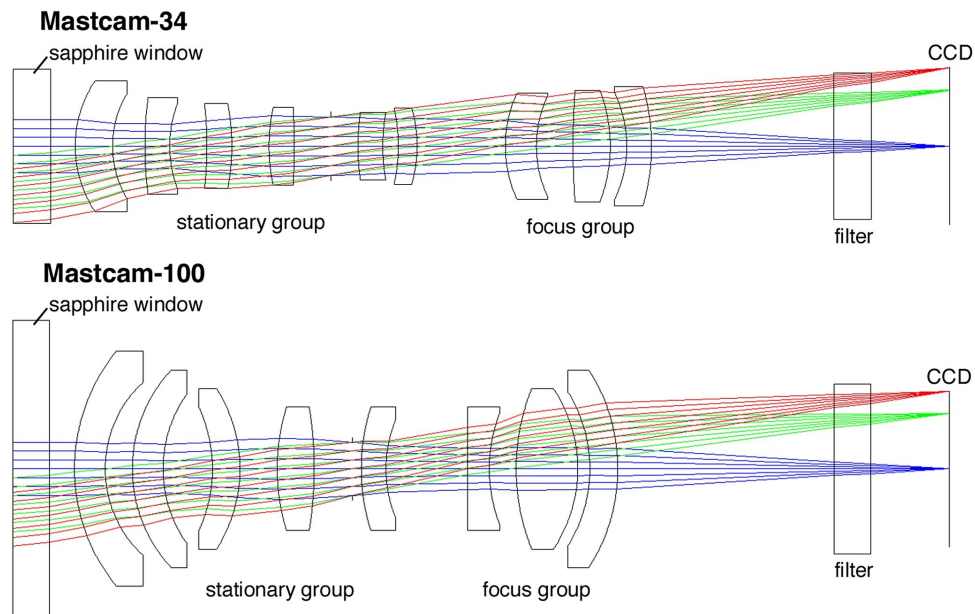
Figure 3.25: Mastcam optics and ray-trace diagrams [35].

The Mastcams have the same detectors (Kodak KAI-2020CM CCD with $1640{\times}1200$ pixels) as MAHLI and MARDI and use the same focus mechanism as MAHLI. The sides and corners of the images are partially occluded by the sunshade and are affected by vignetting effect, which exists because the shapes of their openings were built before the descope of zoom capability, initially Mastcam only planned to produce $1200{\times}1200$ pixel subframes. Most images taken for science purposes crop the image to $1344{\times}1200$ pixels, operationally called a "full frame"

Color imaging and Focus   Like MAHLI and MARDI, each pixel of the Mastcams is also covered with a red, green, or blue filter in a Bayer pattern and each Mastcam eye is equipped with an 8-position filter wheel, because the Bayer color filters on the detectors attenuate infrared wavelengths (Figure 3.26). Each eye's filter wheel has, in turn, one filter with a neutral-density (ND[21]) coating, which enable the Mastcams to directly observe the Sun through a blue (right eye) and infrared (left eye) filter (in Table 3.6 are shown the MSL Mastcam spectral filters and bandpasses). Moreover, each Mastcam can be manually focused, that is the lens focus group is commanded to move to a specified motor count position to acquire an image. The cameras can also be commanded to use the same focus setting as the previous image. The empirical relationship between focus group stepper motor count and distance to a target is as follows:

in which d is the distance between the camera and the focused target in meters; T is the

$$\textbf{Mastcam-34:} \qquad d = 363.64 / \left(2427.50 - f_{34} \right)$$
$$\textbf{Mastcam-100:} \qquad d = 3322.3 / \left(3491.9 - 2.58 \cdot T - f_{100} \right)$$

temperature of the camera in degrees Celsius; f_{34} and f_{100} are the focus motor counts reported by the Mastcam-34 and Mastcam-100 cameras, respectively [35].

Table 3.6: Mastcam spectral filters and bandpasses [8] [36].

Filter Position	Mastcam-34 (L) Wavelength $\pm$ Bandwidth (nm)	Mastcam-100 (R) Wavelength $\pm$ Bandwidth (nm)
0	590 ± 88	575 ± 90
	640 ± 44	638 ± 44
	554 ± 38	551 ± 39
	495 ± 37	493 ± 38
1	527 ± 7	527 ± 7
2	445 ± 10	447 ± 10
3	751 ± 10	805 ± 10
4	676 ± 10	908 ± 10
5	867 ± 10	937 ± 10
6	1012 ± 21	1013 ± 21
7	$880 \pm 10 + \text{ND5}$	$442 \pm 10 + \text{ND5}$

Calibration target   The Mastcam calibration target is $8\,\text{cm}^2$ and has 7 regions useful for calibration, including 4 color chips at the corners and 3 grayscale rings around the black gnomon. It is mounted on the rover deck at a distance of 1.2 meters from the cameras and has magnets that allow the Martian dust to be attracted to them, keeping the centers less dusty than the rest

---

[21]ND filters are quantified by their optical density, so $ND5$ is the minimum for direct eye solar observation without damage of retina.
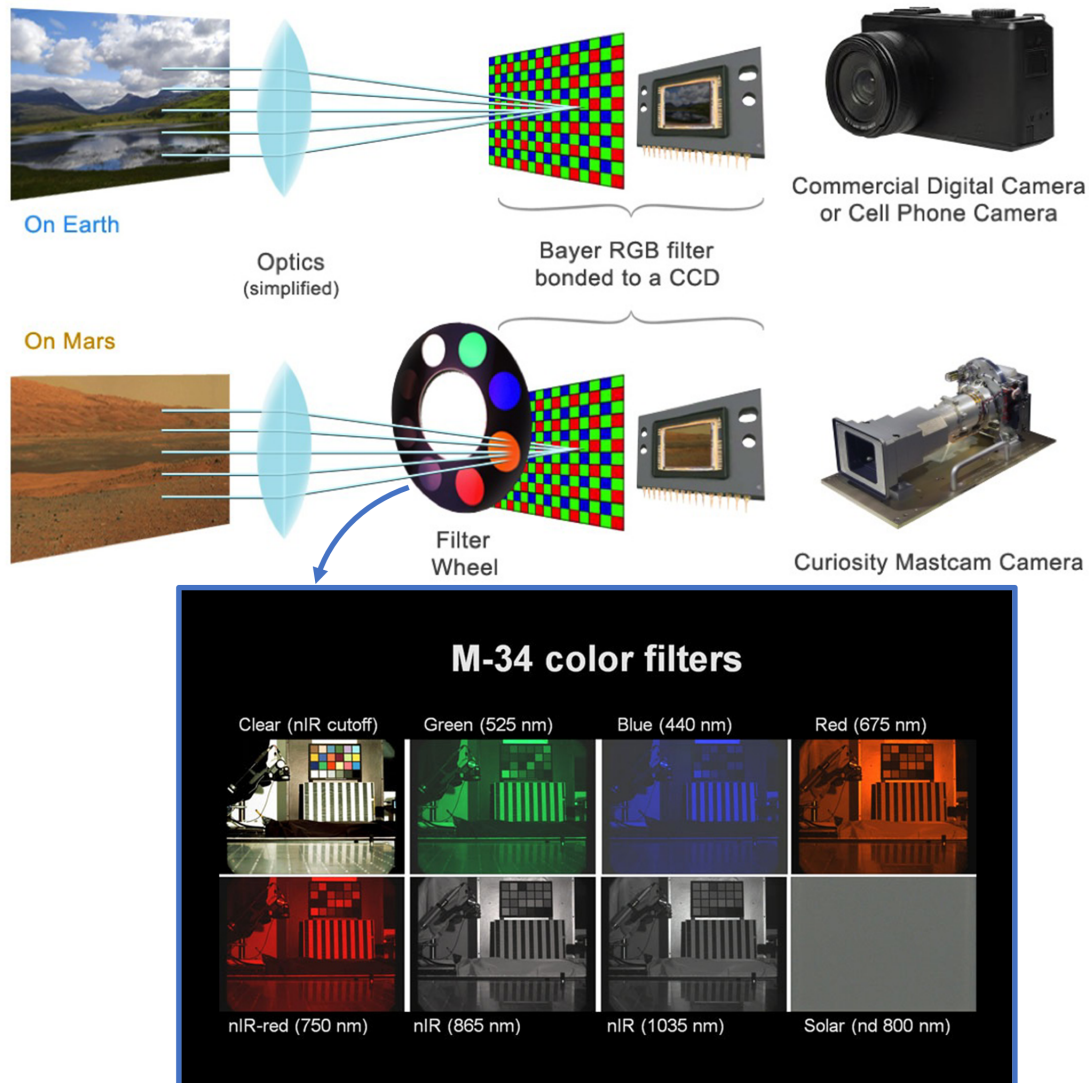
Figure 3.26: The Mastcams use the same type of RGB filter with Bayer pattern as typical commercial colour cameras, but in addition they have a specialised eight-position scientific filter wheel (Table 3.6), which can be rotated to choose the wavelength at which the image is to be reproduced [37]. Below is a series of images captured through each of the eight filters in the Mastcam-34's filter wheel. The images show how the camera can take exposures through a variety of filters to build up a multispectral view. The first image was taken through a transparent filter and those at the bottom appear grey because the Bayer colour array is essentially equally sensitive to those wavelengths. The bottom right image is taken through a neutral density filter that attenuates sunlight to one thousandth of its natural intensity, so it will appear dark except when looking at the sun [38].

of the calibration target (Figure 3.27). Due to the position of the target, it is impossible to image it through both eyes of the Mastcam with a single pointing, in fact the mast head has to rotate almost $360°$ in order to be able to correctly aim it with both cameras. Additionally, as mentioned in Table 3.5 the Mastcam-100 has a minimum focusing distance of $1.6\,\text{m}$, so its images of the calibration target are not in focus, but this problem does not affect the calibration target usefulness.
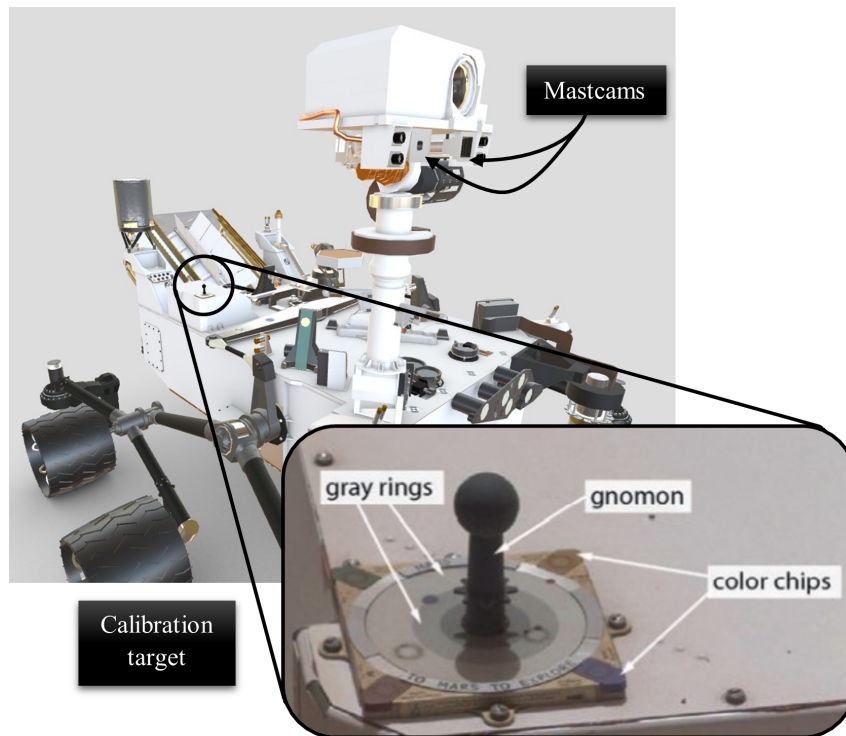
Figure 3.27: Mastcam calibration target [8] [39].

> **Mastcam - Power consumption**
> Mastcam-34 mm
> *Idling operating mode:* $1.8\,\text{W}$;
> *Imaging power operating mode:* $3.5\,\text{W}$.
> Mastcam-100 mm
> *Idling operating mode:* $1.8\,\text{W}$;
> *Imaging power operating mode:* $3.5\,\text{W}$.

3.1.7   MARDI: Mars Descent Imager

The Mars Descent Imager (MARDI) purpose was to help identify the landing location site and provide information about the larger geologic context surrounding the landing site. MARDI

operated by taking 622 images between heat shield separation and touchdown, producing a 4-fps video stream of high-resolution and continuing to acquire images until the rover landed. The video data is stored in digital memory and after a safe landing is transferred to Earth.

During the cruise phase of the mission, MARDI was equipped with an 11.8-watt survival heater (not sized for use on the Mars surface) to ensure that MARDI would remain within its Allowable Flight Temperature between -40–40 °C. MARDI was not required to operate after landing, so was never tested on Earth for survival through Mars temperature cycles, but even if the MARDI components reach temperatures well below its tested AFT during the mission, both its electronics and optics were built with the same design rules as Mastcam and MAHLI.

MARDI components   The MARDI consists of 2 parts (Figure 3.28): a Camera Head, mounted on the rover body and a Digital Electronics Assembly (DEA), housed inside the warm electronics box of the rover, with the same design as MAHLI and Mastcam. The Camera Head also uses a Kodak KAI-2020CM interline transfer CCD with 1600×1200 photoactive pixels, which have a size of $7.4\,\mu m$ (square pixels). The sensor has RGB filtered micro-lenses arranged in a Bayer pattern to provide an image color similar to that perceived by human eyes (twice as much green as red and blue). In Figure 3.29 the MARDI optics and the ray-trace diagram. Some MARDI characteristics are shown in Table 3.7. After landing, the images taken from an altitude of $66\,cm$ above the ground are slightly blurred (out of focus), because the ability of MARDI to resolve the ground features is between 2 meters and infinity.
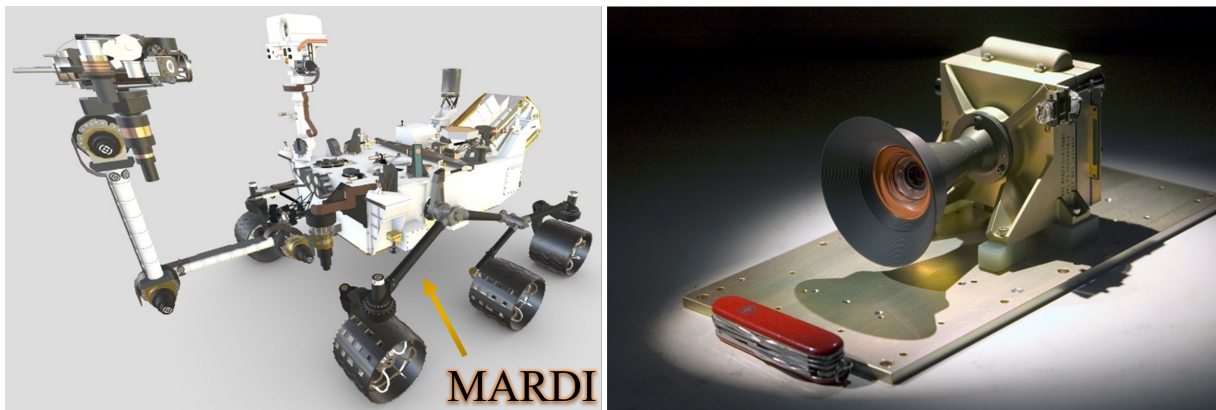
Figure 3.28: The flight MARDI Camera Head on the right and its position on the rover on the left [39] [36].

Table 3.7: MARDI instrument characteristics [35].

Parameter	Description
FOV diagonal	90°
FOV horizontal	70°
FOV vertical	52°
IFOV	764 µrad
Focal ratio	f/3.0
Effective Focal Length	9.7 mm
Focus range	2 m to infinity; ∼1 mm resolution at surface
Band passes	399–675 nm with Bayer pattern filter
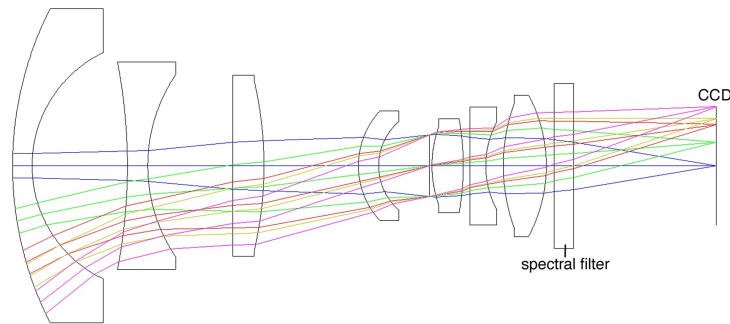
Figure 3.29: MARDI optics and ray-trace diagram [36].

MARDI - Power consumption
Idling operating mode: 1.8 W;
Imaging power operating mode: 3.5 W.

3.1.8 RAD: Radiation Assessment Detector

The Radiation Assessment Detector (RAD) is a passive energetic particle detector, which allows to characterize the full spectrum of the radiation environment at the surface of Mars, including *Galactic Cosmic Rays*[22] (GCRs) and *Solar Energetic Particles*[23] (SEPs), which interact with the atmosphere and penetrate into the soil producing secondary particles, such as γ-rays and neutrons.It was turned on during cruise phase toward Mars to measure radiation in the deep-space environment, while continuing to function on the surface of Mars. These information

---

[22]Probably originate in supernovae: 85–90% are protons and the rest are helium nuclei while electrons and heavy nuclei cover only 1%[8].

[23]During big solar event, solar energetic particles can be found, on the surface of Mars, in greater percentage than galactic cosmic rays, but only for short periods of time. In addition, Mars and the Earth are generally not affected by the same solar particles, because they have different revolution periods and they typically see the Sun from different directions.

are essential to determine the radiation dose rate in order to plan human exploration and assess the planet's ability to sustain life. The RAD instrument is mounted just below the top deck
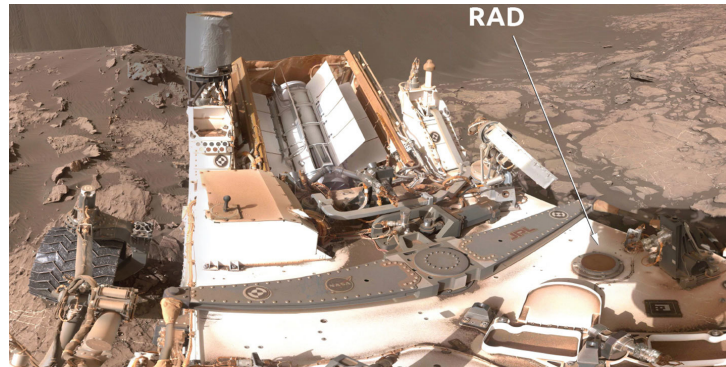
Figure 3.30: The top of the RAD sensor head visible on Curiosity's body [40].

of the rover with the charged particle telescope pointed in the zenith direction (Figure 3.30) and consists of the *RAD Sensor Head* (RSH) and the *RAD Electronics Box* (REB) integrated together in a tiny and compact volume (Figure 3.31).
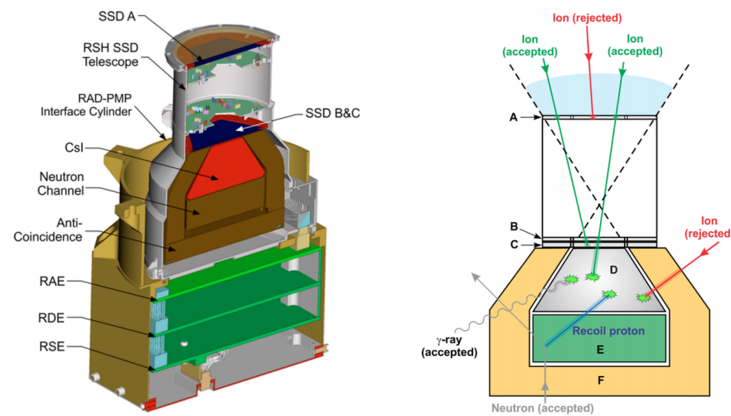
Figure 3.31: Schematic diagram of the RAD detectors. On the left: cross section view of RAD showing the sensor head channels above and electronic board layouts below. On the right: possible colored paths show charged and neutral particles that the RAD can detect: green paths are considered valid events, while red paths are rejected [41].

RAD Sensor Head (RSH)   The RAD sensor head contains multiple silicon detectors arranged vertically. The view cone is $65°$ wide, which size is not causal because it is essential to have a broad view of observation and keep the mass and volume of the instrument as small as possible. As shown in Figure 3.31, it consists of 3 *Solid-state Silicon Detectors* (SSD A, SSD B, and SSD C) of different widths to make sure they detect the same group of particles, a thick *Cesium Iodide Scintillator* (CsI - D) and two Plastic Scintillators (one marked with the letter E and another with the letter F that encloses D and E). High-energy and low-energy charged particles,

respectively can penetrate the entire instrument or be partially blocked. Charged particles to be detected and analysed must pass through the upper detector and register onto the lower detector surface. For example, suppose a charged particle hits only detector A, or any other lower detector without hitting the upper ones. In that case, it will be rejected from the analysis, so for this reason, the role of the anti-coincidence shield (F) and the outer rings of SSD B and C are essential; thus, if the particle triggers detectors D and E without entering the view cone is discarded from analysis.

RAD can determine the mass, energy and charge of the registered particles, but if any of these pass all the layers and deposit most of their energy in the detector, in this case RAD can not determine the mass of these particles; the RAD energy coverage is shown in Figure 3.32. Moreover, neutral particles (γ-rays) and neutrons[24], the viewing cone is not an entry requirement, because RAD detects them as detected events in D and E, but not any of the others. Finally, the high atomic mass of cesium iodide, which constitutes the detector D makes it effective at detecting γ-rays, while the plastic in detector E makes it poorly performing at detecting γ-rays, but efficient at detecting neutrons.
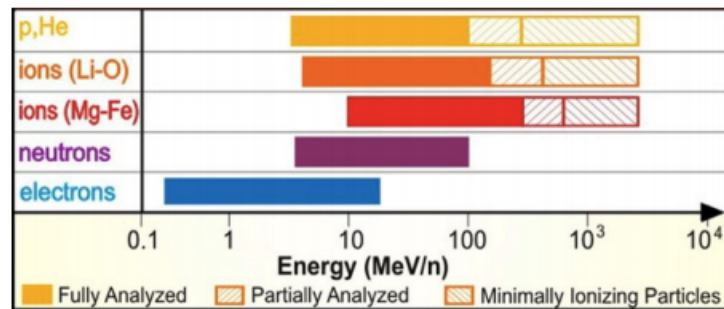
Figure 3.32: RAD energy coverage for both charged and neutral particles [41].

RAD Electronics Box   The *Front-End Electronics* (FEE) consists of a charge-sensitive preamplifier and a shaping amplifier, which changes the shape of the received signal so that it is displayed correctly. The electronics are designed to have very low noise and good stability throughout the temperature range in which the instrument is exposed. Thus, the RAD Electronics Box (REB) contains three circuit boards:

- RAD Analog Electronics Board (RAE): this board receives the seventeen analogue output signals produced by RSH. In addition, the Voltage-Input Readout Electronics for Nuclear Applications (VIRENA), which is a mixed-signal ASIC, provides, for each input channel, one amplification (with 1x, 2x, 4x, 8x gains), two discrimination levels ("Slow Trigger" branch and "Fast Trigger" branch referring to the relative timing of the two pulses), and

---

[24]Curiosity's MMRTG generates a lot of γ-rays and neutrons, although most of them are at low energies, so RAD can detect these particles and reject them before they are analyzed.

two flip-flops (elementary memory devices, used to store status information). Additionally, it has a single multiplexed output for analogue signals, which is connected to an analogue-to-digital converter (ADC) that is also located on the RAE board (Figure 3.33). The signals from the A1, A2, B and C detectors are amplified by two independent shapers in the RSH and each of the two outputs is further divided and amplified in the VIRENA, so that there are four channels for each of these detectors. Fast triggers for individual channels can be enabled or disabled, as can the corresponding slow trigger outputs, but only enabled fast triggers (*BU*, *DH*, and *EH*[25]) are inspected by *Level 1* ($L1$) and when one or more fast triggers are triggered, *Level 2* ($L2$) trigger processing is launched, which looks for specific (configurable) combinations of slow triggers. The BU fast trigger enables $L2$ triggers for charged particles and silicon dosimetry, while the DH and EH fast triggers enable neutral particle detection and E dosimetry. Events are assigned a "hardware priority" by $L2$, which influences downstream processing [41];

- RAD Digital Electronics Board (RDE): once the analogue signals coming out of VIRENA have been digitised, they are analysed by the $L2$ firmware in real time. This analysis is referred to as *Level 3* ($L3$) and takes place in a virtual microprocessor instantiated in the *RDE FPGA*. The $L2$ trigger assigns a hardware priority value (0 or 1) to each event and only particle event data marked as high hardware priority is sent from $L2$ to $L3$ via a FIFO (*First Input First Output*) buffer, and due to its limited space the same proportions of high and low priority events are not digitised. In any case, the aim is to keep as many rare events (in particular, heavy ions) as possible, even under high-speed conditions. At the end of an acquisition period, all data are packed into an observation package and stored until the rover retrieves them [41];

- RAD Sleep Electronics Board (RSE): the RAD is designed to make observations, with an autonomously managed wake/sleep frequency, without the intervention of the RCE. This function is implemented in the RSE Board. While RAD is sleeping[26], the RSE monitors the line receiving RAD's commands for activity (these can be orders sent by the RCE or noise on the line). RAD wakes up from sleep when two events occur (internal sleep timer expired or receipt of a command) and begins the boot process, only when the RSE applies power to the rest of the instrument. The RSE provides information to the software indicating if the wake-up is due to a command or due to the expiration of the sleep timer, then the software through this information decides whether RAD should start an observation, wait for further commands, or go back to sleep, if no other command is received within the next $60\,\mathrm{s}$ (thus avoiding confusing a random line noise with a command).

---

[25]There are VIRENA outputs for low gain (L), medium, gain (M), high gain (H), and ultra-high gain (U) [41].
[26]The sleep circuit is always on, drawing a small current of about $2\,\mathrm{mA}$.
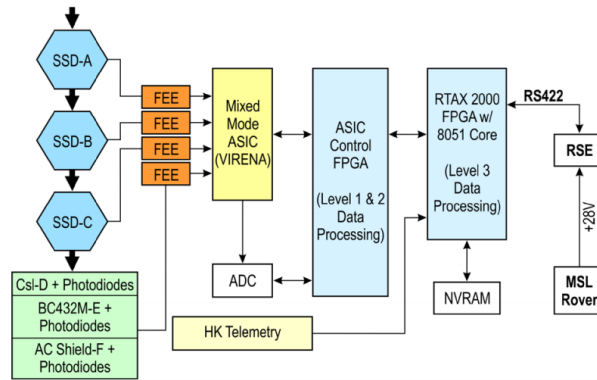
Figure 3.33: Block diagram of the *RAD Electronics Box* (REB) [41].

Electronics and usage time   RAD works independently of the rover's other activities. During the mission RAD takes observations once per hour for $16\,\text{min}$ followed by $44\,\text{min}$ of sleep time. During its sleep period, RAD gathers and stores all observations in a single packet even if the rover's main computer is asleep. RAD transfers all the data to the main computer which sends them to Earth, via telemetry, thanks to the UHF communication. Moreover, each time RAD wakes up, it performs a 10-second "pre-observation" measurement and if it detects high particle flux, it changes automatically mode and makes more frequent observation. RAD can accumulate about $400\,\text{kB}$ of data in an ordinary sol[27] and it has $16\,\text{MB}$ of a Non-volatile random-access memory (NVRAM), which is a random-access memory that retains data without applied power for data storage.

> **RAD - Power consumption**
> *Idling operating mode:* $0.1\,\text{W}$;
> *Normal power operating mode:* $4.2\,\text{W}$.

3.1.9   DAN: Dynamic Albedo of Neutrons

The Dynamic Albedo of Neutrons (DAN) is an active/passive neutron spectrometer that measures the presence and abundance of subsurface hydrogen in a shallow depth (up to a meter) of Mars' subsurface underneath Curiosity's traverse. The science objectives of the DAN instrument are:

1. Detect and provide a quantitative estimate of hydrogen underground for the entire mission duration;

---

[27]A solar day on Mars: approximately lasts 24 hours, 39 minutes, 35 seconds.

2. Examine and model the upper part (up to half a meter) of the subsurface and determine the possible layering structure of hydrogen-bearing materials in the subsurface;

3. Track the abundance of minerals that have water molecules in their crystal structures and monitor the variability of neutron radiation during the mission by periodic analysis.

The analysis of neutron data from planetary bodies (such as Mars in this case) is extremely important, because it provides useful information on the global distribution of hydrogen and highly absorbent elements in the subsurface. The passive neutron measurements onboard could be due to two different sources: the nuclear cascades in the subsurface due to GCRs and irradiation by the MMRTG, because due to the decay of ^{238}Pu also the MMRTG produces a flux of neutrons over a wide energy range (from thermal neutrons to fast neutrons), which takes part in the diffusion and moderation process in the subsurface colliding with atoms in the rocks and soils surrounding the rover (Figure 3.34). The impact can excite atomic nuclei resulting
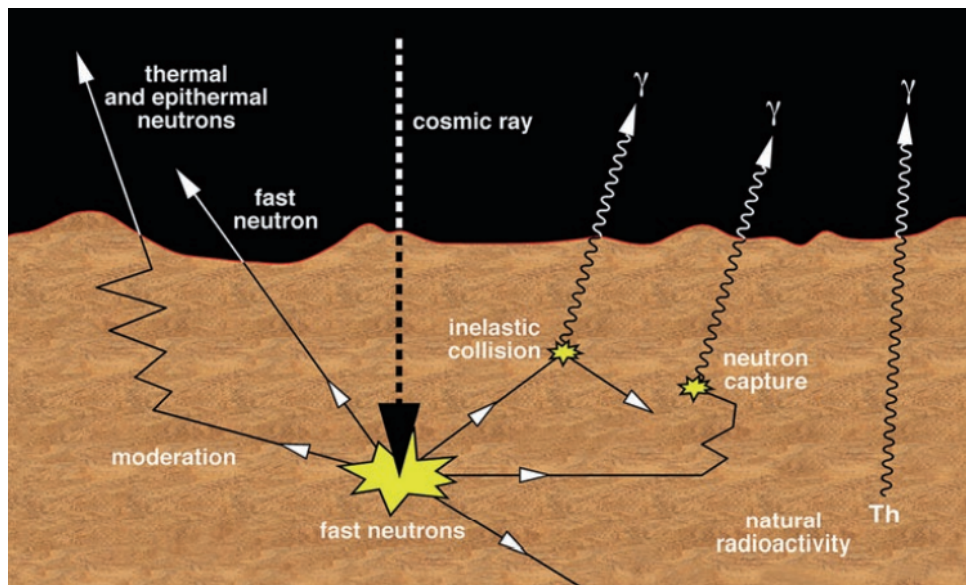
Figure 3.34: Various sources of nuclear radiation from a planetary surface [8].

in a release of nuclear particles and neutrons as they return to their ground states; in addition, neutrons lose kinetic energy with each collision, but they also can escape before experiencing enough collisions without losing too much energy (Table 3.8). Hence, the presence of hydrogen in soil drastically reduces the kinetic energy of neutrons resulting in the emission from the surface of more thermal neutrons than epithermal and fast neutrons, this means that the soil is rich in hydrogen.

The DAN science instrument has two separate units: *Pulsing Neutron Generator* (DAN/PNG) and *Detectors and Electronics* (DAN/DE), which are installed on the rear corners of the rover.

Table 3.8: Classification of free neutrons according to kinetic energies [42].

Neutron energy	Energy Range
Cold neutrons	$0-0.025$ eV
Thermal neutrons	0.025 eV
Epithermal neutrons	$0.025-0.4$ eV
Slow neutrons	$1-10$ eV
Intermediate neutrons	300 eV-1 MeV
Fast neutrons	$1-20$ MeV

DAN/PNG: DAN Pulsing Neutron Generator   The DAN/PNG is a small nuclear fusion re-actor capable of producing α-particles with an energy of 3.5 MeV and neutrons with an energy of 14.1 MeV according to the classical nuclear fusion reaction:

$$^{2}\text{H} + {}^{3}\text{H} \longrightarrow {}^{4}\text{He} + \text{n}$$
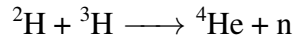
This reaction takes place if the relative kinetic energy of deuterium, ^{2}H, and tritium, ^{3}H, is about 100 keV to overcome the *Coulomb barrier*[28] and it occurs inside a vacuum tube, which accel-erates the deuterium ions, produced by the ion source, thanks to an electric potential difference of 120 keV. The operating temperature covers the range -40 to $50\,°$C, while the survival tem-perature -55 to $75\,°$C.

DAN/DE: DAN Detectors and Electronics   DAN/DE unit has two counters filled with ^{3}He at a pressure of 300 kPa, which differ in their shielding: one is enclosed in a lead shield, and the other in a cadmium shield. One counter is used as a *Counter of Epithermal Neutrons* (CEN) and it is covered by an cadmium enclosure, which is a strong absorber of X-rays and neutrons below the energy of 0.4 eV; the other counter is used as a *Counter of Thermal and Epithermal Neutrons* (CTEN) and it is covered by a lead enclosure which does not absorb neutrons, but only X-rays. Hence, subtracting the counts of the CEN detector from those of the CTEN detector will yield a count of thermal neutrons.

Moreover, the detection reaction is a capture of a neutron by the nuclei of helium-3 followed by the production of a proton and a triton[29] per each detected neutron:
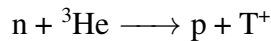
$$\text{n} + {}^{3}\text{He} \longrightarrow \text{p} + \text{T}^{+}$$

The operating temperature covers the range -40 to $50\,°$C, while the survival temperature -55 to $70\,°$C.

---

[28]It is the energy barrier, due to electrostatic interaction, that two nuclei must overcome in order to get close enough to undergo a nuclear reaction.

[29]The cationic form of the tritium isotope.

Usage time   DAN can perform passive neutron detection continuously, without using DAN/PNG, but can also operate in an active mode generating 13.4 million ($\sim 10^7$) neutrons with each pulse, lasting $2-3$ microseconds. Additionally, the pulsing frequency is between $1\,\mathrm{Hz}$ (single pulse per second) to $10\,\mathrm{Hz}$. Experiments with the DAN instrument are limited by two factors: the DAN/PNG has a warranted lifetime of 10 million pulses, so the MSL rover can expect to perform approximately 1000 typical active observations over its lifetime; moreover the DAN/PNG has a clock time limit of approximately 3 years after launch, because the helium generated by the pulses and the tritium target decay ruin the vacuum inside the ion accelerator.

DAN - Power consumption
DAN/PNG
Idling operating mode: $0.1\,\mathrm{W}$;
Power in enabling mode (ready to pulse): $1.4\,\mathrm{W}$;
Power in pulsing mode: $13\,\mathrm{W}$;
DAN/DE
Power at standby mode: $2.8\,\mathrm{W}\ (22\,\mathrm{V}) - 3.5\,\mathrm{W}\ (36\,\mathrm{V})$;
Power in passive mode: $3.7\,\mathrm{W}\ (22\,\mathrm{V}) - 4.5\,\mathrm{W}\ (36\,\mathrm{V})$;

3.1.10   REMS: Rover Environmental Monitoring Station

REMS is a science instrument that measures and monitors six atmospheric parameters: wind speed and direction, atmospheric pressure, relative humidity, air and ground temperature and UV radiation. The measurements provide usable information for studies of atmospheric processes, so the main scientific objectives concern the study of:

1. Microscale dynamics weather systems (e.g. boundary layer turbulence and heat fluxes);

2. Mesoscale phenomena near the surface that include motions larger than those that occur within BL turbulence but smaller than the synoptic scale motions (e.g. fronts, jets);

3. Synoptic meteorology that include local hydrological cycle, thermal tides, mean large-scale circulations, dust storms and low-pressure weather systems (e.g. spatial and temporal variability, diffusive transport from regolith);

4. UV radiation environment: destructive potential of UV radiation, dust UV optical properties and oxidant production;

5. Local water vapor and dust cycles: subsurface habitability based on ground-atmosphere interaction.

REMS consists of four units: two *booms* (*Boom 1* and *Boom 2*) attached to the rover Remote Sensing Mast (RSM), the *Ultraviolet Sensor* (UVS) mounted on the rover top deck, and the electronics box, *Instrument Control Unit* (ICU), located inside the rover body (Figure 3.35).
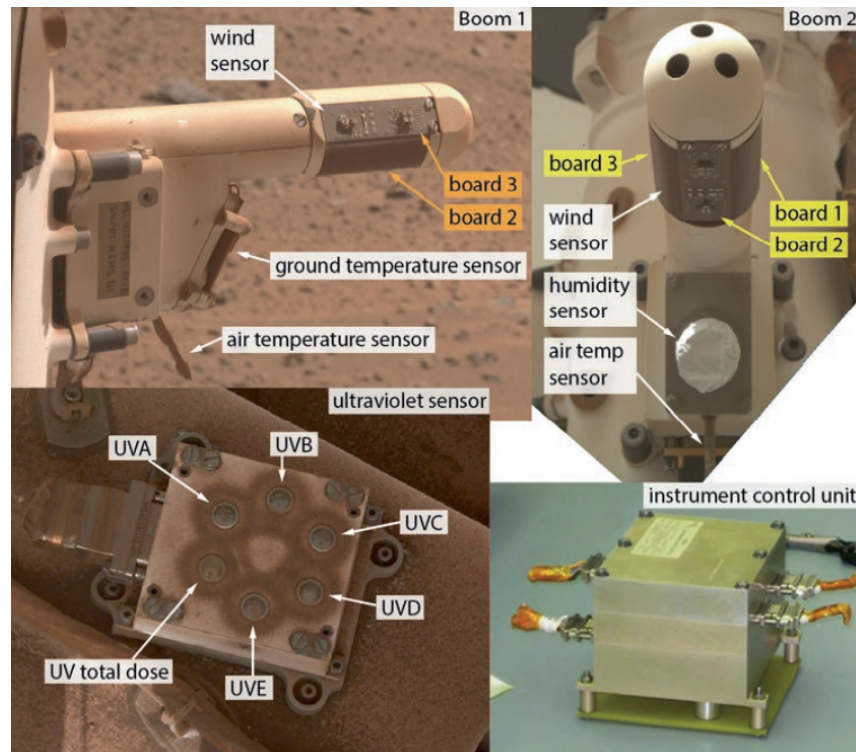
Figure 3.35: REMS components: the electronics box contains a pressure sensor. Both Boom 1 and Boom 2 have Wind and Air Temperature Sensors, however while Boom 1 has a Ground Temperature Sensor, Boom 2 has a Humidity Sensor; in the Ultraviolet Sensor the labels identify the different photodiodes [8].

Instrument Control Unit   The Instrument Control Unit (ICU) performs multiple functions:

- Provides the interface with the rover in terms of data, telemetry and power;

- Powers the Sensor Front-End (SFE) electronics to receive the digital data to be managed and analyzed;

- Processes data from the pressure, humidity and ultraviolet sensor, because they are not connected to the SFE.

The Sensor Front-End (SFE) ASIC[30], in turn, provides the sensor electronic interface for the air temperature, wind and ground sensor (Figure 3.36), so it receives all the low level analogue

---

[30]Application-Specific Integrated Circuit.

signals generated on the sensors and converts them into digital signals ready to be transmitted to the ICU where can be processed and stored.

The ICU also monitors the operating temperature range of each ASICS SFE through a *heater* and a *thermistor*: the heater is powered on when thermistor readings are lower than $-55\,°C$ and the ASIC is powered on when its temperature is higher than $-70\,°C$, becoming functional from $-52\,°C$.
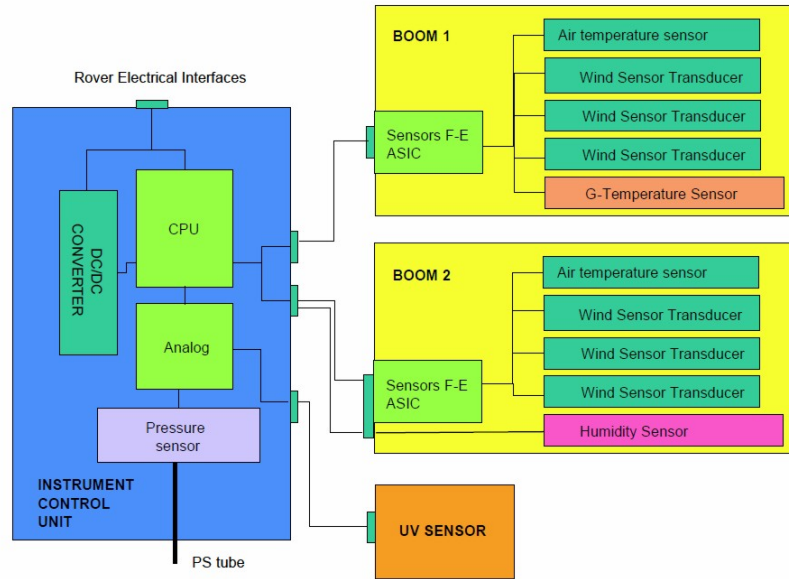
Figure 3.36: REMS block diagram: both booms include their associated SFE ASICS electronics. In Boom 1, the ASIC electronic manage the WS, GTS and ATS signals, while in Boom 2 it is only responsible for the WS signal, because the HS is connected directly to the ICU. Moreover, ASIC-ICU communication are digital to minimize external noise effects [43].

Booms   The booms are approximately $1.5\,m$ above ground level. Boom length is similar to the RSM diameter and they are fixed on a part of the mast that does not rotate, so they cannot change orientation. The two booms are separated in azimuth by $120°$ to make sure that at least one would always experience wind and records clean data for any given wind direction.

Wind Sensor   The Wind Sensors (WS) are based on hot film anemometry and they are composed of three measuring points around each Boom, which are based, in turn, on tiny titanium resistors that to keep them at a constant temperature it is essential to supply a certain amount of power, then an algorithm combines the data from all the six recording points to determine the true wind speed and direction. The booms are located in different position for two reasons: resistors strongly depends on the temperature of the instrument, so it is better to have them separated from the hot rover; it would be more convenient not to obstruct the wind flow.

Air Temperature Sensor   The Air Temperature Sensors (ATS) are mounted on both booms, attached to the lower edge of the SFE ASIC housing, protruding in the direction of the boom front-end and consist of small rods manufactured with low thermal conductivity material with two thermistors: one at the tip to measure the ambient temperature and one at the middle to avoid data contamination due to the rod heating produced by the boom heating itself. The ATS is capable to measure the air temperature near the booms over the range of 150–300 K with a resolution of 0.1 K and an accuracy of 5 K [43], with the Wind Sensor switched off, but the electronic circuits located at the base of each boom, must be kept above $-70\,°C$ and when a sensor detects that the temperature falls below, it turns on its heater.

Ground Temperature Sensor   The Ground Temperature Sensor (GTS) uses three thermopiles to record the infrared (IR) brightness temperature of the Martian surface. The GTS is located on Boom 1 and it is connected to the Sensor Front-End electronics (Figure 3.36). The thermopiles look downwards, pointing at the ground to the right of the rover and covering an area of about 100 m. The sensor includes an active self-calibration system to compensate potential degradation during the mission (e.g. dust amassing on the sensor). The GTS is capable to record the ground brightness temperature over the range of 150–300 K with a resolution of 2 K, by averaging 1 minute reading, and an accuracy of 10 K.

Humidity Sensor   The Humidity Sensor (HS) consist of a polymer film whose electrical properties change as temperature and humidity change. The polymer film constantly responds to changes in the environment, but humidity can only be read when the sensor is powered, this implies a warming up of the sensor itself, which compromises the humidity measurements: the most accurate are the ones made immediately after it has been powered on.
The Humidity sensor is calibrated to measure from 0 to 100% RH and can survive even if the ambient temperature is $-135\,°C$, but below $-70\,°C$ the dynamic range becomes too small for practical humidity observations. Typical sensor accuracy is $\pm2\%$ RH at $0\,°C$, $\pm4\%$ RH at $-40\,°C$, $\pm8\%$ RH at $-70\,°C$. Mars has little water in its air, but at night the temperature drops low enough that relative humidity can reach as high as 70%

UV Sensor   The Ultraviolet Sensor (UVS) is located on the rover's deck, has six photodiodes (Figure 3.35) and UVS sensor signals are transmitted directly to the ICU (Figure 3.36). Due to its location and direction, the upward-pointed light sensor is exposed to dust deposition and design constraints ruled out any active protection system. Nevertheless, to mitigate the dust degradation effect, each photodiode is surrounded by a ring-shaped magnet that creates a magnetic field that deflects Martian dust and prevents it from falling in its center. In addition, the sensor are covered about 10% of the time by shadows (mostly from the rover mast), then these collected data are simply removed from the dataset. The resolution of the sensor is 0.5% and

the accuracy better than 5% of the maximum measurable irradiance.

After calibration the measurement range is:

- UVA: 320–380 nm;

- UVB: 280–320 nm;

- UVC: 200–280 nm;

- UVD: 230–290 nm;

- UVE: 300–350 nm;

- Total Dose (UVABC): 200–380 nm.

The spectral response[31] of the REMS UV photodiodes is shown in Figure 3.37.
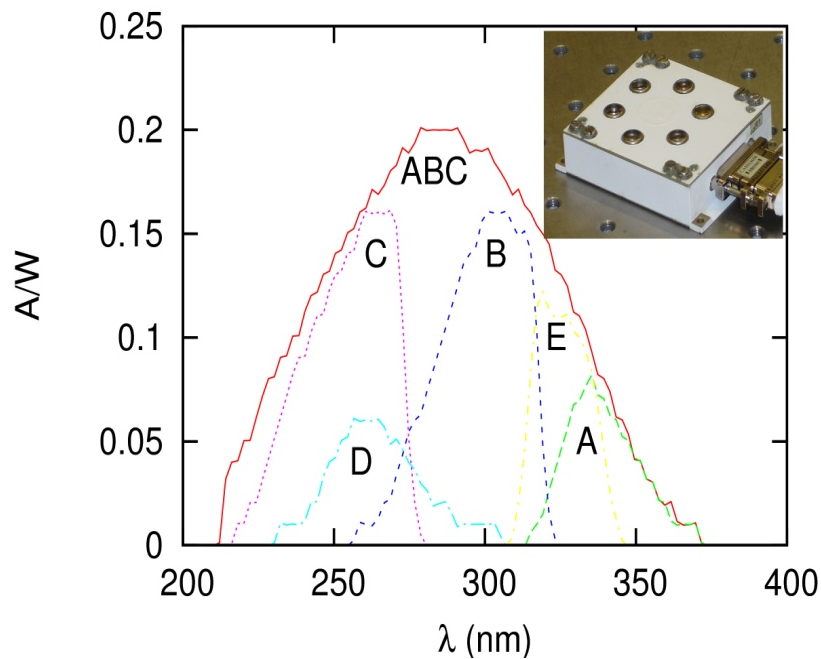
Figure 3.37: Spectral response of the REMS UV photodiodes [44].

Pressure Sensor   The Pressure Sensor (PS) is located inside the REMS electronics box (Figure 3.36) and it is calibrated for Martian pressure range of 4–12 hPa and operational temperature over the range -45–$55\,°$C. The sensor has two transducers, one highly stable and the other highly reactive to pressure changes, both of which record useful measurements for this reason

---

[31]On the ordinate axis it is represented the spectral responsivity, which is the ratio of the generated photocurrent to incident light power, expressed in A/W, when the photodiode is used in photoconductive mode.

they can be used in turn, thus providing some redundancy and improved reliability.

Its measurement range goes from 1–$1150\,\mathrm{Pa}$ with an end-of-life accuracy of $20\,\mathrm{Pa}$, a resolution of $0.5\,\mathrm{Pa}$ and a response time of the overall pressure measurement system of 1 second. In addition, the measurements of the last few minutes are taken into account, because the sensor provide better readings after warming up.

Usage time   REMS performs regular observations for approximately 5 minutes of every hour, all the time, gathering data at a sampling rate of ($1\,\mathrm{Hz}$) or better, depending on the objective. The sensors become operational each hour and after monitoring and storing data, they go into standby mode regardless of the rover's operations. REMS operation is designed assuming a total of three hours of operation (limited by power availability) each day, two hours for 5-minute hourly observations, and the third hour can be pre-scheduled and programmed as a continuous block. Another option implemented in the REMS flight software is a simple algorithm which provides the opportunity of managing some of the regular observations autonomously when an atmospheric event is detected.

> **REMS - Power consumption**
> *Stand by:* $402\,\mathrm{mW}$;
> *Start-up idle:* $4620\,\mathrm{mW}$;
> *ASIC heating:* $8744\,\mathrm{mW}$;
> *Humidity regeneration:* $5479\,\mathrm{mW}$;
> *GTS calibration:* $5174\,\mathrm{mW}$;
> *Data download:* $4760\,\mathrm{mW}$;
> *All sensors measuring (without ASIC heating):* $5432\,\mathrm{mW}$;
> *All sensors measuring (with ASIC heating):* $10\,082\,\mathrm{mW}$.

3.2   Telecommunications

The MSL rover receives commands directly from Earth and returns most of its data through relay orbiters (MRO, Odyssey and MEX[32]). One of the primary limitations of deep-space mission is the telecommunications bandwidth: Curiosity is capable of sending only $500\,\mathrm{Mbit}$ data per sol, because the data volumes transmitted depend on many factors (orbiter range and elevation and pass duration). The rover usually receives the daily commands sequence directly from Earth via an X-band transmission between a Deep Space Network dish and the high-gain

---

[32]MEX, used only in the EDL Sequence, does not receive any data, but records the presence of MSL's UHF Stream as a function of time, indicating up to which point UHF is available, meaning the rover is operational. If the stream will be present up to the surface, MEX will register that and provide time-stamped data to confirm that the Rover is on Martian soil; MEX can register also if the UHF stream be interrupted before landing.

antenna (Figure 3.38) and overnight typically wakes up from sleep to return more data. Earth
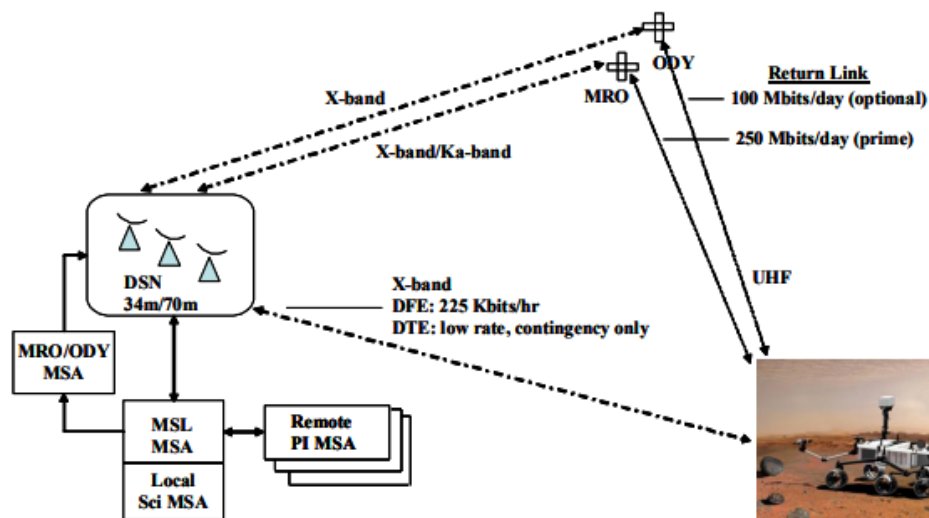
Figure 3.38: Schematic diagram of MSL communication operations [45].

is able to receive faint signals from distant spacecraft thanks to the giant radio antennas of NASA's *Deep Space Network* (DSN), which is one of the largest and most sophisticated telecommunications network with a ground system to transmit to and receive data from the spacecraft (Figure 3.39). The DSN currently includes ground stations, positioned approximately 120° of longitude[33] apart from each other, called Deep Space Stations (DSS), at three Deep Space Communications Complexes (DSCC) around the world:

- CDSCC near Canberra, Australia;

- MDSCC near Madrid, Spain (Figure 3.39);

- GDSCC at Goldstone in the California desert.

Each site includes several 34-m individual stations, referring to the diameter of the antenna in meters, and one 70-m station. In addition, individual stations at a site may be arrayed together to provide more downlink margin (currently being tested for the uplink).

3.2.1   MSL Antennas

The surface telecommunications system uses three antennas: two for X-Band DTE/DFE (Direct to/from Earth) to communicate directly with Earth, and a UHF antenna for communicating with a relay orbiter (Figure 3.40). Curiosity has two X-band antennas: the Low-Gain Antenna (LGA), mainly used for DFE; the High-Gain Antenna (HGA), used for either DTE or DFE.

---

[33]In this way at least one station can receive a spacecraft at any time.
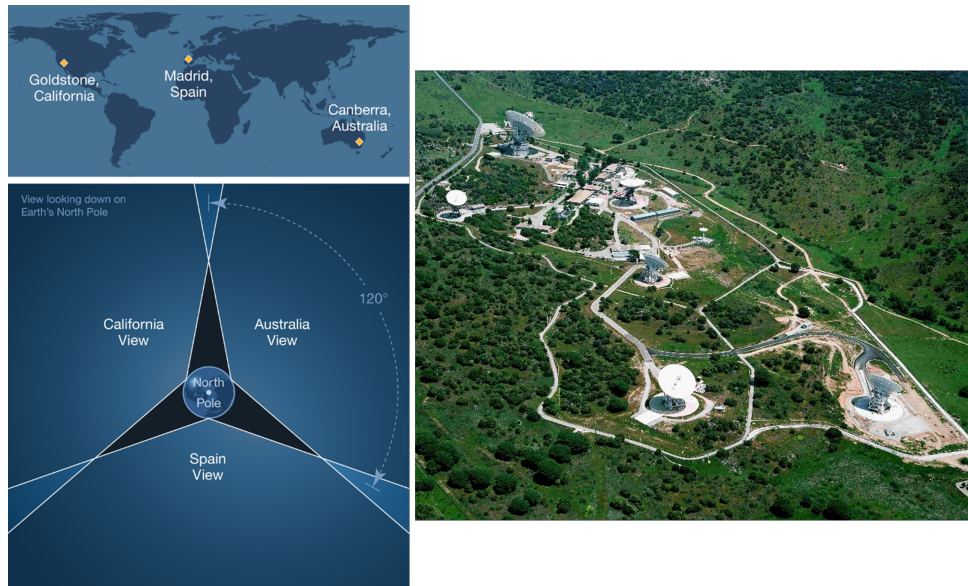
Figure 3.39: Locations of the Deep Space Network stations on the left and the Madrid Deep Space Communications Complex (MDSCC) on the right [46] [47].

In addition, X-band communications happen through one of two redundant *Rover Small Deep Space Transponders* (RSDST). Having multiple antennas is essential, because it provides back-up options in case they are needed.
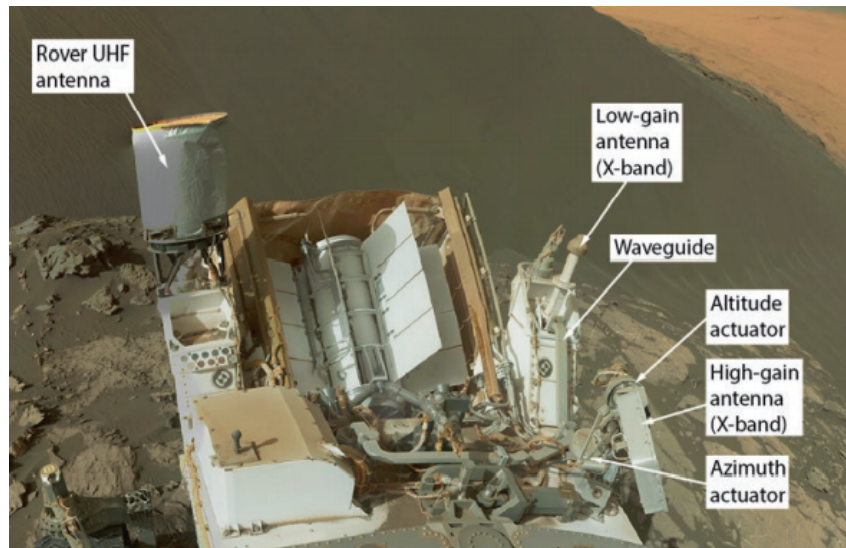
Figure 3.40: Curiosity's telecommunications hardware [8].

The X-Band High-Gain Antenna   The High-Gain Antenna (HGA) is hexagonal shaped with a diameter of $0.28\,\mathrm{m}$ and can be steered in both azimuth and elevation, in this way the entire rover does not necessarily have to change positions to communicate data, but the antenna can
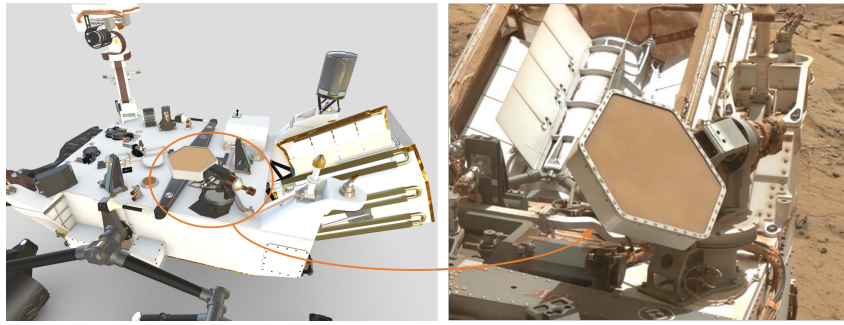
Figure 3.41: High-Gain Antenna located on top of the rover deck [39] [48].

move to point itself directly to any Earth station (Figure 3.41). Curiosity uses its HGA to receive commands and transmit telemetry to Earth, but it has to be aimed properly and it sits on a 2-DOF gimbal, with $5°$ system pointing accuracy[34], limited in part by the accuracy of the rover's knowledge of its own orientation. The basic telecommunication requirement for surface operations on the HGA is to provide a downlink at least of $160\,\mathrm{bit/s}$ to a 34-meter DSN antenna or $800\,\mathrm{bit/s}$ to a 70-meter one. Running in the other direction, the HGA can receive uplinked commands at a rate of 1–$2\,\mathrm{kbit/s}$. A typical daily uplink of command load takes approximately 15 minutes for a total volume of $225\,\mathrm{kbit}$. The characteristics of the HGA are shown in Table 3.9.

Table 3.9: Curiosity HGA characteristics [45].

Parameter	Value	Conditions
Dimensions	$25.5{\times}29.4\,\mathrm{cm}$	
Transmit Gain (dBi)	25.5	$0°$ off bore-sight
	24.1	$2°$ off bore-sight
	20.4	$5°$ off bore-sight
Receive gain (dBi)	20.2	$0°$ off bore-sight
	19.7	$2°$ off bore-sight
	17.3	$5°$ off bore-sight
Loss in gimblas (dB)	1.2	
Polarization	RHCP	
Transmit axial ratio (dB)	3.0	Within $5°$ from bore-sight
Receive axial ratio (dB)	2.4	Within $5°$ from bore-sight
Frequency range (GHz)	$8.395-8.455$	X-band

The X-band Low-Gain Antenna   Curiosity uses its omni-directional Low-Gain Antenna mainly for receiving signals and information in every direction. The antenna transmits radio waves at

---

[34]Relative to the peak gain at bore-sight, the downlink gain is about $4\,\mathrm{dB}$ lower and the uplink gain about $3\,\mathrm{dB}$ lower.

a low rate to the Deep Space Network antennas on Earth. Since landing, it is used every rover morning in the gap between the end of one master sequence and the start of the next, so at the start of the new master sequence, the rover sends a "beep" from its LGA; ground stations receive the acoustic signal, indicating that with the new sequence the operations are proceeding as expected. Apart from this, LGA, which does not require pointing, is also used when the rover is in safe mode, so command uplink will initially be done via DFE-only[35] (Figure 3.38) pass until HGA X-band communication becomes available as rover attitude information improves: one of the first actions in a safe mode recovery is to command the correct pointing to the HGA in order to increase the data transmission rate.
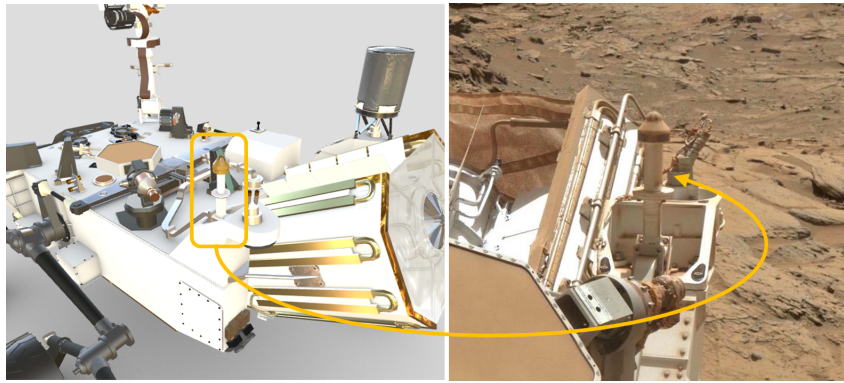
Figure 3.42: 3D model of the Low-Gain Antenna and its position on the rover equipment deck [39] [48].

Ultra-High Frequency Antenna   The single UHF quad-helix antenna is connected to redundant Electra-Lite Transceivers (ELT[36]), based on the MRO Electra transceiver. ELT is less massive and consumes less power than orbiting ones, although the Odyssey and MEX radios are not Electras and do not have the adaptive data rate capability. However, the primary relay communications is via MRO, with two passes per sol to return scientific data from the surface and unless there is enough power to support UHF operations with Odyssey during the sun, communications could also be scheduled through Odyssey to return additional data or when MRO is not available. Using orbiters to relay messages is beneficial both because of their proximity to the rover compared to the DSN antennas on Earth and because the Earth is within their FOV for much longer time periods than the rover does on the ground. As defined by the Consultative Committee for Space Data Systems Proximity-1 (CCSDS[37]), standard-26, three frequency channels are available: When Earth visibility is limited, the UHF system can also be used to receive commands and the UHF link can operate on one of three frequencies (Table 3.10), but in practice Curiosity almost exclusively uses $401.585\,625\,\text{MHz}$ [49]. The MRO pass

---

[35]DFE-only because the expected downlink capability via the LGA is very low, but uplink capability exists up to $125\,\text{bit/s}$ via a 70-m station; during these initial surface operations, downlink will be done at UHF at much higher

Table 3.10: Mars Reconnaissance Orbiter return link frequency.

Channel	Frequency
0	401.585 625 MHz
1	404.4 MHz
2	397.5 MHz

pattern repeats every 17 sols and provides anywhere about 30–60 Mbit per pass, approximately 100–1150 Mbit per sol. The expected average performance per sol is well above the 250 Mbit (Figure 3.38) requirement total for the two passes.
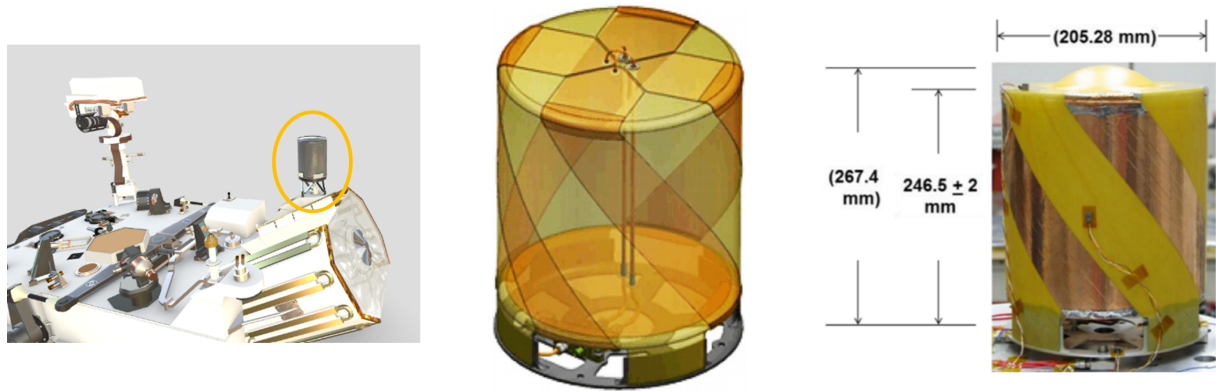
Figure 3.43: Low mass quadrifilar helix antenna, from left to right: UHF antenna located on the rover equipment deck, the schematic model and the real size of the built antenna [39] [45] [50].

Antennas - Power consumption [45]
X-band RSDST
RX: 11.3 W;
RX + Non-Coherent TX (TLM Only: SAFE-MODE): 14.8 W;
RX + Coherent TX (TLM Only: CRUISE-MODE): 14.2 W.
X-band SSPA
Exciter OFF (no RF drive): 45.1 W;
Exciter ON: 62.9 W.
UHF-band - ELT
Stand by mode: 21 W;
Transmitting mode: 69 W.

data rates [45].
[36] A telecommunications package that acts as a communications relay and navigation aid for Mars spacecraft and rovers.
[37] Link Protocol.

3.3 Engineering cameras

The engineering cameras are primarily designed to support operational activities of the MSL rover on the Martian surface, their images provide the first views from the landing and are used to autonomously detect, monitor and avoid hazards, to support rover navigation, its localization and positioning of the robotic arm. During a rover traverse, onboard engineering camera images will be used to assess the viability of the near-field terrain surrounding the rover. Additionally, the Navcams and Hazcams have identical detectors: each one is a frame-

Table 3.11: Engineering Camera optical properties [51].

Parameter	Navcam	Hazcam
Operating temperature	$-55\,°C$ to $+55\,°C$	
Pixel scale at the center of the FOV	$0.82\,\text{mrad/pixel}$	$2.1\,\text{mrad/pixel}$
Effective Focal Length	$14.67\,\text{mm}$	$5.58\,\text{mm}$
Focal ratio	f/12	f/15
FOV horizontal	$45.0°$	$124.0°$
FOV vertical	$45.0°$	$124.0°$
Focus range	$0.5\,\text{m}$ to infinity	$0.10\,\text{m}$ to infinity
Entrance Pupil Diameter	$1.25\,\text{mm}$	$0.37\,\text{mm}$
Hyperfocal Distance	$1.0\,\text{m}$	$0.5\,\text{m}$
Spectral range	600–$800\,\text{nm}$	600–$800\,\text{nm}$

transfer device with a $12.3 \times 12.3\,\text{mm}$ imaging region containing 1024 pixels and each one is $12\,\mu\text{m}$ square. It has 3 readout mode: full-frame mode, in which the readout time is $5.4\,\text{s}$; 4×1 binned mode, in which the readout time is $1.4\,\text{s}$; windowed mode with a variable readout time (proportional to the window size) of less than $5.4\,\text{s}$. For more information see the Table 3.11.

Table 3.12: MSL Engineering Camera configuration [51].

Property	Navcam	Front Hazcam	Rear Hazcam
Stereo baseline	$42.4\,\text{cm}$	$16.7\,\text{cm}$	$10\,\text{cm}$
Stereo co-alignment difference	$< 1°$	$< 2°$	$< 2°$
Bore-sight Pointing	Azimuth: $0° - 360°$ Elevation: $-87° - 91°$	$45°$ below nominal horizon	$45°$ below nominal horizon
Height above Martian Surface	$1.9\,\text{m}$	$0.68\,\text{m}$	$0.78\,\text{m}$

Rover Compute Element (RCE) The MSL imaging flight software runs on the RCE, which consist of two functionally identical *RCE A* and *RCE B*, each connected to a dedicated set of 6

engineering cameras (2 Navcams and 4 Hazcams), for a total of 12 cameras. A single RCE can only interact with the six cameras connected to it, so if the rover wants to acquire images from the other six cameras, it has to switch to the other RCE, this is because the engineering cameras are not cross-strapped between the RCEs. During surface operations, one powered RCE works as the primary computer while the other unpowered RCE works as a backup unit. Switching from one RCE to the other is only performed if necessary and this rarely occurs during the surface mission. Also, since the commands are identical for both RCEs, the same command sequences can be executed on both RCEs.

Navcams   The MSL rover has two pairs of black-and-white Navigation Cameras (Navcams) mounted on the mast, in a fixed position, to support ground navigation (Figure 3.44); these cameras use visible light to capture panoramic and stereoscopic three-dimensional imagery. Each camera has a 45° field of view and they work in cooperation with the hazard avoidance cameras (Hazcams) by providing a complementary view of the terrain. The Navcams sit approximately 1.9 m (exact value depends on elevation of RSM head) above the nominal Martian surface when the rover is level and they are pointed out towards the horizon, but their precise elevation depends upon the tilt of the mast head. They are spaced 42.4 cm from each other, which allows them to provide depth perception up to a distance of 100 meters. A Navcam shoots 8 images at intervals of about 13 s, observing for a total of 91 s. The images are downsampled by a factor of two, producing 512-pixel-square images.

Hazcams   The MSL rover has four pair of black-and-white Hazcams mounted on the lower portion of the front and rear of the rover (Figure 3.44); they can be used to capture a three-dimensional detailed stereo map of the immediate surroundings. The fish-eye Hazcams provide the rover with situational awareness of the surface both in the front and rear of the rover and in between the wheels, mainly in areas not visible to the Navcams. As they are fixed (can not move independently), they have a wide FOV (Table 3.11) to allow a large amount of terrain to be visible and to protect the rover from accidental impacts against unexpected obstacles and work in parallel with the software that allows the rover to make its own safety choices. More information about Engineering Camera configuration are shown in Table 3.12.

Engineering cameras - Power consumption
Navcams - Front and Rear Hazcams
Normal operating mode: 2.15 W.
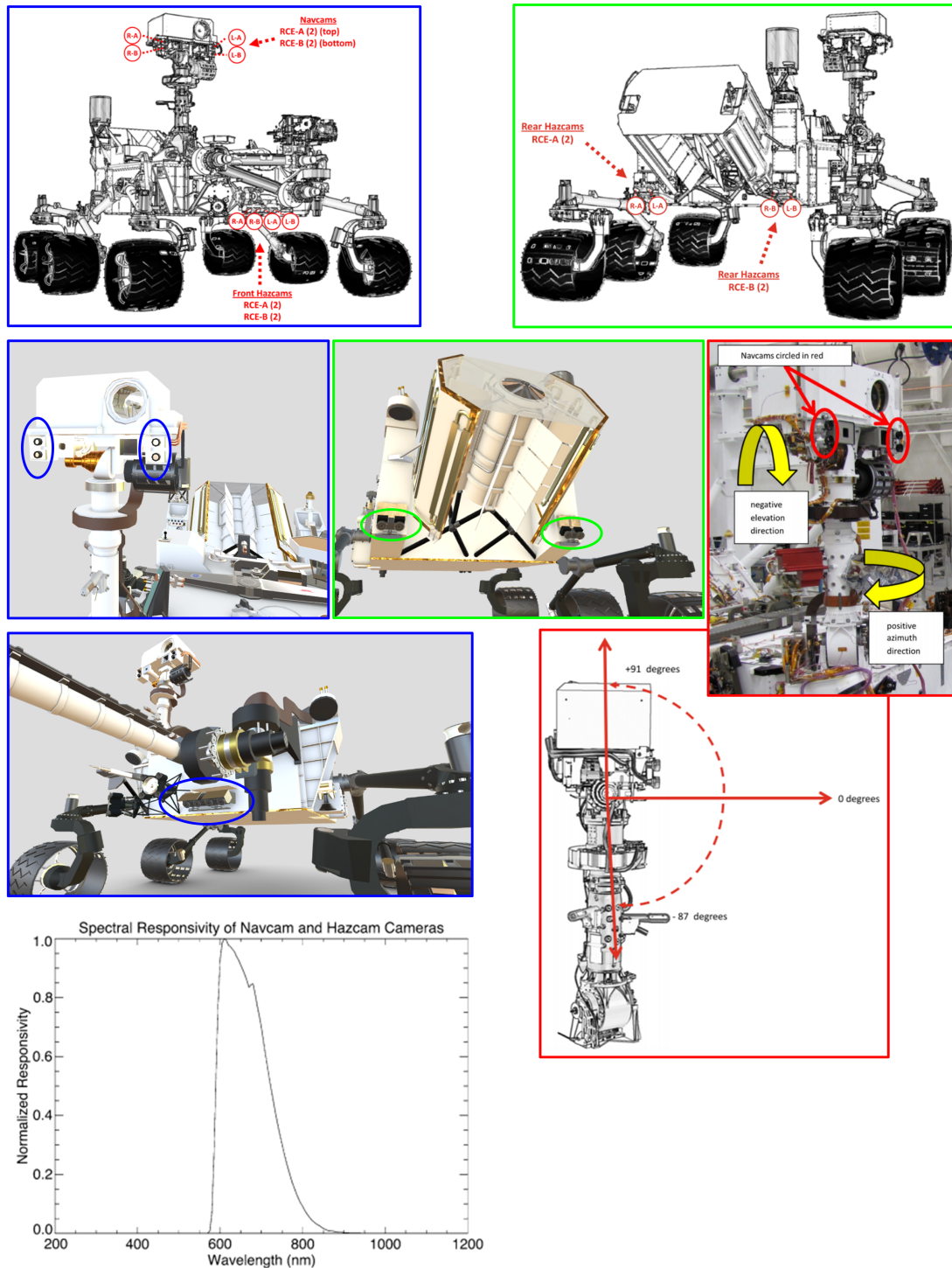
Figure 3.44: In the blue box: positions of Navcam and Front Hazcam Cameras (L and R denotes left and right). The front Hazcams are mounted near the middle of the front of the rover with A-side and B-side cameras interleaved, each offset from the next by $8.2\,\mathrm{cm}$, giving a stereo separation of $16.7\,\mathrm{cm}$ (Table 3.12) for each pair. In the green box: position of the Rear Hazcam. In the red box: allowable elevation manoeuvring range for the RSM head and positive/negative direction of azimuth and elevation. The last image below represents the normalized spectral responsivity of Navcam and Hazcam Cameras [51].

4. Electrical energy storage subsystem

Taking into account what was said about the operation of the batteries in Chapter 1, in the wake of that chapter an electrical design of the batteries (number of cells in series and in parallel) on board the Curiosity rover will be carried out, considering the worst-case scenario of use. Curiosity remains active on average about 6 hours every Martian day to perform the scheduled activities and as seen in Chapter 2, the MMRTG can only provide $110\,\mathrm{W}$ of power, so the rover is completely dependent on its batteries, spending most of its time in minimum power conditions and recharging. The power absorbed by each component of the rover (seen in Chapter3 above), enables a qualitative and quantitative electrical drawing of the on-board battery pack, allowing the right conclusions to be drawn as to why a specific battery was used rather than another.

4.1   General design procedure

The general procedure followed will be that shown in figure 2, repeated for each distinct type of electrochemical cell in order to choose the most suitable one for the mission, by means of a few factors:

1. Ease of construction: comparison between the number of cells in series and parallel, the fewer, the easier to assemble;

2. Battery capacity: total capacity of the battery, the lower the better for the same amount of energy supplied;

3. String current: the lower this value, the better, because as the string current increases, the cross-sectional area of the cables increases, which increases in mass;

4. Volume: depends on the volume provided for the battery pack, it is a decisive factor in the choice of the electrochemical cell, so it is better to have as low a value as possible;

5. Mass: a higher mass results in a non-negligible increase in costs;

6. Bus margin: it is advantageous to have the tightest possible adjustment margins, in order to avoid going below the minimum bus voltage, and for this reason it is advisable not to go beyond 60% Depth of Discharge (DoD[1]);

---

[1]Defined as the ratio of discharge capacity (C_d) to electrochemical cell capacity and is an alternative method of indicating the state of charge (SoC) of a battery (i.e. the capacity removed from a fully charged battery).

7. Internal losses due to Joule heating: these must be limited so as not to lose useful energy in heat and must always be below 3% of the power required by the subsystems.

Mission requirements To successfully complete the mission, the battery must meet a number of requirements and perform certain functions, including [52]:

1. Must not have a drop in performance in the $6-12$ months of storage before use;

2. Provide $920 \, \text{Wh}$ with a voltage greater than $25 \, \text{V}$ and a maximum discharge current of $22 \, \text{A}$ during the launch phase;

3. Withstand the cruise phase (approximately 9 months, from 26-11-2011 to 6-8-2012) with a maximum *DoD* of $30-50\%$ in a temperature range of -20–$40 \, °\text{C}$;

4. Support pulses of $30 \, \text{A}$, with battery at 100% *SoC*, for possible "*turn to entry*" manoeuvres during the cruise phase;

5. Support short duration $25 \, \text{A}$ pulses during the last phase before landing: the final sequence of *EDL* events;

6. Support the mission during surface life for at least 670 sols of operation.

Operational requirements The operational requirements of the battery on the Mars surface include the capability of:

- Being charged and discharged over a wide temperature range (-20–$30 \, °\text{C}$), while being qualified to survive in a range of -30–$40 \, °\text{C}$;

- Operating for more than 2000 cycles, in which the *DoD* shall not exceed 45%;

- Working at a voltage higher than $25 \, \text{V}$.

4.2 Definition of worst-case condition

In choosing the worst case, the activities carried out in the various sols are analysed. In Table 4.1 are shown all the power consumptions of the various instruments onboard the MSL rover. It should be emphasised that the most power-demanding activities are carried out in several sols and never at the same time, so as to distribute the power demand, allowing the size of the battery to be greatly reduced. Analysing the rover's activity in 3078 sols, it can be seen that the most alarming couplings for the battery are those shown in Figure 4.2. In the case of a CheMin analysis, the most stringent condition is considered (i.e. providing good quality results
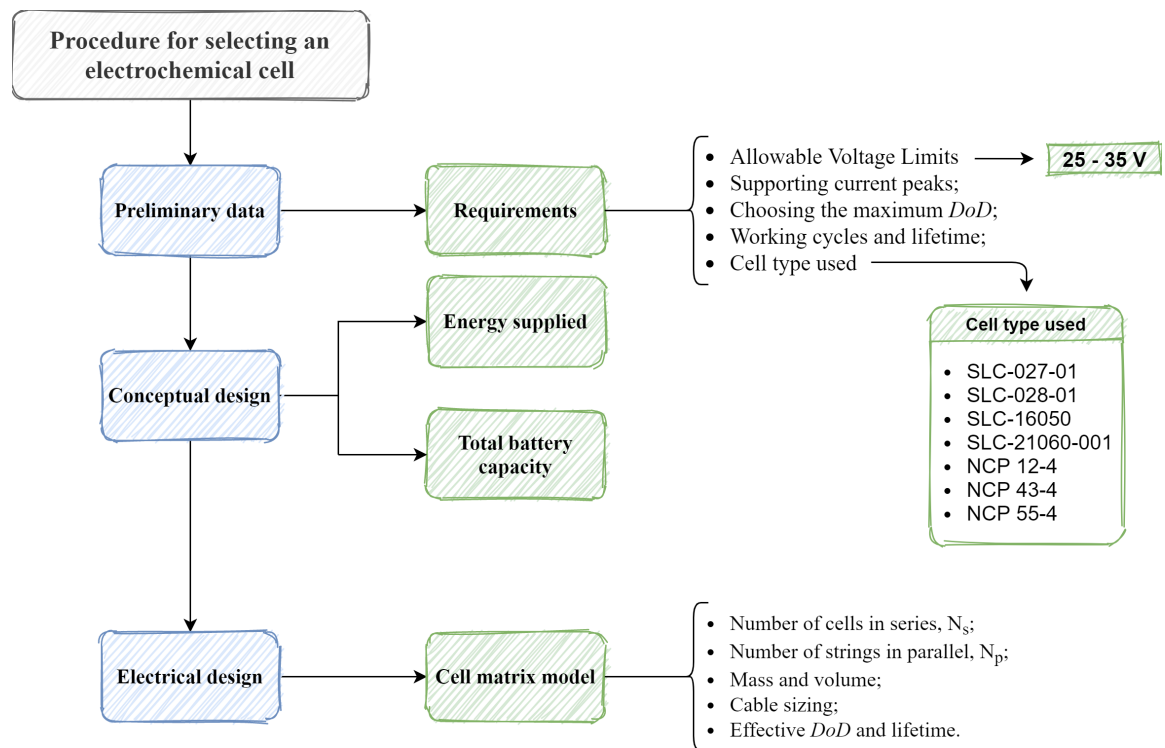
Figure 4.1: Procedure for choosing the right electrochemical cell [53].
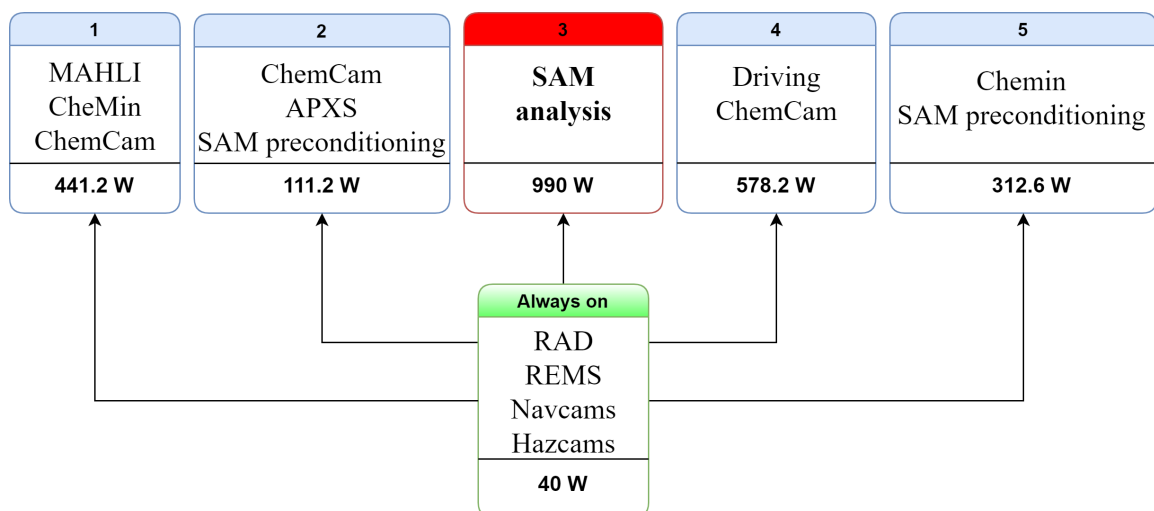
Figure 4.2: Pairings more power-demanding on the basis of which the battery is sized.

Table 4.1: Summary scheme of the power consumption of the various MSL rover instruments. The usage time of the mobility system is calculated knowing that in 1648 sols the rover has covered a maximum distance of $142\,\text{m}$ [8] (the maximum covered by Curiosity in a single sol) at an average speed of $4.2\,\text{cm/s}$ [19].

	Power (W)	**Usage time (hours)**
Science Instruments		
SAM	990	$4 - 6$
CheMin	$719\,\text{W}\,\text{h}$	$2 - 3$
ChemCam	$64.7 + 13.5\,(TEC)$	$2 - 3$
APXS	8	$2 - 3$
MAHLI	3.5	$-$
Mastcams	2×3.5	$-$
MARDI	3.5	$-$
RAD	4.2	6.4
DAN/PNG	13	$-$
DAN/DE	4.5	$-$
REMS	10	2
Telecommunications		
X-band - RSDST	14.8	$-$
X-band - SSPA	62.9	$-$
UHF-band - ELT	69	$-$
Engineering cameras		
Navcams	4×2.15	$-$
Hazcams	8×2.15	$-$
Driving		
Mobility system	500	$0.939\,(56.349\,\text{min})$
Sleep/Wake		
Asleep	$45 - 70$	$-$
Awake	150	$-$

in 2 hours). For the SAM preconditioning, a minimum power consumption of 25 W is assumed and in addition, it is supposed that the instruments inside the green box are always active (even during an analysis in progress) and contribute to the increase in power demand.

The maximum power consumption during a **SAM analysis** is 990 W (maximum peak power), so this is a typical worst case utilisation of power, data and experiment duration resources. For this reason, the power load of a SAM analysis is used to size the batteries and cables that feed the various subsystems.

4.2.1   SAM analysis: power-demand

In order to size the batteries, then calculate the number of cells in series and in parallel, it is necessary to provide an average power value over the time in which this power is absorbed. To do this it is necessary to examine the curves in Figure 3.8 which can be approximated by those in Figure 4.3 (through the use of MATLAB® software), which represent the three MSL power buses that service SAM in a time of about 6 hours. Knowing that the curves can not be approximated to functions (as they are empirical data), the composite *Trapezium rule* between the individual curve points is used to calculate the average power over the whole time interval efficiently and with small errors. Once the area under the curve is obtained, it is divided by the whole interval to get an average power absorption value. The values obtained are shown in Table 4.2. As will be seen in the electrical design in Section 4.4.1, the size of the cable diameter is extremely important, because the value of the Maximum Allowable Current (*MAC*) depends on it, and if it is smaller than it would be in the case of high consumption, it could irreversibly damage the power transfer Bus. Therefore, in order to overcome this problem, the current value that is assumed is the peak current (I_{peak}) defined as the ratio between the peak power and the nominal voltage, while the current of the various strings (I_{string}), for internal dimensioning, depends on the number of strings in parallel (N_p). The input data enabling the dimensioning of the entire battery are shown in Table 4.3.

DoD **and lifetime cycle**   In order to comply with mission constraints, DOD is not chosen above a threshold because battery lifetime depends on its value (Figure 4.4). Since the threshold is set at 45% (as already mentioned in the mission requirements), it can be observed that the number of cycles is quite higher than 2000, correctly meeting the requirements. In the following calculations a DoD of 50% is chosen, corresponding to about 14 000 cycles (curve approximated with *power interpolation*, as $a \cdot x^b$). Actually, at the end of the electrical design with the recalculation of the voltage drop in the cables it will always be lower than the one fixed in the input data (Table 4.3). The following is a detailed procedure leading to the selection of the most suitable electrochemical cell. At the end of the chapter, the numerical results and the selection of a suitable cell will be shown.
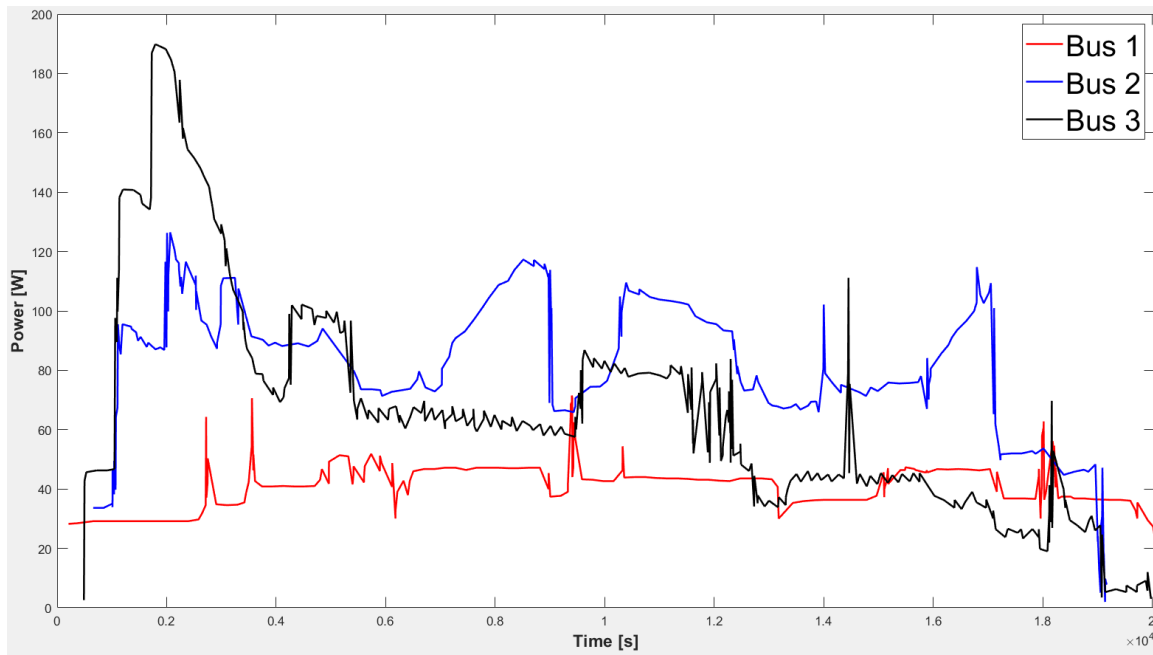
Figure 4.3: Power profile, used for battery design, obtained at the end of a SAM analysis, during a thermal vacuum test.

Table 4.2: Calculation of the average power in the three buses over a time interval of 6 hours (duration of an analysis with good results), essential for sizing the battery under normal operating conditions (of course the appropriate approximations are made at the end of the calculations).

	Bus 1	**Bus 2**	**Bus 3**
Average power [W]	40.6173	82.4360	65.6895
Total power [W]		188.7427	
SIZING BATTERY			
Safety factor		1.6	
Total sizing power (P_{req}) [W]		301.9884	
SIZING CABLES			
Peak power [W]	71.5099	126.4847	189.8709
Total peak power [W]		387.8655	
Safety factor		2	
Total sizing peak power [W]		775.73099	

Table 4.3: Input data: an efficiency of 97% is assumed for the cables and the voltage regulator in the discharge phase (e.g. a Buck/Boost converter). In addition, a cable length to the Buses of $3\,\mathrm{m}$ is assumed, which allows to calculate the voltage drop and joule losses; P_{req} is considered to be absorbed by a single Bus, for this reason it is time-averaged; $I_{L_{nom}}$ is the current value in the nominal operating condition.

Parameter	Value
P_{req} [W]	301.9884
T_{req} [h]	6
DoD	50%
η_{cable}	0.97
η_{reg}	0.97
$V_{BUS_{\min}}$ [V]	25
$V_{BUS_{nom}}$ [V]	28
$V_{BUS_{\max}}$ [V]	35
$I_{L_{nom}}$ [A]	10.7853
I_{peak} [A]	27.7047
Cable length [m]	3
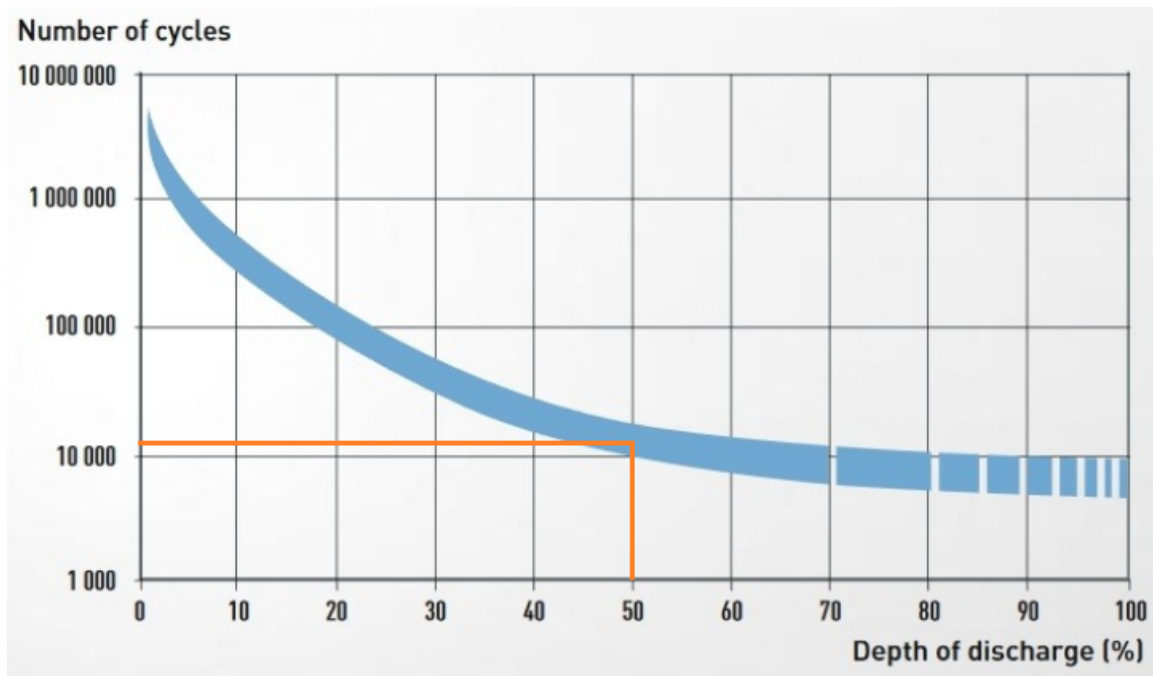
Figure 4.4: Lifetime of a lithium-ion battery (at $20\,^{\circ}\mathrm{C}$), which is expressed in terms of the number of charge and discharge cycles that can be performed depending on the *DoD* [53].

4.3 Conceptual design

The conceptual design calculates the energy supplied by the battery and the conceptual capacity, which will be used as control data in the electrical design that will be explained later. The energy provided by the battery to power payloads, enabling them to perform their scheduled tasks, is obtained from the concept of efficiency because unavoidable losses must be included in the energy transfer process, during discharge (η_d), and in the electrical cables (η_c) is:

$$W_{bat} = \frac{W_u}{\eta_d \cdot \eta_{reg}} = \frac{P_{req} \cdot T_{req}}{\eta} \tag{4.1}$$

where $\eta = \eta_d \cdot \eta_{reg}$, the P_{req} is the power required by the rover and T_{req} is the time in which that power is consumed. In addition, W_u is the energy actually usable by the rover. Knowing that all the energy needed by the rover in a sol has to be supplied within a specific *DoD*, the total energy stored by the battery is inevitably higher:

$$W_{S_{bat}} = \frac{W_{bat}}{DoD} = \frac{P_{req} \cdot T_{req}}{\eta \cdot DoD} \tag{4.2}$$

The conceptual capacity (C_c) of the battery is calculated by dividing the maximum stored capacity by the minimum BUS voltage ($V_{BUS_{\min}}$) set out in the above requirements:

$$C_c = \frac{W_{S_{bat}}}{V_{BUS_{\min}}} = \frac{P_{req} \cdot T_{req}}{\eta \cdot DoD \cdot V_{BUS_{\min}}} \tag{4.3}$$

Clearly, some of the stored energy will never be used, but it is essential to increase the lifetime of the battery.

4.4 Electrical design

Depending on the level of *DoD*, the minimum battery voltage is calculated using the discharge curves (Appendix B), provided by the manufacturer[2] (Eagle Picher-Yardney Division), entering the curve with the discharge capacity (C_d) obtained from the product of the nameplate capacity (C_N) of the cell and *DoD*. Applying Kirchhoff's second law to the electrical circuit, the relationship between the nominal BUS voltage ($V_{BUS_{nom}}$), the number of cells in series (N_s), and the minimum voltage of each cell ($V_{cell_{\min}}$, value obtained by entering the discharge curve with C_d) is obtained. From the above-mentioned expression the number of cells in series is calculated:

$$N_s = \frac{V_{BUS_{nom}} + V_c}{V_{cell_{\min}}} \tag{4.4}$$

---

[2]EaglePicher Technologies is America's leading manufacturer of space, military, medical and aviation batteries [54].

where V_c is the voltage drop in the cables, which is assumed in the worst case condition of $2\,\mathrm{V}$. Following the calculation of N_s, it is verified that the maximum and minimum voltage of the battery is within the admissible limits. Using $V_{BUS_{\min}}$, the value of the total capacity of the battery is recalculated, which is less than the value obtained in the conceptual design, and thanks to the technical documentation provided by the manufacturer, the number of strings in parallel (N_p) is calculated as follows:

$$N_p = \frac{C}{C_N} \tag{4.5}$$

The power and energy values calculated in the conceptual design are used as lower limits in the electrical design:

$$I_L > I_{L_{nom}} \tag{4.6}$$

$$P_{\max} = V_{BUS_{\min}} \cdot I_L > P_{req} \tag{4.7}$$

$$W'_{bat} = V_{BUS_{\min}} \cdot N_p \cdot C_N > W_{S_{bat}} \tag{4.8}$$

where $I_L = N_p I_{string_{nom}}$. The value obtained from the (4.5) must be iterated under the specific constraints (4.7) (4.8) (4.6) as shown in the Figure 4.5: The fixed numbers of cells in series
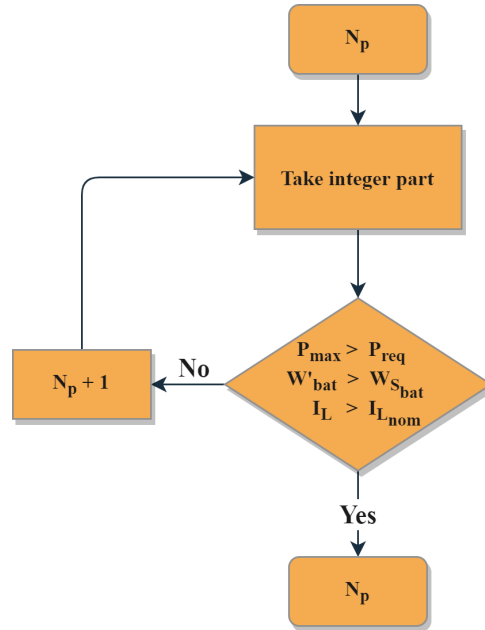
Figure 4.5: Algorithm for choosing the number of strings in parallel [53].

and parallel allow the preliminary estimate of mass and volume (these will be corrected later with the exact value of the battery energy, including the actual voltage drop in the cables) from the specific energy (E_{spec} [Wh/kg]) and energy density (ρ_{spec} [Wh/m^3]) provided by the cell manufacturer:

$$M = \frac{W'_{bat}}{E_{spec}} \qquad\qquad V = \frac{W'_{bat}}{\rho_{spec}} \tag{4.9}$$

4.4.1 Internal and external battery sizing

By knowing N_s and N_p and the size of the individual electrochemical cell (Table 4.4), the full size of the battery can be known (Figure 4.6):

Table 4.4: Calculation methodology for battery length and width.

Parameter	Value
Width (W_{cell})	$N_s \cdot w_{cell}$
Length (L_{cell})	$N_p \cdot l_{cell}$
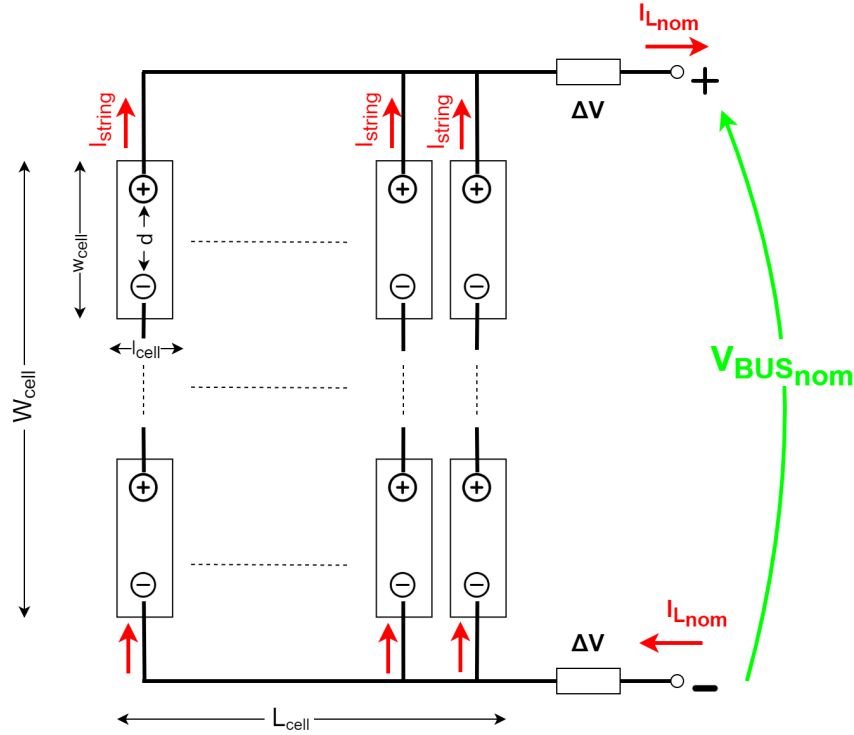
Figure 4.6: $N_s \times N_p$ matrix: function diagram.

External cable size and losses   As already mentioned in Section 4.2, external cables are sized considering the peak current, in order to prevent high current absorption, even for a short time, from damaging the cables. The current carrying a cable must be greater than the current flowing through it under maximum power and rated conditions. A standardised stepped logarithmic gauge system (AWG) is used to assess the size of the cable and the cross-sectional area of each gauge determines its current-carrying capacity (Table 4.5):

$$I_{AWG} \geq I_{peak} \; \longrightarrow \; AWG \; \longrightarrow \; Diameter \text{ (mm)} \; \longrightarrow \; Section$$

Table 4.5: Values are taken for unipolar current (single wire) with temperatures of up to $70\,^\circ$C. MIL-STD-975M (NASA) [55].

AWG	MAC single wire (A)	Section (mm^2)	Copper resistance $70\,^\circ$C (Ω/m)
30	1.3	0.05	0.41257713
26	2.5	0.14	0.147348975
24	3.3	0.25	0.082515426
20	6.5	0.5	0.082515426
16	13.0	1.5	0.013752571
12	25.0	4	0.005157214
8	44.0	10	0.002062886
4	81.0	25	0.000825154
0	147.0	50	0.000412577

From the AWG section, the resistance per unit length (r at $70\,^\circ$C, the last column of Table 4.5) can be obtained for copper. The losses due to the Joule effect, considering the outward and return cable (Figure 4.6), are therefore quantified as follows:

$$P_J = 2 \cdot r \cdot L_{cable}^{ext} \cdot I_{peak}^2 \qquad (4.10)$$

where L_{cable} is the distance between the battery and the transmission Buses of the rover, and the product r by L_{cable} is the resistance (measured in Ω) of the cables to the passage of current. It must be verified that P_J is less than 3% of the P_{req}.

For measuring the voltage drop, the method is the same. It is essential to always check that it is less than $2\,$V:

$$\Delta V = 2 \cdot r \cdot L_{cable}^{ext} \cdot I_{peak} \qquad (4.11)$$

Internal cable size and losses   Also in the case of internal battery losses, the dimensioning is always in the worst case, as mentioned in Section 4.2. Therefore, this time, the distance (d) between the electrodes (provided by the manufacturer) must be subtracted for the length assessment of the internal cables. This allows the internal losses[3] due to the joule effect to be calculated correctly:

$$P_J = r \cdot L_{cable}^{int} \cdot N_p \cdot I_{string_{peak}}^2 \qquad (4.12)$$

where L_{cable}^{int} is equal to $W_{cell} - N_s \cdot d$ and $I_{string_{peak}}$ is the peak current divided by the respective number of strings (this value is only used to design the internal cables).

---

[3]The voltage drop in the internal cables is negligible.

4.5   Final check

After correcting the value of the voltage drop ($V_c = \Delta V$) in the cables, the final step follows by recalculating:

1. The values of the minimum and maximum BUS voltage and check that they are within the limits (AVL) mentioned in section 4.1:

$$V_{BUS_{\min}} = N_s \cdot V_{cell_{\min}} - V_c > 25$$
$$V_{BUS_{\max}} = N_s \cdot V_{cell_{\max}} - V_c < 35$$

2. The energy of the battery, expecting it to be greater than that calculated in the conceptual design:

$$W''_{bat} = V_{BUS_{\min}} \cdot N_p \cdot C_N > W_{S_{bat}}$$

3. The *DoD*, through the energy value calculated in the previous point:

$$DoD = \frac{W_{bat}}{W''_{bat}}$$

4. Finally, the final mass and volume:

$$M = \frac{W''_{bat}}{E_{spec}} \qquad\qquad V = \frac{W''_{bat}}{\rho_{spec}}$$

4.6   Results

In this section only the most suitable electrochemical cell, with its numerical values of the various quantities, will be described, which in comparison with the others presented the most favourable factors among those reported in Section 4.1.

4.6.1 *NCP 43-4*

In Table 4.6 are shown all the results for the *NCP 43-4* electrochemical cell and the dimensions of the entire battery pack. From the results obtained, it can be seen that the number of strings (N_p) is higher than the solution proposed by NASA JPL ($\sim$1600 Wh, with 8 cells in series and 2 strings in parallel). This is because, the average power consumption (or duration) in a SAM analysis is probably lower and especially because the three buses are not dimensioned separately, but only one power transmission bus is assumed, thus increasing the size of the battery. All

other values are well within the requirements defined in Section 4.1. The comparison between the various cells is shown in the Appendix D.

Table 4.6: Summary table with results for the case of batteries with *NCP 43-4* electrochemical cells, the most suitable compared to the others.

NCP 43-4 Battery

CONCEPTUAL DESIGN	
W_u [Wh]	1811.93
W_{bat} [Wh]	1925.74
$W_{S_{bat}}$ [Wh]	3851.48
C_c [Ah]	154.06
ELECTRICAL DESIGN	
C_N [Ah]	43
E_{spec} [Wh/kg]	153
ρ_{spec} [Wh/l]	378
w_{cell} [mm]	106.7
l_{cell} [mm]	30.7
$V_{cell_{\max}}$ [V]	4.1
d [mm]	50.8
V_c [V]	2
$V_{cell_{\min}}$ [V]	3.65
C_d [Ah]	21.5
N_s	8
$I_{string_{nom}}$ [A]	3.583
N_p	4
BATTERY SIZING	
W_{cell} [mm]	853.6
L_{cell} [mm]	122.8
EXTERNAL CABLE SIZING	
I_{peak} [A]	27.7047
AWG	8
P_J [W]	9.5002
ΔV [V]	0.3429
INTERNAL CABLE SIZING	
$I_{string_{peak}}$ [A]	6.9262
AWG	16

P_J [W]	1.1801
FINAL CHECK	
$V_{BUS_{\min}}$ [V]	28.8571
$V_{BUS_{\max}}$ [V]	32.4571
W''_{bat} [Wh]	4963.42
DoD	39%
Mass [kg]	32.4407
Volume [l]	13.1307

5. Heat transfer

Where there is a temperature difference in a medium or between separate media, a heat transfer must occur. It takes place through 3 modes:

- **Conduction**: when exists there is a temperature gradient in a stationary medium (fluid or solid);

- **Convection**: occurs between a surface and a moving fluid at different temperatures;

- **Thermal radiation**: means the transfer of energy in the form of electromagnetic waves, actually all matter, which is at a temperature above $0\,\text{K}$, in its various forms, emits electromagnetic energy at different wavelengths, although the most significant energy content is that relating to wavelengths between 0.1–$100\,\mu\text{m}$ (UV, VIS, IR) so in the absence of a medium (e.g. in deep space) is the only way to transfer heat.

Since there is an atmosphere on Mars, although extremely rarefied (due to low gravity), all three modes of heat transfer can occur.

5.1 Conduction

When talking about thermal conduction, the key concepts of atomic and molecular activity must be invoked, as it is a transfer of energy from the more energetic to the less energetic particles of a substance due to collisions between them [56]. The equation governing conductive heat transfer is *Fourier's law*, which makes it possible to quantify the amount of energy transferred per unit time. For the one-dimensional case the equation is expressed as:

$$\dot{Q} \propto A\frac{\Delta T}{\Delta x} \tag{5.1}$$

The Eq. (5.1) does not depend on the material, so the only way to convert it to an equality is to add the chemical properties of the material, which can be summed up in a coefficient, known as the *thermal conductivity* (λ [W/mK]). Hence, evaluating the equation in the limit as $\Delta x \to 0$, it can be rewritten in differential form as follows:

$$\dot{Q} = \lambda A \frac{\Delta T}{\Delta x} \qquad \Delta x \to 0 \qquad \dot{Q} = -\lambda A \frac{dT}{dx} \qquad [\text{W}] \tag{5.2}$$

The Eq. (5.2) implies that the heat flow ($\dot{q}$, expressed in W/m^2) has a directionality (from the highest to the lowest temperature, hence the minus sign) and is always *normal* to the traversed

cross-section. For this reason, in the most general form possible, the heat flux equation can be rewritten:

$$\dot{q} = -\lambda\,\nabla T = -\lambda\left(\frac{\partial T}{\partial x}\,\hat{i} + \frac{\partial T}{\partial y}\,\hat{j} + \frac{\partial T}{\partial z}\,\hat{k}\right) = -\lambda(q_x\,\hat{i} + q_y\,\hat{j} + q_z\,\hat{k}) \tag{5.3}$$

where $T(x, y, z)$ is the scalar temperature field and $\hat{i}$, $\hat{j}$, $\hat{k}$ are unit vectors of a Cartesian reference system.

In the case of cylindrical shapes such as wheels, motor and motor housing the Eq. (5.3) becomes:

$$\dot{q} = -\lambda\,\nabla T = -\lambda\left(\frac{\partial T}{\partial r}\,\hat{i} + \frac{1}{r}\frac{\partial T}{\partial \Phi}\,\hat{j} + \frac{\partial T}{\partial z}\,\hat{k}\right) = -\lambda(q_r\,\hat{i} + q_\Phi\,\hat{j} + q_z\,\hat{k}) \tag{5.4}$$

From Figure 5.1, developing the terms in series and stopping at the first order (the others
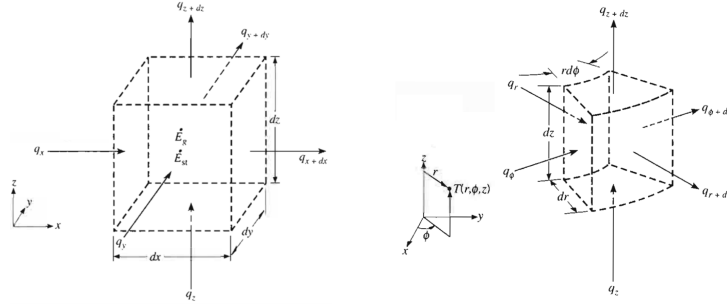
Figure 5.1: On the left: differential control volume for conduction analysis in Cartesian coordinates. On the right: differential control volume for conduction analysis in cylindrical coordinates [56].

are negligible), the general form of the *heat diffusion equations* in Cartesian (Eq. 5.5) and cylindrical (Eq. 5.6) coordinates are obtained:

$$\frac{\partial}{\partial x}\left(\lambda\frac{\partial T}{\partial x}\right) + \frac{\partial}{\partial y}\left(\lambda\frac{\partial T}{\partial y}\right) + \frac{\partial}{\partial z}\left(\lambda\frac{\partial T}{\partial z}\right) + \dot{q} = \rho c_p\frac{\partial T}{\partial t} \tag{5.5}$$

$$\frac{1}{r}\frac{\partial}{\partial r}\left(\lambda r\frac{\partial T}{\partial r}\right) + \frac{1}{r^2}\frac{\partial}{\partial \Phi}\left(\lambda\frac{\partial T}{\partial \Phi}\right) + \frac{\partial}{\partial z}\left(\lambda\frac{\partial T}{\partial z}\right) + \dot{q} = \rho c_p\frac{\partial T}{\partial t} \tag{5.6}$$

where $\dot{q}_v$ is the rate at which energy is generated per unit volume [W/m^3], while $\rho c_p \frac{\partial T}{\partial t}$ is the time rate of change of the thermal energy of the medium per unit volume, being ρ the medium density and c_p specific heat. Starting from Eq. (5.5) and Eq. (5.6), and considering the one-dimensional case, at steady state and with no internal heat generation, it is possible to determine the transmitted heat power, which in a Cartesian reference system is the Eq. (5.2[1]),

---

[1]In the one-dimensional case, at steady state and without heat generation in a Cartesian reference system $R_k = \frac{\lambda}{\Delta x}$.

while in cylindrical coordinates, in radial direction, the expression becomes:

$$\dot{Q} = \frac{\Delta T}{R_k} \qquad \text{with} \qquad R_k = \frac{1}{2 \cdot \pi \cdot L \cdot \lambda} \ln \frac{r_{ext}}{r_{int}} \qquad (5.7)$$

where R_k is the conductive thermal resistance within a cylindrical layer. The temperature distribution inside a body can not be assumed to be uniform a priori, but depends on the *Biot number*, which is the ratio of the thermal resistance by conduction R_k to the thermal resistance by convection R_c:

$$Bi = \frac{R_k}{R_c} = \frac{h\,L}{\lambda} \qquad (5.8)$$

There are 2 limiting cases:

1. $Bi \to 0$ (perfectly conductive material): in the case where $R_k \to 0$ ($R_c \gg R_k$) it is possible to assume the body is all at the same temperature, so there are no thermal gradients within it: in a thermal transient phase it would quickly rise to the same temperature

2. $Bi \to \infty$ (perfectly insulating material): in the case where $R_c \to 0$ ($R_k \gg R_c$), it is assumed that strong thermal gradients exist inside the body, resulting in a high degree of inhomogeneity within it.

Conduction through the wheels   The geometry of the rover's wheels, as well as the suspension system (*rocker-bogie*), by which it is attached to the rover's body, are complex, so assumptions are made to simplify the problem:

1. Heat flow passes through the wheels via a passage area that has as its dimensions the arc of the circumference ($r_{wh} \cdot \theta$, assuming it is completely resting on the ground) and the width of the wheel (W);

2. The wheels are assumed to be a solid cylinder;

3. All the heat flow through the wheel also passes through the suspension system (steady-state conditions), ignoring the heat dissipated by radiation and convection.

Based on the above assumptions, the model studied is the one shown in Figure 5.2. The heat flow is calculated using the following equation:

$$\dot{Q} = \frac{T_{gnd} - T_{rov}}{\sum_{i=1}^{n} R_{k_i}} \qquad (5.9)$$
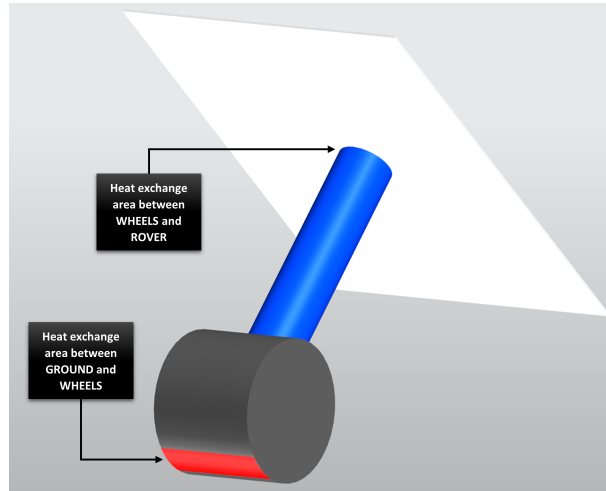
Figure 5.2: Conduction heat exchange involving the wheel-suspension system. In red is the exchange area between the ground and the wheel, considering the thermal conductivity of the *aluminium alloy 7075-T7351*; and the cross-section of the section in blue represents the exchange area between the wheel and the rover, considering the thermal conductivity of *titanium*.

where R_i indicates all the thermal conduction resistances that the heat flow must pass through. In this specific case, Eq. (5.9) becomes:

$$\dot{Q} = \frac{T_{gnd} - T_{rov}}{R_{gnd} + R_{susp}} = \frac{T_{gnd} - T_{rov}}{\frac{L_{wh}}{\lambda_{alum} \cdot A_{wh}} + \frac{L_{susp}}{\lambda_{tit} \cdot A_{susp}}} \tag{5.10}$$

with:

$L_{wh} = 2 \cdot r_{wh}$, with $r_{wh} = 0.25\,\text{m}$;

$L_{susp} = 0.39\,\text{m}$;

$\lambda_{alum} = 130\,\frac{\text{W}}{\text{m K}}$;

$\lambda_{tit} = 17\,\frac{\text{W}}{\text{m K}}$;

$A_{wh} = r_{wh}\theta \cdot W$, with $W = 0.40\,\text{m}$ and $\theta = 45°$;

$A_{susp} = \pi r_{susp}^2$, with $r_{susp} = \frac{r_{wh}}{3}$.

5.2 Convection

The convection heat transfer takes place both by bulk, or macroscopic, movement of molecules in fluids, and by diffusive[2] molecular motion [56]. When a fluid interacts with the boundary of a surface, two regions of fluid can develop: one region (*hydrodynamic boundary layer*), is generated when the fluid flows over the heated surface, producing a velocity field that varies between 0 and the velocity of the undisturbed flow (u_∞); another region (*thermal*

---

[2]Brownian motion of individual particles in the fluid.

boundary layer), is generated when the temperatures of the fluid and the surface are distinct, specifically, if the temperature of the surface (T_s) is greater than the undisturbed external one (T_∞), a convection heat transfer from the first to the second can occur (Figure 5.3). Depending
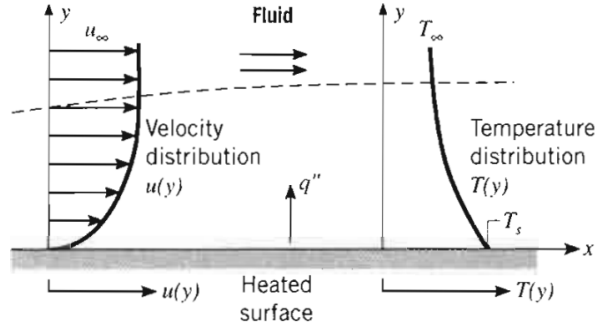
Figure 5.3: Boundary layer development in convection heat transfer [56].

on the nature of the flow, a distinction is made between *forced convection*, when the fluid is forced to flow over the surface by external devices (i.e. pump, atmospheric wind), and *natural convection*, when the movement of the fluid is caused by buoyancy forces induced by density differences related to temperature variations, by the acceleration of gravity and by the thermal expansion coefficient of the fluid. Regardless of the nature of the convection heat transfer process, the equation governing the phenomenon and defining the convective heat flow emitted by the transfer wall of area A is the *Newton's law of cooling*:

$$\dot{Q} = h \left(T_s - T_\infty \right) A \tag{5.11}$$

where h is the convective heat transfer coefficient [W/m^{2}K] (Table 5.1). The Eq. (5.11) per unit area becomes:

$$\dot{q} = \frac{T_s - T_\infty}{\frac{1}{h}} = \frac{T_s - T_\infty}{R_c} \tag{5.12}$$

5.3   Thermal radiation

Heat transfer through thermal radiation occurs through the emission of electromagnetic waves by matter that is at a non-zero temperature, so it can also propagate in a vacuum without being affected by any attenuation. Regardless of the form of matter, the emission may be attributed to changes in the electron configurations of the constituent atoms or molecules [56]. In environments with a rarefied atmosphere, typical of space applications, it becomes the most decisive heat transfer. The thermal energy emitted by a *blackbody*[3] at a certain temperature is

---

[3]The three important properties of a blackbody: it absorbs all incident radiation, regardless of wavelength and direction; for a specific temperature and wavelength, no surface can emit more energy than it; it is independent of

Table 5.1: Typical values of the convective heat transfer coefficient [56].

Process	h
Free convection	
Gases	$2 - 25$
Liquids	$50 - 1000$
Forced convection	
Gases	$25 - 250$
Liquids	$100 - 20000$
Convection with phase change	
Boiling or condensation	$2500 - 100000$

described by *Stephan-Boltzmann law* and represents the upper limit of the radiant energy flux emitted by a blackbody in all directions:

$$\dot{q}_{rad} = \sigma\, T_s^4 \tag{5.13}$$

which is the result of the integration of the *Planck distribution*[4] (Figure 5.4) with respect to
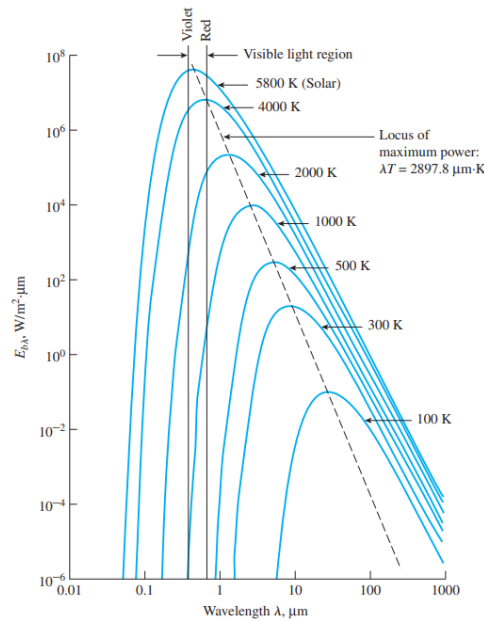
Figure 5.4: Spectral blackbody emissive power as the wavelength varies [57].

the wavelength. In Eq. (5.13) $\dot{q}_{rad}$ is measured in [W/m^2], T_s [K] is the absolute temperature of the emitting surface and $\sigma = 5.67 \cdot 10^{-8}$ [W/m^{2}K^4] is the *Stephan-Boltzmann constant*. A blackbody absorbs all the energy impinging on it without reflecting any part of it. Actually, the

direction, although the radiation is a function of wavelength and temperature [56].

[4]It is the spectral emissive power expression of a blackbody.

energy flux emitted by a real surface (*a grey body*) at the same temperature as the blackbody is lower and equal to:

$$\dot{q}_{rad} = \epsilon\, \sigma\, T_s^4 \tag{5.14}$$

where ϵ is a dimensionless number varying between 0 and 1, and represents the total emissivity of the body. Under equilibrium conditions the absorbed radiation is equal to the emitted radiation (*Kirchhoff law*), so the ϵ must be equal to the absorption factor (α) of the incident radiation, which is the fraction of radiation that is not reflected from the surface[5].

If the transfer of thermal radiation occurs between two grey surfaces that are at different tem-
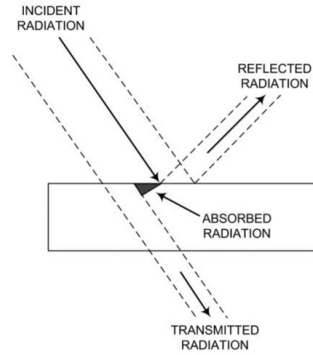
Figure 5.5: Thermal radiation interactions on a surface [57].

peratures, the analysis becomes more complicated, because part of the radiation not completely absorbed can undergo multiple reflections. While, assuming that the surfaces are blackbodies, the radiative fluxes exchanged between a surface of area A_i at temperature T_i and the other of area A_j at temperature T_j are expressed by the following relations:

$$\dot{Q}_{ij} = A_i\, F_{ij}\, \sigma\, T_i^4 \tag{5.15}$$

$$\dot{Q}_{ji} = A_j\, F_{ji}\, \sigma\, T_j^4 \tag{5.16}$$

$$\dot{Q}_i = \dot{Q}_{ji} - \dot{Q}_{ij} \tag{5.17}$$

where F_{ij} and F_{ji} are the view factors from the emitting surface to the intercepted surface and vice versa, thus Eq. (5.15) and Eq. (5.16) represent the total radiation fractions. In the case of grey surfaces (i.e. $\epsilon \neq 1$) and unit view factor, Eq. (5.17) per unit area can be rewritten as follows:

$$\dot{q}_i = \epsilon_{ij}\, \sigma\, \left(T_j^4 - T_i^4\right) \qquad \text{with} \qquad \frac{1}{\epsilon_{ij}} = \frac{1}{\epsilon_i} + \frac{1}{\epsilon_j} - 1 \tag{5.18}$$

The Eq. (5.18) shows that the lower the emissivity, the more the transmitted thermal radiation is reduced, so making surfaces reflective increases the thermal insulation. The effective emissivity between two surfaces depends strongly on the optical properties of the surface, on mutual

---

[5]The incident radiation that is reflected is equal to 1-ϵ.

reflections and on reflections through other neighbouring surfaces, but in the simple case of two parallel surfaces, separated by a small distance from their surfaces, the ϵ_{ij} of Eq. (5.18) is used.

5.4 Mars thermal environment

Once the rover reaches Mars, it is essential to comply the thermal operation requirements of the different subsystems. The subsystem that must be safeguarded is the electrical energy storage subsystem (the batteries), which is indispensable for carrying out all the rover's activities, so its permissible flight temperatures vary between -20–$30\,°C$, while for the electronics the permissible range is wider, allowing temperature excursions from -40–$50\,°C$ (Table 5.2). Knowing the Martian environment makes it possible to correctly size the Heat Rejection System, since in the case of high thermal loads it is essential to use a mechanically pumped loops to control the temperature of the rover (system used for the curiosity rover). Thus, the main sources of environmental heating are: direct solar radiation; solar radiation reflected from the planet (albedo radiation); thermal energy radiated from the planet (planetary radiation). The rover is in thermal equilibrium when the sum of the radiant energy received from the above heating sources, together with any internal thermal dissipation, is equal to the energy radiated into Martian environment. This equilibrium determines the physical temperature of the rover.

Table 5.2: Allowable Flight Temperature Limit on Mars surface.

Allowable Flight Temperature Limit [°C] (RAMP interfaces)	
Avionics	$-40/50$
Instruments	$-40/50$
Battery	$-20/30$
SDST/Electralite	$-35/50$
SSPA	$-35/55$

5.4.1 Solar radiation

The fundamental aspects of solar radiation of interest are: the spectral distribution, which can be considered constant throughout the solar system; the intensity of the radiation, which is not constant and varies with wavelength, approximating a black body at 5777 K (Figure 1.4); and the degree of collimation. Most of the solar energy (99%) is between $150\,\text{nm}$ and $10\,\mu\text{m}$ wavelength, with a maximum near $450\,\text{nm}$ (yellow part of the visible spectrum). The solar intensity depends on the distance, d, from the Sun and can be calculated from the following relationship:

$$I_s = \frac{P}{4\pi\,d^2} \tag{5.19}$$

where P is the total power emitted by the Sun, 3.856×10^{26} W [11]. Mars is at an average distance from the sun of 2.2794×10^{11} m (1.524 AU), so the Eq. (5.19) gives an average solar radiation intensity of about $590.59 \, \text{W/m}^2$. The thermal power of solar radiation absorbed by a flat surface of area A is calculated using the following expression:

$$\dot{Q}_{sun} = \alpha I_s A_{solar} F_{s/r} \tag{5.20}$$

where α is the *absorptivity*, since the rover is not a blackbody, but absorbs only a fraction of the incident energy; and $F_{s/r}$ is the *view factor* between the solar flux and rover's planar surface, which varies over time and according to latitude, unlike the other variables that are fixed once the rover's geometry and material is selected.

5.4.2   Albedo

The albedo is the fraction of solar radiation that is reflected from the surface or atmosphere of a planet and its value depends on the local properties of the surface and atmosphere. It is one of the factors that determine planetary surface temperature. For Mars, it varies from a maximum of 0.4 in dust-covered surface regions to a minimum of 0.15 in regions with volcanic rock basalt on the surface. However, the average value that can be used for thermal design purpose is 0.29 [58]. Thermal flux due to albedo (b) of solar radiation is:

$$\dot{Q}_{albedo} = b \, \alpha I_s A_{albedo} F_{s/r} \tag{5.21}$$

5.4.3   Planetary radiation

As already mentioned in Section 5.3 all bodies with a temperature above absolute zero emit thermal radiation, so since the planets in the solar system all have a temperature other than $0 \, \text{K}$, they radiate heat. Because of its relatively low temperature, Mars radiates all its heat at infrared wavelengths (for this reason, the radiation is often referred to as thermal radiation). In addition, Martian atmosphere has an important transparent window at around 14–$16 \, \mu\text{m}$. Some of the radiation is reflected, partly absorbed and then re-emitted as IR radiation or blackbody radiation. For most practical purposes, the ideal temperature at which Mars radiates precisely all the energy it receives from the sun is assumed to be:

$$T_{eff} = \sqrt[4]{\frac{P \, (1 - b)}{16\pi\sigma \, d^2}} \tag{5.22}$$

Substituting all the values, the T_{eff} of the planet Mars is about $207.3\,\mathrm{K}$. Thanks to Wien's displacement law, which is a direct consequence of Planck's law[6], it is possible to calculate the wavelength peak ($\lambda_{peak} = q/T_{eff}$, with $q \approx 2898\,\mathrm{\mu m\,K}$, Wien's displacement constant) which is equal to $13.8\,\mathrm{\mu m}$. The heat exchange between two radiating surfaces is represented

$$\dot{Q}_{IR} = J_p\, A_{planetary} \tag{5.23}$$

where J_p[7] is equal to $70.7281\,\mathrm{W/m^2}$ in the worst-case *hot conditions*, while J_p[8] is equal to $16.8812\,\mathrm{W/m^2}$ in the worst-case *cold conditions*. The same result is approximated by the expression $J_p = \epsilon_{pl}\, \sigma\, T_{eff}^4$, assuming an emissivity of the planet Mars of 0.71.

---

[6]Planck's law describes the spectral brightness of blackbody radiation as a function of wavelength at any given temperature.

[7]This value is taken from MCD_v5.3 with climatology maximum solar scenario, at the Curiosity landing site (latitude: $-4.6°$ N; longitude: $137.4°$ E), $Ls = 225°$, and at an altitude of $0.0\,\mathrm{m}$ above the Martian surface - $15.0\,\mathrm{h}$ (local time) [59].

[8]This value is taken from MCD_v5.3 with climatology minimum solar scenario, at the Curiosity landing site (latitude: $-4.6°$ N; longitude: $137.4°$ E), $Ls = 105°$, and at an altitude of $0.0\,\mathrm{m}$ above the Martian surface - $7.0\,\mathrm{h}$ (local time) [59].

6. Thermal Control System

In any space mission, keeping the temperature of the subsystems within the allowed limits is a difficult challenge. Parts exposed to the Sun need to be cooled because temperatures rise extremely high, while parts not directly exposed to the Sun need to be heated, because temperatures can drop dramatically. The vacuum does not conduct heat, so the only way to transfer energy is through *electromagnetic radiation*, generated by the thermal motion of particles in matter. Mars' thin atmosphere mitigates the strong temperature gradients that would occur in a vacuum, nevertheless the external parts of the rover are exposed to temperature range between -123–$40\,^{\circ}\mathrm{C}$, so it was designed to handle more extreme temperature changes between -128–$50\,^{\circ}\mathrm{C}$, regardless of the landing site. Each rover instrument has different thermal requirements: the on-board avionics are kept between -40–$50\,^{\circ}\mathrm{C}$, although they can actually tolerate temperatures between -55–$70\,^{\circ}\mathrm{C}$; other instruments, in particular the ChemCam body, can not stand heat, so they have a TEC that is used for conducting waste heat to the rover's *Heat Rejection System* (HRS); SAM, too, has components that generate a lot of heat, so it needs built-in coolers to keep its electronics at safe temperatures. Furthermore, as a result of using the MMRTG, an advanced thermal control system is required that is able to recover and reject waste heat in order to keep the on-board electronics within the operating temperature range.

6.1 Rover Avionics Mounting Panel, sensor and heaters

The *Rover Avionics Mounting Panel* (RAMP) is a nearly rectangular box used as the main compartment for all electronics and temperature-sensitive parts. The panel is attached to the rover's upper deck with *titanium structures* designed not to conduct heat from inside to outside the rover. The volume is larger than that of *Spirit and Opportunity* rovers, so the MSL requires more heat to keep the temperature within allowable limits at night. The Martian atmosphere that occupies the remaining internal space of the rover consists mainly of CO_2 (95%), which inhibits heat transfer between the internal hardware and the underlying panel and the two side panels. In order to check that each individual instrument is operating correctly in the temperature range for which it was designed, the rover has been equipped with 221 temperature sensors, although only half are in use at any one time; the others, however, have been installed for redundancy due to the fail-safe principle. The battery, being a critical component, has dedicated survival and warm-up heaters controlled by 8 mechanical thermostats to keep the temperature around the desired set-point. The 17 cameras (MAHLI, MARDI, Navcams, Hazcams, Mastcams, ChemCam) and other equipment (e.g. motors) withstand all expected temperature changes between day and night outside the rover body, but need to operate at minimum temperatures between $-55\,^{\circ}\mathrm{C}$ and

$-40\,°C$: in fact, they often need to be heated (by means of *RCEs*, which manage the switching on and off of these warm-up heaters) when temperatures are too low (i.e. during the night, and depending on the season also during the day).

6.2 Heat Rejection System

The rover's heat rejection system (RHRS) must be able to dissipate the large amount of heat produced by the MMRTG that is not converted into electrical energy that can be used to power the various subsystems. Basically, a *Mechanically Pumped single-phase Fluid Loop* (MPFL) is used for different reasons:

- Scalability in heat rejection;

- Ability to absorb and supply heat at different points in the rover;

- Flexibility in positioning all the equipment needed to dissipate heat;

- Adaptability to last minute changes in design.

The system uses approximately $60.96\,\text{m}$ of tubing ($45.41\,\text{m}$ of aluminium tubing, used in heat transfer areas; $8.53\,\text{m}$ of High-Purity Stainless Steel Tubing; only to transport the working fluid and $3.35\,\text{m}$ of flex lines) to pump fluid through the tubes that pass close to the MMRTG to pick up waste heat to warm the electronics (Figure 6.1). The working fluid is *CFC-11*, *Galden H-*
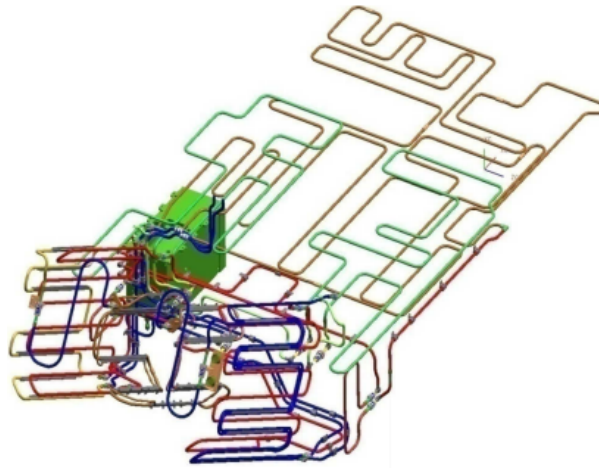
Figure 6.1: Rover heat rejection system (tubing and RIPA): brown lines, RAMP; green lines, top deck; blue lines, cold plates $(-Y)$ away from the pump; yellow lines, cold plates $(+Y)$ close to the pump; red lines, hot plates [19].

170 (trichlorofluoromethane), an artificial type of fluid, typically called Freon, which has: high density, both in the aeriform and liquid phases; high enthalpy of vaporisation; high thermal capacity; and high stability under operating conditions. The Rover Integrated Pump Assembly

(RIPA) is the heart of the rover, as it pumps fluid to all parts of the rover that need to be warmed and cooled. It also contains a large reservoir, which allows the Freon to expand as it heats up. The system consists of two honeycomb sandwich panel Heat Exchangers (HXs) at the back of the rover on either side of the MMRTG, which have a coil of tubes attached on both sides. On the inward-facing side of each HX is the hot plate, through which the fluid picks up waste heat from the MMRTG and returns to the pump. While, on the outward-facing side is the cold plate, where the fluid dissipates excess heat. A layer of Aerogel[1] is placed between the two plates (Figure 6.2), thermally separating the hot inner face from the cold outer face. The working fluid system can handle temperatures between $-97\,°C$ and $170\,°C$ (the developed hardware survives at temperatures between $-111\,°C$ and $90\,°C$) [60], , with a system pressure of about $1.36\,MPa$ to prevent boiling, and operates correctly if the diurnal fluctuation of the plate temperature is less than $60\,°C$ (Figure 6.2). So, when the internal temperature is outside the allowable limits, the
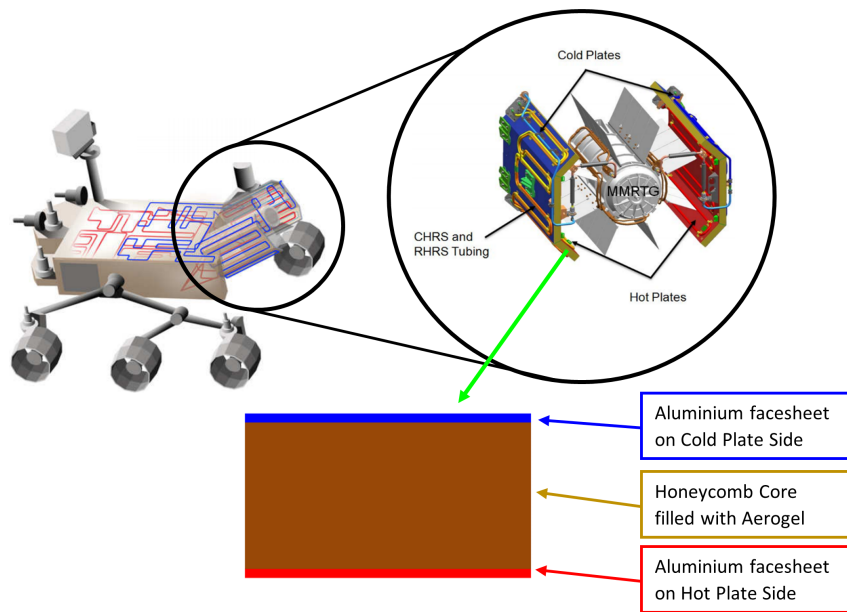
Figure 6.2: Top: the inward and outward facing side of the heat exchangers [61]. Bottom: a model of the heat exchanger honeycomb sandwich panel [19].

pump transfers the heated fluid from the MMRTG through the tubing connected to the RAMP, vice versa if the temperature is high, the pump sends the fluid from the RAMP to the cold plates on the outside of the HXs. The two side heat exchangers, the body and a windbreaker on the back protect the MMRTG from the Martian wind (especially during the colder winter months) and other external factors that could affect its proper functioning and deprive it of the heat it needs to survive. Also due to the fail-safe principle, it is extremely vital to safeguard the health of the rover and thus it is essential to redundant the pump (only one is powered at any time) and the two mixing and splitter valves. The mixer and splitter valves operate passively and work

---

[1]The Aerogel is a lightweight porous synthetic material, a rigid foam derived from a gel, in which the liquid component is replaced by a gas without causing the gel structure to collapse.
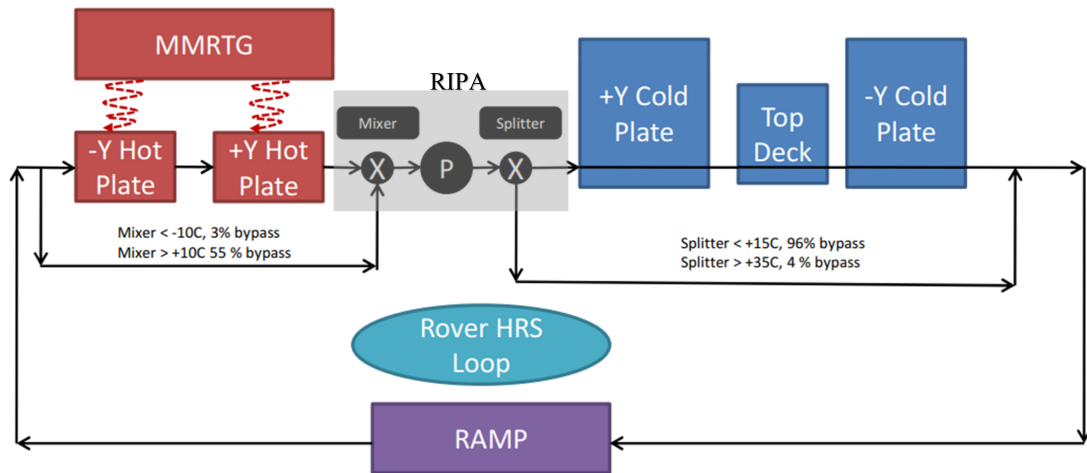
Figure 6.3: Rover HRS Loops. The circuit remains the same even during cruise with the rover inside the Cruise Stage, except that the fluid also passes through the CHRS radiator to perform the CHRS loop, which is not taken into account in the following analysis [62].

independently of any onboard computers, controlling the flow of fluid to the hot and cold plates, allowing the system, respectively, to heat or cool as needed. The mixer and splitter valves allow the heat rejection system to selectively heat or cool the Freon as needed. For rover safety, they work independently of any computer, operating passively in response to the temperature of the fluid flowing through them. The mixer valve controls the amount of flow across the rover's hot plates. If the mixer valve falls below a temperature of –10°C, it opens all the way, sending 97% of the fluid through the hot plates. If the mixer valve measures a temperature of 10°C, it closes to its minimum setting of 55%, which runs just enough fluid in the hot plates to keep the fluid temperatures below 90°C (Figure 6.3). The splitter valve controls the flow to the cold plates and top deck. When its temperature rises above 35°C, it opens all the way to 96%; it closes to its minimum setting of 4% at 15°C. If the mixing valve measures a temperature below $-10\,°\text{C}$, it opens fully, transferring 97% of the working fluid through the hot plates, while if the temperature exceeds $10\,°\text{C}$, it closes at its minimum setting of 55%, flowing only 45% of the fluid, just to keep fluid temperatures below $90\,°\text{C}$. Whereas, when the splitter valve measures a temperature above $35\,°\text{C}$, it opens fully at 96%; it closes at its minimum setting of 4% below $15\,°\text{C}$.

6.3 Thermal Balance

Spacecraft and, more specifically, rovers are generally very complex structures within which temperatures vary continuously as a function of position and time, and their detailed calculation is very complex. The approximate solution presented in this section allows the orders of magnitude involved to be understood and a preliminary analysis to be carried out. An equilibrium between thermal powers is carried out: the input power is subtracted from the out-

put power and the balance temperature of the system is calculated under steady state conditions. This preliminary analysis allows the internal temperature to be known without the use of active heat rejection. Thus, a positive net heat flux result indicates a radiation heat gain from the rover surface that must be dissipated to maintain the optimum temperature inside, helping the battery and on-board avionics to function properly. The temperature of the rover in the worst case hot and cold provides an insight into whether or not active temperature control is required, and if the first case is necessary then the heat exchanger is sized and the flow rate of working fluid required to maintain that internal temperature is calculated. The net heat absorbed per unit time is given by the following equation:

$$\dot{Q}_{in}^{ext} + \dot{Q}_{in}^{int} - \dot{Q}_{conv} = \dot{Q}_{out} \tag{6.1}$$

Assumptions   The assumptions made in the calculations are:

1. Biot number tending to 0 (perfectly conductive material), so it is assumed that the temperature of the walls of the rover body is uniform, excluding the formation of any thermal gradients;

2. A unitary view factor is considered (conservative choice);

3. Internal heat convection within the rover is neglected;

4. Only natural convection is considered, so the wind speed is assumed to be zero;

5. The rover body is considered to be an isothermal sphere with the diameter equal to the total outer surface of the rover in order to obtain first-order estimates of thermal performance, so the rover is considered to be at the same equilibrium temperature T_{rov}, which means that the rover surfaces are not independent and isolated from each other.

6.3.1 External heat input

The first term of Eq. (6.1) is actually the sum of four thermal powers, which can be determined from the following equations:

$$\dot{Q}_{in}^{ext} = \dot{Q}_{sun} + \dot{Q}_{albedo} + \dot{Q}_{IR} + \dot{Q}_{cond} \tag{6.2}$$

in which:

$$\dot{Q}_{sun} = \alpha I_s A_{\perp} F_{s/r}$$

$$\dot{Q}_{albedo} = b\,\alpha I_s A_{\perp} F_{s/r}$$

$$\dot{Q}_{IR} = J_p\, A_{\perp} \tag{6.3}$$

$$\dot{Q}_{cond} = 6 \cdot \frac{T_{gnd} - T_{rov}}{R_{gnd} + R_{susp}}$$

where A_{solar}, A_{albedo} and $A_{planetary}$ of the Eqs. (5.20) (5.21) and (5.23) are equal to $A_{\perp}$, which is the surface perpendicular to the direction of radiation. In addition, the heat exchanged by conduction is calculated taking into account what is defined in Section 5.1 and multiplied it by the number of wheels the rover is made of (six in this case).

6.3.2   Internal heat input

The second term of Eq. (6.1), in turn, is the sum of two thermal powers, which can be determined as:

$$\dot{Q}_{in}^{int} = \dot{Q}_e + \dot{Q}_{MMRTG} \tag{6.4}$$

in which:

$$\dot{Q}_e = 301.9884\,\text{W}$$

$$\dot{Q}_{MMRTG} = 2000\,\text{W} \tag{6.5}$$

where that values written above are taken from Table 4.3 (considering it as thermal power produced) and Section 2.2 respectively.

6.3.3   Heat output

The heat flow rates mentioned above must be equal to the heat flow rate disposed of by the rover through the heat rejection system, under steady-state conditions. By writing the equation for the second member term of Eq. (6.1) with A being as before the area of the isothermal sphere

$$\dot{Q}_{out} = \sigma \epsilon_{rov} \left(T_{rov}^4 - T_{amb}^4 \right) A_{sph} \tag{6.6}$$

where A_{sph} is the external surface of the isothermal sphere. Substituting Eq. (6.6) together with (6.3) and (6.5) into (6.1), the only unknown variable is exactly the temperature of the rover (T_{rov}) under thermal equilibrium conditions.

Convection term   The third term in Eq. (6.1) concerns the heat dissipated by the rover due to *natural convection*, so any movement of the fluid is caused by natural means such as the *buoyancy effect*, the hot flow goes up and the cold flow goes down, due to gravity and different

densities. The calculation of the natural convection coefficient is complex and requires the intervention of several variables. Its value can be calculated as follows:

1. Input variables depending on fluid and boundary conditions (Table 6.1):

   Table 6.1: Fluid characteristics and boundary conditions.

Fluid variables	SI units
Density (ρ)	$\mathrm{kg/m^3}$
Dynamic viscosity (μ)	$\mathrm{Ns/m^2}$
Specific heat (c_p)	$\mathrm{J/kgK}$
Thermal conductivity (λ)	$\mathrm{W/mK}$
Thermal expansion coefficient (β)	$\mathrm{1/K}$
Boundary conditions	
Rover temperature (T_{rov})	K
Ambient temperature (T_{amb})	K
Characteristic length (L)	m
Gravitational acceleration (g)	$\mathrm{m/s^2}$

2. This is followed by the calculation of *Pradtl's number*, which expresses the comparison between the kinematic and thermal boundary layer formed near the wall as a result of the simultaneous presence of a kinematic and thermal field; *Grasohf's number*, which expresses the relationship between the buoyancy forces and the viscous forces of a fluid; *Raylaigh's number*, which characterises the regime of motion of the fluid in natural convection:

$$Pr = \frac{\mu c_p}{\lambda}$$
$$Gr = \frac{g\beta(T_{rov} - T_{amb})\,L^3}{\left(\frac{\mu}{\rho}\right)^2} \qquad (6.7)$$
$$Ra = Gr \cdot Pr$$

   The second equation is only valid for $0.002 < Pr < 8 \cdot 10^3$ and $10^{-4} < Ra < 10^9$ representing laminar flow. The characteristic length (L) is defined as the sphere diameter (D_{sph}).

3. and finally *Nusselt's number*, which expresses the relationship between the heat flow exchanged by convection and the heat flow exchanged by conduction. In the case of natural convection heat transfer from a *isothermal sphere*, the Nusselt's number is:

$$Nu = 2 + \frac{0.589 Ra^{1/4}}{[1 + (0.469/Pr)^{9/16}]^{4/9}} \qquad (6.8)$$

valid for $Ra \leq 10^{11}$ and $Pr \geq 0.7$.

4. Finally, knowing that Nu is equal to:

$$Nu = \frac{h\,D_{sph}}{\lambda} \tag{6.9}$$

it is easy to calculate h. Thus, the convection transfer coefficient decreases with decreasing density (i.e. pressure). In addition, its value for a gas at a pressure of $0.6\,\text{kPa}$ is 7.75% of the convection coefficient of a gas at $100\,\text{kPa}$, so in the calculations, taking into account the Martian atmosphere, a value of $1\,\text{W}/(\text{m}^2\text{K})$ is taken as a good approximation [63].

Thus, the heat flux exchanged by convention, which is part of the thermal equilibrium, is *Newton's law of cooling*, Eq. (5.11), where the temperatures are that of the rover and the environment:

$$\dot{Q}_{conv} = h\,(T_{rov} - T_{amb})\,A_{sph} \tag{6.10}$$

where A_{sph} [m^2] is the surface area of the sphere.

6.3.4 Worst case hot temperature

In the worst case hot temperature all the contributions of Eq. (6.1) are considered, the heat balance can be seen in Figure 6.4. The temperature that solves the equation is the *equilibrium temperature* (T_{rov}), to which the rover is brought, in the absence of an active heat rejection system, so this thermal control method relies only on the passive connection between the innards of the rover and the surrounding environment. The ground and ambient temperature are strongly dependent on the time of year, the time of day and the latitude and longitude of the location of the body under study. Thus, the ground temperature (T_{gnd}) is equal to $292.79\,\text{K}$, while for the ambient temperature (T_{amb}), the arithmetic mean between the temperature at ground level and the temperature at $58.82\,\text{m}$ height is assumed. Figure E.1 shows that T_{amb} is equal to $270.73\,\text{K}$. Rewriting Eq. (6.1) by substituting all the terms gives the equation:

$$
\begin{aligned}
\alpha I_s F_{s/r} A_\perp &+ b\,\alpha I_s A F_{s/r} A_\perp + J_p A_\perp + \\
&+ 6 \cdot \frac{T_{gnd} - T_{rov}}{R_{gnd} + R_{susp}} + \dot{Q}_e + \dot{Q}_{MMRTG} + \\
-h\,(T_{rov} &- T_{amb})A_{sph} = \sigma\epsilon_{rov}(T_{rov}^4 - T_{amb}^4)A_{sph}
\end{aligned} \tag{6.11}
$$

where the only unknown variable is exactly the balance temperature of the rover (T_{rov}).

Figure 6.4: Thermal bus architecture in worst case *hot conditions*: red shows the thermal power input to the rover and blue the output.

Isothermal sphere   As mentioned before, the rover is assumed to be an isothermal sphere at temperature T_{rov} with area A equal to the area of the outer surface of the rover. The diameter of the sphere is calculated as follows:

$$
\begin{aligned}
A_{sph} &= 4 \cdot \pi \left(\frac{D_{sph}}{2} \right)^2 = \pi \, D_{sph}^2 \longrightarrow D_{sph} = \sqrt{\frac{A_{total}}{\pi}} \\
A_{\perp} &= \pi \, \frac{D_{sph}^2}{4}
\end{aligned}
\tag{6.12}
$$

Results   The thermal equilibrium results for worst-case hot conditions are shown in Table 6.2.

Table 6.2: Balance temperature under worst-case hot conditions with passive thermal control. The table shows the results for a *white paint* (low α/ϵ) [58]. Paints generally consist of a binder (transparent in visible light), opaque in the infrared which results in high ϵ-values and a filler material which gives its colour. Under the influence of ultraviolet radiation, many binders degrade and become less transparent, which is why the white paint on the outside of the rover will increase its α/ϵ value over time, which is to be avoided [11].

Worst case HOT condition

Boundary conditions	
T_{gnd} [K]	292.790
T_{amb} [K]	270.730
D_{sph} [m]	1.426

EXTERNAL HEAT INPUT	
Direct Solar Radiation	
I_s [W/m^2]	587.424
α [$-$]	0.2
$F_{s/r}$ [$-$]	1
$A_\perp$ [m^2]	1.598
$\dot{Q}_{sun}$ [W]	187.688
Indirect Solar Radiation	
b [$-$]	0.4
$F_{s/r}$ [$-$]	1
$A_\perp$ [m^2]	1.598
$\dot{Q}_{albedo}$ [W]	75.075
Planetary Radiation	
J_p [W/m^2]	70.72
$A_\perp$ [m^2]	1.598
$\dot{Q}_{IR}$ [W]	112.979
Conduction Radiation	
λ_{alum} [W/mK]	130
λ_{tit} [W/mK]	17
θ [rad]	0.785
r_{wh} [m]	0.250
r_{susp} [m]	0.083
L_{wh} [m]	0.500
L_{susp} [m]	0.390
A_{wh} [m^2]	0.079
A_{susp} [m^2]	0.022

R_{gnd} [K/W]	0.049
R_{susp} [K/W]	1.052
$\dot{Q}_{cond}$ [W]	-212.342

INTERNAL HEAT INPUT

$\dot{Q}_e$ [W]	301.988
$\dot{Q}_{MMRTG}$ [W]	2000

HEAT OUTPUT

Convection Radiation

h [W/m^{2}K]	1
A_{sph} [m^2]	6.390
$\dot{Q}_{conv}$ [W]	389.851

Thermal Radiation

$F_{r/e}$ [$-$]	1
ϵ_{rov} [$-$]	0.85
A_{sph} [m^2]	6.390
$\dot{Q}_{rad}$ [W]	2075.540

Balance temperature

T_{rov} [K]	$331.738\,(58.588\,°\mathrm{C})$

From the result of the thermal balance, the high temperature would lead to the collapse of the on-board avionics and batteries, whose optimum operating temperature is around $20\,°\mathrm{C}$. For this reason, the rover can not be controlled using body-mounted radiators, but an active heat rejection system based on the one mentioned in Section 6.2 is required. All calculations are performed using *Wolfram Mathematica*® software.

6.3.5   Worst case cold temperature

In the cold worst case temperature not all contributions of the Eq. (6.1) are considered, in fact the contribution of solar radiation ($\dot{Q}_{sun}$) and consequently the albedo ($\dot{Q}_{albedo}$) have to be excluded from the heat balance, which can be seen in Figure 6.5. Therefore Eq. (6.11) can be rewritten as follows:

$$J_p A_\perp + 6 \cdot \frac{T_{gnd} - T_{rov}}{R_{gnd} + R_{susp}} + \dot{Q}_e + \dot{Q}_{MMRTG} +$$
$$-h\,(T_{rov} - T_{amb})A_{sph} = \sigma \epsilon_{rov}(T_{rov}^4 - T_{amb}^4)A_{sph} \tag{6.13}$$

In this case, the ground temperature (T_{gnd}) is equal to 178.868 K, while the ambient temperature

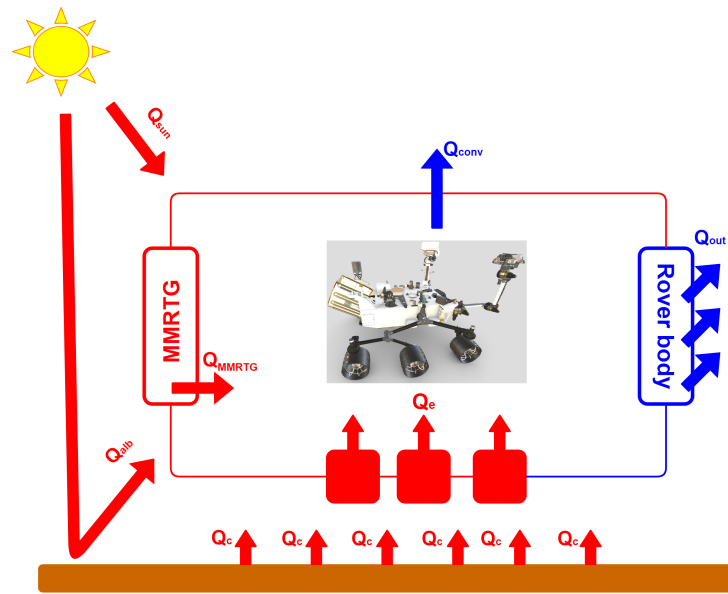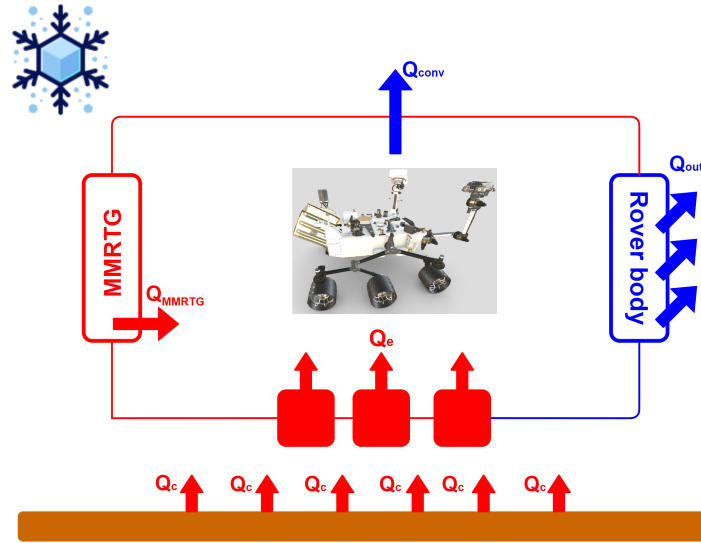
Figure 6.5: Thermal bus architecture in worst case *cold conditions*: red shows the thermal power input to the rover and blue the output.

(T_{amb}) is equal to 183.23 K, also in this case the arithmetic mean between the temperature at ground level and the temperature at 58.82 m height is assumed (Figure E.2).

Results   The thermal equilibrium results for worst-case cold conditions are shown in Table 6.3.

Table 6.3: Evaluation of balance temperature under worst-case cold conditions with passive thermal control. The power dissipated by the electronics, $\dot{Q}_e$ (Table 4.1), is considered to be the minimum power required by the subsystems in their minimum operating condition.

Worst case COLD condition

Boundary conditions	
T_{gnd} [K]	178.868
T_{amb} [K]	183.2305
D_{sph} [m]	1.426
EXTERNAL HEAT INPUT	
Planetary Radiation	
J_p [W/m^2]	16.881
$A_\perp$ [m^2]	1.598
$\dot{Q}_{IR}$ [W]	26.9686
Conduction Radiation	

λ_{alum} [W/mK]	130
λ_{tit} [W/mK]	17
θ [rad]	0.785
r_{wh} [m]	0.250
r_{susp} [m]	0.083
L_{wh} [m]	0.500
L_{susp} [m]	0.390
A_{wh} [m^2]	0.079
A_{susp} [m^2]	0.022
R_{gnd} [K/W]	0.049
R_{susp} [K/W]	1.052
$\dot{Q}_{cond}$ [W]	-455.039

INTERNAL HEAT INPUT

$\dot{Q}_e$ [W]	45
$\dot{Q}_{MMRTG}$ [W]	2000

HEAT OUTPUT

Convection Radiation

h [W/m^{2}K]	1
A_{sph} [m^2]	6.390
$\dot{Q}_{conv}$ [W]	505.468

Thermal Radiation

$F_{r/e}$ [$-$]	1
ϵ_{rov} [$-$]	0.85
A_{sph} [m^2]	6.390
$\dot{Q}_{rad}$ [W]	1111.460

Balance temperature

T_{rov} [K]	$262.331\,(-10.819\,°\text{C})$

In this case, it is not necessary to adopt an active system to control the temperature, but the use of only body-mounted radiators would be sufficient to manage the internal temperature. In Table 6.3, observing the values reported, it can be seen that thanks to the presence of the approximately constant thermal power of the MMRTG, temperatures do not fall too far below $0\,°\text{C}$.

6.4 MPFL active control system

As seen from the calculations above, an active control system is needed to monitor the temperature inside the rover. Referring to the real system implemented on curiosity it is assumed that in the worst hot case the fluid does not flow in the hot plates near the MMRTG, but they are bypassed, while in the worst cold case the cold plates are, also, bypassed, allowing the rover to warm up to the optimal temperature. The loop considered in the following calculations for the hot case and cold case is shown in Figure 6.6.

Assumption   In order to make a preliminary analysis, it is advisable to make some assumptions that will simplify the calculations without losing either the physics of the problem or the order of magnitude of the variables:

1. Hot and cold plates are completely bypassed, respectively in the worst hot and cold conditions;

2. The difference in fluid temperature between the inlet and outlet of the plate is equal to that between the inlet and outlet of the rover;

3. A fully developed laminar flow ($\mathbb{Re} < 2300$) is considered in order to have a relation between the flow rate, the cross-sectional diameter of the tube and the pressure drop via the Hagen-Poiseuille's law[2];

4. The total pressure drop is assumed to be approximately $25\,\mathrm{kPa}$;

5. Radiator area must be less than $2.3\,\mathrm{m}^2$ for design reasons;

6. The outer diameter (D) of the cross-section of the tubes must not exceed $9.0\,\mathrm{mm}$.

6.4.1 Preliminary design process

After defining the allowable temperature limits of the rover equipment (Table 5.2), it is assumed that the temperature of the rover (T_{rov}), referring to the most restrictive battery limits, is $25\,^{\circ}\mathrm{C}$ ($30\,^{\circ}\mathrm{C}$ upper equipment limit minus $5\,^{\circ}\mathrm{C}$ thermal margin) in the worst warm case and $-15\,^{\circ}\mathrm{C}$ in the worst cold case ($-20\,^{\circ}\mathrm{C}$ upper equipment limit plus $5\,^{\circ}\mathrm{C}$ thermal margin). Taking into account Figure 6.6 and the assumptions made, the equations that allow the flow to be resolved

---

[2]The Hagen-Poiseuille's law is only valid for laminar and stationary flow of a homogeneous liquid in a rigid tube. As a first approximation, even when the flow is in a turbulent regime, it is possible to use this law to get a reasonably accurate idea of how the flow rate changes with the diameter of the tube. For Reynolds numbers above the critical value, the steady-state flow and velocity field become more complex.
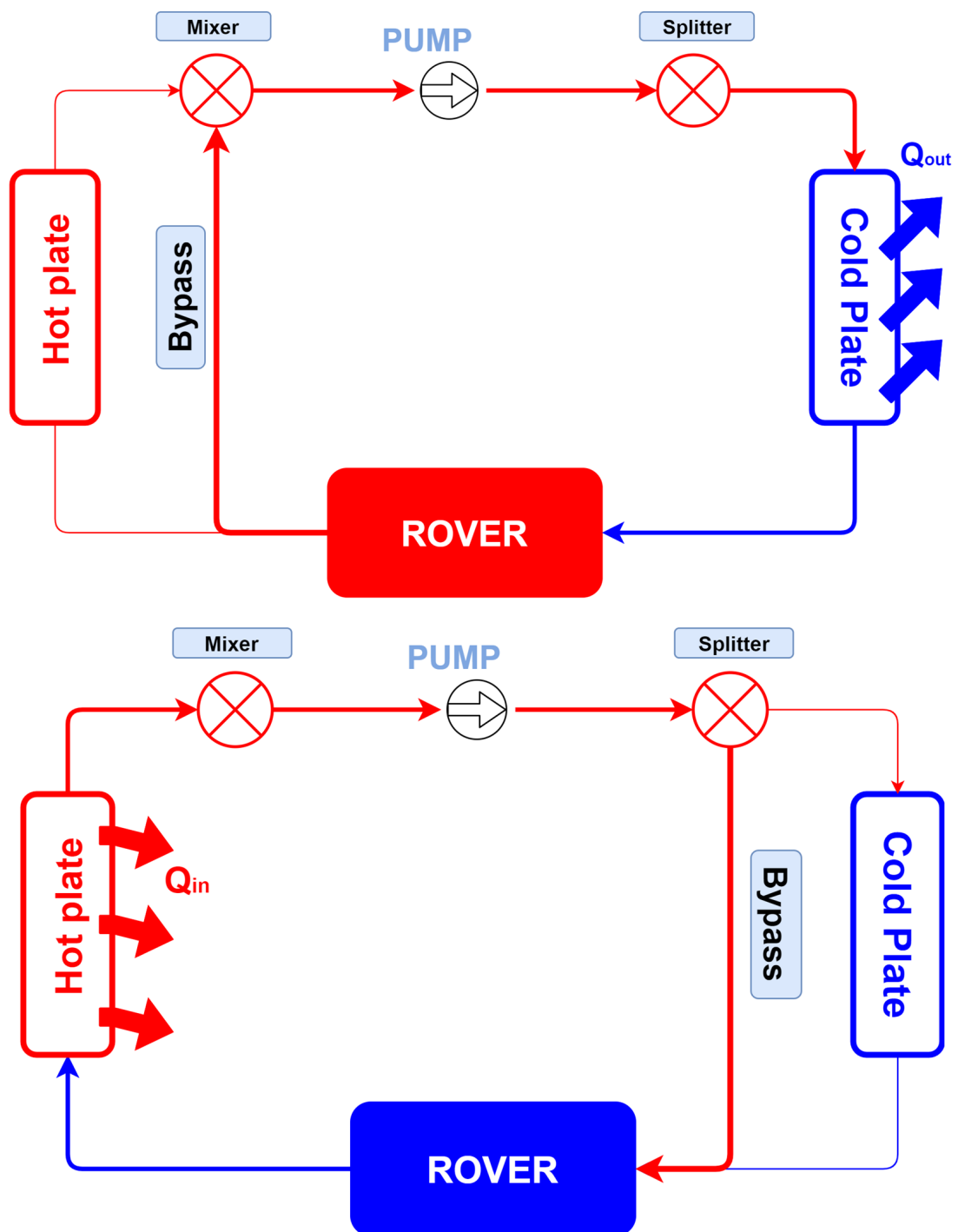
Figure 6.6: Loop pattern for sizing the active thermal control system in the worst hot (above) and cold (below) conditions.

are as follows:

$$\sigma\epsilon_{rov}\left[(T_s^c)^4 - T_{amb}^4\right]A_{out} = \dot{m}\,c_p\,(T_{in} - T_{out})$$

$$\frac{m_{rov}\,c_{rov}\,(T_{rov} - T_{des})}{\tau} = \dot{m}\,c_p\,(T_{in} - T_{out})$$

(6.14)

where T_{amb} depends on the condition analysed, m_{rov} and c_{rov} are respectively the mass and the specific heat of the rover, τ is the time in which the rover disposes of the thermal load and reaches the optimum operating temperature (T_{des}), which in the case of the batteries is $20\,°\text{C}$. Not knowing the value of some variables, a *MATLAB®* script was implemented in order to define the temperature variation of the fluid entering and leaving the plates and the time required for the rover to reach the desired temperature, as the flow rate varies, knowing only that the area of the cold plates must be smaller than defined in the assumptions.

Results worst-case hot conditions Using the variables defined in Table 6.4 and the assumptions made in the previous section, the diagrams in Figure 6.7 are derived. Remember that the

Table 6.4: Input data in the worst-case hot conditions.

Input data	
Radiative properties	
σ [W/m^{2}K]	$5.670373 \cdot 10^{-8}$
Emissivity (ϵ_{rov})	0.85
Fluid parameters	
Density (ρ) [kg/m^3]	1770
Dynamic viscosity (μ) [Pa s]	0.0032
Kinematic viscosity (ν) [m^2/s]	$1.8 \cdot 10^{-6}$
Specific heat (c_p) [J/kgK]	962.964
Rover parameters	
Specific heat (c_{rov}) [J/kgK]	870
Rover mass (m_{rov}) [kg]	899
Rover temperature (T_{rov}) [K]	298.15
Desire temperature (T_{des}) [K]	293.15
Cold plate temperature (T_s^c) [K]	323.15
Boundary conditions	
Ambient temperature (T_{amb}) [K]	270.730
Loop parameters	
Tube length (L) [m]	60.96
Pressure drop (ΔP) [Pa]	$25 \cdot 10^3$
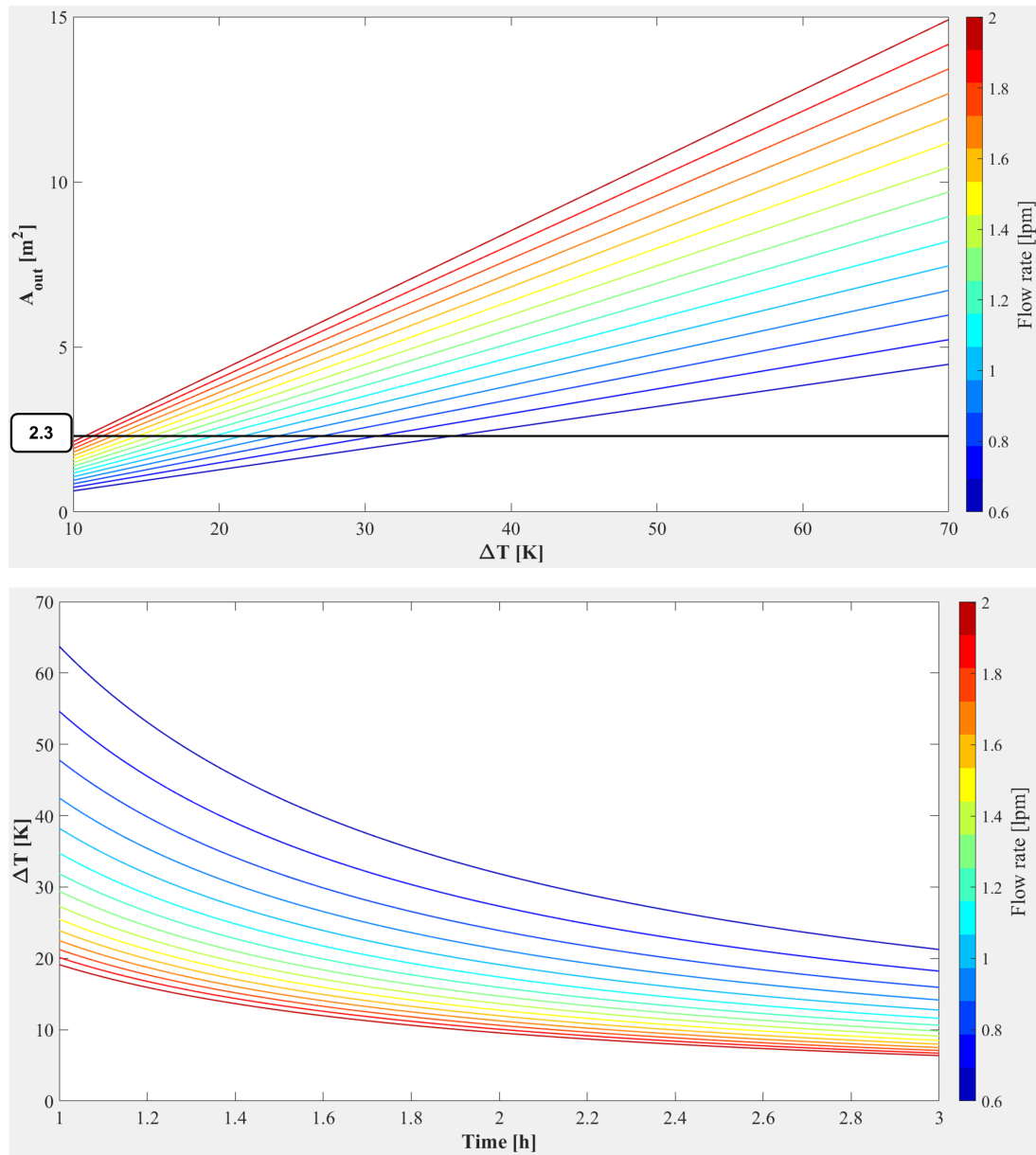
Figure 6.7: Iterative procedure to fit the optimal worst-case hot solution.

cross-sectional diameter of the tubes is calculated using the Hagen-Poiseuille's law:

$$D = 2 \cdot \sqrt[4]{\frac{8\mu L}{\pi \rho \, \Delta P} \, \dot{m}} \qquad (6.15)$$

thus, by cross-referencing the various data obtained in Figure 6.7 and respecting the assumptions made, the best solution is obtained, discriminating all the possible couplings, iterating the procedure, to ensure that the outer diameter and the exchange time are the lowest. The best solution is shown in Table 6.5.

Table 6.5: Optimal solution in the worst-case hot conditions.

A_{out} [m^2]	2.2904
ΔT [K]	25
$\dot{m}$ [kg/s]	0.0254 (0.86 [lpm])
τ [h]	1.7786 (42.6864 min)
D [mm]	8.2071

Results worst-case cold conditions   Using the variables defined in Table 6.6 and the assumptions made in the previous section, the diagrams in Figure 6.8 are derived. In the case of cold, the equations to be used are slightly different, because the ambient temperature (T_{amb}) is neglected in the radiative heat transfer and the temperature of the hot plate (T_s^h) is assumed to be 345.15 K (72.0 °C):

$$\sigma \epsilon_{rov} \left(T_s^h\right)^4 A_{out} = \dot{m}\, c_p \left(T_{in} - T_{out}\right)$$

$$\frac{m_{rov}\, c_{rov} \left(T_{rov} - T_{des}\right)}{\tau} = \dot{m}\, c_p \left(T_{in} - T_{out}\right) \tag{6.16}$$

By repeating the same iteration as in the previous case, the optimal solution is obtained (Table 6.7).

Table 6.6: Input data in the worst-case cold conditions.

Input data	
Radiative properties	
σ [W/m^{2}K]	$5.670373 \cdot 10^{-8}$
Emissivity (ϵ_{rov})	0.85
Fluid parameters	
Density (ρ) [kg/m^3]	1770
Dynamic viscosity (μ) [Pa s]	0.0032
Kinematic viscosity (ν) [m^2/s]	$1.8 \cdot 10^{-6}$
Specific heat (c_p) [J/kgK]	962.964
Rover parameters	
Specific heat (c_{rov}) [J/kgK]	870
Rover mass (m_{rov}) [kg]	899
Rover temperature (T_{rov}) [K]	258.15
Desire temperature (T_{des}) [K]	293.15
Hot plate temperature (T_s^h) [K]	345.15
Loop parameters	
Tube length (L) [m]	60.96
Pressure drop (ΔP) [Pa]	$25 \cdot 10^3$

Table 6.7: Optimal solution in the worst-case cold conditions.

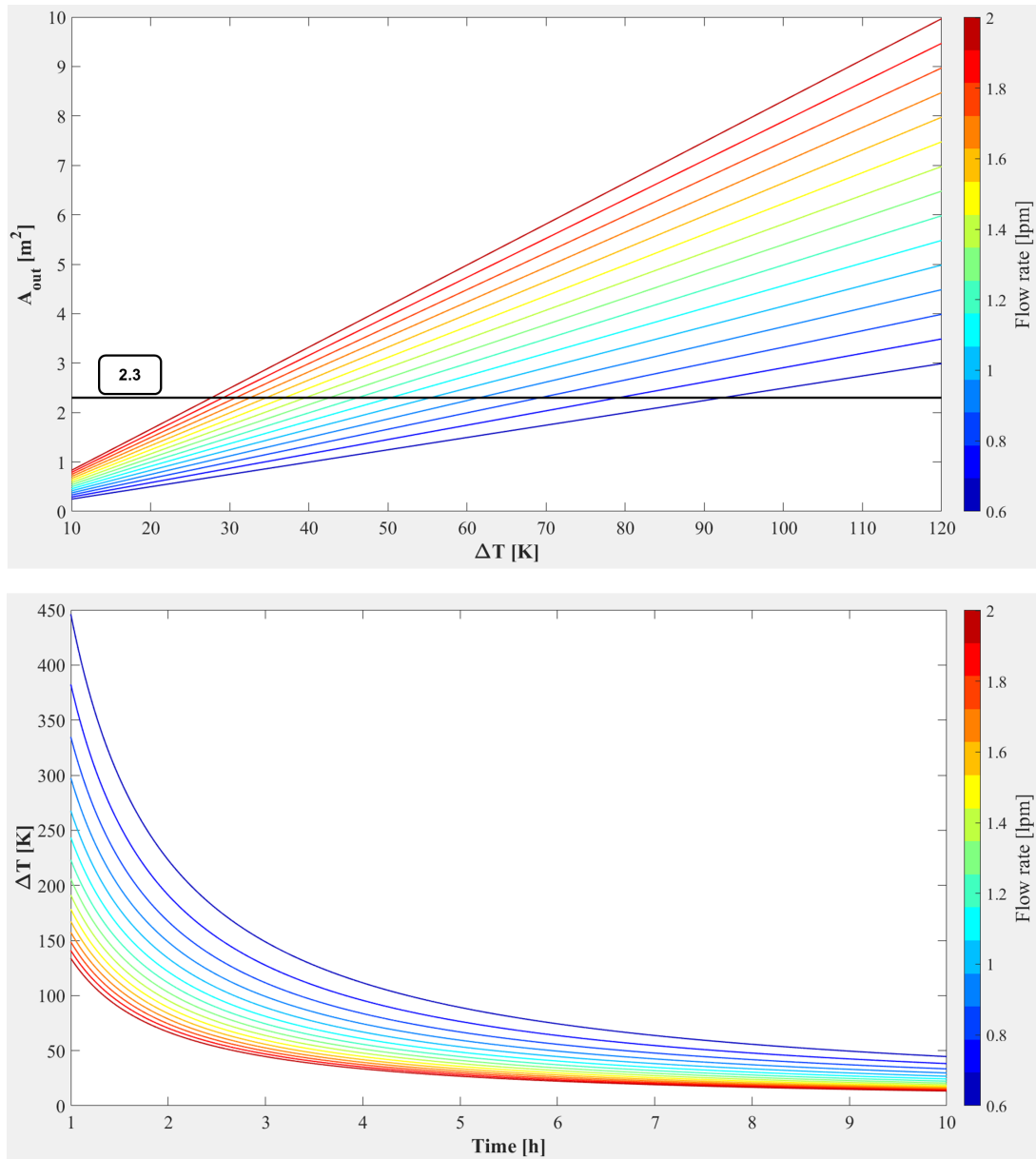|	
A_{out} [m^2]	2.2327
ΔT [K]	64
$\dot{m}$ [kg/s]	0.02478 (0.84 [lpm])
τ [h]	4.9791 (119.4984 min)
D [mm]	8.1590

Figure 6.8: Iterative procedure to fit the optimal worst-case cold solution.

6.4.2 Turbulent flow case

The previous problem was solved by *Hagen Poiseuille's law*, which is only valid if the flow is laminar and stationary (as already described). In the case studied, the flow is definitely turbulent (easily verified by calculating the Reynolds number knowing the diameter of the tubes and the velocity, kinematic viscosity and density of the working fluid). The turbulent regime guarantees the maximum efficiency of heat exchange in the case of forced convection, while the minimum efficiency is obtained in the case of natural convection in laminar regime. The main difficulty is the lack of a complete theory able to describe them satisfactorily due to the presence of interacting vortical structures, which is a consequence of the chaotic nature of the motion and the lack of orderly trajectories as in the case of the laminar regime. More recently, thanks to the development of numerical methods applied to fluid dynamics and the computational power achieved by computers, it is possible to obtain new information on the dynamics of turbulent motion through the direct solution of the Navier-Stokes equations by means of *Direct Numerical Simulation* (DNS), which is only possible in small problems: the solution is useful for understanding various phenomena and for producing simplified models that can be used in less computationally intensive methods. It is possible to filter the Navier-Stokes equations, eliminating the low wavelengths (the most of the energy resides in the high wavelengths), thus in this case the resolution is called *Large Eddy Simulation* (LES).

Operationally a *Fully Developed Turbulent Flow* (FDTF) occurs when the Reynolds number is greater than 4000. The FDTF in ducts can be characterised by the *Swamee-Jain equation* (one of many Darcy-Weisbach friction factor formulae that provides an accuracy within $\pm 1.5\%$), which allows the *Darcy-Weisbach friction factor* (f_d) for a full-flow circular tube to be solved directly:

$$f_d = \frac{0.25}{\left[\log_{10}\left(\frac{\varepsilon/D}{3.7} + \frac{5.74}{Re_D^{9/10}}\right)\right]^2} \tag{6.17}$$

where ε is the absolute roughness of the tube.

The relationship between volumetric flow rate ($\dot{V}$) and the circular tube diameter (D) is obtained from the following equations:

$$\Delta P = f_d \frac{\rho v^2}{2} \frac{L}{D}$$
$$\dot{V} = A\,v \tag{6.18}$$

where A is the cross-sectional area of the circular tube. Manipulating the two equations, the expression required is obtained:

$$D = \sqrt[5]{f_d \frac{8\rho}{\pi^2} \frac{L}{\Delta P} \dot{V}^2} \tag{6.19}$$

To evaluate the diameter in Eq. (6.19), it is necessary to calculate the friction factor using the *Moody diagram*[3] or Eq. (6.17). Figure 6.9 shows the calculation of the diameter in the two flow regimes. By increasing the Reynolds number to a much higher value of 4000, the friction factor decreases (assuming that the pressure drop and the relative roughness remain constant), but the curve in the turbulent regime case always remains below the same case study in the laminar regime. This leads to the conclusion that the choice of having initially assumed the laminar motion regime is ***conservative***.

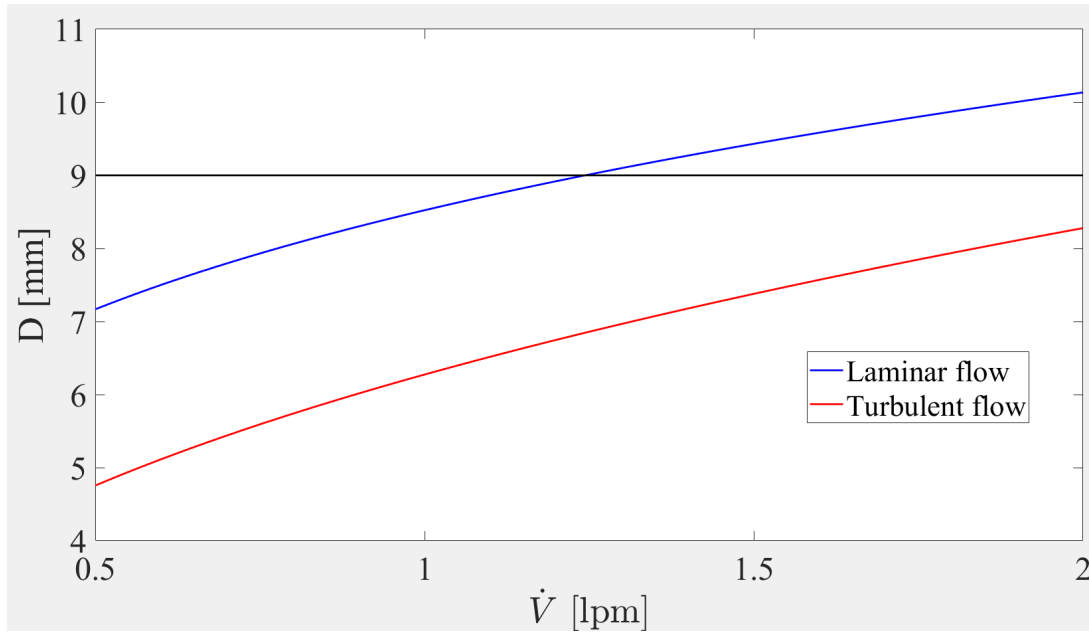Figure 6.9: Comparison between the diameter calculated using Hagen Poiseuille's law and the diameter calculated using Eq. (6.19) as the volumetric flow rate varies.

---

[3]The Moody chart is a omni-comprehensive non-dimensional form that relates the friction factor (f_d), the Reynolds number ($\mathbb{R}e$), and relative roughness (ε/D) for fully developed flow in a circular tube.

7. Conclusions

In Chapter 2, the functioning of the MMRTG was explained in detail, highlighting its advantages and disadvantages. Basically, the real problem with MMRTG is the low energy conversion efficiency due to the materials used for the hot shoes and cold shoes (Section 2.2) of the thermocouples. For this reason, new materials have been investigated to improve the efficiency of MMRTG, and the best proposal has been a compound called *Multiple-Filled Skutterudite* (SKD), which has been shown to have good mechanical strength and excellent thermoelectric properties that provide much more efficient energy conversion at a lower cost than current solutions. In addition, its lower operating temperature would provide much less risk of overheating. The efficiency of a thermocouple is directly related to Z, the dimensionless number most commonly used to evaluate the performance of a material for thermoelectric applications, thus the general equation describing the maximum efficiency (assuming that the material properties remain constant over a given temperature range) can be written as [64]:

$$\eta_{\mathrm{max}} = \eta_{\mathrm{C}} \frac{\sqrt{1 + ZT_{\mathrm{avg}}} - 1}{\sqrt{1 + ZT_{\mathrm{avg}}} + \frac{T_{\mathrm{C}}}{T_{\mathrm{H}}}}$$
$$Z = \frac{S^2}{\rho_m \lambda}$$

(7.1)

where T_{H} and T_{C} are the temperatures of the hot and cold sides of the material respectively, that define the ideal *Carnot cycle* and η_{C}[1], is the cycle efficiency; ρ_m is the is electrical resistivity of the material; S is the Seebeck coefficient and λ the thermal conductivity of the material. As for ZT_{avg}, it is the Z at the average temperature of an expected operating range. From Eq. (7.1), it can be seen that the increase in output power can be achieved by increasing the nominal hot-side temperature from $525\,^{\circ}\mathrm{C}$ (MMRTG) to $600\,^{\circ}\mathrm{C}$ (eMMRTG), which is enabled by the higher thermal stability of SKD materials. A further improvement in generator efficiency and reliability is provided by the inclusion of aerogel insulation, which suppresses sublimation on the surface of the thermoelectric materials with an associated reduction in heat loss.

Instead, Chapter 6 aims to analyse the rover from a thermal point of view in order to understand the response and performance of the structure in an environment with certain characteristics. The thermal analysis presented is useful, especially to understand the quantities involved and their order of magnitude. In addition, the thermal analysis can be carried out by generating a model of the rover to approximate it mathematically. This representation is known as a *Thermal Mathematical Model* (TMM). Thus, the rover is split into a number of discrete regions within

---

[1]The efficiency of the ideal *Carnot cycle* takes on the important form: $(T_{\mathrm{H}} - T_{\mathrm{C}})/T_{\mathrm{H}}$.

which thermal gradients can be neglected. In detail, the rover is divided into six thermal zones: top/rear/front, right side, left side, bottom, right side and left side wheels. Preliminarily each node is considered independent and isolated from each other. As a result, since there is no thermal interaction between them and assuming the steady state condition, the temperature of each node can be calculated separately.

Over the years, many integrated thermal analysis programs have been developed that allow to generate complete TMM and the Generalised Method of Moments (GMM), to perform and visualise temperature distributions under stationary and non-stationary motion conditions. Most of the codes are based on the *Monte Carlo algorithm* or the *diffuse-gray hypothesis* (the radiation model assumes that surfaces are grey and diffuse, emissivity and absorbance being independent of wavelength). The Monte Carlo algorithm was developed as a way of dealing with problems in which the events at a given location are known, at least in the form of statistical distributions, so it has the advantage that almost any problem of arbitrary complexity can be tackled with relative ease, but there are two disadvantages that should not be underestimated: statistical scattering of results and high computational cost. Commercially available thermal analysis software packages are as follows:

Simcenter STAR-CCM+® developed by *Siemens Digital Industries Software*;

Simcenter FloTHERM-XT® distributed by *Cadlog*;

Simcenter FLOEFD® by *Siemens Digital Industries Software*;

ESATAN Thermal Modelling Suite® by *ITP Aero*;

MSC Nastran® by *MSC Software Corporation*;

MSC Patran® by *MSC Software Corporation*;

Ansys Fluent® by *Ansys Incorporation*;

OpenFOAM® developed primarily by *OpenCFD Ltd*, is an open source CFD software;

C&R Thermal Desktop® developed by *C&R Technologies*, is a pre- and post-processor for SINDA Thermal Analyzer;

Thermal Synthesizer System® by *SpaceDesign Corporation*;

THERMICA® by *EADS Astrium*, is a plug-in application of the SYSTEMA environment;

Elmer® developed by *CSC-IT Center for Science* (CSC), is an open source multiphysical simulation software.

Bibliography

[1] *Schematized structure of a photovoltaic solar cell.*
    https://sites.suffolk.edu/malkhaldi/page/2/.

[2] Mukund R Patel. *Spacecraft power systems.* CRC press, 2004.

[3] *Fuel cell schematization.*
    https://www.socalgas.com/for-your-business/power-generation/fuel-cell-technology.

[4] Onsite Sycom. Review of combined heat and power technologies. *Office of Industrial
    Technologies, Office of Energy Efficiency and Renewable Energy, US Department of En-
    ergy*, 1999.

[5] Qi Chen, Zhigang Liu, Xiaofeng Zhang, and Liying Zhu. *Spacecraft Power System Tech-
    nologies.* Springer, 2020.

[6] *State-of-art MMRTG.*
    https://mars.nasa.gov/.

[7] *RPS technology.*
    https://rps.nasa.gov/technology/.

[8] Emily Lakdawalla. *The design and engineering of Curiosity: how the Mars Rover per-
    forms its job.* Springer, 2018.

[9] David Woerner. The mars science laboratory's mmrtg: a missions perspective. 2012.

[10] *Insulating material of an MMRTG.*
    http://anstd.ans.org/.

[11] Peter Fortescue, Graham Swinerd, and John Stark. *Spacecraft systems engineering.* John
    Wiley & Sons, 2011.

[12] J.M. Cleveland. *The Chemistry of Plutonium.* American Nuclear Society,U.S., 1979.

[13] Space Studies Board, National Research Council, Radioisotope Power Systems Committee, et al. *Radioisotope power systems: an imperative for maintaining US leadership in space exploration*. National Academies Press, 2009.

[14] Glenn Theodore Seaborg, Ralph A James, and Leon O Morgan. *The new element americium (atomic number 95)*. Technical Information Division, Oak Ridge Directed Operations, 1948.

[15] Paul A Lessing. High purity americium-241 for fuel cycle r&d program. Technical report, Idaho National Laboratory (INL), 2011.

[16] Vasilii Semenovich Yemel'Yanov and AI Yevstyukhin. *The metallurgy of nuclear fuel: properties and principles of the technology of uranium, thorium and plutonium*. Elsevier, 2013.

[17] Richard M Ambrosi, Hugo Williams, Emily Jane Watkinson, Alessandra Barco, Ramy Mesalam, Tony Crawford, Christopher Bicknell, Piyal Samara-Ratna, David Vernon, Nigel Bannister, et al. European radioisotope thermoelectric generators (rtgs) and radioisotope heater units (rhus) for space science and exploration. *Space Science Reviews*, 2019.

[18] Glen A Robertson, David Young, Karen Cunningham, Tony Kim, Richard M Ambrosi, and Hugo R Williams. Preliminary analysis: Am-241 rhu/teg electric power source for nanosatellites. 2014.

[19] Gajanana Birur. Thermal control of msl rover'curiosity'using an active fluid loop. 2013.

[20] *SAM instruments*.
https://mars.nasa.gov/msl/spacecraft/instruments/sam/.

[21] Paul R Mahaffy, Christopher R Webster, Michel Cabane, Pamela G Conrad, Patrice Coll, Sushil K Atreya, Robert Arvey, Michael Barciniak, Mehdi Benna, Lora Bleacher, et al. The sample analysis at mars investigation and instrument suite. *Space Science Reviews*, 2012.

[22] David Blake, David Vaniman, Cherie Achilles, Robert Anderson, David Bish, Tom Bristow, Curtis Chen, Steve Chipera, Joy Crisp, David Des Marais, et al. Characterization and calibration of the chemin mineralogical instrument on mars science laboratory. *Space Science Reviews*, 2012.

[23] *Three-dimensional model of the Chemin*.
https://mars.nasa.gov/msl/spacecraft/instruments/chemin/.

[24] *Results of the first analysis of Martian soil by CheMin.*
https://photojournal.jpl.nasa.gov/catalog/PIA16217.

[25] *Crystal structure of Quartz 101 and Beryl 112.*
https://www.smorf.nl/crystals_search.php.

[26] Wayne Zimmerman, Dave Blake, William Harris, John Michael Morookian, Dave Randall, Leonard J Reder, and Phillipe Sarrazin. Msl chemistry and mineralogy x-ray diffraction x-ray fluorescence (chemin) instrument. In *2013 IEEE Aerospace Conference*. IEEE, 2013.

[27] S Maurice, RC Wiens, M Saccoccio, B Barraclough, O Gasnault, O Forni, N Mangold, David Baratoux, S Bender, G Berger, et al. The chemcam instrument suite on the mars science laboratory (msl) rover: Science objectives and mast unit description. *Space science reviews*, 2012.

[28] *ChemCam Spectrum from Martian Rock.*
https://mars.nasa.gov/msl/spacecraft/instruments/chemcam/for-scientists/.

[29] Roger C Wiens, Sylvestre Maurice, Bruce Barraclough, Muriel Saccoccio, Walter C Barkley, James F Bell, Steve Bender, John Bernardin, Diana Blaney, Jennifer Blank, et al. The chemcam instrument suite on the mars science laboratory (msl) rover: Body unit and combined system tests. *Space science reviews*, 2012.

[30] CS Dickinson, R Gellert, P Dietrich, and D Hiemstra. Apxs on mars science laboratory-first results from post-landing checkout. In *International Workshop on Instrumentation for Planetary Missions*, volume 1683, page 1035, 2012.

[31] Ralf Gellert and Albert S Yen. Elemental analyses of mars from rovers using the alpha-particle x-ray spectrometer. *Remote Compositional Analysis: Techniques for Understanding Spectroscopy*, 2019.

[32] *Mars Hand Lens Imager.*
https://mars.nasa.gov/msl/spacecraft/instruments/mahli/.

[33] Kenneth S Edgett, R Aileen Yingst, Michael A Ravine, Michael A Caplinger, Justin N Maki, F Tony Ghaemi, Jacob A Schaffner, James F Bell, Laurence J Edwards, Kenneth E Herkenhoff, et al. Curiosity's mars hand lens imager (mahli) investigation. *Space science reviews*, 2012.

[34] *Mastcam on the MSL rover's Remote Sensing Mast.*
https://mars.nasa.gov/msl/spacecraft/instruments/mastcam/for-scientists/.

[35] Michal C Malin, Michael A Ravine, Michael A Caplinger, F Tony Ghaemi, Jacob A Schaffner, Justin N Maki, James F Bell III, James F Cameron, William E Dietrich, Kenneth S Edgett, et al. The mars science laboratory (msl) mast cameras and descent imager: Investigation and instrument descriptions. *Earth and Space Science*, 2017.

[36] MC Malin, MA Caplinger, KS Edgett, FT Ghaemi, MA Ravine, JA Schaffner, JN Maki, RG Willson, JF Bell, JF Cameron, et al. The mars science laboratory (msl) mars descent imager (mardi) flight instrument. In *Lunar and Planetary Science Conference*, page 1199, 2009.

[37] *Filters for Color Imaging and for Science*.
https://photojournal.jpl.nasa.gov/catalog/PIA16799.

[38] *Illustrating MastCam Capabilities with a Terrestrial Scene*.
https://photojournal.jpl.nasa.gov/catalog/PIA15109.

[39] *3D model of the MSL rover*.
https://mars.nasa.gov/msl/rover-3d/.

[40] *RAD sensor head visible on Curiosity's deck*.
https://mars.nasa.gov/msl/spacecraft/instruments/rad/.

[41] Donald M Hassler, C Zeitlin, RF Wimmer-Schweingruber, S Böttcher, C Martin, J Andrews, E Böhm, DE Brinza, MA Bullock, S Burmeister, et al. The radiation assessment detector (rad) investigation. *Space science reviews*, 2012.

[42] *Neutron energy distribution range*.
https://www.nuclear-power.net/.

[43] J Gómez-Elvira, C Armiens, L Castañer, M Domínguez, M Genzer, Francisco Gómez, R Haberle, A-M Harri, V Jiménez, H Kahanpää, et al. Rems: The environmental sensor suite for the mars science laboratory rover. *Space science reviews*, 2012.

[44] María-Paz Zorzano, Javier Martín-Soler, and Javier Gómez-Elvira. Uv photodiodes response to non-normal, non-collimated and diffusive sources of irradiance. In *Photodiodes-Communications, Bio-Sensings, Measurements and High-Energy Physics*. IntechOpen Limited London, UK, 2011.

[45] Andre Makovsky, Peter Ilott, and Jim Taylor. Mars science laboratory telecommunications system design. *DESCANSO Design and Performance Summary Series, Article*, 2009.

[46] *The Madrid Deep Space Communications Complex*.
https://www.nasa.gov/directorates/heo/scan/services/overview/AntennaGallery-007.html.

[47] *Locations of the Deep Space Network stations.*
https://solarsystem.nasa.gov/basics/chapter18-1/.

[48] *Zoom on the High-Gain Antenna.*
https://photojournal.jpl.nasa.gov/catalog/PIA19920.

[49] CD Edwards Jr, B Arnold, R DePaula, G Kazz, C Lee, and G Noreen. Relay communications strategies for mars explorati... In *56th International Astronautical Congress of the International Astronautical Federation, the International Academy of Astronautics, and the International Institute of Space Law*.

[50] Faramaz Davarian, Sami Asmar, Matt Angert, John Baker, Jay Gao, Richard Hodges, David Israel, Damon Landau, Norman Lay, Leigh Torgerson, et al. Improving small satellite communications and tracking in deep space—a review of the existing systems and technologies with recommendations for improvement. part ii: Small satellite navigation, proximity links, and communications link science. *IEEE Aerospace and Electronic Systems Magazine*, 2020.

[51] J Maki, D Thiessen, A Pourangi, P Kobzeff, T Litwin, L Scherr, S Elliott, A Dingizian, and M Maimone. The mars science laboratory engineering cameras. *Space science reviews*, 2012.

[52] Marshall Smart, Bugga Ratnakumar, Larry Whitcanack, Elizabeth Dewell, Loren Jones, Christopher Salvo, Frank Puglia, Robert Gitzendanner, and S Cohen. Performance testing of yardney li-ion cells and batteries in support of jpl's 2009 mars science laboratory mission. In *6th International Energy Conversion Engineering Conference (IECEC)*, 2008.

[53] Arturo Canceller Icardo, Cristina Cervera Llansol, José Luis Galiana Amorós, Laura Cristina Smith Ballester, Andrea Pittari, and Diego Viñuela Alonso. Diseño del sistema energético de un vehículo aeroespacial. 2020.

[54] *EaglePicher Technologies.*
https://www.eaglepicher.com/products/secondary-batteries-rechargeable/.

[55] *MIL-STD-975M (NASA), MILITARY STANDARD: NASA STANDARD ELECTRICAL, ELECTRONIC, AND ELECTROMECHNICAL (EEE) PARTS LIST (5 AUG 1994).*
http://everyspec.com/MIL-STD/MIL-STD-0900-1099/MIL_STD_975M_1166/.

[56] Frank P Incropera, Adrienne S Lavine, Theodore L Bergman, and David P DeWitt. *Fundamentals of heat and mass transfer*. Wiley, 2007.

[57] Yunus A.. Çengel and Afshin Jahanshahi Ghajar. *Heat and Mass Transfer: Fundamentals & Applications*. McGraw Hill Education, 2015.

[58] Wiley J Larson and James Richard Wertz. Space mission analysis and design. Technical report, Torrance, CA (United States); Microcosm, Inc., 1992.

[59] *Mars Climate Database v5.3*.
http://www-mars.lmd.jussieu.fr/mcd_python/.

[60] *CFC-11, Galden H170 working fluid*.
http://www.testbourne.com/galden-ht-fluids.

[61] AJ Mastropietro, John Beatty, Frank Kelly, Gajanana Birur, Pradeep Bhandari, Michael Pauken, Peter Illsley, Yuanming Liu, David Bame, and Jennifer Miller. Design and preliminary thermal performance of the mars science laboratory rover heat exchangers. In *40th International Conference on Environmental Systems*, 2010.

[62] Keith Novak, Anthony Paris, Frank Kelly, and Jennifer Miller. Thermal response of the mars science laboratory spacecraft during entry, descent and landing. 46th International Conference on Environmental Systems, 2016.

[63] Inka Hublitz. *Heat and mass transfer of a low-pressure Mars greenhouse: Simulation and experimental analysis*. University of Florida, 2006.

[64] Hannah Armstrong, Matthew Boese, Cody Carmichael, Hannah Dimich, Dylan Seay, Nathan Sheppard, and Matt Beekman. Estimating energy conversion efficiency of thermoelectric materials: constant property versus average property models. *Journal of Electronic Materials*, 2017.

[65] *Ionizing radiation*.
https://www.ans.org/nuclear/radiation/.

[66] *Decay schemes of Plutonium-238 and Americium-241*.
https://www.atsdr.cdc.gov/toxprofiles/.

A. Appendix

Characteristics of Emitted Radiation

Each decay transforms an unstable configuration of nucleons into a more stable configuration with liberation of a certain amount of energy defined by the difference between the energy associated with the initial resting mass and the sum of the energies associated with the final resting masses, knowing the mass–energy equivalence, $E = m \cdot c^2$.

Nuclides can be classified into several types:

- Isotopes: If atoms of the same chemical element have the same atomic number (Z), but they differ in number of nucleons (A);

- Isobars: If atoms of different chemical elements differs in the chemical property, but has the same physical property, in other words they have the same number of nucleons, but differ in atomic number;

- Isomers: If atoms have the same atomic number and the same mass number, but different energies (i.e. energy difference between excited[1] and ground state).

Alpha decay   An atomic nucleus transforms into a different nucleus with 4 fewer nucleons by emitting α-particle[2] according to the relation:

$$X(A, Z) \longrightarrow Y(A - 4, Z - 2) + {}^4_2\alpha$$
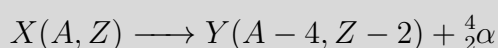
This type of decay is typical of heavy nuclei with $Z > 82$ and $A > 210$ and involves a variation of both the atomic number and the mass number. In these heavy nuclei the electrostatic repulsive force between the protons is not compensated by a sufficient number of neutrons, consequently the emissions of an α-particle result in the disappearance from the nuclide of 2 protons and 2 neutrons, as a means of increasing stability by reducing size.

Beta decay β^--*decay* is characteristic of unstable nuclei with *excess of neutrons* compared to the corresponding stable isobars. This means that an excess neutron decays into a proton,

---

[1]The excited state is indicated with an asterisk.

[2]Nucleus of ^{4}He: consisting of 2 protons and 2 neutrons.

which remains inside the nucleus (the mass number does not change, while the atomic number increases by one), causing the emission of 2 leptons[3] which take on the kinetic energy released from decay and are expelled from the nucleus:

$$n \longrightarrow p + \beta^- + \bar{\nu}_e$$

Therefore, this type of decay is an isobaric transition, that is an unstable nucleus transforms into an isobar with the emission of an electron (β^--particle and an *electron antineutrino*[4] according to the relation:

$$X(A, Z) \longrightarrow Y(A, Z + 1) + e^- + \bar{\nu}_e$$

β^+-*decay* is characteristic of unstable nuclei with *neutron defect* compared to the corresponding stable isobars. This means that inside the nucleus an excess proton transforms into a neutron with the emission of 2 leptons, so the atomic number varies (decreases by one) and the mass number does not change:

$$p \longrightarrow n + \beta^+ + \nu_e$$

Thus, an unstable nucleus is transformed into an isobar with the emission of a positron (β^+-particle, antiparticle of the electron) and of an *electron neutrino*[5] according to the relation:

$$X(A, Z) \longrightarrow Y(A, Z - 1) + e^+ + \nu_e$$

Electron capture   It is a process in which an electron of the internal orbitals of the atom is absorbed by a proton-rich nucleus and from the reaction a neutron is obtained, for this reason this process leads to the same result as the β^+-decay, so it leads to an element with an atomic number less than one unit and unchanged mass number. With lighter and unstable isotopes, electron capture occurs with respect to β^+-decay, because they have an energy difference, between the

---

[3]The basic building blocks of matter, elementary particles with small mass that do not partake in strong interactions.

[4]Antiparticle of the electron neutrino

[5]Elementary particle with neutral electric charge and extremely small mass, rarely it interacts with matter and is only susceptible to the weak subatomic force, moreover they can practically go through enormous thicknesses of matter undisturbed. The theoretical physicist W. Pauli to justify the continuous energy spectra and how energy, momentum and angular momentum could conserve in β- decay. He hypothesized the existence of an undetected particle that would appear when the radioactive nucleus emitted an electron, because during the decay a part of the energy it disappeared, denying the conservation of energy principle, which states that the total energy of an isolated system does not change, can be transferred or changed from one form to another, but can neither be created nor destroyed.

initial and final nucleus formed, less than $1.022\,\mathrm{MeV}$, so positron emission is forbidden due to unavailable decay energy to allow it. The process takes place according to the relation:

$$X(A, Z) + e^{-} \longrightarrow Y(A, Z - 1) + \nu_{e}$$
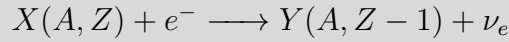
So an electron is captured by the internal shell of the atom and occurs the emission of an electron antineutrino. A consequence of this process is the *X-ray photons emission*, when an outer electron drop to fill the vacancy replacing the captured electron, but sometimes the process can lead to the *Auger effect*[6].

Gamma decay   This type of decay process is an *isomeric transition* that can occur when at the end of a α or β-decay a final excited nucleus is obtained due to a part of the energy released in the process. Therefore, the emission of a γ-photon or a quantum of electromagnetic energy is the mechanism that allows this nucleus to de-energize, reaching a lower and more stable energy level, without particles ejection from the nucleus.
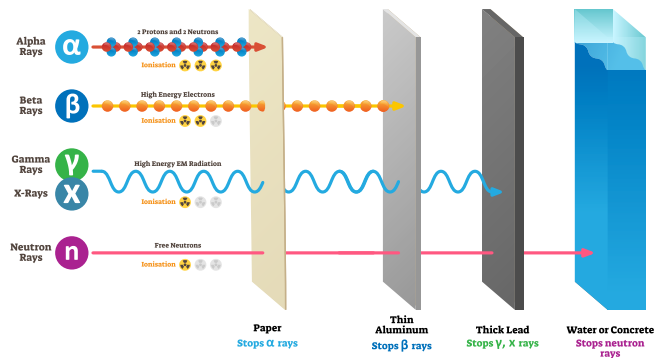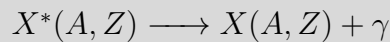
$$X^{*}(A, Z) \longrightarrow X(A, Z) + \gamma$$

Figure A.1: Types of ionizing radiation [65].

---

[6]If the quantum energy released by the downward transition is transferred to one of the outer electrons, which is ejected from the atom.

B. Appendix

^{241}Am and ^{238}Pu decay [66]

Plutonium-238 decay scheme

Pu	^{238}Pu 87.7 years					
Np	↓					
U	^{234}U 2.46x10^5 years					
Pa	↓					
Th	^{230}Th 7.54x10^4 years					
Ac	↓					
Ra	^{226}Ra 1599 years					
Fr	↓					
Rn	^{222}Rn 3.8325 days					
At	↓	^{218}At 1.5 sec				
Po	^{218}Po 3.10 minutes		^{214}Po 164 μseconds		^{210}Po 138.38 days	
Bi	↓	^{214}Bi 19.9 minutes	↓	^{210}Bi 5.01 days	↓	
Pb	^{214}Pb 27 minutes	↓	^{210}Pb 22.3 years	↓	^{206}Pb Stable	
Tl		^{210}Tl 1.3 minutes		^{206}Tl 4.20 minutes		

↓ alpha (α) decay   ╱ beta (β$^-$) decay

Americium-241 decay scheme

Nuclide	Half-life	Alpha (α) keV	Alpha (α) %	Beta (β) max MeV	Beta (β) max %	Gamma (γ) keV	Gamma (γ) %
²⁴¹Am ↓	432.2 years	5,485 5,443	84.5 13.0			13.9 59.5 26.3	42 35.9 2.4
²³⁷Np ↓	2.144x10⁶ years	4,788 4,771 4,766 4,639 4,664	47 25 8 6.2 3.3			13.3 29.4 86.5 8.2 95.9	58 15 12.4 9 2.7
²³³Pa ↓	26.97 days			232 156 260 174 572	40 27.7 17 16.4 4	13.6 312.2 98.4 94.7 111.0	56 38.6 17.7 10.9 8.2
²³³U ↓	1.592x10⁵ years	4,824 4,784	84.4 13.2			13.0	6.0
²²⁹Th ↓	7,340 years	4,845 4,901 4,815 5,053 4,968	56.2 10.2 9.3 6.6 6.0			12.3 88.5 85.4 100.0 11.1	79 24.7 15.0 11.3 8
²²⁵Ra ↓	14.9 days			331 371	69.5 30.5	40.0 12.7	30.0 15.2
²²⁵Ac ↓	10.0 days	5,830 5,792 5,791 5,732 5,637	50.7 18.1 8.6 8.0 4.4			12.0 10.6	20.9 9.3
²²¹Fr ↓	4.9 minutes	6,341 6,126	83.4 15.1			218.2 11.4	11.6 2.2
²¹⁷At ↓	0.323 seconds	7,066	99.9			258.5	0.056
²¹³Bi 97.84% ↓ 2.16%	45.59 minutes	5,869	1.94	1422 982	65.9 31.0	440.5 79.3	26.1 2.0
²¹³Po ↓	3.65 micro-seconds	8,376	100.0			778.8	0.005
²⁰⁹Tl ↓	2.2 minutes			660	98.8	1567.1 465.1 117.2 75.0 10.6	99.8 96.9 84.3 10.7 9.4
²⁰⁹Pb ↓	3.253 hours			0.644	100		
²⁰⁹Bi	stable						

C. Appendix

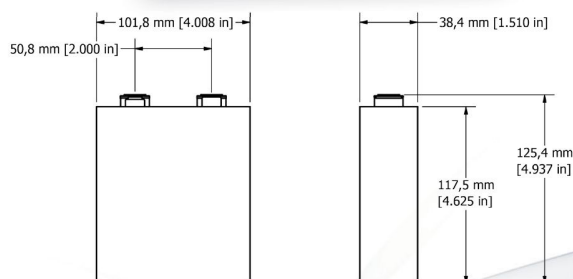# EaglePicher database of lithium-ion battery datasheets

EaglePicher™ Technologies, LLC
An OMG Company

Multi-Purpose Hard Case Cell

Lithium-Ion (Li-Ion) NCM High-Energy Rechargeable

Lithium-Ion provides higher energy levels at a lower weight and smaller volume than Ni-H$_2$ or Ni-Cd.

101,8 mm [4.008 in]
50,8 mm [2.000 in]
38,4 mm [1.510 in]
125,4 mm [4.937 in]
117,5 mm [4.625 in]

Features & Benefits

+ Prismatic cell design
+ Fully welded, hermetically-sealed construction
+ Compression seals
+ 175 ± 25 psi rupture disk vent
+ High reliability
+ Low cyclic capacity fade
+ Long calendar life
+ Broad temperature operating range
+ Aluminum case and cover

Applications

+ Aircraft power backup
+ Scientific and exploratory satellite missions
+ Launch vehicle
+ Terrestrial high energy applications

Specifications

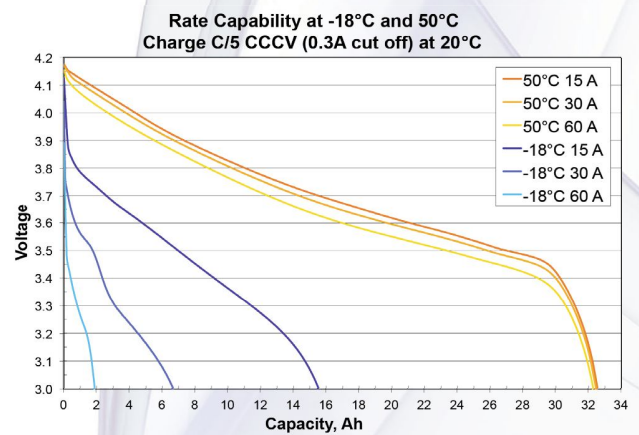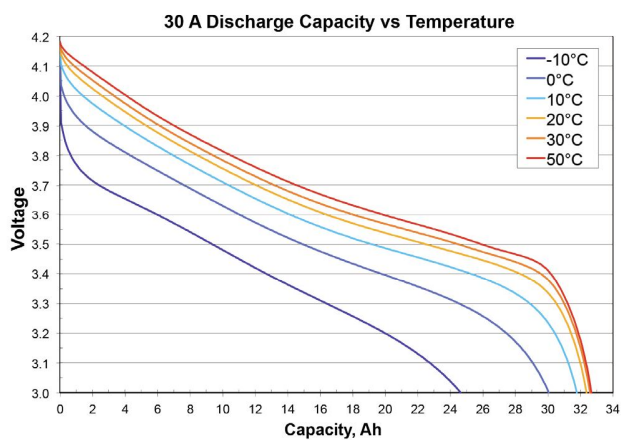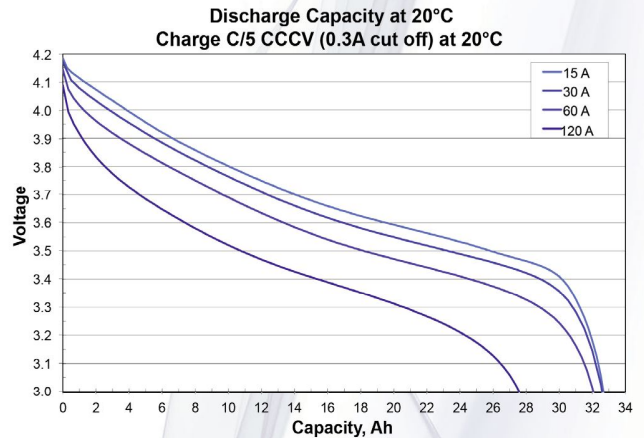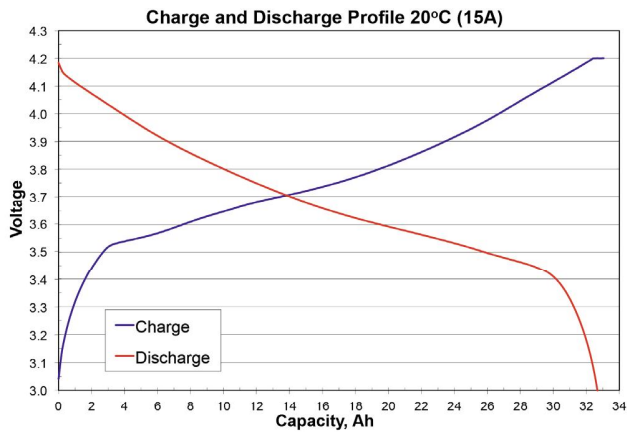|	
Part Number	SLC-027-01
Cell Design	Lithium-Ion Secondary Cell
Electrical	
Beginning of Life Capacity*	34Ah, 139 Wh at 20˚C
Nameplate Capacity*	30Ah, 112 Wh at 20˚C
Maximum Charge Voltage	4.2V
Minimum Discharge Voltage	3.0V
Charge Current Limit	30.0A to 4.2 EOCV CC/CV
Discharge Current Limit	120.0A to 3.0 EODV
Pulse Current Limit	240A for 10 seconds
Mechanical	
Weight	1000 g/2.2 lbs.
Specific Energy*	139.0 Wh/kg
Energy Density*	283.5 Wh/l
Dimensions	125.4 x 101.8 x 38.4 mm (4.94 x 4.01 x 1.51 in)
Storage Temperature	-20°C to 50°C (-4°F to 122°F)
Operating Temperature	-10°C to 50°C (14°F to 122°F)
Vibration Limit	Random 24.7 g
Transportation	Class 9 ID number – UN 3090**

*EODV 4.2 CC/CV (C/5, 0.3A cut off), C/2 discharge, 20˚C

**For complete transportation regulations, contact EaglePicher Technologies, LLC

Charge and Discharge Profile 20°C (15A)

Discharge Capacity at 20°C
Charge C/5 CCCV (0.3A cut off) at 20°C

30 A Discharge Capacity vs Temperature

Rate Capability at -18°C and 50°C
Charge C/5 CCCV (0.3A cut off) at 20°C

EaglePicher SLC-028-01 Cell

Lithium-Ion (Li-Ion)
High-Energy Rechargeable

Features:

- Prismatic cell design
- Fully welded, hermitically-sealed construction
- Compression seals
- 175 ± 25 psi rupture disk vent

Benefits:

- High-reliability
- Low cyclic capacity fade
- Long calendar life

Applications:

- Aircraft Power Backup
- Low-Earth Orbit (LEO) satellite mission
- Mid-Earth Orbit (MEO) satellite mission
- Geosynchronous Earth Orbit (GEO) satellite mission
- Scientific and Exploratory satellite missions
- Launch vehicle

Specifications:

|	
Part Number	SLC-028-01
Cell Design	Lithium-Ion Secondary Cell
Beginning of Life Capacity	34.5 Ah, 128 Wh at 20°C EOCV 4.2 CC/CV, C/2
Nameplate Capacity	30 Ah, 110 Wh at 20°C EOCV 4.2 CC/CV, C/2
Mass	1020 g, (2.24 lbs.)
Dimensions	125.4 x 101.8 x 38.4mm (4.94 x 4.00 x 1.51 in.)
Specific Energy	125.0 Wh/Kg
Energy Density	283.5 Wh/l
Storage Temperature	-5° to 5°C (23° to 41°F)
Operating Temperature	-10° to 50°C (14° to 122°F)
Charge Current Limit	32.5 A to 4.1 EOCV CC/CV
Discharge Current Limit	120 A to 3.0 EODV
Pulse Current Limit	240 A for 10 seconds
Vibration Limit	Random 24.7 Grms
Transportation	Class 9 Identification Number UN 3090*

All performance values are typical.
* For complete transportation regulations, contact EaglePicher Technologies, LLC.
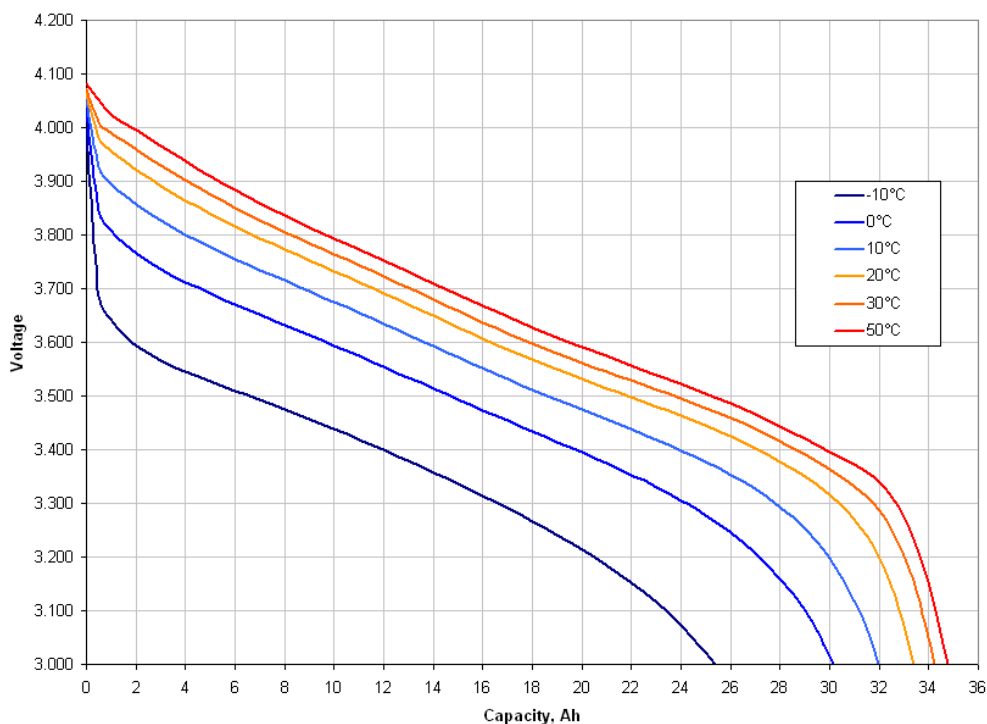
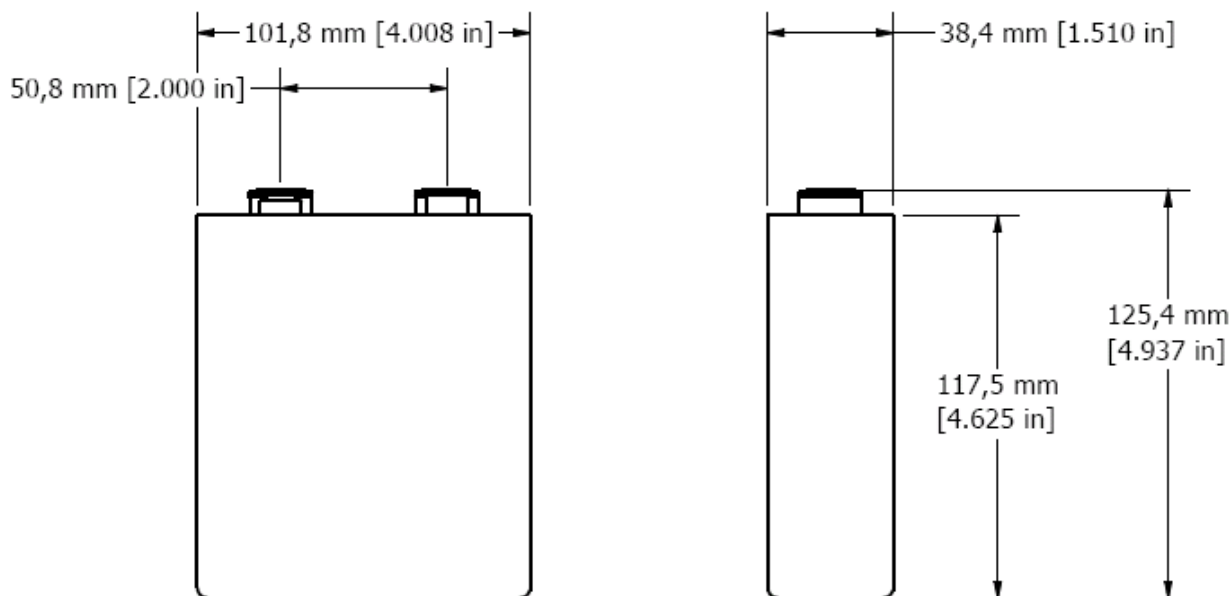# EaglePicher Li-Ion Cell
SLC-028-01
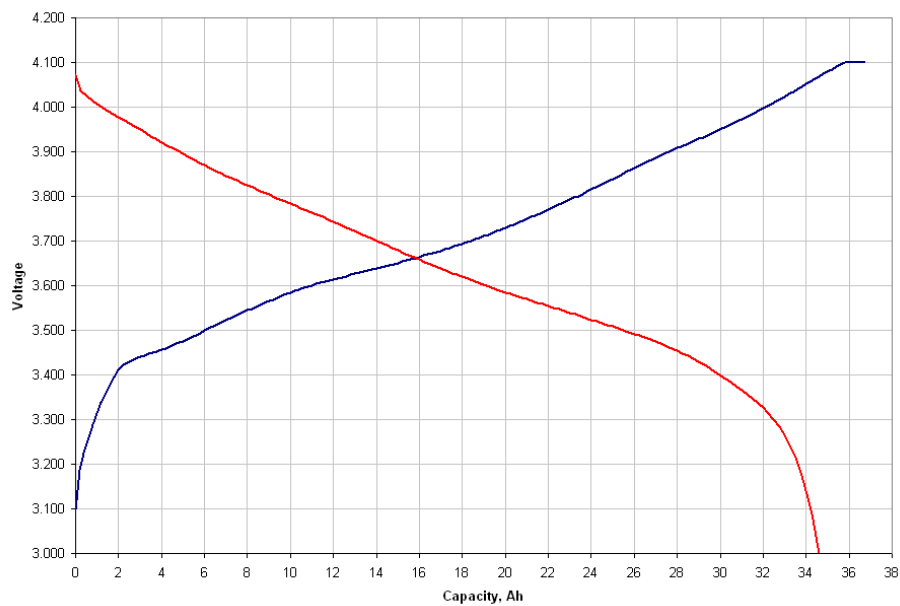
CHARGE/DISCHARGE VOLTAGE PROFILES
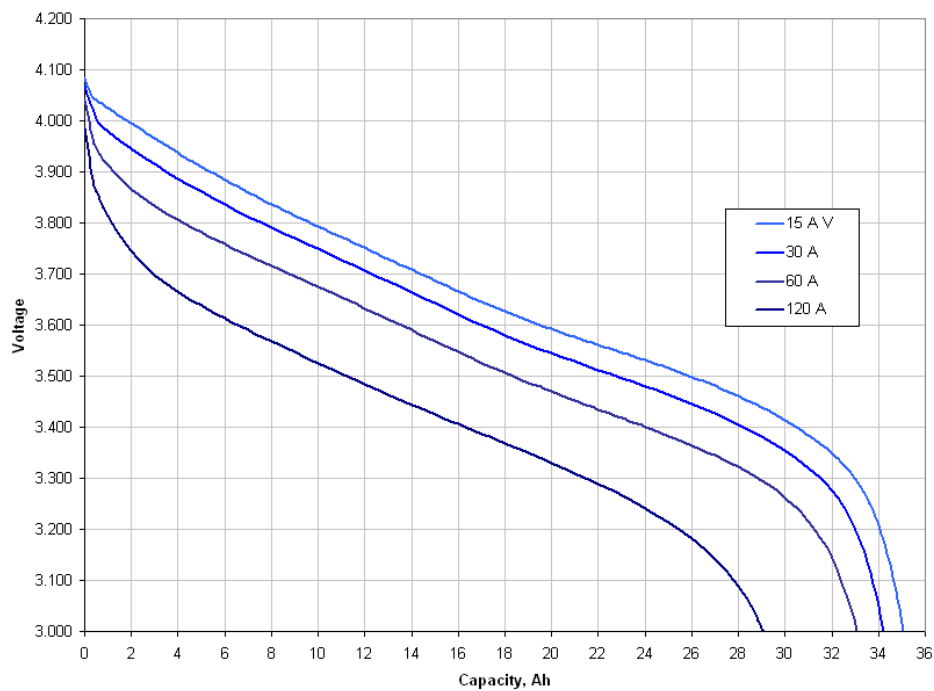
DISCHARGE RATE PROFILES

EaglePicher™
Technologies, LLC
An OMG *Company*

EaglePicher Li-Ion Cell
SLC-028-01

DISCHARGE TEMPERATURE PROFILES

CELL DIMENSIONS

EaglePicher™
Technologies, LLC
An OMG Company

INTERTEK
AS9100 • ISO 9001

EaglePicher™ Technologies, LLC
An OMG Company

EaglePicher Space Cell

Lithium-Ion

Lithium-Ion provides higher energy levels at a lower weight and smaller volume than Ni-H$_2$ or Ni-Cd.

6.81 in
[173 mm]

3.21 in
[81.5 mm]

7.92 in
[201.3 mm]

2.24 in
[56.9 mm]
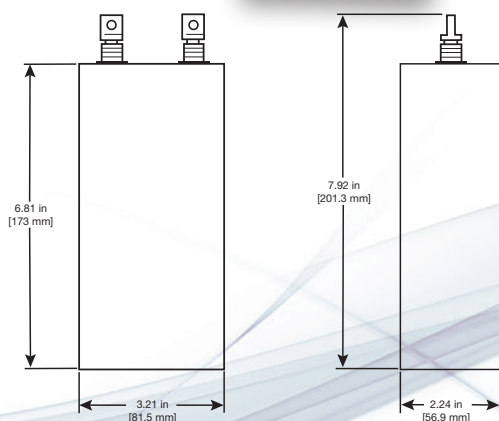
Specifications

Part Number	SLC-16050
Cell Design	Lithium-Ion Secondary Cell
Electrical	
Beginning of Life Capacity	62.5 Ah, 245 Wh at 20°C EOCV 4.1 CC/CV, C/2
Nameplate Capacity	52 Ah, 204 Wh at 20°C EOCV 4.1 CC/CV, C/2
Charge Current Limit	31.25A to 4.1 EOCV CC/CV
Discharge Current Limit	62.5A to 3.0 EODV
Pulse Current Limit	125A for 10 seconds
Mechanical	
Weight	2020 g/4.44 lb
Specific Energy	121.3 Whr/kg
Energy Density	305.4 Wh/l
Dimensions (less terminal)	173 x 81.5 x 56.9 mm (6.81 x 3.21 x 2.24 in)
Storage Temperature	-5°C to 5°C (23°F to 41°F)
Operating Temperature	10°C to 30°C (50°F to 86°F)
Vibration Limit	Random 24.7 g
Transportation	Class 9 ID number – UN3090*

*For complete transportation regulations, contact EaglePicher Technologies, LLC

Features & Benefits

+ Qualified for space flight
+ Prismatic cell design
+ Fully-welded, hermetically-sealed construction
+ Compression seals
+ 175 ± 20 psi rupture disk vent
+ High energy density
+ Highly reliable
+ Low cyclic capacity fade
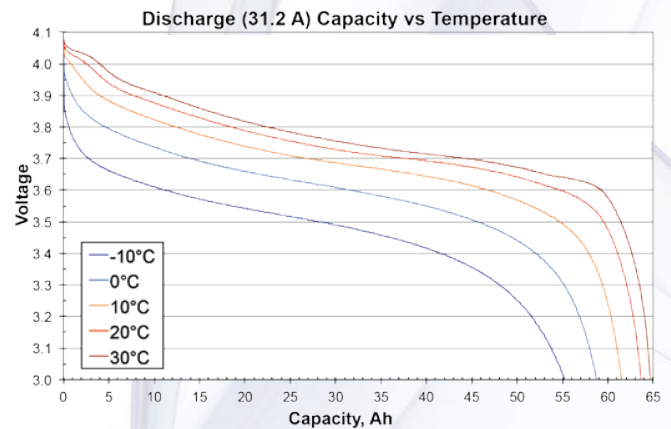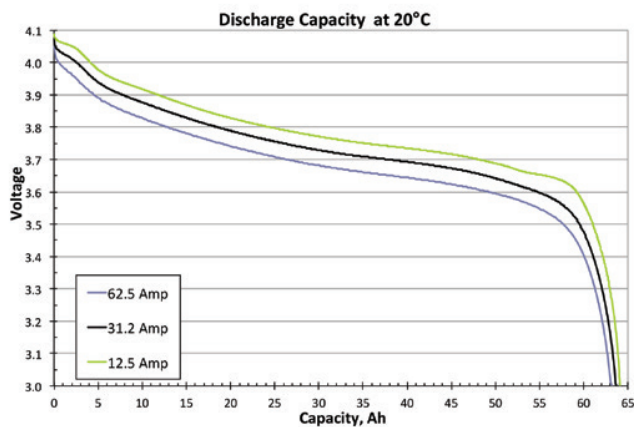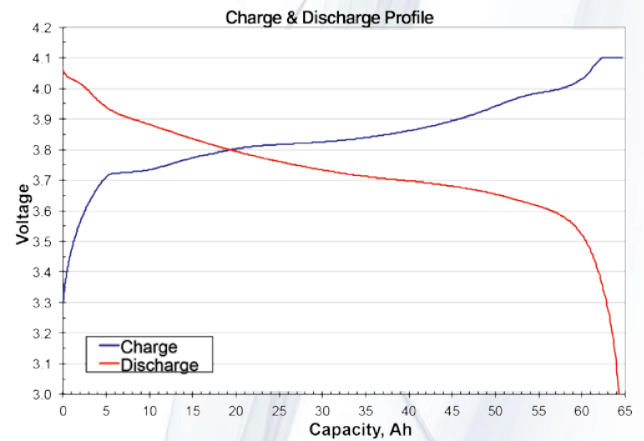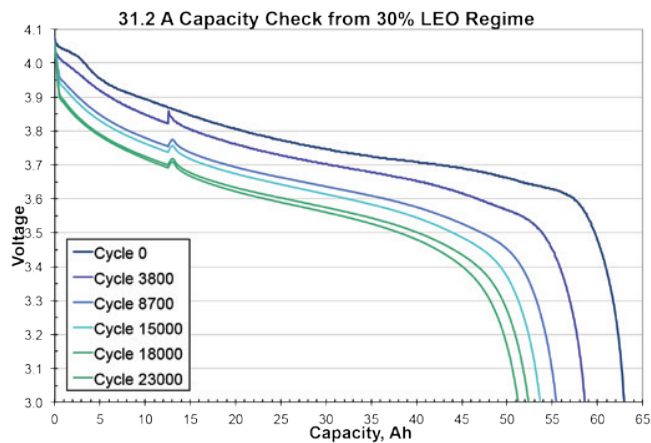+ Long calendar life
+ Stainless steel case and cover

Applications

+ Low-Earth Orbit (LEO) Satellite Mission
+ Mid-Earth Orbit (MEO) Satellite Mission
+ Geosynchronous-Earth Orbit (GEO) Satellite Mission
+ Scientific and Exploratory Satellite Missions
+ Launch Vehicle

PO Box 47 | Joplin, Missouri 64802-0047 USA | tel 417.623.8000 | fax 417.623.0850 | *www.eaglepicher.com*

This material is released to the public domain in accordance with ITAR 22 CFR 120.11.
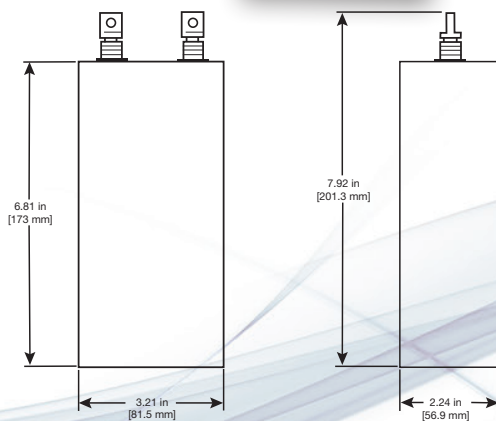
SLC-16050

31.2 A Capacity Check from 30% LEO Regime

Legend: Cycle 0, Cycle 3800, Cycle 8700, Cycle 15000, Cycle 18000, Cycle 23000

Charge & Discharge Profile

Legend: Charge, Discharge

Discharge Capacity at 20°C

Legend: 62.5 Amp, 31.2 Amp, 12.5 Amp

Discharge (31.2 A) Capacity vs Temperature

Legend: -10°C, 0°C, 10°C, 20°C, 30°C

EaglePicher™
Technologies, LLC
An OMG Company

INTERTEK
AS9100 · ISO 9001

SLC-21060-001

EaglePicher™ Technologies, LLC
An OMG Company

EaglePicher Space Cell

Lithium-Ion

Lithium-Ion provides higher energy levels at a lower weight and smaller volume than Ni-H$_2$ or Ni-Cd.

6.81 in [173 mm]

7.92 in [201.3 mm]

3.21 in [81.5 mm]

2.24 in [56.9 mm]

Specifications

Part Number	SLC-21060-001
Cell Design	Lithium-Ion Secondary Cell
Electrical	
Beginning of Life Capacity	72 Ah, 260 Wh at 20°C EOCV 4.1 CC/CV, C/2
Nameplate Capacity	70 Ah, 256 Wh at 20°C EOCV 4.1 CC/CV, C/2
Charge Current Limit	36.0 A to 4.1 EOCV CC/CV
Discharge Current Limit	72.0 A to 3.0 EODV
Pulse Current Limit	146 A for 10 seconds
Mechanical	
Weight	1974 g/4.34 lb
Specific Energy	131.7 Whr/kg
Energy Density	324.1 Wh/l
Dimensions (less terminal)	173 x 81.5 x 56.9 mm (6.81 x 3.21 x 2.24 in)
Storage Temperature	-5°C to 5°C (23°F to 41°F)
Operating Temperature	10°C to 30°C (50° F to 86°F)
Vibration Limit	Random 24.7 g
Transportation	Class 9 ID number – UN3090*

*For complete transportation regulations, contact EaglePicher Technologies, LLC

Features & Benefits

+ Qualified for space flight
+ Prismatic cell design
+ Fully-welded, hermetically-sealed construction
+ Compression seals
+ 175 ± 20 psi rupture disk vent
+ High energy density
+ Highly reliable
+ Low cyclic capacity fade
+ Long calendar life
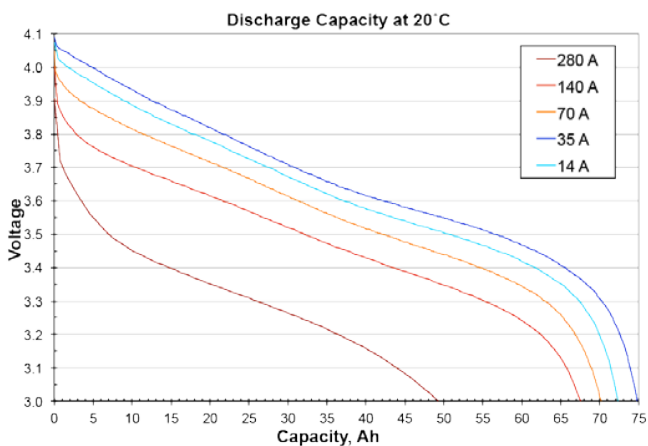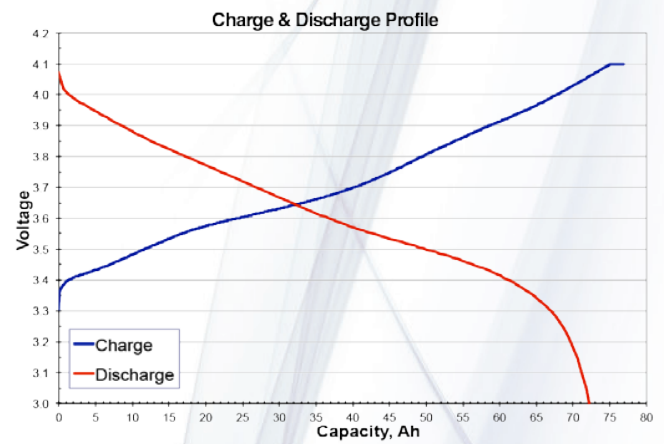+ Stainless steel case and cover

Applications

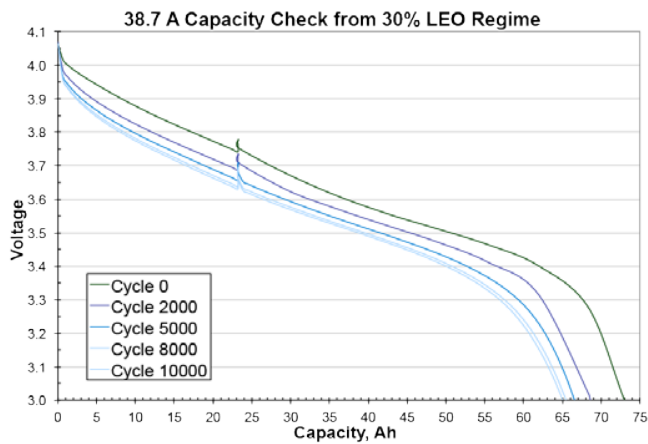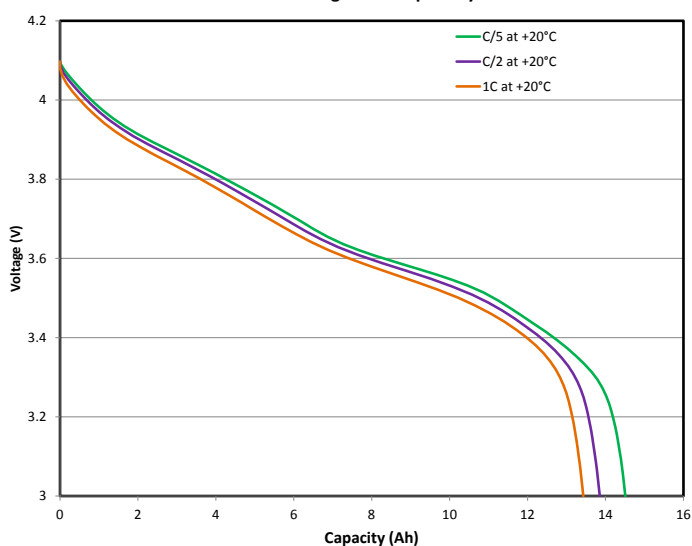+ Low-Earth Orbit (LEO) Satellite Mission
+ Mid-Earth Orbit (MEO) Satellite Mission
+ Geosynchronous-Earth Orbit (GEO) Satellite Mission
+ Scientific and Exploratory Satellite Missions
+ Launch Vehicle

38.7 A Capacity Check from 30% LEO Regime

Charge & Discharge Profile

Discharge Capacity at 20°C

Discharge (35 A) Capacity vs Temperature

EaglePicher™
Technologies, LLC
An OMG Company

EaglePicher™
Technologies, LLC
A VECTRA *Company*

12Ah Space Cell

Model LP 32975
Lithiated Nickel Cobalt Aluminum Oxide

*High energy, long cycle life and
LOW maintenance Lithium-Ion cell
for DEMANDING applications*

Features & Benefits

✦ Case neutral

✦ Safety vent feature

✦ True prismatic design

✦ Hermetically sealed

✦ Stainless steel case

✦ Long life-over 40,000 LEO cycles @ 40% DOD over 10 years of operation

✦ Qualified for operation from -20°C to +60°C

✦ Proven Reliability

Applications

✦ Aerospace

✦ Mars Lander

✦ Low-Earth Orbit (LEO) Satellite Mission

✦ Mid-Earth Orbit (MEO) Satellite Mission

✦ Geosynchronous-Earth Orbit (GEO) Mission

✦ Scientific and Exploratory Satellite Missions

Specifications
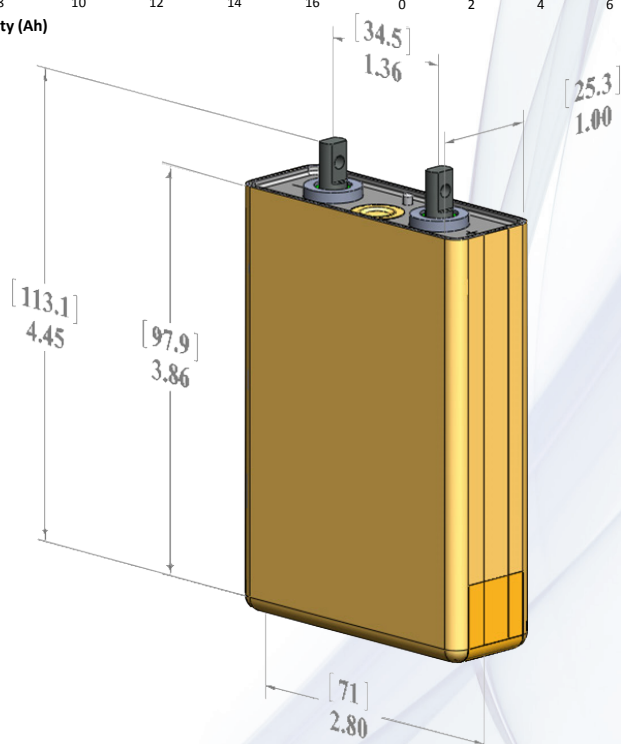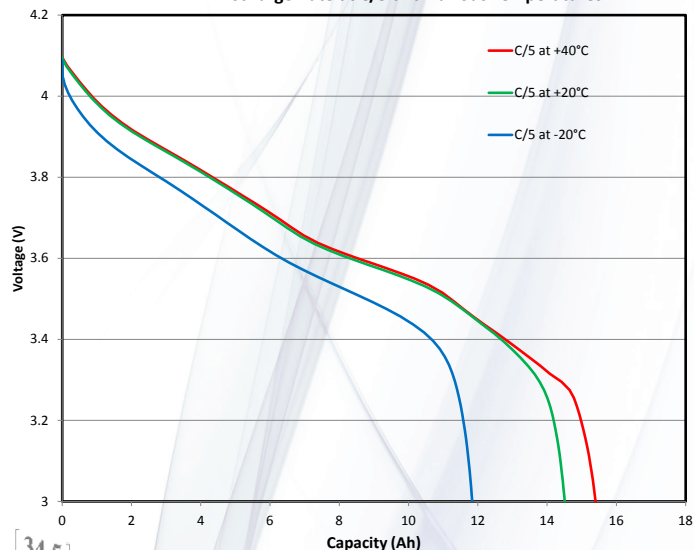
Model Number		LP 32975
Nominal Capacity		12Ah @ C/5 @ 20°C
Nominal Voltage		3.6 Volts
Voltage Range		3.0V to 4.10V
Nominal Cell Impedance @ 20°C		5mΩ
Cycle Life to 80% Capacity Measured at 0.5C discharge current at 20°C		>2000 @ 100% DOD
Nominal Cell Weight		465g
Standard Charging Method	Constant Current	6A (0.5C) to 4.1V
	Constant Voltage	4.1V to 0.24A (C/50)
Operating Temperature		-20°C to +60°C
Storage Temperature		-40°C to +60°C
Dimensions		See Detail on Back
Energy Density		285 Wh/L
Specific Energy		114 Wh/kg
Discharge Rates	Max Constant Current	96A
	Max Pulse Current (<1 sec)	180A

NCP 12-4

Discharge Rate Capability at 20°C

Legend:
- C/5 at +20°C
- C/2 at +20°C
- 1C at +20°C

Y-axis: Voltage (V)
X-axis: Capacity (Ah)

Discharge Rate at C/5 and Various Temperatures

Legend:
- C/5 at +40°C
- C/5 at +20°C
- C/5 at -20°C

Y-axis: Voltage (V)
X-axis: Capacity (Ah)

Dimensions:
- 34.5 / 1.36
- 25.3 / 1.00
- 113.1 / 4.45
- 97.9 / 3.86
- 71 / 2.80

EaglePicher™
Technologies, LLC
A **VECTRA** *Company*

INTERTEK
AS9100 • ISO 9001

EaglePicher™
Technologies, LLC
A \VECTRA\ *Company*

43Ah Space Cell

Model LP 31950
Lithiated Nickel Cobalt Aluminum Oxide

High energy, long cycle life and LOW maintenance Lithium-Ion cell for DEMANDING applications

Features & Benefits

+ Case neutral
+ Safety vent feature
+ True prismatic design
+ Hermetically sealed
+ Stainless steel case
+ Long life-over 40,000 LEO cycles @ 40% DOD over 10 years of operation
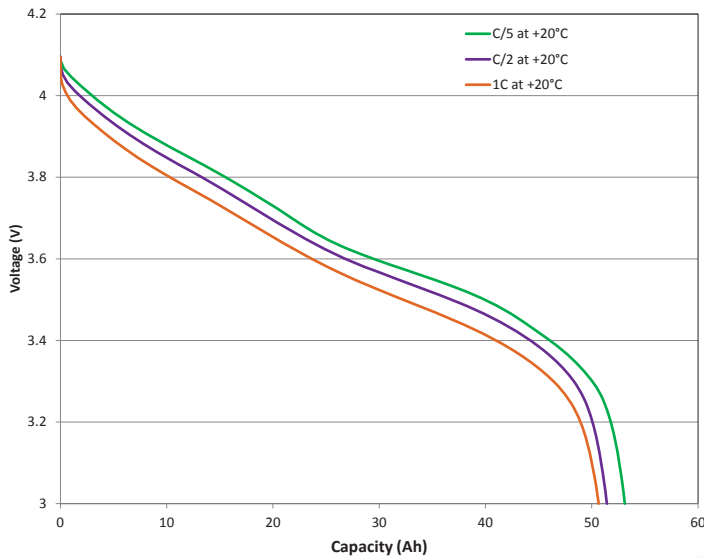+ Qualified for operation from -20°C to +60°C

Applications

+ Aerospace
+ Mars Lander
+ Low-Earth Orbit (LEO) Satellite Mission
+ Mid-Earth Orbit (MEO) Satellite Mission
+ Geosynchronous-Earth Orbit (GEO) Mission
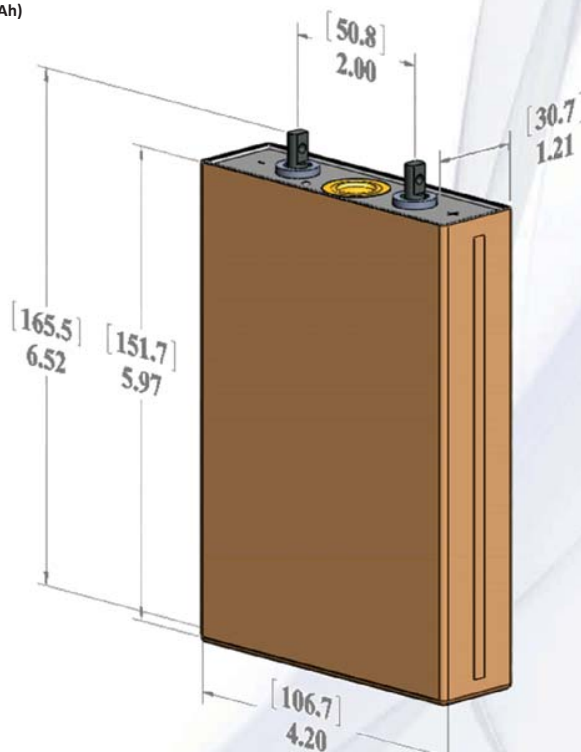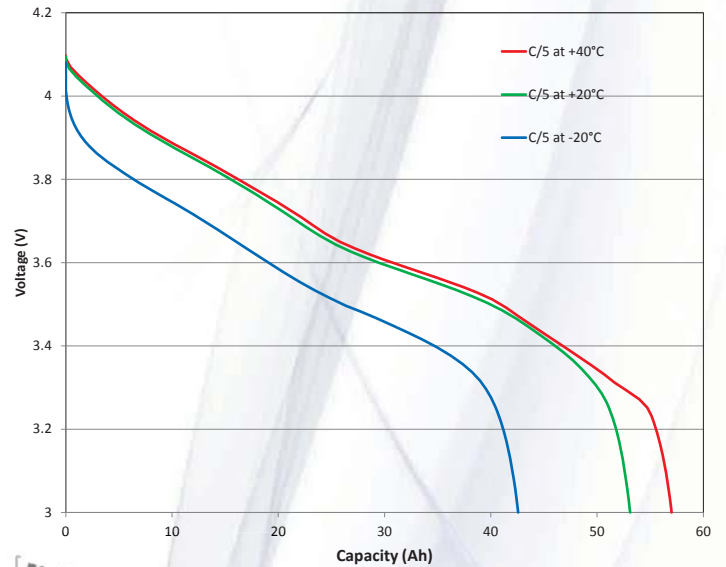+ Scientific and Exploratory Satellite Missions

Specifications

Model Number		LP 31950
Nominal Capacity		43Ah @ C/5 @ 20°C
Nominal Voltage		3.6 Volts
Voltage Range		3.0V to 4.10V
Nominal Cell Impedance @ 2mΩ		5mΩ
Cycle Life to 80% Capacity Measured at 0.5C discharge current at 20°C		>2000 @ 100% DOD
Nominal Cell Weight		1.27kg
Standard Charging Method	Constant Current	21.5A (0.5C) to 4.2V
	Constant Voltage	4.2V to 0.86A (C/50)
Operating Temperature		-20°C to +60°C
Storage Temperature		-40°C to +60°C
Dimensions		See Detail on Back
Energy Density		378 Wh/L
Specific Energy		153 Wh/kg
Discharge Rates	Max Constant Current	200A
	Max Pulse Current (<1 sec)	400A

NCP 43-4

Discharge Rate Capability at 20°C

Legend:
- C/5 at +20°C
- C/2 at +20°C
- 1C at +20°C

X-axis: Capacity (Ah)
Y-axis: Voltage (V)

Discharge Rate Capability at C/5 and Various Temperatures

Legend:
- C/5 at +40°C
- C/5 at +20°C
- C/5 at -20°C

X-axis: Capacity (Ah)
Y-axis: Voltage (V)

Dimensions:
- [50.8] 2.00
- [30.7] 1.21
- [165.5] 6.52
- [151.7] 5.97
- [106.7] 4.20

EaglePicher™ Technologies, LLC
A VECTRA Company

INTERTEK
AS9100 · ISO 9001

02/2016

EaglePicher™ Technologies, LLC
A VECTRA Company

55Ah High Rate Lithium Ion Cell

Model LP 32770

High energy, long cycle life and LOW maintenance Lithium-Ion cell for DEMANDING applications

Features & Benefits

- ✦ Case neutral
- ✦ Safety vent feature
- ✦ True prismatic design
- ✦ Hermetically sealed
- ✦ Stainless steel case
- ✦ Wide operational temperature range
- ✦ Vibration resistant
- ✦ Proven in demanding applications
- ✦ Advanced low temperature electrolyte
- ✦ High power
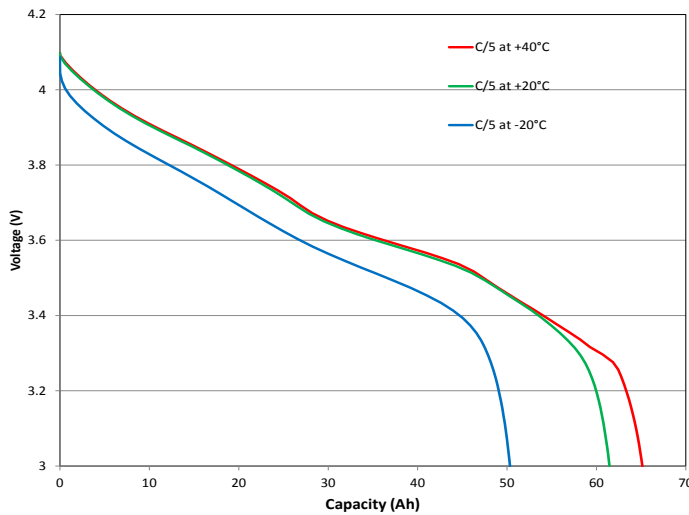- ✦ Moderate energy

Applications
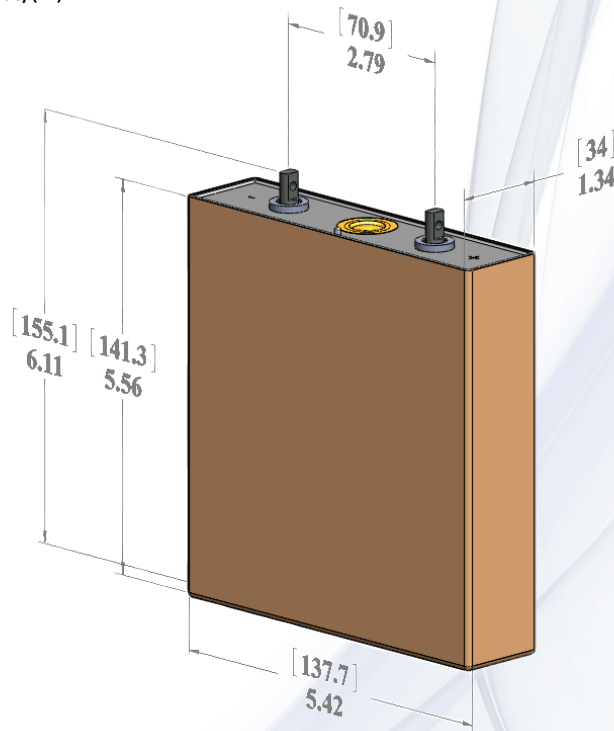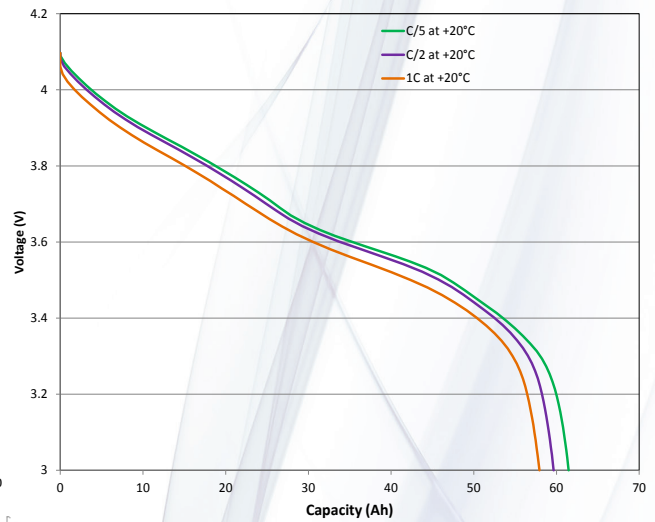
- ✦ Aircraft
- ✦ Aerospace

Specifications

Model Number		LP 32770
Nominal Capacity		55Ah @ C/5 @ 20°C
Nominal Voltage		3.6 Volts
Voltage Range		3.0V to 4.10V
Nominal Cell Impedance @ 2mΩ		5mΩ
Cycle Life to 80% Capacity Measured at 0.5C discharge current at 20°C		>2000 @ 100% DOD
Nominal Cell Weight		1.680kg
Standard Charging Method	Constant Current	27.5A (0.5C) to 4.1V
	Constant Voltage	4.1V to 1.1A (C/50)
Operating Temperature		-20°C to +60°C
Storage Temperature		-40°C to +60°C
Dimensions		See Detail on Back
Energy Density		343 Wh/L
Specific Energy		134 Wh/kg
Discharge Rates	Max Constant Current	440A
	Max Pulse Current (<1 sec)	660A

NCP55-4

Discharge Rate Capability at C/5 and Various Temperatures

Legend:
- C/5 at +40°C
- C/5 at +20°C
- C/5 at -20°C

Y-axis: Voltage (V)
X-axis: Capacity (Ah)

Discharage Rate Capability at 20°C

Legend:
- C/5 at +20°C
- C/2 at +20°C
- 1C at +20°C

Y-axis: Voltage (V)
X-axis: Capacity (Ah)

Dimensions:
- [70.9] 2.79
- [34] 1.34
- [155.1] 6.11
- [141.3] 5.56
- [137.7] 5.42

D. Appendix

Battery comparison

E. Appendix

Selection of T_{ground} and T_{amb}

Figure E.1: Environmental and ground temperature profile during the worst case hot conditions. The Figure above shows the ground temperature (height $0.0\,\mathrm{m}\ ALS$) with climatology maximum solar scenario, with latitude and longitude those of the Curiosity landing site (latitude: $-4.6°$ N; longitude: $137.4°$ E), in the period of the year with Ls equal to $195°$ and at local time $13.0\,\mathrm{h}$. While the Figure below shows the temperature variation in the first $2\,\mathrm{km}$ from the surface [59].
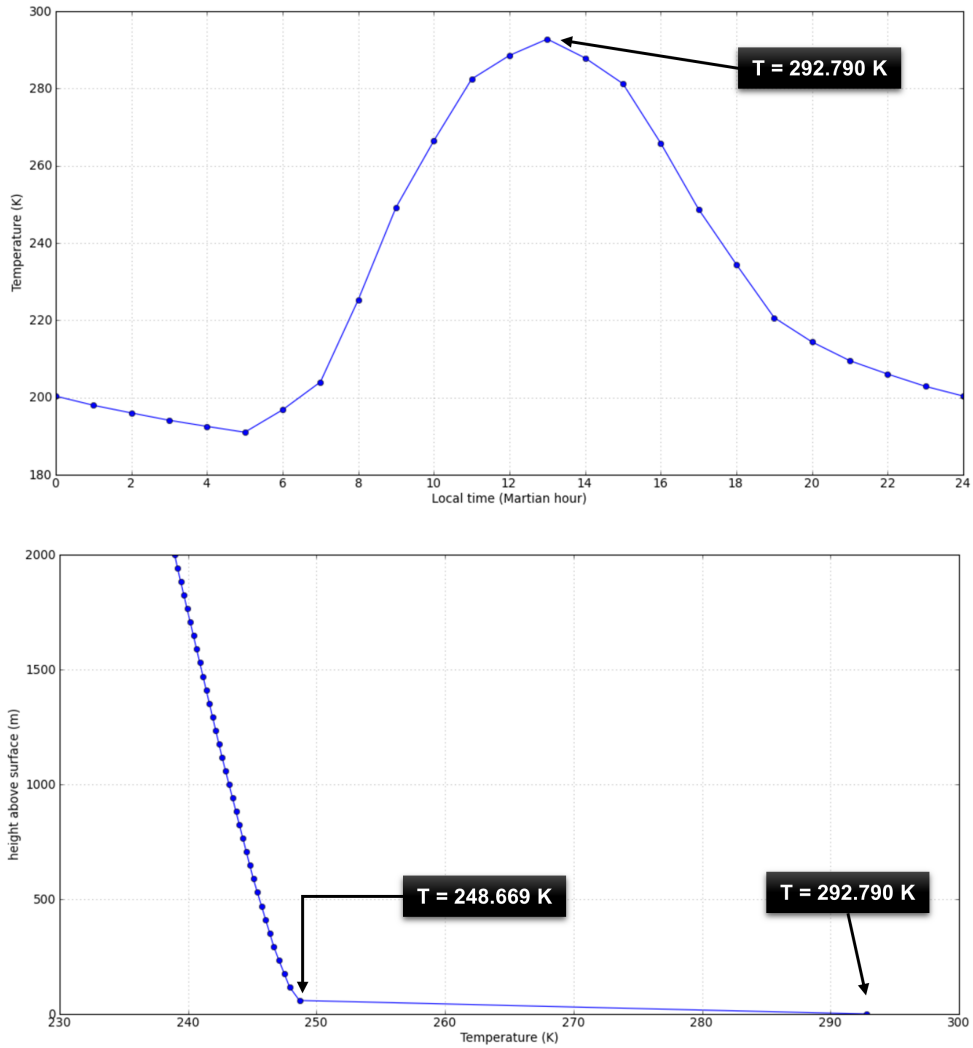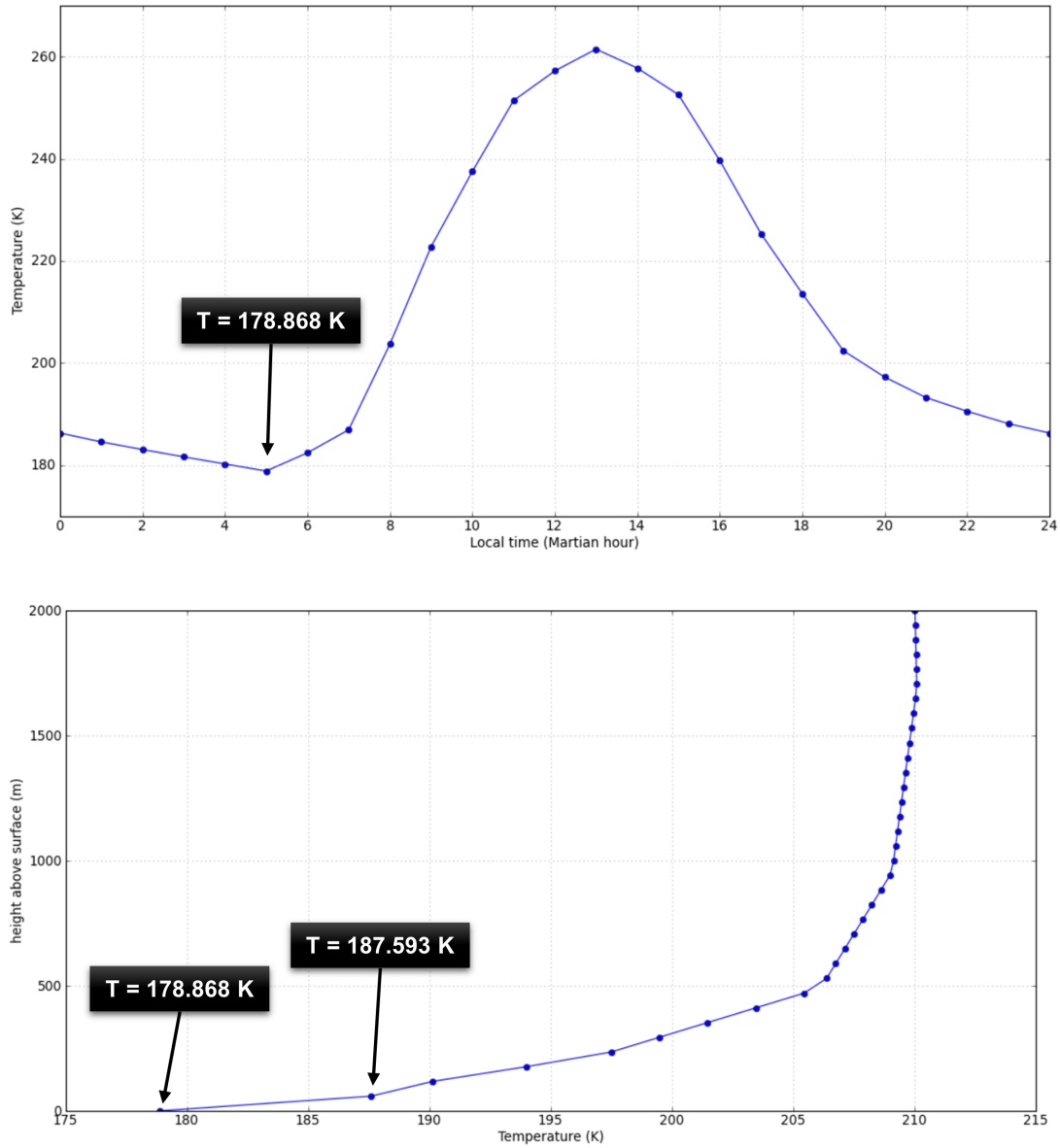
Figure E.2: Environmental and ground temperature profile during the worst case cold conditions. The Figure above shows the ground temperature (height $0.0\,\mathrm{m}$ ALS) with climatology minimum solar scenario, with latitude and longitude those of the Curiosity landing site (latitude: $-4.6°$ N; longitude: $137.4°$ E), in the period of the year with Ls equal to $105°$ and at local time $5.0\,\mathrm{h}$. While the Figure below shows the temperature variation in the first $2\,\mathrm{km}$ from the surface [59].

F. Appendix

MATLAB script for active thermal control system solution

WORST-CASE HOT CONDITIONS

```matlab
1  clearvars
2  close all
3  clc
4
5  % PLOT
6  data = 'ON';
7  onPlot = 'ON';
8
9  % radiative properties
10 sigma = 5.670373e-8;    % [W/(m^2*K)]
11 eps = 0.85;             % [-]
12
13 % fluid
14 cp = 962.964;    % [J/(Kg*K)]
15 rho = 1770;      % [Kg/m^3]
16 nu = 1.8e-6;     % [m^2/s]
17 mu = nu*rho;     % [Pas]
18 deltaP = 25e3;   % [Pa]
19 L = 60.96;       % [m]
20
21 % boundary conditions
22 Tamb = 270.730;      % [K]
23 deltaT = 10:1:70;    % [K]
24 Ts = 50+273.15;      % [K]
25
26 % friction factor
27 fd = 0.01;           % [-]
28
```

```matlab
29  % rover properties
30  mrover = 899;          % [Kg]
31  crover = 870;          % [J/(Kg*K)]
32  Trover = 25+273.15;    % [K]
33  Ti = 20+273.15;        % [K]
34
35  if strcmp(data, 'ON')
36      Vpunto = 0.3:0.01:1.5;
37      mpunto = Vpunto*rho/(60*1e3);
38      n = length(mpunto);
39
40      AoutdeltaT = zeros(length(mpunto), 7);
41      for i = 1:n
42      Aout = mpunto(i)*cp*deltaT/(sigma*eps*(Ts^4 - Tamb^4));
43      index = find(Aout>=2.2,1);
44      Dl = 2*(((8*mu*L*(mpunto(i)/rho))/(pi*deltaP))^(1/4));
45      Dt = ((8*fd/pi^2)*(mpunto(i)^2/rho)/(deltaP)*L)^(1/5);
46      AoutdeltaT(i,1) = Vpunto(i);
47      AoutdeltaT(i,2) = ((Dl^2/4)^2)*deltaP/(8*mu*L);
48      AoutdeltaT(i,3) = deltaT(index);
49      AoutdeltaT(i,4) = Aout(index);
50      AoutdeltaT(i,5) = Dl*10^3;
51      AoutdeltaT(i,6) = Dt*10^3;
52      AoutdeltaT(i,7) = ((mrover*crover*(Trover-Ti))/(mpunto(i)*
            cp*deltaT(index)))/3600;
53      end
54
55      j = 1;
56      for i=1:size(AoutdeltaT,1)
57          if AoutdeltaT(i,4) <= 2.3 %&& AoutdeltaT(i,5) <= 9
58              AoutdeltaTmod(j,1:7) = AoutdeltaT(i,:);
59              j = j + 1;
60          end
61      end
62      [~,idx] = sort(AoutdeltaTmod(:,7));
63      AoutdeltaTmod = AoutdeltaTmod(idx,:);
64  end
65
```

```matlab
66    if strcmp(onPlot, 'ON')
67        Vpunto = 0.6:0.1:2;
68        mpunto = Vpunto*rho/(60*1e3);
69        n = length(mpunto);
70
71        %%%%%%%%%%% COLOR %%%%%%%%%%%%%%%%%%%%%%
72        max_Vpunto = max(Vpunto);
73        min_Vpunto = min(Vpunto);
74        colourShades = length(Vpunto);
75        colours = jet(colourShades);
76        %%%%%%%%%%%%%%%%%%%%%%%%%%%%%%%%%%%%%%%%
77
78        % 1st equation
79        figure(1)
80        for i = 1:n
81        Aout = mpunto(i)*cp*deltaT/(sigma*eps*(Ts^4 - Tamb^4));
82        plot(deltaT, Aout,'Color',colours(i,:),'LineWidth', 1.2);
              hold on;
83        plot(deltaT, 2.3*ones(length(deltaT),1),'k','LineWidth', 2)
              ; hold on;
84        xlabel('\DeltaT [K]','FontSize', 14,'FontWeight','bold');
85        ylabel('A_{out} [m^2]','FontSize', 14,'FontWeight','bold');
86        %title(sprintf('Flow rate [lpm] = %.2f', Vpunto(i)));
87        %pause(0.1);
88        end
89        h = colorbar;
90        colormap(colours)
91        caxis([min(Vpunto)*.999, max(Vpunto)*1.001])
92        ylabel(h,'Flow rate [lpm]','FontName','Times New Roman','
              FontSize',20)
93        set(gca, 'FontName','Times New Roman', 'fontsize', 18)
94
95        % 2nd equation
96        a = 1 * 3600;
97        b = 3 * 3600;
98        time = a:b;
99
100       figure (2)
```

```matlab
101     for i = 1:n
102     deltaTemp = ((mrover*crover*(Trover-Ti))./time)/(mpunto(i)*
            cp);
103     plot(time/3600, deltaTemp,'Color',colours(i,:) ,'LineWidth'
            , 1.2); hold on;
104     xlabel('Time [h]','FontSize', 14,'FontWeight','bold');
105     ylabel('\DeltaT [K]','FontSize', 14,'FontWeight','bold');
106     end
107     h = colorbar;
108     colormap(colours)
109     caxis([min(Vpunto)*.999, max(Vpunto)*1.001])
110     ylabel(h,'Flow rate [lpm]','FontName','Times New Roman','
            FontSize',20)
111     set(gca, 'FontName','Times New Roman', 'fontsize', 18)
112
113     % Diameter comparisons
114     figure (3)
115     plot(AoutdeltaT(:,1), AoutdeltaT(:,5),'b','LineWidth', 1.7)
            ; hold on;
116     plot(AoutdeltaT(:,1), AoutdeltaT(:,6),'r','LineWidth', 1.7)
            ; hold on;
117     plot(AoutdeltaT(:,1), 9*ones(length(AoutdeltaT(:,6)),1),'k'
            ,'LineWidth', 1.7); hold on;
118     legend('Laminar flow', 'Turbulent flow', 'Location', 'best'
            );
119     xlabel('$\dot{V}$ [lpm]','interpreter','latex','FontSize',
            14,'FontWeight','bold');
120     ylabel('D [mm]','FontSize', 14);
121     set(gca, 'FontName','Times New Roman', 'fontsize', 30)
122 end
```

WORST-CASE COLD CONDITIONS

```matlab
1  clearvars
2  close all
3  clc
4
5  % PLOT
```

```matlab
6   data = 'ON';
7   onPlot = 'ON';
8
9   % radiative properties
10  sigma = 5.670373e-8;      % [W/(m^2*K)]
11  eps = 0.85;               % [ - ]
12
13  % fluid
14  cp = 962.964;     % [J/(Kg*K)]
15  rho = 1770;       % [Kg/m^3]
16  nu = 1.8e-6;      % [m^2/s]
17  mu = nu*rho;      % [Pas]
18  deltaP = 25e3;    % [Pa]
19  L = 60.96;        % [m]
20
21  % boundary conditions
22  deltaT = 10:1:120;   %[K]
23  Ts = 72+273.15;      %[K]
24  %Tamb = 183.2305;     %[K]
25
26  % friction factor
27  fd = 0.01;        % [ - ]
28
29  % rover
30  mrover = 899;             % [Kg]
31  crover = 870;             % [J/(Kg*K)]
32  Trover = -15+273.15;      % [K]
33  Ti = 20+273.15;           % [K]
34
35  if strcmp(data, 'ON')
36      Vpunto = 0.5:0.01:0.97;
37      mpunto = Vpunto*rho/(60*1e3);
38      n = length(mpunto);
39
40      AoutdeltaT = zeros(length(mpunto), 7);
41      for i = 1:n
42      Aout = mpunto(i)*cp*deltaT/(sigma*eps*(Ts^4));
43      index = find(Aout>=2.2, 1);
```

```matlab
44        Dl = 2* ((( 8*mu*L*(mpunto(i)/rho) )/( pi*deltaP ))^(1/4));
45        Dt = ((8*fd/pi^2)*(mpunto(i)^2/rho)/(deltaP)*L)^(1/5);
46        AoutdeltaT(i,1) = Vpunto(i);
47        AoutdeltaT(i,2) = ((Dl^2/4)^2)*deltaP/(8*mu*L);
48        AoutdeltaT(i,3) = deltaT(index);
49        AoutdeltaT(i,4) = Aout(index);
50        AoutdeltaT(i,5) = Dl*10^3;
51        AoutdeltaT(i,6) = Dt*10^3;
52        AoutdeltaT(i,7) = abs((mrover*crover*(Trover-Ti))/(mpunto(i
            )*cp*deltaT(index))/3600);
53     end
54
55     j = 1;
56     for i=1:size(AoutdeltaT,1)
57         if AoutdeltaT(i,4) <= 2.3 %&& AoutdeltaT(i,5) <= 9
58             AoutdeltaTmod(j,1:7) = AoutdeltaT(i,:);
59             j = j + 1;
60         end
61     end
62     [~,idx] = sort(AoutdeltaTmod(:,6));
63     AoutdeltaTmod = AoutdeltaTmod(idx,:);
64 end
65
66 if strcmp(onPlot, 'ON')
67     Vpunto = 0.6:0.1:2;
68     mpunto = Vpunto*rho/(60*1e3);
69     n = length(mpunto);
70
71     %%%%%%%%%% COLOR %%%%%%%%%%%%%%%%%%%%%
72     max_Vpunto = max(Vpunto);
73     min_Vpunto = min(Vpunto);
74     colourShades = length(Vpunto);
75     colours = jet(colourShades);
76     %%%%%%%%%%%%%%%%%%%%%%%%%%%%%%%%%%%%%%%%
77
78     % 1st equation
79     figure(1)
80     for i = 1:n
```

```matlab
81      Aout = mpunto(i)*cp*deltaT/(sigma*eps*(Ts^4));
82      plot(deltaT, Aout,'Color',colours(i,:),'LineWidth', 1.2);
            hold on;
83      plot(deltaT, 2.3*ones(length(deltaT),1),'k','LineWidth', 2)
            ; hold on;
84      xlabel('\DeltaT [K]','FontSize', 14,'FontWeight','bold');
85      ylabel('A_{out} [m^2]','FontSize', 14,'FontWeight','bold');
86      %title(sprintf('Flow rate [lpm] = %.2f', Vpunto(i)));
87      %pause(0.1);
88      xlim([10 120])
89      end
90      h = colorbar;
91      colormap(colours)
92      caxis([min(Vpunto)*.999, max(Vpunto)*1.001])
93      ylabel(h,'Flow rate [lpm]','FontName','Times New Roman','
            FontSize',20)
94      set(gca, 'FontName','Times New Roman', 'fontsize', 18)
95
96      % 2nd equation
97      a = 1 * 3600;
98      b = 10 * 3600;
99      time = a:b;
100     figure (2)
101     for i = 1:n
102     deltaTemp = ((mrover*crover*abs((Trover-Ti)))./time)/(
            mpunto(i)*cp);
103     plot(time/3600, deltaTemp,'Color',colours(i,:) ,'LineWidth'
            , 1.2); hold on;
104     xlabel('Time [h]','FontSize', 14,'FontWeight','bold');
105     ylabel('\DeltaT [K]','FontSize', 14,'FontWeight','bold');
106     end
107     h = colorbar;
108     colormap(colours)
109     caxis([min(Vpunto)*.999, max(Vpunto)*1.001])
110     ylabel(h,'Flow rate [lpm]','FontName','Times New Roman','
            FontSize',20)
111     set(gca, 'FontName','Times New Roman', 'fontsize', 18)
112 end
```